



SCUOLA INTERNAZIONALE SUPERIORE DI STUDI AVANZATI

The impact of cosmological neutrinos on large-scale structure observables

Author:

GABRIELE PARIMBELLI

Supervisor:

PROF. MATTEO VIEL

A thesis submitted in fulfillment of the requirements
for the degree of Philosophiæ Doctor in
ASTROPHYSICS & COSMOLOGY

September 2020

Contents

Abstract	v
List of publications	vii
List of Figures	xv
List of Tables	xviii
1 Introduction: the standard cosmological model	1
1.1 A historical background to motivate this work	1
1.2 The homogeneous Universe	5
1.2.1 From the cosmological principle to Friedmann equations	5
1.2.2 Density parameters	7
1.2.3 Distances	8
1.2.4 A standard model for cosmology	8
1.3 The perturbed Universe	10
1.3.1 Equations of motion	10
1.3.2 Growth of perturbations	12
1.3.3 Non-linear growth: PT vs. N-body simulations	13
1.4 Statistical tools for cosmology	15
1.4.1 Random fields and two-point statistics	16
1.4.2 Initial conditions	18
1.4.3 Linear evolution of power spectrum and 2PCF	19
1.4.4 Non-linearities	21
1.5 Observables of large-scale structure	25
1.5.1 Clustering of biased tracers	26
1.5.2 Cosmic shear	27
1.5.3 Other large-scale structure observables	32

2	Massive neutrino cosmology	34
2.1	Why “massive” neutrinos? Why cosmology?	34
2.2	Impact on background cosmology	36
2.2.1	Thermal history and density parameter	36
2.2.2	Distances	39
2.3	Impact on density perturbations	40
2.3.1	Equations of motion	40
2.3.2	Free-streaming and linear power spectrum	42
2.3.3	Non-linear growth	45
2.4	Impact on large-scale structure observables	48
2.4.1	Clustering of biased tracers	48
2.4.2	BAOs in the 2PCF	49
2.4.3	Cosmic shear	51
2.4.4	Other large-scale structure observables	53
3	The effects of massive neutrinos on the linear point of the correlation function	54
3.1	BAOs, linear point and massive neutrinos	54
3.2	Methodology	57
3.2.1	Effects of massive neutrinos in linear theory	58
3.2.2	Simulations	59
3.2.3	Estimating the 2PCF from simulations	61
3.2.4	Estimating the linear point from simulations	62
3.3	Results	66
3.3.1	Linear perturbation theory: linear point redshift evolution	67
3.3.2	Non-linear gravity: linear point redshift evolution	67
3.3.3	The linear point as a standard ruler	69
3.3.4	Detecting the neutrino mass with the linear point	71
4	Degeneracies between massive neutrinos and nuisances in matter clustering and weak lensing	78
4.1	Motivation	78
4.2	Theoretical framework	81
4.2.1	Observables: CDM+b power spectrum and cosmic shear	82
4.2.2	Impact of massive neutrinos	83
4.2.3	Impact of baryon feedback	84
4.3	Method	88

4.3.1	Clustering survey	88
4.3.2	Cosmic shear survey	91
4.4	Results	93
4.4.1	Fitting baryon feedback on massive neutrino cosmologies	93
4.4.2	Baryonic feedback and massive neutrinos degeneracies	95
4.4.3	Degeneracy with intrinsic alignment	99
4.5	Discussion	104
4.6	Future work	106
5	Neutrino clustering in the Milky Way	108
5.1	Detecting relic neutrinos with clustering	108
5.2	Neutrino gravitational clustering	110
5.3	Forward versus backward N -one-body method	112
5.4	Computing neutrino clustering with back-tracking	114
5.5	Density profiles and gravitational potential	115
5.5.1	The Milky Way	116
5.5.2	Other objects: Virgo & Andromeda	119
5.5.3	Gravitational potential grid	120
5.6	Results	124
6	Conclusions	129
6.1	Summary	129
6.2	Future work	133
	Appendices	137
A	Non-linear power spectra: HALOFIT	138
A.1	A quick prediction for non-linearities	138
A.2	The original HALOFIT	139
A.3	Addition of massive neutrinos	140
A.4	The Takahashi model	141
A.5	HMcode: a halo model approach	142
B	Solving the Poisson equation	145
B.1	A general solution	145
B.2	Spherical symmetry	146
B.2.1	Navarro-Frenk-White profile	146
B.2.2	Einasto profile	147

B.2.3	Milky Way bulge	147
B.3	Disks	148
B.3.1	General solution of Poisson equation in cylindrical coordinates	149
B.3.2	Exponential disks	149
	Bibliography	150

Abstract

In the last couple of decades, several cosmological experiments probing the Cosmic Microwave Background (CMB) and the large-scale structure of the Universe have confirmed the wonderful agreement between data and the standard cosmological model, the Λ CDM paradigm. According to the latter, our Universe is filled, besides ordinary baryonic matter, with a cosmological constant which makes the expansion accelerate and cold dark matter (CDM) as the main driver for structure formation. A small amount of energy is carried by cosmological neutrinos. While the Standard Model of particle physics predicts them to be massless, the detection of flavor oscillations highlighted how they do indeed have a mass. Unfortunately, these experiments are not able to constrain the mass scale. On the other hand cosmology has the power to do so, thanks to the considerable impact that neutrinos have on the cosmological observables.

Neutrinos decouple from the photon-baryon plasma in the very early Universe, when they are still in the relativistic regime. While on large scales they essentially behave like CDM, the high thermal velocities they possess prevent them from clustering, at linear level, on scales smaller than the free-streaming length. This induces a back-reaction on the growth of CDM density perturbations, which becomes scale-dependent, and affects the matter power spectrum and all the observables that depend upon it.

Future surveys like Euclid, the Large Synoptic Survey Telescope (LSST), the Dark Energy Survey Instrument (DESI) and the Square Kilometer Array (SKA) will likely measure the sum of the three neutrino masses (M_ν) for the first time. In order to have a correct estimate of M_ν , considerable efforts must be made on the theoretical side to assess which observables are the most suitable for the detection, to accurately quantify the impact of neutrino mass on such observables and to carefully study of the systematics, nuisances and biases that can affect such measurements. The research I have been carrying out during my Ph.D. was developed with this goal in mind. This thesis presents the main and most relevant results of papers published on refereed journals, sorted according to the degree of non-linearity involved in the problem.

The first analysis presented extends previous works on the linear point (LP) of the two-point correlation function (2PCF) to the case of massive neutrino cosmologies. So far, the LP has been shown to be an excellent standard ruler for cosmology. By using state-of-art N -body simulations, we show that also in cosmologies with massive neutrinos the LP retains its nature of standard ruler for the CDM and halo real-space

2PCF. To do so, we use a model-independent parametric fit in the range of scales of the Baryon Acoustic Oscillations (BAOs). We also propose a procedure to constrain neutrino masses by comparing the measured LP from data to the LP of a mock galaxy catalog with massless neutrinos and the same remaining cosmological parameters. We find that the sum of the neutrino masses could in principle be detected provided that several redshift bins are used, the survey volume is sufficiently large and the shot noise of the galaxy sample is sufficiently low.

In the second work we investigate the possibility that the degeneracies between the effects of neutrino mass and those of baryons on the large-scale matter distribution (e.g. AGN feedback, galactic winds) could bias the measurement of M_ν in future surveys probing galaxy clustering and cosmic shear. To this end, we generate synthetic data sets and fit them using the Markov Chain Monte Carlo (MCMC) technique. Baryon feedback is modelled with fitting functions that describe the suppression to the matter power spectrum through free parameters with well-established physical meaning, while neutrinos are modelled through the HALOFIT operator calibrated on N -body simulations. The covariance matrix entering in the likelihood function contains cosmic variance and shot/shape noise as sources of statistical uncertainties, while theoretical inaccuracies are accounted for through a mode-coupling function with a given correlation length. For the weak lensing analysis we also take into account the systematic carried by the intrinsic alignment effect. Overall, for both clustering and shear, we are always able to recover the right input neutrino mass well within $1\text{-}\sigma$. In the shear survey, we also report some interesting degeneracy between M_ν and the parameter controlling the amplitude of the intrinsic alignment effect.

Finally, the third work concerns the clustering of relic neutrinos in the Milky Way. Since neutrinos are massive, they feel the gravitational attraction of the Galaxy and should therefore be more abundant at the Earth position than the average cosmological value. This could enhance the event rate of future experiments aiming at a direct detection of the cosmic neutrino background. This work improves past analyses by performing full 3-D calculations and including in the budget close-by structures like the Virgo cluster and the Andromeda galaxy. The neutrino clustering is computed by back-tracking particles in the Milky Way gravitational field using the N -one body technique. Our results overall confirm previous findings, but highlight how the contribution of the Virgo cluster is relevant. The local neutrino density (and in turn the detection rate) is found to be enhanced by 0.53% for a neutrino mass of 10 meV, 12% for 50 meV, 50% for 100 meV or 500% for 300 meV.

List of publications

The following thesis is the result of the scientific research that I carried out as a Ph.D. student in the Astrophysics & Cosmology sector at SISSA, Trieste (Italy), under the supervision of Prof. Matteo Viel and in collaboration with several people from SISSA as well as other different institutions. In particular, this thesis is based upon the following publications:

- G. Paribelli, M. Viel, E. Sefusatti
On the degeneracy between baryon feedback and massive neutrinos as probed by matter clustering and weak lensing
JCAP01(2019)010, [arXiv:1809.06634](#)
- P. Mertsch, G. Paribelli, P.F. de Salas, S. Gariazzo, J. Lesgourgues, S. Pastor
Neutrino clustering in the Milky Way and beyond
JCAP01(2020)015, [arXiv:1910.13388](#)
- G. Paribelli, S. Anselmi, M. Viel, C. Carbone, F. Villaescusa-Navarro, P.S. Corasaniti, Y. Rasera, R. Sheth, G.D. Starkman and I. Zehavi
The effects of massive neutrinos on the linear point of the correlation function
Submitted to JCAP, [arXiv:2007.10345](#)
- G. Paribelli, G. Scelfo, M. Viel, A. Schneider, S. Camera
Testing degeneracies among non-standard dark matter paradigms with cosmic shear
in prep., (2021)

List of Figures

1.1	The black solid line shows the matter linear matter power spectrum at $z = 0$ computed using the best-fit parameters from Planck (2018) in the Λ CDM model. The dotted black line represents the non-linear counterpart (see Section 1.4.4 for an insight). Dots of different colors are extrapolated values for $P(k)$ - coming from different experiments and probes - which are in impressive agreement with theory over four decades in scales. Taken from Planck Collaboration (2018).	21
1.2	Summary of two-point statistics for total matter in the Λ CDM model. In the left panel power spectra at different redshifts are shown whereas in the right panels we display 2PCF multiplied by a r^2 factor to better show the BAO feature. Solid lines show the non-linear prediction according to Mead et al. (2015), where we have also smoothed the BAO peak using the prescription of Tegmark et al. (2006). Dashed lines instead represent linear theory. Different colors label different redshift.	25
1.3	Shear power spectrum for a distribution of galaxies in 3 redshift bins. The distribution is chosen to be $\mathcal{P}(z) \propto z^2 \exp(-z/0.24)$, the bin edges are at $z = 0.1, 0.478, 0.785, 1.5$. In each panel, the solid black line represents the measured shear power spectrum for that pair of bins. The latter can be split into the cosmological signal (solid blue lines) and the intrinsic alignment contributions (GI in green, II in red). The dotted lines represent the same quantities, but assuming linear theory for the matter power spectrum. The dotted magenta line is the shape-noise term, where we assumed a RMS ellipticity of 0.3. Gold shaded areas represent the cosmic variance expected from a survey with $f_{\text{sky}} = 0.366$; grey shaded areas are regions were measurements will likely be excluded from the analysis in future surveys.	31

2.1	The two allowed schemes for neutrino masses: normal hierarchy (NH) and inverted hierarchy (IH). The minimum masses allowed in each scenario are found by setting the lowest neutrino eigenstate mass to zero. Taken from Lesgourgues & Pastor (2006).	36
2.2	Evolution of density parameters as a function of scale factor or, equivalently, redshift for a flat Universe. The green line is the radiation density parameter that dominates at early times before dropping down, leaving the stage to a matter dominated era (with baryons in red and CDM in blue). The black line is the cosmological constant. The solid, dashed and dotted lines represent the density parameter of three different neutrino species with masses 0.05, 0.01 and 0 eV, respectively. As it can be clearly seen, the most massive species become non-relativistic first and when it occurs, they start behaving like a pressureless fluid. The total energy density (which is always equal to 1) is denoted by the dotted black line. Finally, the dot-dashed vertical line at $a = 1$ denotes present time.	40
2.3	Impact of neutrino mass on various distance measures as a function of redshift. Top panels show the inverse Hubble distance measure c/H (left), the comoving distance (center, accompanied by the luminosity distance - dashed line - and the angular diameter distance - dot-dashed line) and the isotropic volume distance (right) for a Λ CDM Universe. Bottom panels show the relative differences when including one massive neutrino species with $M_\nu = 0.2, 0.4, 0.6$ eV, denoted by the dashed, dot-dashed and dotted lines respectively.	41
2.4	Suppression due to massive neutrinos in various power spectra at $z = 0$. Different colors label different M_ν (a single massive species is assumed): blue for 0.2 eV, red for 0.4 eV, green for 0.6 eV. Solid lines represent the non-linear suppression on the total matter power spectrum according to eq. 2.33, whereas dashed and dotted lines do the same for the linear total matter and CDM plus baryons power spectra, respectively. . . .	47
2.5	Impact of neutrino mass on the 2PCF of CDM+b at $z = 0$. The top panel shows both the linear (dashed lines) and the non-linear (solid lines) 2PCFs for different neutrino masses: Λ CDM in black, 0.2 eV in blue, 0.4 eV in red, 0.6 eV in green. A single massive neutrino species is assumed. The bottom panel shows the ratios of all the above said 2PCFs with respect to the Λ CDM case.	50

2.6	Impact of massive neutrinos on the shear power spectrum. The same settings of fig. 1.3 (redshift bins, galaxy distribution and cosmological parameters except for neutrino mass) have been used here. In each panel we show the suppression on the measured shear power spectrum (black lines), split in its contributions (GG in blue, GI in green, II in red), with respect to the Λ CDM case. Solid lines show such suppression for $M_\nu = 0.2$ eV, dashed lines for 0.4 eV and dotted lines for 0.6 eV. Grey bands show multipole regions likely excluded in upcoming surveys. Gold shaded areas represent cosmic variance for a survey with $f_{\text{sky}} = 0.366$	52
3.1	2PCF of CDM from the DEMNUni and the Quijote sets, as measured with eq. 3.3. We show here, only for the common redshift between the two sets, the 2PCF multiplied by r^2 and divided by the σ_8^2 and the growth factor for Λ CDM squared in order to make it easier a comparison between different sets. To facilitate the comparison, we plot the mean of the 50 DEMNUni and of the first 50 Quijote realizations, each with an uncertainty corresponding to the standard error on the mean. In the left panels we display the two Λ CDM cases, with the DEMNUni in dark red and the Quijote in dark blue; the right panels are left for the massive neutrino models, with the DEMNUni in light red and the Quijote with 0.1 eV (0.2 eV) in blue (light blue).	63
3.2	Covariance of the 2PCF in our simulations for the Λ CDM at $z = 0$. The left panels refer to the DEMNUni set, while the right panels show the same but for the Quijote simulations. Here we rescale the covariance by the number of realizations, i.e. we represent the covariance of the 2PCF in a cubic box of side 1000 Mpc/ h . Dots and diamonds represent the measured covariance of CDM (top panels) and halos (bottom), respectively, while solid and dashed lines are the analytical equivalent under the assumption of a Gaussian density field (see eq. 3.9). Different colors label different elements of the covariance matrix: red is for the diagonal elements (i.e. the variance of the 2PCF), while blue, green and yellow show respectively the 10-th, 20-th and 30-th off-diagonal elements (with an offset introduced for sake of clarity).	65

3.3	The evolution of the dip (left), LP (center) and peak (right) positions of the cold dark matter plus baryons 2PCF in the $z - M_\nu$ plane, according to linear theory. For each neutrino mass, the percentage difference between the quantity considered and its value at $z = 0$ is plotted. Solid contour lines denote positive differences, whereas dashed lines denote negative values. Here we keep σ_8 fixed for different neutrino masses, but the result for fixed A_s is almost identical.	66
3.4	We plot 68% confidence limits on the position of the dip, the peak and the LP of the 2PCF for every snapshot of our simulation sets. The top panels refer to the DEMNUni set, for which we have the Λ CDM model (top left) and the massive neutrino model (top center). The bottom panels refer to the Quijote set with its three different models: Λ CDM (bottom left), $M_\nu = 0.1$ eV (bottom center) and $M_\nu = 0.2$ eV (bottom right). For each subpanel, dotted vertical lines represent the linear-theory prediction of the LP. The gray area shows the $\pm 0.5\%$ LP intrinsic-bias range identified in Anselmi et al. (2016) (see main text). The remaining solid and dashed lines show the evolution in redshift of the LP, the dip and the peak, respectively, according to eq. 3.11. Blue and red bars refer to the results for CDM and halos, respectively. Small offsets with respect to the snapshot redshifts have been introduced for the sake of clarity. In the Quijote sector, the red bars relative to the $z = 3$ snapshot are missing because the high shot noise made it impossible to have a clear estimate of the LP. It can be noticed that the LP is particularly stable and always in agreement with the linear prediction at the 0.5% level both for Λ CDM and when massive neutrinos are included.	69
3.5	Signal-to-noise ratio, computed with eq. 3.12, for a possible neutrino mass detection using the LP shift with respect to the Λ CDM case. The S/N caused by a neutrino mass of 0.1 (0.2) eV is displayed on the left (right) panels. Top panels show the results for CDM only, while the bottom ones show the same for halos. The left columns of the bottom panels are missing because we do not perform the analysis for halos at $z = 3$	72

3.6	The figure shows the signal-to-noise ratio for a possible neutrino-mass detection using the LP shift with respect to the Λ CDM case. Here we compare the signal-to-noise for the 50 realizations of the DEMNUni set with the 50 of the Quijote (i.e. our reference volume). Squares represent the ratio for the DEMNUni set, light-blue and pink for CDM and halos respectively. Circles refer to the Quijote set, where we distinguish the model with $M_\nu = 0.1$ eV (dashed line) and the one with $M_\nu = 0.2$ eV (dotted line). Like in the previous figures, CDM is represented in blue, whereas halos are in red. Finally, the dotted black horizontal line symbolizes a S/N ratio equal to 1.	74
3.7	LP position uncertainty as a function of redshift and volume (i.e. number of realizations) in the Quijote set. We show the case for the Λ CDM (left) and the two massive neutrino models (center and right). The blue surfaces show the 68% uncertainty on the LP in the 2PCF of the CDM, while the red ones are the equivalent for halos.	76
4.1	The four panels show the effect of the neutrino mass and of the three different feedback parameters of the BCM on the matter power spectrum at $z = 1$ (approximately the median redshift of future surveys). All the ratios are taken with respect to a CDM+b power spectrum model (linear with respect to the linear, non-linear w.r.t. the non-linear) in a cosmology with minimum-allowed neutrino mass $M_\nu = 0.056$ eV and no baryon feedback. In the top left panel the neutrino mass is varied while the ratio in both linear and non-linear regime are shown. The top right panel shows the effect of increasing $\log M_c$, in the bottom left panel we change the parameter η_b , while in the bottom right we display how the redshift parameter affects the feedback fitting function. The gold shaded areas represent cosmic variance for a survey like in Audren et al. (2013) in a redshift bin of $\Delta z = 0.1$ centered at $\bar{z} = 1$. The grey shaded areas represent the theoretical uncertainty on the matter power spectrum due to the HALOFIT fitting formulae, 4.14. In all the panels a vertical line at $k = 0.5$ h/Mpc is drawn, to mark the maximum k at which our analysis is extended.	84

4.2	This picture is the same of fig. 4.1 but here the cosmic shear power spectrum is shown, with a source distribution like in Audren et al. (2013), a sky coverage of $f_{\text{sky}} = 0.375$ and with all galaxies in a single bin, i.e. no tomography has been performed.	85
4.3	Contour plots showing the posterior probability distribution for the three feedback parameters. These are obtained when matter (blue and green, where we stop at 2 different k_{max}) and shear (red) spectra for cosmologies with minimal neutrino mass ($M_\nu = 0.056$ eV) and baryon feedback are fitted on spectra in massive neutrino cosmologies ($M_\nu = 0.45$ eV in this plot) with no baryon feedback.	94
4.4	1-D posterior probability distributions for neutrino mass for all the cases analysed in Section 4.4.2. The error-bars represent the 68% confidence level on M_ν using clustering (blue) and weak lensing (red). The left columns show the feedback parameters used to generate the mock data. The top panels show the results when $M_\nu = 0.15$ eV, while the bottom ones do the same for the case $M_\nu = 0.30$ eV. The grey shaded area in the top panels mark the region $M_\nu < 0.056$ eV, forbidden by particle physics experiments.	97
4.5	1-D and 2-D posterior PDFs for M_ν , $\log M_c$ and η_b for 2 of the 16 runs described in Sections 4.4.2 whose parameters are displayed in the plot. The blue contours show the results for clustering, while the red contours represent the results from the cosmic shear survey. The grey dashed lines show the “true” values, used to generate the mock data.	98
4.6	Percentage difference on the shear power spectrum $C(\ell)$ due to an increasing neutrino mass (from red to blue) or an increasing IA (from green to yellow) with respect to a model with minimal neutrino mass and no IA. We assume here a single tomographic bin.	101
4.7	Results obtained from the 16 different runs for a cosmic shear survey including the IA effect. For clarity we have separated the runs with same neutrino mass and IA parameters. The black vertical lines represent the true input value, the error-bars mark the 68% confidence level for neutrino mass (red) and IA parameter A_{IA} (green). The left columns report the values of the feedback parameters used to generate mock data (z_c has been set to 2). The grey shaded area is forbidden by the solar neutrino experiments.	103

4.8	Triangle plot showing 1-D and 2-D posterior PDFs for M_ν , $\log M_c$, η_b and A_{IA} for two of the 16 runs described in Sections 4.4.2 and 4.4.3 whose parameters are displayed in the plot. The red and green contours represent the results from the cosmic shear survey with and without IA, respectively. The grey dashed lines show the “true” values, used to generate the mock data.	103
4.9	This picture shows the degeneracy between neutrino mass and the IA parameter for the 16 different cases analysed in Section 4.4.3. The top plots have $M_\nu = 0.15$ eV, while the bottom ones have $M_\nu = 0.3$ eV; odd columns have $A_{IA} = 1.3$, even columns have $A_{IA} = -1.3$ (the dashed lines help the view in marking the true value). The parameters of the set are written inside each panel. The contour lines shown are 68% and 95% confidence level, while the dashed black lines show the true values for the parameters. It is clearly visible that in some cases the degeneracy between the two parameters is totally absent, but even where is present it will be likely not to bias the measurement on neutrino mass.	104
5.1	Relative position of the Milky Way, Andromeda Galaxy and the Virgo Cluster. The size of the dots matches the virial radius of the object. The grey shaded plane represents the plane of the Milky Way. . . .	121
5.2	The colormap shows the potential generated by an exponential disk. The red lines denote isocontours for this potential, while the black ones denote the isocontours for the potential generated by a point-like source with the same mass. At $R/R_s \sim z/R_s \sim 25$ the difference between the spherical and cylindrical potentials is smaller than 1%. .	123
5.3	For each neutrino mass state, we plot the ratio $n_\nu/n_{\nu,0}$ at the Earth’s position as a function of the neutrino mass m_ν . We consider contributions to the gravitational potential from the Galactic DM halo (<i>top panel</i> : NFW profile, <i>bottom panel</i> : Einasto profile), from baryons in the Galaxy, from the Virgo cluster and from the Andromeda galaxy. We also compare with earlier studies (Ringwald & Wong (2004); de Salas et al. (2017); Zhang & Zhang (2018)).	125
5.4	Clustering factor as a function of the earliest redshift z_{back} at which neutrino trajectories are integrated, for different values of the neutrino mass and different astrophysical configurations.	127

List of Tables

1.1	Fiducial values for the Λ CDM cosmology used in this and in the following Chapter. When we add massive neutrinos in Chapter 2, we will keep Ω_m and Ω_b fixed, so that an increase in M_ν will correspond to a decrease in Ω_c	25
3.1	Different specifics of the two simulation sets employed in this work.	60
3.2	Average number of halos per realization, per snapshot and simulation set.	61
3.3	The table summarizes the results for the LP (including the 0.5% correction) for the DEMNUni (left) and the Quijote (right) simulations. We show the LP position with 1- σ uncertainty.	70
4.1	Best-fit values of the baryon parameters obtained from the analysis of Section 4.4.1, where we fitted spectra with baryonic features onto spectra containing massive neutrinos. We also report the difference in the reduced chi-squared $\Delta\chi_{\text{red}}^2$ with respect to the one obtained using the “true” model. M_c is in units of M_\odot/h while the errors or lower limits represent the 68% confidence level. The priors are $\log M_c [M_\odot/h] \in [12, 30]$, $\eta_b \in [0, 30]$, $z_c \in [0, 30]$	94
4.2	Best-fit values and 68% confidence level intervals for the parameters obtained from the power spectrum, $P(k)$, as well as from the cosmic shear, $C(\ell)$, analysis. The mark \times means that such parameter is not constrained at all. See Section 4.4.2 for details.	96
4.3	This table shows the 68% confidence level intervals for the parameters obtained from the analysis of cosmic shear power spectra to which the IA contribution has been added. See Section 4.4.3 for details.	102

5.1	DM density parameters for the Milky Way at $z = 0$, obtained by fitting the data from Pato & Iocco (2015), following the same procedure as in de Salas et al. (2017).	117
5.2	Density profile parameters for the baryonic components at $z = 0$. We also provide the total mass for each component. All the components have a profile described by eq. 5.18, except for the bulge, which follows a de Vaucouleurs profile (eq. 5.17). The scale radii and heights are taken from Misiriotis et al. (2006), as specified in the main text. The redshift evolution of the total mass is found following the N -body simulation results of Marinacci et al. (2014), while we assume that R_s and z_s do not evolve in time.	118
5.3	DM density parameters for the Andromeda galaxy and the Virgo cluster at $z = 0$. The parameters for Virgo are taken from Fouque et al. (2001), and for Andromeda from Kafle et al. (2018).	121
5.4	Characteristics of the grid used for the derivative of the contributions to the potential.	123
A.1	The Table shows the values of the parameters used by HMcode (Mead et al. (2015, 2016)) to fit the matter power spectrum from DM only simulations in Λ CDM cosmologies. In this work we typically use these parameters for the non-linear power spectrum.	143

1

Introduction: the standard cosmological model

*If you wish to make an apple pie
from scratch, you must first invent
the Universe.*

Carl Sagan

*We became self-aware only to
realize this story is not about us.*

1.1 A historical background to motivate this work

Since the dawn of its existence, mankind has tried to find explanations for celestial phenomena. While in ancient times astronomy was tightly related to philosophy and religion, it was only around the 16-th century that a scientific approach started to be used. Observations by Brahe, Kepler and Galileo and the development of the theory of gravitation by Newton represent some of the fundamental milestones of this process of transformation.

We can argue that the birth of modern cosmology (from the ancient Greek *κόσμος*, “order”, and *λόγος*, “study”) dates back in the 1920s after the “Great Debate” about

the nature of the spiral nebulae took place. The discovery, by Edwin Hubble in 1924, that the Andromeda nebula was an actual galaxy proved that the Universe was much wider than it was thought back then and that the Milky Way was just one of the existing billions of galaxies.

On the theoretical side, Albert Einstein’s new theory of gravity, General Relativity (GR), had successfully been tested against observations of gravitational lensing and the precession of the orbit of Mercury. These combined efforts, together with the striking discovery of the expansion of the Universe (Hubble (1929)) paved the way to the development of a completely new branch of physics.

In the following decades, the idea that the Universe had evolved from an initial state of high energy and temperature started to take hold in the scientific community. Little by little, all the pieces of the puzzle came together: in the late 1940s Big Bang Nucleosynthesis (BBN) was proposed as the mechanism that created the lightest elements in the first 3 minutes (Alpher et al. (1948)); the discovery of the Cosmic Microwave Background (CMB, Penzias & Wilson (1965)) confirmed the key prediction of a relic radiation from the Big Bang; rotation curves of galaxies and cluster dynamics (see e.g. Clowe et al. (2006)) indirectly proved the existence of dark matter (DM) as the dominating form of matter in the Universe and as the main driver for galaxy formation; the theory of inflation (first proposed by Guth (1981)) explained, among other things, how the small density perturbations that would give rise to galaxies were created in the primordial Universe; finally, the unexpected discovery of the accelerated expansion of the Universe through the observation of distant type-Ia supernovae (SNIa, Perlmutter et al. (1999); Riess et al. (1998)) unveiled how the dominant form of energy that permeates our Universe is completely unknown.

All these contributions were crucial to build the standard model of cosmology, the Λ CDM paradigm. Under the assumption of homogeneity and isotropy, the Universe is ruled by Einstein’s field equations for a Friedmann-Lemaître-Robertson-Walker (FLRW) metric. The background expansion is driven by the so-called density parameters Ω_i , i.e. the energy densities of the different species of particles in the Universe. Constraints on these cosmological parameters have extraordinarily improved in the last two decades, especially thanks to the latest CMB experiments (Hinshaw et al. (2013); Planck Collaboration et al. (2018)). Thanks to these probes, we know that $\sim 70\%$ of the energy density of the Universe is in the form of a cosmological constant (Λ) associated to dark energy (DE). Ordinary matter (which is referred to as “baryonic matter” or simply “baryons” in cosmology) only makes up $\sim 5\%$ of the energy density, while the remaining $\sim 25\%$ is made by DM. This component is supposed to

be massive enough (i.e. cold, CDM) and collisionless in order to be able to form the galaxies and the large-scale structures that we observe today. However, warm dark matter (WDM) models, in which DM was quasi-relativistic at decoupling but behaves as CDM today, have become very popular in the last decades (see e.g. Bode et al. (2001) for a review).

A little fraction of energy density today is carried by photons and neutrinos. The existence of a relic neutrino background (Cosmic Neutrino Background, $C\nu B$), analogous to the CMB and with density and temperature tightly related to it, is a key prediction of the Big Bang model which has not been detected yet. While for the photons the energy density is well constrained by CMB temperature (Planck Collaboration et al. (2018)) through blackbody radiation laws, for neutrinos the situation is much more subtle. According to the Standard Model of particle physics, neutrinos are massless particles which come in three different species (flavors). If this were the case, from a cosmological point of view they would be indistinguishable from photons, adding a contribution to their energy density of about $\sim 70\%$. However, the detection of neutrino oscillations showed that neutrinos do in fact possess a mass. These experiments were only able to constrain the difference of square masses between different species, leading to a lower limit of the total neutrino mass $M_\nu = \sum_i m_{\nu,i}$ of ≈ 0.06 eV assuming normal hierarchy (NH) and ≈ 0.1 eV assuming inverted hierarchy (IH) (see e.g. Lesgourgues & Pastor (2006)).

On the other hand, cosmology has the power to constrain M_ν providing upper limits. As we will see more in detail in Chapter 2, neutrinos decouple in the very early Universe from the baryon-photon plasma, when they are still relativistic. The high thermal velocity to which they are subject prevents them from clustering on scales smaller than the free-streaming length λ_{fs} . The net result is a suppression of the growth of density fluctuations at small scales, which can in principle be detected by CMB or large-scale structure experiments. In fact, cosmology has so far been able to place either upper limits (e.g. Giusarma et al. (2016)) or show marginal preference for a non-vanishing neutrino mass (Beutler et al. (2014); Battye & Moss (2014); Di Valentino et al. (2017)). While the latest “large-scale-structure-only” experiments including weak lensing, SNIa and Baryon Acoustic Oscillations (BAOs) have determined $M_\nu < 0.26$ eV at 95% confidence level (Abbott et al. (2018)), the most stringent constraint on M_ν is currently represented by the combination of CMB (Planck Collaboration et al. (2016)) with BOSS Lyman- α forest data, providing $M_\nu < 0.12$ eV at 95% confidence level (Palanque-Deslattes et al. (2015a)).

The number of relativistic degrees of freedom, i.e. the number of active neutrinos corrected for non-instantaneous decoupling, has also been well constrained to $N_{\text{eff}} = 2.99 \pm 0.17$ by Planck Collaboration et al. (2018), in agreement with the standard model prediction of 3.046 (Mangano et al. (2005)). Actually, the measured value of N_{eff} could in principle be due to any relativistic species in the primordial Universe, such as axions, gravitinos, scalar fields oscillating in a quartic potential, (self-)interacting relics and so on. All these exotic species have specific values for their effective sound speed ($c_{\text{eff}}^2 = \delta P / \delta \rho$) and viscosity speed (c_{vis}^2 , which controls the amount of anisotropic stress), see e.g. Trotta & Melchiorri (2005); Archidiacono et al. (2011). The case of standard active neutrinos, in particular, requires $c_{\text{eff}}^2 = 1/3$ and $c_{\text{vis}}^2 = 1/3$ (in units where $c = 1$). These phenomenological parameters were constrained by Planck Collaboration et al. (2016) to $c_{\text{vis}}^2 = 0.331 \pm 0.037$ and $c_{\text{eff}}^2 = 0.3242 \pm 0.0059$, i.e. consistent with the expected values at $\sim 0.1 \sigma$ and $\sim 1.5 \sigma$, respectively.

As a final relevant point, despite not having an absolute mass measurement yet, the narrow gap between the minimum mass allowed by particle physics and the cosmological constraints is sufficient to mildly favor NH over IH (Hannestad & Schwetz (2016); Gerbino et al. (2017); Vagnozzi et al. (2017); Capozzi et al. (2017)). Therefore, cosmological observations are fundamental tools not only for cosmology itself, but also for particle physics.

The next few years will see a flourishing of experiments that will be devoted to large-scale structure measurements: while the Dark Energy Survey¹ (DES) is already ongoing, Euclid², the Large Synoptic Survey Telescope (LSST)³, the Dark Energy Spectroscopic Instrument⁴ (DESI) and the Square Kilometer Array⁵ (SKA) will soon start operating.

These ambitious projects will likely be able to measure neutrino mass for the very first time (e.g. Euclid Collaboration et al. (2019a); Zhan & Tyson (2018); Yohana et al. (2019); Sprenger et al. (2019)). Therefore, a detailed study of the effect of neutrino mass on cosmological observables, along with a careful analysis of the systematics, nuisances and biases that affect measurements and theoretical predictions is of primary importance in order to obtain accurate results: in summary, this has been the twofold goal of my work as a Ph.D. student, summarized in this thesis.

¹<https://www.darkenergysurvey.org/>

²<https://www.euclid-ec.org/>

³<https://www.lsst.org/>

⁴<http://desi.lbl.gov/>

⁵<https://www.skatelescope.org/>

The thesis is structured in a way that allows first to familiarize with the standard Λ CDM model without massive neutrinos (Chapter 1), by defining the main quantities that will be employed. In Chapter 2, we dig into the details of massive neutrino cosmology, describing how much the picture changes with respect to the pure Λ CDM paradigm and quantifying the impact that neutrino mass has on both background quantities and large-scale structure observables. The following three Chapters are dedicated to describe the actual research that I have been carrying out during my Ph.D., based on as many papers that have been published on or submitted to refereed journals. These Chapters are sorted by the degree of non-linearity of the physical phenomena described in each of them, starting from the most linear: in Chapter 3 we investigate the impact of M_ν on the linear point of the two-point correlation function (Parimbelli et al. (2020)); in Chapter 4 we carefully test whether baryonic processes will bias the measurements of neutrino mass in future galaxy clustering and cosmic shear surveys (Parimbelli et al. (2019)); in Chapter 5 we extend previous works (Ringwald & Wong (2004); Zhang & Zhang (2018); de Salas & Pastor (2016)) on gravitational neutrino clustering in the Milky Way in order to predict a possible future direct detection of the cosmic neutrino background (Mertsch et al. (2020)). The latter is accompanied by Appendix B, where we show how we solved the Poisson equation to compute neutrino clustering. The final Chapter of the thesis (Chapter 6) draws the conclusions for the single papers and eventually frames them in the big picture, summarizing which are the possibilities at the state-of-the-art and exploring future prospects for massive neutrino cosmology and beyond.

1.2 The homogeneous Universe

Since the fundamental interaction responsible for the formation of structures we observe today in the Universe is gravity, the correct theory to use to describe it is Einstein's General Relativity (GR). In this Section we briefly show the steps that led to the building of the standard cosmological model. Then, we will define all the fundamental quantities we will deal with in this work, including ages, distances and the main cosmological parameters.

1.2.1 From the cosmological principle to Friedmann equations

GR describes gravity as curvature of space-time through Einstein's field equations:

$$R_{\mu\nu} - \frac{1}{2}g_{\mu\nu}R + g_{\mu\nu}\Lambda = \frac{8\pi G}{c^4}T_{\mu\nu}. \quad (1.1)$$

The left hand side is fully determined by the metric tensor $g_{\mu\nu}$, which characterizes the properties of space-time. The Ricci tensor $R_{\mu\nu}$ and the Ricci scalar $R = g^{\mu\nu} R_{\mu\nu}$ are a measure of how the geometry of space-time affects distances, while Λ is the cosmological constant. On the right hand side the stress-energy tensor $T_{\mu\nu}$ contains energy densities and pressures as responsible for the space-time curvature.

The standard cosmological model bases itself on the fundamental observation (also supported by theoretical arguments) called the *cosmological principle*, which states:

The Universe is homogeneous and isotropic on large enough scales.

It can be shown (Weinberg (1972)) that the only space-time metric that satisfies these requirements is the Friedmann-Lemaître-Robertson-Walker (FLRW) one:

$$ds^2 = c^2 dt^2 - a^2(t) \left[\frac{dr^2}{1 - Kr^2} + r^2 (d\theta^2 + \sin^2 \theta d\varphi^2) \right], \quad (1.2)$$

where t is the *cosmic time*, $a(t)$ is the *scale factor* which rules the expansion of the Universe and relates the coordinate labels (r, θ, φ) to physical distances and K is a constant that can take the values $+1, 0, -1$ and that describes the curvature of space. Substituting eq. 1.2 into eq. 1.1 and assuming that the stress-energy tensor is generated by a uniform ideal fluid, one obtains the so-called *Friedmann* and *acceleration equations*:

$$\left(\frac{\dot{a}}{a}\right)^2 = \frac{8\pi G}{3}\rho - \frac{Kc^2}{a^2} + \frac{\Lambda c^2}{3} \quad (1.3)$$

$$\frac{\ddot{a}}{a} = -\frac{4\pi G}{3}\left(\rho + 3\frac{P}{c^2}\right) + \frac{\Lambda c^2}{3}, \quad (1.4)$$

where $\rho = \sum_i \rho_i$ is the sum of the mass densities for each species and $P = \sum_i P_i$ is the total pressure. The typical assumption is that for each species $P_i = w_i \rho_i c^2$, where w_i is called *parameter of state*. For relativistic particles, such as photons and neutrinos ⁶ $w_\gamma = w_\nu = 1/3$ while for cold dark matter (CDM) and baryons $w_c = w_b \approx 0$.

We define the *Hubble parameter* $H(t)$ as the rate of change of scale factor in time:

$$H(t) = \frac{\dot{a}(t)}{a(t)}. \quad (1.5)$$

Its value at present time is called the *Hubble constant* H_0 and it is often used in its rescaled version $h = H_0 / (100 \text{ km s}^{-1} \text{ Mpc}^{-1})$.

⁶In this Chapter we only consider the standard picture where neutrinos are massless. The effect of neutrino mass on these quantities will be examined in Chapter 2.

Another way to parametrize time is using *redshift*: taking advantage of the fact that photons travel on null geodesics, redshift and the scale factor are related by:

$$a = \frac{1}{1+z}, \quad (1.6)$$

so that $a_0 \equiv a(t_0) = 1$ at present time. In the following, we will use cosmic time, scale factor and redshift as the time variable interchangeably.

1.2.2 Density parameters

Eq. 1.3 can be recast in a way that is of easier comprehension by introducing the density parameters. First of all, the left hand side is just $H^2(t)$. Then, it can be noticed that the cosmological constant can be seen as a component with “mass” density $\rho_\Lambda = \Lambda c^2 / (8\pi G)$ and negative pressure $P_\Lambda = -\rho_\Lambda c^2$, i.e. $w_\Lambda = -1$. We define also the *critical density* at a time t to be the density for which $K = 0$, namely:

$$\rho_{\text{crit}}(t) = \frac{3H^2(t)}{8\pi G}. \quad (1.7)$$

and the *density parameter* for the i -th specie:

$$\Omega_i(t) = \frac{\rho_i(t)}{\rho_{\text{crit}}(t)}. \quad (1.8)$$

We can define as well a density parameter for curvature as:

$$\Omega_K(t) = -\frac{Kc^2}{H^2(t)a^2(t)}. \quad (1.9)$$

From now on, Ω_i will denote the density parameter for the i -th species evaluated at present time, while we will refer to the time-dependent quantity only if it is explicitly written in the text.

Combining all these quantities we end up with:

$$H^2(z) = H_0^2 \sum_i \Omega_i (1+z)^{3(1+w_i)}, \quad (1.10)$$

where we also included curvature as a component with $w_K = -1/3$.

1.2.3 Distances

Defining a distance for an expanding background is a somewhat subtle task. To measure redshift, we use electromagnetic radiation, for which $ds = 0$. Plugging this into eq. 1.2 and assuming a radial trajectory ($d\theta = d\varphi = 0$), after few steps one finds:

$$\chi(z) = \int_0^z \frac{c dx}{H(x)}, \quad (1.11)$$

where χ is the *comoving distance* whose relation to r depends on the value of the curvature parameter K :

$$\chi = \begin{cases} \sin^{-1} r & \text{if } K = +1 \\ r & \text{if } K = 0 \\ \sinh^{-1} r & \text{if } K = -1 \end{cases}. \quad (1.12)$$

The *proper distance* is instead given by $D_p(t) = a(t)\chi(t)$. Unfortunately, none of them is measurable. What we can observe, depending on whether we measure a luminosity flux or an object of a given angular size, are the *luminosity distance* D_L and or the *angular-diameter distance* D_A , respectively, which in a flat Universe ($K = 0$) can be written as:

$$D_L(z) = \chi(z) (1 + z) \quad (1.13)$$

$$D_A(z) = \frac{\chi(z)}{1 + z}. \quad (1.14)$$

A final distance, useful in BAO analyses, is the *isotropic volume distance*, defined as:

$$D_V(z) = \left[(1 + z)^2 D_A^2(z) \frac{cz}{H(z)} \right]^{1/3}. \quad (1.15)$$

1.2.4 A standard model for cosmology

With the quantities defined above, cosmologists have built a successful model that up to now is in excellent agreement with observational data. In this paradigm, called Λ CDM, the Universe is filled, besides baryons, with CDM, which is responsible for the growth of cosmic structures, and a dark energy (DE) component corresponding to Einstein's cosmological constant that accelerates the expansion of the Universe itself. The main source of cosmological constraints in the last decades has surely been the CMB: while the COBE satellite (Smoot et al. (1992)) first measured anisotropies in

the background radiation and WMAP (Bennett et al. (2013)) first detected its polarization, the Planck satellite extended these measurements to very small angular scales with unprecedented accuracy. The tightest constraints on the cosmological parameters currently come from the third data release of the latter (Planck Collaboration et al. (2018)), combined with large-scale structure surveys such as BOSS/SDSS mapping galaxies in the near Universe (Alam et al. (2017), $z < 0.7$) and constraints on weak lensing coming from the Dark Energy Survey (Abbott et al. (2018, 2019)).

These sets of data show that our Universe is described by a flat geometry ($\Omega_K = 0$) as consequence of a nearly-exponential expansion phase the Universe underwent when it was $\sim 10^{-36} - 10^{-34}$ s old. In this phase, called *inflation*, small density perturbations were generated by a stochastic quantum mechanism. These would later become the cradles where galaxies are born. The lightest elements were assembled in the first 3 minutes in the Big Bang Nucleosynthesis (BBN). The baryon content of the Universe is tightly constrained by deuterium abundance data by Cooke et al. (2018) and CMB to $\Omega_b h^2 = 0.02242 \pm 0.00014$. At $z \sim 1100$ the CMB was released soon after photon-electron decoupling and the consequent formation of neutral hydrogen atoms. The radiation content of the Universe is fixed by the CMB temperature and its density parameter is pretty negligible today, $\Omega_\gamma h^2 \approx 2.45 \times 10^{-5}$. Neutrino density is also in tight relation with the photon one, with $\Omega_\nu \approx 0.68 \Omega_\gamma$, assuming three species with zero mass. Meanwhile, perturbations in CDM kept growing under influence of gravity, giving rise first to galaxies and then to clusters and super-clusters. The CDM density parameter has been measured to be $\Omega_c h^2 = 0.11933 \pm 0.00091$ from Planck. The remaining energy density is in form of DE: while in principle it can be any component which accelerates the expansion of the Universe, with a redshift-dependent parameter of state for instance, so far no significant deviation from Einstein's cosmological constant has been detected. The dimensionless Hubble parameter is constrained by Planck to $h = 0.674 \pm 0.005$ and it is currently subject of several studies (see e.g. Guo et al. (2019); Desmond et al. (2019)) concerning the tensions between this value and the one obtained by observations of distant SNIa, the most recent result being 4.4σ away (Riess et al. (2019)). See Bernal et al. (2016) and Knox & Millea (2020) for reviews.

Another tension worth mentioning concerns the mild discrepancy between the amplitude of density fluctuations on spheres of radius 8 Mpc/h (σ_8 , see Section 1.4.3) as measured by CMB (Planck Collaboration et al. (2018)) and the slightly smaller one obtained from weak lensing experiments (Hildebrandt et al. (2017); Köhlinger et al. (2017); Abbott et al. (2018, 2019); Joudaki et al. (2020)).

In addition to this, the Λ CDM model clearly suffers from some limitations at sub-galactic scales. In particular, the dwarf galaxies predicted by N -body simulations largely outnumber the observed ones (*missing satellite problem*, see Klypin et al. (1999); Moore et al. (1999)); the innermost DM profiles seem to be much more diverse (*diversity problem*, Oman et al. (2015); Tulin & Yu (2018)) and steeper than the observed ones (*cuspy-core problem*, Donato et al. (2009)); finally, sub-halos in principle massive enough to be able to ignite galaxy formation remain unseen (*too-big-to-fail problem*, Boylan-Kolchin et al. (2012)).

1.3 The perturbed Universe

While the cosmological principle holds true on large enough scales (say $\gtrsim 100$ Mpc), on smaller scales we observe a considerably inhomogeneous Universe. The large-scale structures we observe today are the result of the secular growth of small density perturbations generated stochastically in the very early stages of the life of the Universe. When the CMB was released at $z \simeq 1100$, density fluctuations were of the order of $\delta\rho/\rho \sim \delta T/T \sim 10^{-5}$, while today galaxy clusters and galaxies themselves can reach densities of order 10^3 and 10^6 times larger than the average background density, respectively. How density perturbations grew under the influence of gravity to form cosmic structures is therefore a fundamental question that needs to be answered.

In this Section we derive the equations that rule the time evolution of density perturbations. We then solve them assuming that these perturbations are small, i.e. we perform a linear perturbation theory, and mention some ways to extend the predictions to the non-linear regime.

1.3.1 Equations of motion

We assume that some initial perturbations with respect to the homogeneous Universe are generated by some physical mechanism (we will see it more in detail in Section 1.4.2). It is useful to use the following notation for the quantities. The comoving coordinate \mathbf{x} is related to the proper one $\mathbf{r} = a\mathbf{x}$, while the proper velocity $\mathbf{u} = \frac{d\mathbf{r}}{dt} \equiv \dot{\mathbf{r}}$ can be written as $\mathbf{u} = \dot{a}\mathbf{x} + \mathbf{v} = H a\mathbf{x} + \mathbf{v}$, where $\mathbf{v} = a\dot{\mathbf{x}}$ is called *peculiar velocity*. We therefore denote $\nabla \equiv \nabla_{\mathbf{x}} = a\nabla_{\mathbf{r}}$. We also make the assumption, for the time being, that these perturbations are non-relativistic and can be treated with Newtonian dynamics.

The most important quantity that we will deal with in this work is the density fluctuation, defined as:

$$\delta(\mathbf{x}, t) = \frac{\rho(\mathbf{x}, t) - \bar{\rho}(t)}{\bar{\rho}(t)}, \quad (1.16)$$

where $\bar{\rho}$ is the average cosmic density at time t .

The equation that describes the evolution of the phase-space distribution f of a particle species of mass m is the Boltzmann equation, which can be written simply:

$$\frac{df}{dt} = \left(\frac{\partial f}{\partial t} \right)_c, \quad (1.17)$$

where f is normalized in such a way that $dN = f(\mathbf{x}, \mathbf{p}, t) d^3\mathbf{x} d^3\mathbf{p}$ and $\left(\frac{\partial f}{\partial t} \right)_c$ describes variations in f due to collisions among particles. Expanding the total derivative with respect to cosmic time in comoving coordinates and using the Newtonian approximation we obtain the Vlasov equation:

$$\frac{\partial f}{\partial t} + \frac{\mathbf{p}}{ma^2} \cdot \nabla f - m \nabla \Phi \cdot \frac{\partial f}{\partial \mathbf{p}} = \left(\frac{\partial f}{\partial t} \right)_c, \quad (1.18)$$

where Φ is a perturbation in the gravitational potential that satisfies Poisson equation:

$$\nabla^2 \Phi = 4\pi G \bar{\rho} a^2 \delta. \quad (1.19)$$

Eq.1.18 is of difficult solution, but one can expand it in its \mathbf{p} moments by defining, for a certain quantity Q :

$$\langle Q \rangle(\mathbf{x}, t) = \frac{1}{n} \int d^3\mathbf{p} f(\mathbf{x}, \mathbf{p}, t) Q, \quad (1.20)$$

where

$$n = \int d^3\mathbf{p} f(\mathbf{x}, \mathbf{p}, t) \quad (1.21)$$

is the comoving number density of particles at \mathbf{x} . In this case, the fluctuation density field is related to number density by $n = \bar{\rho} a^3 \frac{1+\delta}{m}$. Multiplying eq. 1.18 by Q and integrating over \mathbf{p} one obtains:

$$\frac{\partial}{\partial t} [n \langle Q \rangle] + \frac{1}{ma^2} \nabla \cdot [n \langle Q \mathbf{p} \rangle] + mn \nabla \Phi \cdot \left\langle \frac{\partial Q}{\partial \mathbf{p}} \right\rangle = 0, \quad (1.22)$$

where the right hand side vanishes since Q is conserved in a collision. The conservation of mass can be obtained by setting $Q = m$ (continuity equation):

$$\frac{\partial \delta}{\partial t} + \frac{1}{a} \sum_j \frac{\partial}{\partial x_j} [(1 + \delta) \langle v_j \rangle] = 0, \quad (1.23)$$

while the conservation of momentum (Euler's equation) can be found by setting $Q = v_i$ and manipulating a little the result:

$$\frac{\partial \langle v_i \rangle}{\partial t} + \frac{\dot{a}}{a} \langle v_i \rangle + \frac{1}{a} \sum_j \langle v_j \rangle \frac{\partial \langle v_i \rangle}{\partial x_j} = -\frac{1}{a} \frac{\partial \Phi}{\partial x_i} - \frac{1}{a(1+\delta)} \sum_j \frac{\partial}{\partial x_j} [(1+\delta)\sigma_{ij}], \quad (1.24)$$

where $\sigma_{ij} = \langle v_i v_j \rangle - \langle v_i \rangle \langle v_j \rangle$ is proportional to the stress tensor and therefore plays the role of pressure in a collisional fluid or of velocity stress in a collisionless one. In principle, one could continue with an infinite hierarchy of equations, where each moment depends on the higher order one. However, one can truncate this series by making some assumptions. Assuming a monoatomic perfect gas with temperature T , entropy per unit mass S and a sound speed $c_s^2 = \frac{dP}{d\rho}$, the last sum of eq. 1.24 becomes $\sum_j c_s^2 \frac{\partial \delta}{\partial x_j} + \frac{2T}{3}(1+\delta) \frac{\partial S}{\partial x_j}$ (see e.g. Mo et al. (2010)). As we will see in Section 1.4.2, initial isentropic perturbations are a natural prediction of inflation. Therefore we will consider only the case where S is a constant.

1.3.2 Growth of perturbations

The continuity equation 1.23, Euler's equation 1.24 and the Poisson equation 1.19 are the three starting points from which perturbation theory (PT) is developed. In linear PT, only the lowest order terms in δ and \mathbf{v} are kept. Furthermore, it is simpler to write the equations in Fourier space where gradients and Laplacians are substituted by a factor $i\mathbf{k}$ and $-k^2$ respectively. The fundamental equation of perturbation evolution in linear PT is:

$$\frac{\partial^2 \delta_{\mathbf{k}}}{\partial t^2} + 2\frac{\dot{a}}{a} \frac{\partial \delta_{\mathbf{k}}}{\partial t} - \left(4\pi G \bar{\rho} - \frac{k^2 c_s^2}{a^2} \right) \delta_{\mathbf{k}} = 0. \quad (1.25)$$

It is easy to notice that in linear PT each scale grows independently as there are no couplings between different \mathbf{k} . The growth of density perturbations therefore can be compared to a damped harmonic oscillator, where the friction term is carried by the Hubble expansion and the source term is a competition between gravity and pressure forces. In the Λ CDM model, the dominant component of matter is CDM, which can be assumed to be a collisionless perfect fluid. We can therefore neglect the pressure term in eq. 1.25. It can be shown that, neglecting radiation in the Hubble term, the two independent solutions are a decaying mode ($\propto H$) which can safely be ignored at late times and a growing mode given by:

$$D_1(z) \propto H(z) \int_z^\infty dx \frac{1+x}{E^3(x)}, \quad (1.26)$$

where $E(z) = H(z)/H_0$. This particular solution tends to $(1+z)^{-1}$ at high redshift, where the Universe is close to a Einstein-de Sitter one (EdS, with $\Omega_m = 1$).

By using eq. 1.25 with different assumptions on the epoch, fluids and couplings among them, we can reconstruct the history of growth of fluctuations in linear PT. During radiation domination, CDM fluctuations inside the horizon are frozen due to the Meszaros effect (Meszaros (1974)), while they start growing only once entered in the matter dominated era ($z \sim 3500$). On the other hand, baryons are coupled to photons via Compton scattering and they produce acoustic waves due to the competition between self-gravity and radiation pressure. These waves are called Baryon Acoustic Oscillations (BAO) and are today observed both in CMB and galaxy surveys. In this phase, a fraction of photons manages anyway to escape high-density regions due to the non-vanishing mean free path and since acoustic waves are supported by photon pressure, these are damped in this process known as Silk damping (Silk (1968)). As a result, at decoupling, perturbations in baryons are much smaller than the ones in CDM. Baryons, having lost the radiation pressure support, start then falling into CDM potential wells. In exchange, due to the mutual gravitational interaction, baryons leave the imprint of the BAOs also on the CDM distribution. It is important to notice that in a Universe without CDM, only baryonic fluctuations with a mass $\gtrsim 10^{13} M_\odot/h$ would survive Silk damping. Consequently, the only way in which galaxies could have formed is through fragmentation of non-damped structures, in a top-down scenario. This requires anyway initial perturbations in baryons to be too large to match observations of the CMB. On the contrary, observations have shown how cosmic structures become more and more massive at low redshift: this bottom-up scenario represents a strong evidence of the existence of DM as the driver for structure formation.

1.3.3 Non-linear growth: PT vs. N-body simulations

After baryons are dragged into CDM overdensities, perturbations keep growing as just exposed until eventually the condition $\delta \ll 1$ is not valid anymore and linear theory breaks down. If one wants to stick to PT, there are several choices that can be made. For this Section, we refer to Bernardeau et al. (2002)⁷. One solution could be to use higher-order standard perturbation theory (SPT), where the density field is expanded in series $\delta_{\mathbf{k}}(t) = \delta_{\mathbf{k}}^{(1)}(t) + \delta_{\mathbf{k}}^{(2)}(t) + \dots$ and at each order the solution can

⁷Notice that in Bernardeau et al. (2002) a different normalization of the Fourier transform is used, so that many quantities differ by a factor $(2\pi)^3$.

be written as:

$$\delta_{\mathbf{k}}^{(n)}(t) = \int \frac{d^3\mathbf{q}_1}{(2\pi)^3} \dots \int \frac{d^3\mathbf{q}_n}{(2\pi)^3} \delta_D(\mathbf{k} - \mathbf{q}_{1\dots n}) F_n(\mathbf{q}_1, \dots, \mathbf{q}_n) \delta_{\mathbf{q}_1}^{(1)}(t) \dots \delta_{\mathbf{q}_n}^{(1)}(t), \quad (1.27)$$

where F_n is a kernel that describes couplings between different modes, $\mathbf{q}_{1\dots n} \equiv \mathbf{q}_1 + \dots + \mathbf{q}_n$ and the Dirac delta ensures conservation of momentum. Notice that while this solution is explicitly derived assuming an EdS Universe, the dependence of the kernels on cosmological parameters is very weak, so that eq. 1.27 is approximately valid at low redshift in a Λ CDM model.

A different approach is Lagrangian perturbation theory (LPT), where instead of studying the dynamics of the density field, trajectory of particles are followed. In this picture, we are interested in the displacement field $\Psi(\mathbf{q})$ that maps the initial position \mathbf{q} into the final one \mathbf{x} , i.e. $\mathbf{x}(t) = \mathbf{q} + \Psi(\mathbf{q}, t)$. The relation between the latter and the density field can be written as:

$$1 + \delta(\mathbf{x}) = \frac{1}{\det \left(\delta_{ij} + \frac{\partial \Psi_i}{\partial q_j} \right)}, \quad (1.28)$$

where the displacement field is expanded in series, namely: $\Psi(\mathbf{q}, t) = \Psi^{(1)}(\mathbf{q}, t) + \Psi^{(2)}(\mathbf{q}, t) + \dots$

However, these two PT suffers from some problems. The first is related to the fact that these are not perturbation theories as intended in the common sense. In fact, while typical PTs expand the calculation around a small parameter, here we expand over δ which is not a parameter. Therefore we expect the theory to break down at scales and redshifts where $\delta \sim 1$. For instance, at $z = 0$ the inaccuracy of SPT can reach 20% at $k \approx 0.2 h/\text{Mpc}$ (Scoccimarro (2004)) when computing the power spectrum (see Section 1.4.1). On the other hand, LPT breaks down when shell crossing happens, i.e. when two fluid elements with different initial \mathbf{q} end up at the same final position \mathbf{x} . In that case, the Jacobian goes to zero and the dynamics cannot be described in terms of mapping anymore.

The second problem concerns the fact that in SPT, at any order, the contributions are not a small correction to the previous ones and some terms even turn out to be negative: this leads to large cancellations at all scales both in the infrared and in the ultraviolet, which must be dealt with. An alternative is to use Renormalized PT (RPT, Crocce & Scoccimarro (2006)), where the linear propagator is resummed so that each order only has a small range of scales (smaller for increasing order) where it carries a relevant contribution.

A completely different approach is to follow the dynamics of a large number of particles through N -body simulations. In typical N -body simulations, particles on a cubic grid are initially displaced using first-order or second-order LPT (the former is known as *Zel'dovich approximation*, the latter often denoted as 2LPT) and then evolved according to Newton's second law: this equation is solved accurately up to very small scales. Different approaches can be adopted here also. The fastest one in terms of time is to assign each particle a cell in a grid and compute potential and forces on the grid. This procedure is known as *particle mesh*. On the other hand, *tree methods* divide space into cubic cells, each of which is recursively divided into smaller ones until each cell is occupied by one particle only. Forces are then calculated between the different cells. There are, finally, also codes which combine the two approaches (*TreePM*), where the force is computed on a grid above a certain distance and with the tree algorithm below it. Clear examples of these three different methods are RAMSES (Teyssier (2002)), PDKGRAV (Stadel (2001)) and GADGET (Springel (2005)), respectively. A detailed study of these different codes (Schneider et al. (2016)), has underlined how the three different prescriptions agree within $\sim 3\%$ at $z = 0$ for $k = 10 h/\text{Mpc}$ at the power spectrum level (see Section 1.4.4). Despite remarkable, this result is not enough to achieve the desired goals for future surveys, for which a 1% accuracy is required.

1.4 Statistical tools for cosmology

The current explanation of the large-scale structure is that the present matter distribution is the result of the growth of small fluctuations caused by a stochastic process in the very early Universe (inflation). Since we do not have observational access to these, i.e. we cannot observe the points where the initial overdensities were, and since the evolution time-scale is way longer than the one which we can make observations, we cannot predict deterministically where galaxies will be born. In other words, we can only test our Universe in a statistical fashion, considering it as one of the infinite possible stochastic realizations of itself. The statistical prediction we make depend on the statistical properties of the primordial perturbations.

In this Section we first briefly describe random fields, introducing the notions of statistical homogeneity and isotropy. Then, we define the main statistical quantities that we can predict, paying particular attention to the two-point statistics, i.e. the power spectrum or the two-point correlation function. Finally, we describe in detail the

shape of the latter, emphasizing of the different physical processes that are involved in the different ranges of scales.

1.4.1 Random fields and two-point statistics

A random field is a quantity $\phi(\mathbf{x}, t)$ which has its own probability distribution function $\mathcal{P}(\phi)$. Given a function $f(\phi)$, its expectation value is given by:

$$\langle f(\phi) \rangle = \int d\phi \mathcal{P}(\phi) f(\phi). \quad (1.29)$$

In the following, we will mostly consider the density fluctuation field (i.e. $f(\phi) = \delta$). Most cosmological models, including Λ CDM, predict that δ is statistically homogeneous and isotropic. The former means that the probability distribution function $\mathcal{P}(\delta)$ and its moments are invariant for translations of the coordinates in space; the latter means that the probability distribution function is invariant under spatial rotations. The distribution is completely known when all its moments are known.

The lowest order statistics than can be built out of the fluctuation density field is the two-point one. The *two-point correlation function* (2PCF), representing the excess probability of finding two objects (galaxies, clusters...) at a given separation r with respect to a random distribution, can be defined as:

$$\xi(r) = \langle \delta(\mathbf{x}) \delta(\mathbf{x} + \mathbf{r}) \rangle, \quad (1.30)$$

where ξ only depends on $r = |\mathbf{r}|$ due to statistical isotropy and the mean is intended as ensemble average, i.e. a summation over all possible realizations of the Universe. Practically, when dealing with observations, we cannot perform such an average. In this case the *ergodic* hypothesis is assumed (Peebles (1973)): the finite part of the universe accessible to observations is a fair sample of the whole, so that the ensemble average can be replaced by an integration over the observed volume.

If we wanted to compute the 2PCF in Fourier space we should write:

$$\begin{aligned} \langle \delta_{\mathbf{k}} \delta_{\mathbf{k}'} \rangle &= \int d^3\mathbf{x} d^3\mathbf{r} \langle \delta(\mathbf{x}) \delta(\mathbf{x} + \mathbf{r}) \rangle e^{-i[\mathbf{k}\cdot\mathbf{x} + \mathbf{k}'\cdot(\mathbf{x}+\mathbf{r})]} \\ &= \int d^3\mathbf{r} \xi(r) e^{i\mathbf{k}\cdot\mathbf{r}} \int d^3\mathbf{x} e^{i(\mathbf{k}+\mathbf{k}')\cdot\mathbf{x}} \\ &= (2\pi)^3 \delta_D(\mathbf{k} + \mathbf{k}') P(k), \end{aligned} \quad (1.31)$$

so that we have defined the *power spectrum* $P(k)$ as:

$$P(k) = \langle |\delta_{\mathbf{k}}|^2 \rangle, \quad (1.32)$$

and found that it constitutes a Fourier transform pair with the 2PCF, namely:

$$P(k) = \int_0^\infty dr 4\pi r^2 \xi(r) j_0(kr), \quad \xi(r) = \int_0^\infty \frac{dk k^2}{2\pi^2} P(k) j_0(kr), \quad (1.33)$$

where $j_0(x) = \sin x/x$ is the 0-th order spherical Bessel function.

An important remark needs to be explained about two-point statistics. The power spectrum and the 2PCF are the lowest-order non-vanishing statistics of a random field with zero mean (like for instance δ). In general, one can combine 3 or more random fields and build higher order statistics, whose expressions become more and more difficult to deal with. But in the special case where the random field follows a Gaussian distribution, i.e. $\mathcal{P}(\delta(\mathbf{x})) \propto \exp[-\delta^2(\mathbf{x})/(2\sigma^2)]$, the two-point statistics is the *only* non-vanishing one, as all higher central moments of the distribution are identically zero. Therefore a Gaussian random field is fully characterized by its power spectrum or its 2PCF. This is of outstanding importance, since as we will shortly see (Section 1.4.2), inflationary models typically predict Gaussian initial conditions for the density field: if this is the case, as long as the growth of perturbations is in the linear regime, the density field remains Gaussian and the power spectrum contains all the relevant information about large-scale structure.

There are a couple more of convenient definitions that must be introduced for the linear power spectrum, i.e. the power spectrum computed assuming that the density field evolves according to linear theory. The density field can be filtered with some window function to get a smoothed field on a scale R . It is easier to perform this operation in Fourier space, where convolutions become products:

$$\delta_{\mathbf{k}}(R) = \delta_{\mathbf{k}} W(kR). \quad (1.34)$$

The typical choice (but not the only one) for the window function is a top-hat in configuration space which in Fourier space becomes:

$$W(x) = \frac{3}{x^3} (\sin x - x \cos x). \quad (1.35)$$

We can then define the RMS mass fluctuation on a scale R as:

$$\sigma_R^2 \equiv \langle \delta^2(\mathbf{x}; R) \rangle = \int_0^\infty d \ln k \Delta_{\text{lin}}^2(k) W^2(kR), \quad (1.36)$$

where we have introduced the dimensionless linear power spectrum:

$$\Delta_{\text{lin}}^2(k) = \frac{k^3}{2\pi^2} P_{\text{lin}}(k). \quad (1.37)$$

In particular, eq. 1.36 with the linear power spectrum at $z = 0$ with $R = 8 \text{ Mpc}/h$ is often used in literature as a normalization of the amplitude of the power spectrum. This value was initially chosen so that $\sigma_8 \sim 1$, i.e. at $8 \text{ Mpc}/h$ non-linearities start to become important. Its current best constraints comes from Planck Collaboration et al. (2018) and it is $\sigma_8 = 0.8102 \pm 0.0060$.

1.4.2 Initial conditions

In the Λ CDM model, the Universe was subjected to a nearly exponential expansion in its very early stages. This phase, called inflation, was originally proposed by Guth (1981) to solve problems related to the homogeneity of the CMB, the flatness of the Universe and the lack of magnetic monopoles. However, it was soon realized that this event, caused by a scalar field slow-rolling towards the minimum of its potential, was also responsible for the creation of the initial conditions that later would give birth to large-scale structures.

By using some heuristic arguments, we can deduce how these perturbations looked like. The typical assumption is that the scalar field has negligible self-interaction. This means that different modes in quantum fluctuations should be independent of each other: consequently, the density perturbations are expected to be Gaussian. Furthermore, at the end of inflation, the perturbations in the energy density of the scalar field are converted to photons and other particles (this process is known as *reheating*): since no segregation between particle species is expected, the resulting perturbations are isoentropic. Finally, slow-rolling causes an exponential expansion, so that during inflation the Hubble parameters is almost constant. This means that space is invariant under time translation: the perturbations in the metric generated are therefore expected to be scale-invariant. The last requirement translates into a flat dimensionless power spectrum in the potential:

$$\Delta_{\text{ini},\Phi(k)}^2 \propto k^{n_s-1}, \quad (1.38)$$

where n_s is the scalar index and $n_s = 1$ defines the Harrison-Zel'dovich prescription (Harrison (1970); Zeldovich (1972)). This result is particularly elegant and desirable, since it means that all the scales re-enter the horizon with the same amplitude, thus avoiding divergences in the potential that could cause too large density perturbations. The scalar index has been measured with incredible precision by Planck (Planck Collaboration et al. (2018)) to $n_s = 0.9665 \pm 0.0038$, where the difference from unity is caused by small deviations from a perfectly exponential expansion (i.e. the slow-rolling parameters).

By using the Poisson equation (eq. 1.19) in Fourier space,

$$k^2 \Phi_{\mathbf{k}} = -\frac{3}{2} H_0^2 \Omega_m a^{-1} \delta_{\mathbf{k}}, \quad (1.39)$$

one obtains that the initial power spectrum of density fluctuations coming out from inflation is:

$$P_i(k) \propto A_s k^{n_s}, \quad (1.40)$$

where A_s is called scalar amplitude and its constraints are $A_s = (2.105 \pm 0.030) \times 10^{-9}$ (Planck Collaboration et al. (2018))⁸.

1.4.3 Linear evolution of power spectrum and 2PCF

The relation between the initial conditions and the linearly evolved density field is called the *transfer function* $T(k)$. By using what we learned in Section 1.3, we can find how the initial power spectrum (eq. 1.40) evolves with time in linear PT and how it looks like today.

Once inflation is over and reheating has occurred, we enter in a phase where the energy density is dominated by radiation. Outside the horizon ($k < aH/c$) density perturbations grow as $D_1(a) \propto a^2$, while inside of it Meszaros effect freezes CDM fluctuations, which are constant. This induces a scale-dependent growth that affects all the scales that re-enter the horizon before radiation-matter equality ($z_{\text{eq}} \sim 3500$). The net result is that the initial power spectrum is suppressed at scales smaller than $k_{\text{eq}} = 2\pi a_{\text{eq}}/(ct_{\text{eq}})$. It can be shown that this “missing growth” at small scales can be described as a damping proportional to k^{-2} in the density field for $k \gg k_{\text{eq}}$.

Combining all these results, including the scale-dependent transfer function and the linear growth factor, the linear matter power spectrum can be written in the following way:

$$P_{\text{lin}}(k) = P_i(k) D_1^2(z) T^2(k) \propto \begin{cases} k^{n_s} & \text{for } k \ll k_{\text{eq}} \\ k^{n_s-4} & \text{for } k \gg k_{\text{eq}} \end{cases}. \quad (1.41)$$

The first attempts to find an analytical formula for the transfer function were done in the 1980s. The most interesting case for our purposes is the case of a CDM dominated Universe whose density perturbations grow adiabatically. In their seminal paper, Bardeen et al. (1986) provided a simple formula for the CDM linear transfer function:

$$T(k) = \frac{\ln(1 + 2.34q)}{2.34q} [1 + 3.89q + (16.1q)^2 + (5.46q)^3 + (6.71q)^4]^{-1/4}, \quad (1.42)$$

⁸Notice that in the Λ CDM model, where the growth of perturbations is scale-independent, A_s and σ_8 are perfectly degenerate.

where $q = \frac{1}{\Gamma} \left(\frac{k}{h/\text{Mpc}} \right)$ and Γ is the shape parameter $\Gamma = \Omega_m h$.

However, when the baryonic fraction becomes sufficiently large, eq. 1.42 no longer returns a good description of the transfer function. In fact, when baryons fall into DM potential wells after recombination, they leave the imprint of the BAOs on the CDM distribution, i.e. an oscillatory feature in the matter power spectrum. The typical scale of this oscillations corresponds to the distance traveled by acoustic waves from the Big Bang to decoupling, named *sound horizon*, which is roughly $r_s \approx 100 \text{ Mpc}/h$. In this case, one must resort to more complicated fitting functions such as Eisenstein & Hu (1998).

However, the accuracy of this formulae ($\sim 10\%$) is not enough to achieve strong constraints in current analyses. Nowadays, to compute accurate transfer functions and power spectra, Boltzmann solvers are employed. These codes solve the linear Boltzmann equation (eq. 1.17) for all species and redshifts. The most widely used state-of-art solvers are CAMB⁹ (Lewis et al. (2000)) and Class¹⁰ (Lesgourgues (2011); Blas et al. (2011)) which can predict the linear matter power spectrum with an accuracy of $\sim 0.1\%$.

The solid line of Figure 1.1 shows the linear matter power spectrum computed using the best-fit cosmological parameters from Planck Collaboration et al. (2018). There is a striking agreement between the theory and the data coming from a huge variety of experiments (the various dots) testing different probes over a range of four decades in scales. See Planck Collaboration (2018), from where this plot was actually taken, for more details.

The shape of the linear matter power spectrum is the result of the mechanisms described in this and in the previous Section. The largest scales, larger than the size of the horizon at the radiation-matter equality, did not experience Meszaros effect and therefore they have kept the original form given by the Harrison-Zel'dovich formula. In other words, in this regime $T(k \ll k_{\text{eq}}) \rightarrow 1$. The peak of the power spectrum corresponds at the wavenumber of those perturbations which entered the horizon exactly at radiation-matter equality. At small scales ($k \gtrsim 0.5 h/\text{Mpc}$) the power spectrum decreases as $\propto k^{n_s-4}$ due to the missing growth caused again by the Meszaros effect. On intermediate scales, roughly $0.01 \lesssim k/(h/\text{Mpc}) \lesssim 0.5$, baryons falling in DM potential wells leave an imprint on the matter power spectrum, the BAOs. As already said, the wavelength of these oscillations corresponds to the size of the sound horizon at recombination. This oscillating feature is much more visible

⁹<https://camb.info/>

¹⁰<http://class-code.net/>

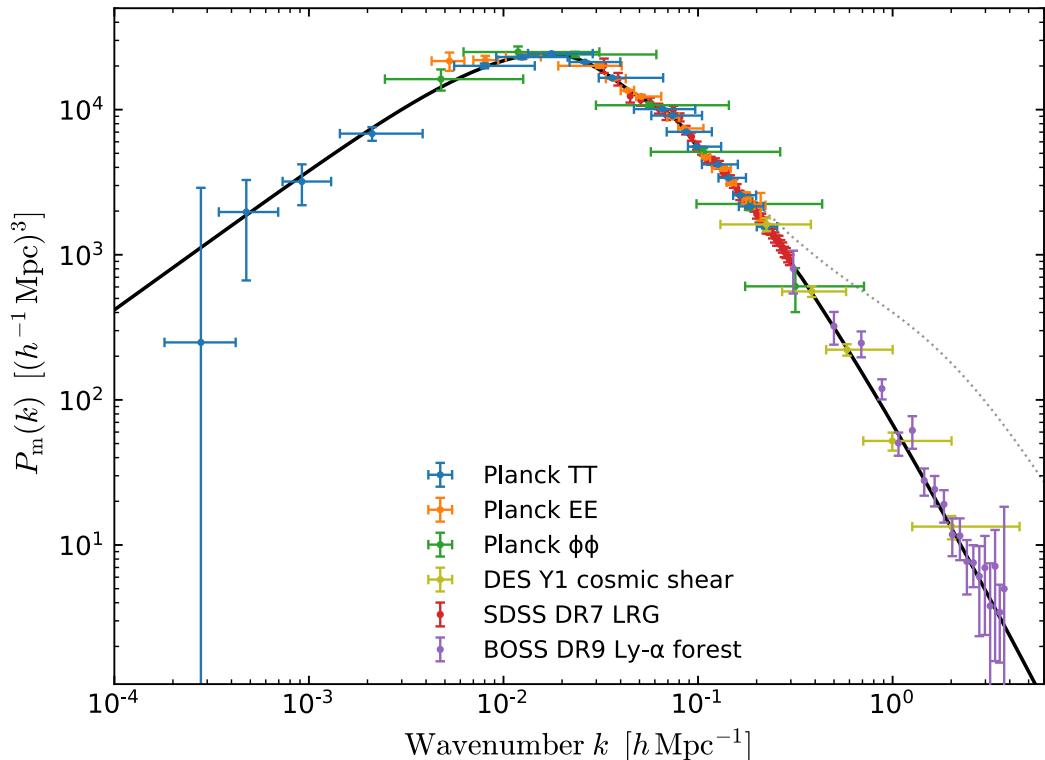


Figure 1.1: The black solid line shows the matter linear matter power spectrum at $z = 0$ computed using the best-fit parameters from Planck (2018) in the Λ CDM model. The dotted black line represents the non-linear counterpart (see Section 1.4.4 for an insight). Dots of different colors are extrapolated values for $P(k)$ - coming from different experiments and probes - which are in impressive agreement with theory over four decades in scales. Taken from Planck Collaboration (2018).

in configuration space, i.e. in the 2PCF (see the right panel of fig. 1.2). In fact, whenever Fourier transforming a sinusoidal function, a Dirac delta is involved: here is the reason of the appearing of a bump in the 2PCF that peaks approximately at r_s . The net effect of BAOs on large-scale structure is therefore an excess of galaxies at a separation of $\sim 100 \text{ Mpc}/h$ (first detected in galaxy surveys by Eisenstein et al. (2005)).

1.4.4 Non-linearities

Besides the fact that DM is not directly observable, we do not have access to the linear power spectrum, because at a given time and at a given scale, linear theory breaks down. This occurs when $\Delta_{\text{lin}}^2(k, z) \sim 1$, so that we can roughly predict the scales below which non-linearities become important at a given redshift (Smith et al. (2003)):

$$k_{\text{nl}}(z) = k_{\text{nl}}(0) (1 + z)^{\frac{2}{2+n_s}}, \quad (1.43)$$

where a typical value for $k_{\text{nl}}(0)$ is $0.2 h/\text{Mpc}$ (Sprenger et al. (2019)). Therefore, smaller scales enter the non-linear regime before large scales.

Like in Section 1.3.3, the two main ways to predict the non-linear power spectrum are PTs, N -body simulations or halo models (e.g. Cooray & Sheth (2002)).

In SPT, the power spectrum can be computed from its definition (eq. 1.32) expanding the density field δ (see e.g. Bernardeau et al. (2002) for the complete expressions):

$$P^{\text{SPT}}(k) = P_{11}(k) + P_{13}(k) + P_{22}(k) + \dots, \quad (1.44)$$

where P_{ij} is the power spectrum computed using the solutions at i -th and j -th order for δ (so that P_{11} is actually the linear power spectrum). For Gaussian initial conditions only terms with $i + j = \text{even}$ survive. However, as already said, this treatment breaks down when $\delta \sim 1$ and has a convergence problem, in the sense that higher order corrections happen to be of the same order of magnitude of the previous ones and sometimes these terms are even negative and lead to huge cancellations between different orders.

On the other hand, using the Zel'dovich approximation (ZA) in LPT, one can find (e.g. Crocce & Scoccimarro (2006)):

$$P^{\text{ZA}}(k) = \int d^3\mathbf{r} e^{i\mathbf{k}\cdot\mathbf{r}} \left[e^{-k^2\sigma_v^2 + I(\mathbf{k},\mathbf{r})} - 1 \right] \quad (1.45)$$

where

$$I(\mathbf{k}, \mathbf{r}) = \int \frac{d^3\mathbf{p}}{(2\pi)^3} \cos(\mathbf{p} \cdot \mathbf{r}) \frac{(\mathbf{p} \cdot \mathbf{k})^2}{p^4} P_{\text{lin}}(p) \quad (1.46)$$

and $\sigma_v^2 = I(\mathbf{k}, 0)/k^2$ is the variance of the displacement field (and also the one-dimensional velocity dispersion in linear theory),

$$\sigma_v^2(z) = \int_0^\infty \frac{dq}{6\pi^2} P_{\text{lin}}(q, z). \quad (1.47)$$

The Zel'dovich approximation has a limited range of validity when dealing with the power spectrum, but it has been widely used in literature for the 2PCF since it can predict the correct clustering down to scales of some tens of Mpc/h (White (2014)). In fact, non-linearities smear the BAO peak in the 2PCF (see fig. 1.2 for a visual example) by a quantity that in first approximation depends on σ_v^2 . This smoothing is caused by the differential motion of pairs of tracers driven by bulk flows. The Zel'dovich approximation is nowadays used to trace back galaxies to their original positions in order to enhance the signal of the BAO peak: this technique is known as *BAO reconstruction* (Eisenstein et al. (2007); Noh et al. (2009); Padmanabhan et al. (2009); Seo et al. (2010), see Padmanabhan et al. (2012) for an application).

A similar way of modelling the BAO smearing consists of “de-wiggling” the linear power spectrum before Fourier transforming it, namely: (Tegmark et al. (2006); Eisenstein et al. (2007))

$$P_{\text{dw}}(k) = [P(k) - P_{\text{nw}}(k)] e^{-k^2 \sigma_v^2} + P_{\text{nw}}(k), \quad (1.48)$$

where σ_v^2 is given by eq. 1.47 and $P_{\text{nw}}(k)$ is the no-wiggle power spectrum, i.e. a power spectrum where the BAO have been completely smeared out (e.g. Eisenstein & Hu (1998)).

Alternatively to PTs there are N -body simulations, which can return accurate power spectra up to very small scales. Comparison of different codes implementing different ways to compute forces (particle mesh, tree algorithms and a mixture of the two) have highlighted a difference of $\sim 3\%$ on the non-linear matter power spectrum at $k = 10 h/\text{Mpc}$ and $z = 0$ (Schneider et al. (2016)). Of course running simulations requires time and a large computational power and it is not an effective solution if one needs quick estimates of non-linear clustering, for example in Markov Chain Monte Carlo (MCMC) samplings, where thousands of spectra must be evaluated for different cosmological parameters.

An innovative approach was developed at the end of the 1990s to describe non-linear matter clustering as the hierarchical formation and evolution of collapsed and virialized DM structures called halos. In this *halo model* paradigm, all DM particles reside in halos whose density profiles are assumed to be universal and dependent only on mass: the usual choice falls on the Navarro-Frenk-White profile (NFW, Navarro et al. (1997)). Furthermore, the halo mass function, i.e. the number of halos per unit mass per unit volume, can be computed from a universal function which is cosmology-independent: this was first shown by the seminal work of Press & Schechter (1974) and later perfected by Bond et al. (1991). A follow up work by Sheth & Tormen (1999) improved the agreement of the halo mass function with simulations by relaxing the assumption of spherical collapse. The non-linear power spectrum as computed in this picture has two contributions: the former is coming from the small scales, where the density field is related to the density distribution inside single halos (1-halo term); the latter comes from the correlation among DM particles belonging to separate halos (2-halo term) and reflects the large-scale fluctuations. The region where the two contributions are of the same order of magnitude can be seen as the scale of the typical halo sizes ($\sim 1 \text{ Mpc}$). For the details of this model, we refer to Cooray & Sheth (2002). Unfortunately, the halo model cannot reproduce well the results from N -body simulations, especially in the transition regime between the 1-halo and the

2-halo terms, where there are differences with respect to simulations up to $\sim 20\%$ (e.g. Massara et al. (2014), where the halo model is extended to include also massive neutrinos).

The two valid alternatives to the halo model are represented by emulators and fitting functions. The first class predicts the non-linear correction to the linear power spectrum by interpolating a grid of power spectra given by N -body simulations run with different sets of cosmological parameters. Emulators can reach an accuracy of $2 - 3\%$ up to scales of $\sim 10 h/\text{Mpc}$ (see e.g. Euclid Collaboration et al. (2019b); Angulo et al. (2020)), i.e. the typical accuracy of N -body codes. The second alternative precisely consists of finding fitting functions to simulations in order to be as close as possible to the theoretical prediction. This technique is commonly referred to as HALOFIT. The first version of HALOFIT dates back to Smith et al. (2003), where the non-linear matter power spectrum was written as the sum of two terms, a quasi-linear one dominating at large scales and a “halo” one, catching the small-scale physics. Following versions would include effects of massive neutrinos (Bird et al. (2012)) and improve the accuracy (Takahashi et al. (2012)). The latest version, which is the one we make constant use of throughout this work, is the one by Mead et al. (2015, 2016), also called HMcode. It consists of a reinterpretation of the halo model, where new degrees of freedom are introduced to relieve the discrepancies the original halo model suffers from. This version is accurate at 5% at scales up to $10 h/\text{Mpc}$. For details about every model just discussed, see Appendix A.

In fig. 1.2 we summarize the things discussed in this Section. We set the cosmological parameters to $\Omega_b = 0.0486$, $\Omega_m = \Omega_b + \Omega_c = 0.3089$, $h = 0.6774$, $A_s = 2.14 \times 10^{-9}$, $n_s = 0.9667$ and these will be used as the fiducial ones for the ΛCDM model throughout Chapters 1 and 2 (we report these values in Table 1.1). In the left panel we show with solid lines the non-linear matter power spectrum computed with the HALOFIT prescription by Mead et al. (2015). Dashed lines represent the linear prediction, computed with CAMB. It is interesting to notice how non-linearities cause an enhancement of power at small scales and that the departure from linear theory occurs at larger scales for decreasing redshift, like already anticipated in eq. 1.43. The right panel shows instead the linear (dashed lines) and non-linear (solid lines) 2PCF multiplied by a factor r^2 to make the BAO feature clearly visible. The latter has been smoothed following the procedure by Tegmark et al. (2006), in which the linear power spectrum is de-wiggled before being turned non-linear and Fourier transformed. Apart from this smearing effect, the linear and the non-linear 2PCFs do not differ

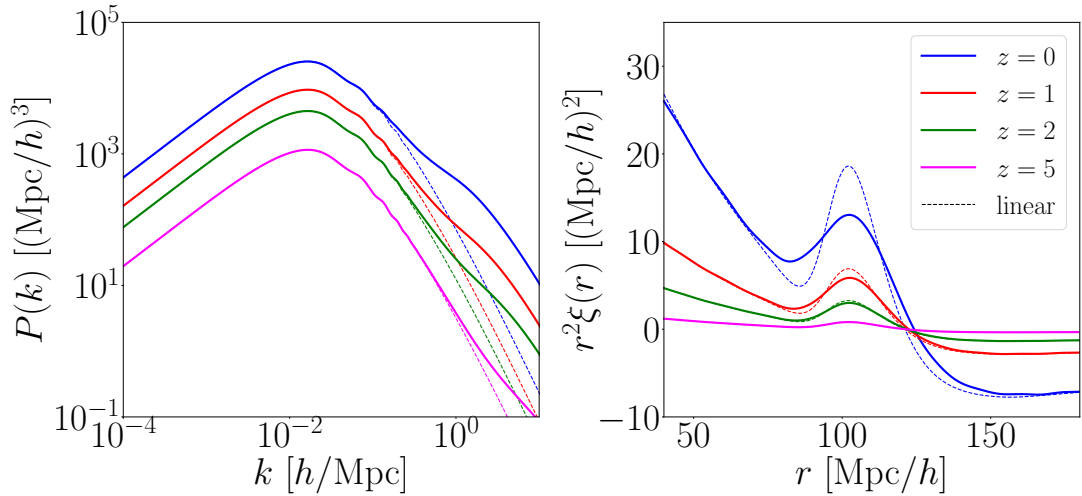


Figure 1.2: Summary of two-point statistics for total matter in the Λ CDM model. In the left panel power spectra at different redshifts are shown whereas in the right panels we display 2PCF multiplied by a r^2 factor to better show the BAO feature. Solid lines show the non-linear prediction according to Mead et al. (2015), where we have also smoothed the BAO peak using the prescription of Tegmark et al. (2006). Dashed lines instead represent linear theory. Different colors label different redshift.

Parameter	Value	Notes
Ω_m	0.3089	Fixed when adding massive neutrinos
Ω_b	0.0486	
Ω_c	0.2603	Will decrease when adding massive neutrinos
h	0.6774	
A_s	2.14×10^{-9}	
n_s	0.9667	

Table 1.1: Fiducial values for the Λ CDM cosmology used in this and in the following Chapter. When we add massive neutrinos in Chapter 2, we will keep Ω_m and Ω_b fixed, so that an increase in M_ν will correspond to a decrease in Ω_c .

much from each other down to scales of $\sim 5 - 10$ Mpc/h at $z = 0$ (not shown in the Figure), where $\xi(r) \sim 1$.

1.5 Observables of large-scale structure

As already mentioned, DM and in turn the matter power spectrum are not directly observable. Therefore, to infer constraints on the cosmological parameters, one has to choose a proxy, i.e. an observable which is strictly related to the DM distribution. Large-scale structure offers several different possibilities, depending on which scales need to be probed and which physical processes we are interested. In this Section we

expose the main quantities we are going to deal with in this work, what they can be used for and what their statistical uncertainties are.

1.5.1 Clustering of biased tracers

While DM is not accessible, the objects we observe in the Universe (e.g. galaxies, DM halos, galaxy clusters) indirectly trace its distribution. The relation between the clustering of the tracer and the actual matter distribution is called *biasing*.

Bias is a functional that links the matter density field δ to the tracer density field δ_g :

$$\delta_g = \mathcal{B}[\delta]. \quad (1.49)$$

On very large scales, gravity is linear and the density perturbations are small: it makes sense therefore to perform a Taylor expansion in the local mass density with unknown coefficients. On top of that, one may also add terms that reflect non-locality or contributions due to primordial non-Gaussianity in the initial density field (Desjacques et al. (2013)). For a full review, see Desjacques et al. (2018).

To a first approximation, therefore, the tracer density field is just a multiple of the matter density field, namely:

$$\delta_g = b_1 \delta, \quad (1.50)$$

where b_1 is the linear bias parameter which is assumed to be constant in k . For the purposes of this thesis, this expression will be enough. It is just worth mentioning the fact that linear bias and in general all bias parameters may depend on many different quantities, e.g. the magnitude threshold or color when observing galaxies or the minimum mass when observing galaxy clusters or DM halos.

Given this linear relation between tracers and underlying matter density fields, the power spectrum of a biased tracer in the linear approximation is just given by:

$$P_g(k) = b_1^2 P(k), \quad (1.51)$$

where the full non-linear power spectrum must be used in eq. 1.51. An analogous relation holds for the 2PCF.

When measuring the power spectrum from data or simulations, one runs up against uncertainties of observational and statistical nature. It can be shown that the covariance between the power spectrum measured at k_i and k_j can be written as the sum of two terms (e.g. Scoccimarro et al. (1999)):

$$\begin{aligned} \text{Cov}_{ij}^P &\equiv \langle P(k_i)P(k_j) \rangle - \langle P(k_i) \rangle \langle P(k_j) \rangle = \\ &= \frac{(2\pi)^2}{k_i^2 \Delta k V} \left[P(k_i) + \frac{1}{\bar{n}} \right]^2 \delta_{ij}^K + \frac{\bar{T}(k_i, k_j)}{V}. \end{aligned} \quad (1.52)$$

In the first term, V is the survey volume, Δk is the bin size in k , \bar{n} is the average number density of objects, δ_{ij}^K is the Kronecker delta. This contribution is called *cosmic variance* and here comes from the Gaussianity of the field: in fact, in the Gaussian limit, all the Fourier modes evolve independently (hence the Kronecker delta) and the power spectrum exactly represents the variance of the density perturbation field on a scale \mathbf{k} . All the terms before the square brackets are inversely proportional the number of modes \mathbf{k} of a given shell of a sphere in Fourier space. Moreover, the $1/\bar{n}$ term is called *shot noise* (here assumed to follow Poisson statistics) and arises because of self-correlations of objects.

The second contribution comes from the non-linear evolution of the density field, when non-Gaussianities induced by growth of perturbations give rise to a non-vanishing four-point statistics. Therefore it is expected to become non-negligible only for $k \gtrsim k_{\text{nl}}$. In this case, $\bar{T}(k_i, k_j)$ is the trispectrum for objects in a parallelogram configuration, averaged over all the possible orientations (following from statistical isotropy of the power spectrum).

If, on the other hand, one wanted to compute the covariance matrix for the 2PCF, it is easy to show that:

$$\begin{aligned} \text{Cov}_{ij}^{\xi} \equiv & \frac{2}{V} \int_0^{\infty} \frac{dk k^2}{2\pi^2} \left[P(k) + \frac{1}{\bar{n}} \right]^2 j_0(kr_i) j_0(kr_j) + \\ & + \frac{1}{V} \int_0^{\infty} \frac{dk k^2}{2\pi^2} j_0(kr_i) \int_0^{\infty} \frac{dk' k'^2}{2\pi^2} j_0(k'r_j) \bar{T}(k, k'). \end{aligned} \quad (1.53)$$

1.5.2 Cosmic shear

Gravitational lensing is the deflection of light caused by the gravity of a massive object. It was one of the first predictions of GR to be confirmed by Eddington in 1919. Potential perturbations in the FLRW metric affect the geodesics of photons thus distorting the images of distant galaxies. In the limit where the deflection is small, we talk about weak gravitational lensing; when the distortion is caused by perturbations in the large-scale structure gravitational potential, we name it *cosmic shear*. Measurements of orientations of large catalogues of galaxies have become more and more popular in the last decade as cosmic shear surveys have proved to be a promising and powerful tool for cosmological parameter inference (Hildebrandt et al. (2017); Köhlinger et al. (2017); Hildebrandt et al. (2020); Abbott et al. (2018, 2019); Joudaki et al. (2020)).

The derivation of the equations that rule light deflection is purely geometrical and can be found e.g. in Mo et al. (2010) or Bartelmann & Schneider (2001). Here

we just summarize the essential steps, assuming a flat Universe. Let us assume that the sources of light (galaxies) are distributed along the line-of-sight according to some function $\mathcal{P}(\chi)$, where χ denotes the comoving distance. For each source, the mapping between its real angular position θ_S at a distance χ_S and the observed one θ_0 , in the weak lensing limit ($\Phi \ll c^2$), is governed by the Jacobian of the transformation:

$$A_{ij}(\theta_0, \chi_S) = \frac{\partial \theta_{S,i}}{\partial \theta_{0,j}} = \delta_{ij} - \partial_i \partial_j \Psi [\chi \theta_0, \chi_S], \quad (1.54)$$

where i, j are the two direction in the plane of the sky. Ψ is the distance-weighted projection of Newtonian gravitational potential, namely:

$$\Psi(\mathbf{x}_\perp, \chi_S) = \frac{2}{c^2} \int_0^{\chi_h} d\chi g(\chi) \Phi(\mathbf{x}_\perp, \chi), \quad (1.55)$$

where the integral extends from the observer to the horizon χ_h and

$$g(\chi) = \chi \int_\chi^{\chi_h} d\chi' \frac{\chi' - \chi}{\chi'} \mathcal{P}(\chi') \quad (1.56)$$

is called *lensing efficiency*. From the Jacobian matrix the main random fields for weak lensing are defined. *Convergence* κ quantifies how much the distorted image is stretched; *shear* $\gamma = \gamma_1 + i\gamma_2$ describes how much the image is rotated. Here, 1 and 2 are the two directions in the plane of the sky. In formulae:

$$\kappa(\theta_0) = \frac{1}{2} (\partial_1 \partial_1 \Psi + \partial_2 \partial_2 \Psi) \quad (1.57)$$

$$\gamma(\theta_0) = \frac{1}{2} (\partial_1 \partial_1 \Psi - \partial_2 \partial_2 \Psi) + i \partial_1 \partial_2 \Psi. \quad (1.58)$$

These two are the fundamental fields upon which the statistical observables are built. Interestingly, from a statistical point of view, under some conditions the shear and the convergence power spectra are equivalent. We can manipulate the definition of convergence by adding a second derivative in the line-of-sight direction $\partial_3 \partial_3$. In this way we build a Laplacian operator that can be applied to the potential in eq. 1.55 to recover Poisson equation. The addition of such derivative does not carry any contribution to the observable, because integrating along the line-of-sight cancels out all the possible contributions. Making use also of Poisson equation (eq. 1.39), we get:

$$\kappa(\theta_0) = \frac{3}{2} \Omega_m \left(\frac{H_0}{c} \right)^2 \int_0^{\chi_h} d\chi (1 + z(\chi)) g(\chi) \delta[\chi \theta_0, \chi]. \quad (1.59)$$

To obtain the *convergence* (or equivalently the *shear*) *power spectrum*, we need to perform few more steps. First, we square 1.59 and switch to Fourier space in order

to obtain a matter power spectrum at right hand side. Second, we assume the flat-sky approximation, so that the Fourier modes are plane waves. Third, we assume Limber's approximation (Limber (1953)), valid at small angles or equivalently at high multipoles ℓ , thanks to which Bessel functions arising from spherical harmonics expansion can be replaced by Dirac deltas. Finally, we generalize the above expression for different bins of sources. All in all, the shear power spectrum is given by:

$$C^{(ij)}(\ell) = \int_0^\infty dz \frac{c}{H(z)} \frac{W^{(i)}(z)W^{(j)}(z)}{\chi^2(z)} P\left(\frac{\ell}{\chi^2(z)}, z\right), \quad (1.60)$$

where we have changed the integration variable $d\chi = c dz/H(z)$ and $W^{(i)}(z)$ are the window functions for shear:

$$W^{(i)}(z) = \frac{3}{2}\Omega_m \left(\frac{H_0}{c}\right)^2 (1+z) \chi(z) \int_z^\infty dx \mathcal{P}(x) \frac{\chi(x) - \chi(z)}{\chi(x)}. \quad (1.61)$$

The meaning of eq. 1.60 is pretty straightforward: the shear power spectrum measures correlations of galaxy pairs orientations when both of these are lensed by large-scale structure.

Of course, when we observe the shape of a galaxy (i.e. its convergence and its orientation), we may not know *a priori* whether this is lensed or not. Therefore, when measuring the shear spectrum from data, also spurious correlations are measured. This important systematic must be dealt with and it is called *intrinsic alignment*: it arises when two galaxies are aligned but only one or none of them is lensed. This may occur when galaxies are born in the same gravitational environment, where tidal forces could align galaxies right at the time of their formation. The observed shear of a galaxy is a sum of two contribution, one due to lensing, the other being intrinsic to the galaxy $\gamma_{\text{tot}} = \gamma_G + \gamma_I$. When correlating this object with itself to obtain the power spectrum, it gives rise to three terms:

$$C_{\text{tot}}^{(ij)}(\ell) = C_{GG}^{(ij)}(\ell) + C_{GI}^{(ij)}(\ell) + C_{II}^{(ij)}(\ell). \quad (1.62)$$

The first term (*GG*) represents the cosmological signal, eq. 1.60; the second term (*GI*) arises when some galaxy at a given redshift is lensed by a structure at a lower redshift and aligned to a galaxy which is not lensed; the last term (*II*) arises when two galaxies are already aligned without the need of lensing but their correlation is accounted for anyway in the survey. There are different ways to model the *GI* and *II* terms (see Joachimi et al. (2015) for a review), but typically the effect is proportional to $P(k, z)$. We will discuss this in detail in Chapter 4.

From eq. 1.60, it is straightforward to realize that the statistical and observational uncertainties on the shear power spectrum are directly related to the ones on the matter power spectrum. If one wanted to compute the covariance matrix of the shear power spectrum, the result would be (see e.g. Scoccimarro et al. (1999); Cooray & Sheth (2002)):

$$\begin{aligned} \text{Cov}\{C^{(ab)}(\ell), C^{(cd)}(\ell')\} &= \frac{\delta_{\ell\ell'}}{(2\ell+1)\Delta\ell f_{\text{sky}}} \left[\tilde{C}^{(ac)}(\ell) \tilde{C}^{(bd)}(\ell') + \tilde{C}^{(ad)}(\ell) \tilde{C}^{(bc)}(\ell') \right] + \\ &+ \frac{1}{4\pi f_{\text{sky}}} \bar{T}^{(abcd)}(\ell, -\ell'). \end{aligned} \quad (1.63)$$

Similarly to the power spectrum case, the first term represents cosmic variance, i.e. the Gaussian contribution which dominates at small multipoles. The factor $(2\ell+1)\Delta\ell$ is analogous to the factor $k_i^2\Delta k$ in eq. 1.52, i.e. the number of modes in a given multipole shell, while f_{sky} is the fraction of the sky actually being observed (analogous to the volume in eq. 1.52). The various $\tilde{C}^{(ij)}(\ell)$ in square brackets represent the signal (including the intrinsic alignment contribution) plus a *shape-noise* term $N^{(ij)}(\ell)$, analogous to shot-noise in galaxy surveys. The latter can be written as $N^{(ij)}(\ell) = \delta_{ij}\sigma_\epsilon^2/\bar{n}$, where σ_ϵ^2 is the RMS ellipticity of the galaxies in the sample. The second term, finally, is the non-Gaussian contribution: this arises because of non-linearities in the matter power spectrum and therefore introduces correlations between different multipoles. It starts to be non-negligible already at $\ell \gtrsim (2-3) \times 10^2$ (Sgier et al. (2019)). Like in the case of the power spectrum, the shear four-point function $T^{(abcd)}$ is involved, averaged on a circular shell in ℓ and integrated over all the possible parallelogram configurations.

We summarize this last Section in fig. 1.3, where we show the shear power spectrum split into all its contributions. We use three redshift bins, with a distribution $\mathcal{P}(z) \propto z^2 \exp(-z/0.24)$ and with edges (0.1, 0.478), (0.478, 0.785) and (0.785, 1.5). For each combination of pairs of bins, in the corresponding panel we plot the shear power spectrum (solid blue lines), the *GI* and *II* intrinsic alignment contributions (solid green and red, respectively) and the total measured shear spectrum (solid black lines). For intrinsic alignment, we use the linear alignment model by Hirata & Seljak (2004). As expected, the intrinsic alignment contributions are relatively large for bins closer in redshift, as galaxies are born in the same gravitational environment. The dashed lines represent the same quantities, but to compute them we used the linear power spectrum instead of the full non-linear one: in this way it becomes clear where non-linearities start becoming important ($\ell \gtrsim 10^2$). The dotted magenta lines appearing in the panels on the diagonal are the shape-noise term (assuming $\sigma_\epsilon = 0.3$). The gold

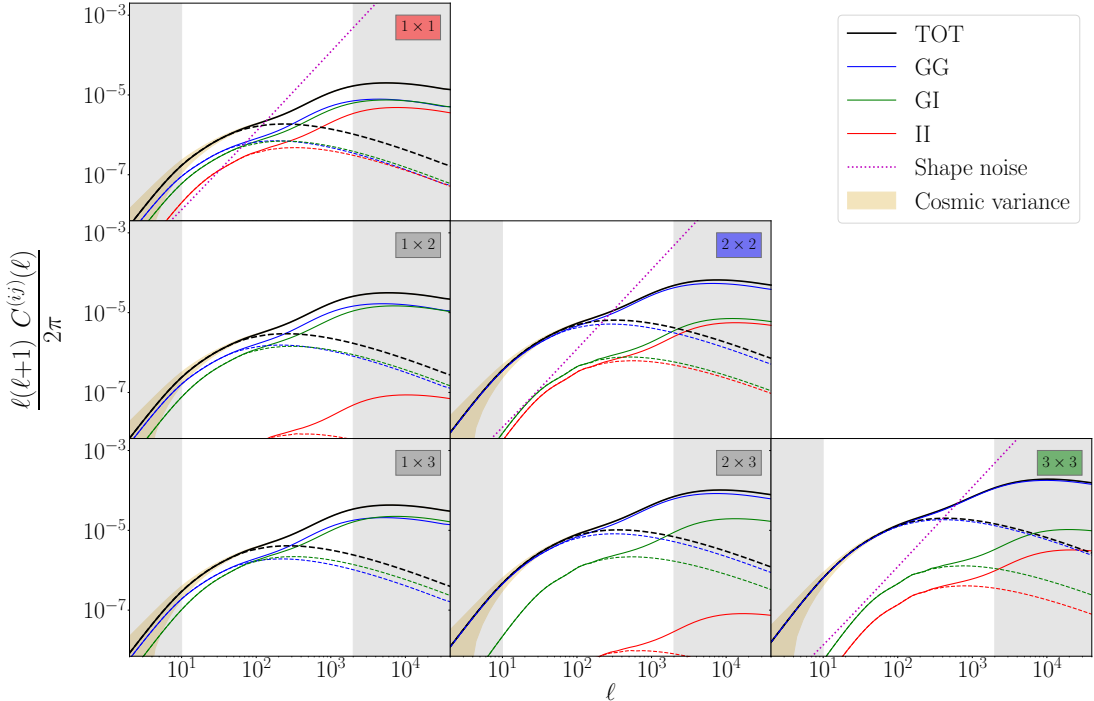


Figure 1.3: Shear power spectrum for a distribution of galaxies in 3 redshift bins. The distribution is chosen to be $\mathcal{P}(z) \propto z^2 \exp(-z/0.24)$, the bin edges are at $z = 0.1, 0.478, 0.785, 1.5$. In each panel, the solid black line represents the measured shear power spectrum for that pair of bins. The latter can be split into the cosmological signal (solid blue lines) and the intrinsic alignment contributions (GI in green, II in red). The dotted lines represent the same quantities, but assuming linear theory for the matter power spectrum. The dotted magenta line is the shape-noise term, where we assumed a RMS ellipticity of 0.3. Gold shaded areas represent the cosmic variance expected from a survey with $f_{\text{sky}} = 0.366$; grey shaded areas are regions were measurements will likely be excluded from the analysis in future surveys.

shaded area represent cosmic variance (first term of right hand side of eq. 1.63) for a survey with $f_{\text{sky}} = 0.366$. The grey shaded areas at the sides of each panel are the regions that are likely to be excluded in future surveys: at low multipoles ($\ell \lesssim 10$) because Limber’s approximation breaks down; at large multipoles ($\ell \sim 2000 - 5000$, see Sprenger et al. (2019); Audren et al. (2013); Euclid Collaboration et al. (2019a)) because the uncertainties on the matter power spectrum become too large to add any constraining power to the survey.

1.5.3 Other large-scale structure observables

Along with the observables just described, there are several more which can be used to infer constraints on cosmological parameters. Here we briefly summarize the more widely used among them.

The first is the Ly- α forest. Light from distant quasar interacts with intergalactic medium (IGM) clouds at lower redshift, giving rise to a series of absorption lines at different wavelengths, according to the redshift of the cloud and its relative velocity:

$$\lambda_{\text{abs}} = \lambda_{\text{Ly-}\alpha}(1+z)\sqrt{\frac{1+v/c}{1-v/c}}, \quad (1.64)$$

where $\lambda_{\text{Ly-}\alpha} = 1215.67 \text{ \AA}$. Since quasars are very luminous objects and can be found up to relatively high redshifts, the Ly- α forest constitutes a powerful tool for cosmological constraints in a redshift range of 2–5 (Viel et al. (2005, 2013)). Moreover, it can probe the DM properties up to very small scales ($0.5 \text{ Mpc}/h \lesssim \lambda \lesssim 20 \text{ Mpc}/h$). The observable is the flux power spectrum $P_F(k)$ of the transmitted bolometric photon flux. The only limitation with Ly- α data comes from the thermal cut-off in the power spectrum induced by pressure and thermal motions of the gas inside the photo-ionised IGM: this is the reason why this observable has provided tight constraints on various DM scenarios that present small-scale power suppressions (see e.g. Iršič et al. (2016); Murgia et al. (2018)). Moreover, one of the current tightest constraints on total neutrino mass comes from combining Ly- α data with CMB, providing $M_\nu < 0.12 \text{ eV}$ at 95% confidence level (Palanque-Deslauriers et al. (2015a)).

Another observable, always related to the IGM, that is expected to play a key role in the near future is the 21 cm intensity mapping (Bharadwaj et al. (2001); Bharadwaj & Sethi (2001); Battye et al. (2004); McQuinn et al. (2006); Chang et al. (2008); Loeb & Wyithe (2008); Bull et al. (2015)). The 21 cm emission line corresponds to the spin-flip transition of the neutral hydrogen (HI) atom. Despite this transition is particularly rare, being only a hyper-fine structure effect, the large amount of HI present in galaxies and in the IGM makes its flux relatively intense. The idea is to measure the 21 cm emission from unresolved galaxies with a low angular resolution survey (Santos et al. (2015)). The HI power spectrum is expected to follow the shape of the matter one, with a different amplitude that depends both on the HI bias and its density parameter $\Omega_{\text{HI}}(z)$ (see e.g. Villaescusa-Navarro et al. (2015)):

$$P_{21 \text{ cm}}(k, z) = \overline{\delta T_b}^2(z) b_{\text{HI}}^2(z) \left(1 + \frac{2}{3}\beta(z) + \frac{1}{5}\beta^2(z) \right) P_{\text{mm}}(k), \quad (1.65)$$

where

$$\overline{\delta T_b}(z) = 189 \frac{H_0 (1+z)^2}{H(z)} \Omega_{\text{HI}}(z) h \text{ mK} \quad (1.66)$$

is the average brightness temperature, $\beta(z) = -\frac{1}{b_{\text{HI}}(z)} \frac{d \ln D_1(z)}{d \ln(1+z)}$ is the redshift-space distortion parameter (Kaiser (1987)).

Since the redshift evolution consists essentially of a re-scaling of the total matter, non-linear power spectrum, HI intensity mapping can be used to place tight constraints on cosmological parameters (see Bull et al. (2015) for a forecast analysis).

2

Massive neutrino cosmology

I have done a terrible thing: I have postulated a particle that cannot be detected.

Wolfgang Pauli

Neutrinos... win the minimalist contest: zero charge, zero radius and very possibly zero mass.

Leon Lederman

2.1 Why “massive” neutrinos? Why cosmology?

Neutrinos were first theorized in 1930 by Wolfgang Pauli to explain the continuous energy spectrum of protons and electrons in β -decays. In order to avoid a violation of energy conservation, it was proposed that the missing energy was carried by a particle that needed to be electrically neutral and weakly interacting with detectors. The first neutrino detection dates back in 1956, thus making Pauli’s quote above wrong.

According to the Standard Model of particle physics, neutrinos come in three different flavors (ν_e, ν_μ, ν_τ , one for each corresponding lepton), only interact via the weak nuclear force and are massless. However, while the first two predictions have been

confirmed by the latest experimental data (Tanabashi et al. (2018)), there are well-motivated physical models where neutrinos acquire mass (e.g. Gonzalez-Garcia & Nir (2003); Hirsch & Valle (2004); Altarelli & Feruglio (2004); Mohapatra & Smirnov (2006)).

One way to detect whether neutrinos are massive was proposed by Bruno Pontecorvo through the detection of neutrino oscillations, i.e. a process that does not conserve neutrino flavor. This phenomenon was first proposed to explain the measured flux of electron neutrinos from the Sun, which was much smaller than expected. In fact, if the mass is small, oscillations actually occur on astronomical distances. From a theoretical point of view, this means that the neutrinos we measure are not exact eigenstates of the Standard Model Lagrangian, but a linear combination of three mass states (ν_1, ν_2, ν_3). Neutrino oscillations have nowadays been detected by several independent experiments, claiming the need of a theory beyond the Standard Model (and disproving also the second quote above). Unfortunately, neutrino oscillations only depend on the difference of square masses between different species, making it impossible to solve the full system of equations and constrain the total mass scale, i.e. the sum of the neutrino masses $M_\nu = \sum_i m_{\nu,i}$. The up-to-date constraints can be found in Tanabashi et al. (2018):

$$\Delta m_{21}^2 = (7.55^{+0.20}_{-0.16}) \times 10^{-5} \text{ eV}^2 \quad (2.1)$$

$$\Delta m_{32}^2 = \begin{cases} (2.42^{+0.03}_{-0.03}) \times 10^{-3} \text{ eV}^2 & \text{(NH)} \\ (-2.50^{+0.04}_{-0.03}) \times 10^{-3} \text{ eV}^2 & \text{(IH)}, \end{cases} \quad (2.2)$$

where we have separated the cases of *normal hierarchy* (NH) and *inverted hierarchy* (IH) as the two possible schemes neutrino masses can take (see fig. 2.1). In particular, with these data we can infer a lower limit on the sum of neutrino masses in the two scenarios:

$$M_{\nu,\text{min}} \approx \begin{cases} 0.058 \text{ eV} & \text{(NH)} \\ 0.1 \text{ eV} & \text{(IH)} \end{cases} \quad (2.3)$$

An appealing possibility is that the number of massive neutrinos is larger than 3. In this case, the extra neutrino states must be *sterile* (as opposed to the usual *active* ones), i.e. singlets of the Standard Model that only interact via gravity. While this particular new particle has some interesting consequences in cosmology (see e.g. Abazajian (2017) for a review), in this work we will only talk about active neutrinos. As we will see more in detail in the following Sections, cosmology is mainly sensitive to the sum of the three neutrino masses M_ν , at least at first order, while it is completely blind to neutrino mixing angles. Neutrino cosmology therefore constitutes a powerful

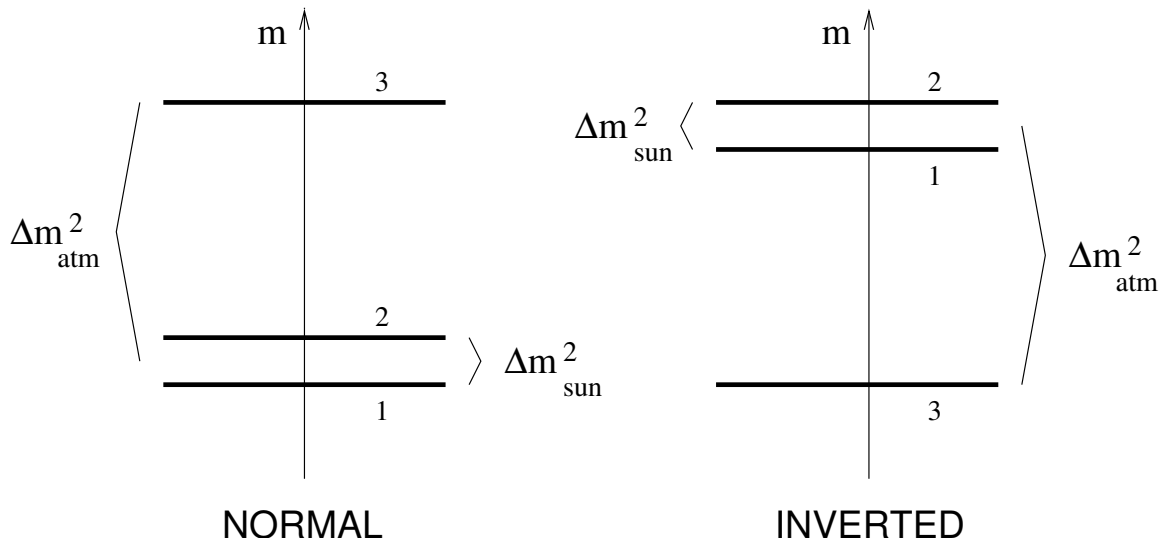


Figure 2.1: The two allowed schemes for neutrino masses: normal hierarchy (NH) and inverted hierarchy (IH). The minimum masses allowed in each scenario are found by setting the lowest neutrino eigenstate mass to zero. Taken from Lesgourgues & Pastor (2006).

way of combining particle physics and astrophysics. If neutrinos were massless, they would be completely indistinguishable from photons, since they would behave like a relativistic gas at present time as they would have always done through cosmic ages. However, if neutrinos do possess a mass, they freely stream across the Universe at early times and become non-relativistic at redshift $z \sim 10^2 - 10^3$, starting to cluster in halos like CDM and baryons, although in a much weaker way. This has sizeable effects on the growth of perturbations and on large-scale structure in general. Therefore, an extension of the Λ CDM model we described in Chapter 1 needs to be introduced: describing the Universe in presence of massive neutrinos is the aim of this Chapter.

2.2 Impact on background cosmology

We shortly investigate on the effect of neutrinos on background. We first start by summarizing the main events of neutrino thermal history, focusing in particular on the evolution of the density parameters; we then turn to addressing the impact of neutrino mass on the distance measures introduced in the previous Chapter.

2.2.1 Thermal history and density parameter

Neutrinos were copiously produced in the very early Universe and kept at thermal equilibrium by weak interactions. The momentum spectrum of each neutrino species

is given by the Fermi-Dirac distribution:

$$f_{\text{FD}} = \frac{g}{h_P^3} \frac{1}{\exp[\beta(E - \mu)] + 1}, \quad (2.4)$$

where $g = 1$ is the spin-multiplicity for neutrinos, h_P is the Planck constant, $\beta = (k_B T_\nu)^{-1}$ and $E = (p^2 c^2 + m^2 c^4)^{1/2}$. The chemical potential μ can be safely neglected, since no neutrino-antineutrino asymmetry is predicted.

The energy density of the primordial Universe is mainly carried by relativistic particles and so is its entropy. As long as neutrinos interact in the primordial plasma, their temperature is the same of radiation and scales as $T_\nu \propto a^{-1}$. Neutrinos then decouple from the photon fluid when they are still relativistic, ~ 1 s after the Big Bang and their momentum distribution is frozen from that moment onwards, i.e. $E = pc$ at denominator of eq. 2.4. However, when the temperature drops below the electron mass (~ 0.511 MeV), electrons and positrons start to annihilate and freeze-out from the photon fluid. The entropy released is transferred to the photons, but not to neutrinos. Therefore the temperature of C ν B is expected to be smaller than the one of the CMB according to the entropy conservation law, that yields:

$$T_\nu = \Gamma_{\nu, \text{inst}} T_\gamma, \quad (2.5)$$

where $\Gamma_{\nu, \text{inst}} = \left(\frac{4}{11}\right)^{1/3}$. This value must be slightly modified if we want to take into account the distortions in the neutrino temperature spectrum introduced by flavor oscillations and the fact that the decoupling between photons and neutrinos is not an instantaneous process. Such corrections are usually expressed in terms of an effective number of relativistic degrees of freedom defined as:

$$N_{\text{eff}} = N_\nu \frac{\Gamma_\nu^4}{\Gamma_{\nu, \text{inst}}^4}, \quad (2.6)$$

where $N_\nu = 3$ is the number of active neutrinos and $\Gamma_\nu \approx 0.71649$. All in all, $N_{\text{eff}} \approx 3.046$ (Mangano et al. (2005)) and the predicted temperature of the C ν B is $T_{\nu,0} \approx 1.95$ K at present time.

From eq. 2.4 one can compute the density and pressure of neutrinos for each species as:

$$\rho_{\nu,i} = \int d^3 \mathbf{p} \frac{E(p)}{c^2} \frac{1/h_P^3}{e^{\beta pc} + 1} \quad (2.7)$$

$$P_{\nu,i} = \int d^3 \mathbf{p} \frac{p^2 c^2}{3E(p)} \frac{1/h_P^3}{e^{\beta pc} + 1}. \quad (2.8)$$

It is easier to relate the cosmological neutrino density to the CMB density. For a single species we have:

$$\rho_{\nu,i}(z) = \frac{15}{\pi^4} \Gamma_\nu^4 \rho_\gamma(z) \mathcal{F} \left[\frac{m_{\nu,i}}{(1+z)k_B T_{\nu,0}} \right], \quad (2.9)$$

where

$$\mathcal{F}(y) = \int_0^\infty dx x^2 \frac{\sqrt{x^2 + y^2}}{e^x + 1}. \quad (2.10)$$

Using eqs. 2.9-2.10 is useful to find the parameter of state for each species at a given redshift:

$$w_{\nu,i} = \frac{1}{3} \left[1 - \frac{d \ln \mathcal{F}(y)}{d \ln y} \right], \quad (2.11)$$

where $y = \frac{m_{\nu,i}}{(1+z)k_B T_{\nu,0}}$. It is easy to verify that at high redshifts, where $y \ll 1$, \mathcal{F} is approximately constant and $w_\nu \rightarrow 1/3$, so that neutrinos behave like radiation. However, as the Universe expands, they become non-relativistic at

$$1 + z_{\text{nr}} = 1890 \frac{m_{\nu,i}}{1 \text{ eV}} \quad (2.12)$$

and their parameter of state slowly approaches zero, meaning that neutrinos behave like pressureless matter at late times. When this happens, the neutrino density parameter (for all species) can be well approximated by:

$$\Omega_\nu = \frac{M_\nu}{93.14 h^2 \text{ eV}}. \quad (2.13)$$

This double behaviour of neutrinos at different times has a direct impact on the Hubble parameter. Inserting massive neutrinos in the energy budget of the Universe yields, in the most general case,

$$H^2(z) = H_0^2 \left\{ \Omega_{\text{cb}}(1+z)^3 + \Omega_\Lambda + \Omega_\gamma(1+z)^4 + \Omega_K(1+z)^2 + \sum_{i=1}^{N_\nu} \frac{15}{\pi^4} \Gamma_\nu^4 \Omega_\gamma \mathcal{F} \left[\frac{m_{\nu,i}}{(1+z)k_B T_{\nu,0}} \right] (1+z)^4 \right\}, \quad (2.14)$$

where we have gathered CDM and baryons in a single ‘‘CDM+b’’ fluid (cb). The evolution of the density parameters Ω_i for a flat Universe with massive neutrinos is sketched in fig. 2.2, split in all its contributions. The cosmological parameters chosen are given in Table 1.1, to which we add three different neutrino species with masses $m_\nu = [0.05, 0.01, 0] \text{ eV}$ (so that $M_\nu = 0.06 \text{ eV}$). It must be stressed that, here like everywhere else in this work, what we keep fixed in the different cosmological models is the total matter density ($\Omega_{\text{m}} = \Omega_{\text{c}} + \Omega_{\text{b}} + \Omega_\nu$): in other words, an increase in neutrino

mass comes at the expenses of a decrease in Ω_c . Therefore here $\Omega_c = 0.2589$. The green solid line represents Ω_γ (here fixed by $T_\gamma = 2.7255$ K), the radiation density parameter, which dominates the energy content of the Universe at early times. After radiation-matter equality, CDM (solid blue) and baryons (solid red) give rise to the matter dominated era. In the right part of the plot, dark energy (solid black line) rises up to dominate at present time (denoted by the dot-dashed vertical line). The solid, dashed and dotted magenta lines show the evolution of the density parameter of the three different neutrino species with different masses - 0.05, 0.01 and 0 eV, respectively. As expected, all the species are relativistic at early times and contribute to the energy density like radiation. As the temperature drops below their mass, each species makes a non-relativistic transition, starting from the most massive. This occurs at $z_{\text{nr}} \lesssim 100$ for the two non-vanishing masses considered here. This has important consequences for instance when running simulations with massive neutrinos: in fact, initial conditions are typically set in this transition epoch and neglecting the contribution of relativistic particles to the Hubble parameter may lead to incorrect results (Zennaro et al. (2017)).

2.2.2 Distances

The fact that neutrinos change the expansion rate of the Universe of course affects also the distances we measure at fixed redshift. This is shown in fig. 2.3. In each of the top panels we show some key background quantities in Λ CDM cosmology. In the left one we plot the quantity $c/H(z)$ which enters in the computation of all the other distances which are shown in the center and right panels. The central panel is reserved to the comoving, luminosity and angular diameter distances, represented by the solid, dashed and dot-dashed lines respectively. Finally, the right panel shows the isotropic volume distance. The bottom panels represent the relative difference of the various quantities $Q = \{c/H, \chi, D_L, D_A, D_V\}$ with respect to the Λ CDM case when we add a single massive neutrino species, with mass $M_\nu = 0.2$ eV (dashed line), 0.4 eV (dot-dashed) and 0.6 eV (dotted). Once again we remark that every time we increase M_ν we automatically decrease Ω_c . Notice that for χ, D_L and D_A the relative differences are the same. The differences in the background quantities only reach 1% for redshifts of order $z \sim 10^3$ and for neutrino masses which are already excluded at 95% confidence level, making it challenging to put constraints on neutrino mass using only background quantities. In fact, as we will show in the next Section, the greatest differences with respect to Λ CDM come from the growth of perturbations and this is where the true constraining power of cosmology on M_ν comes from.

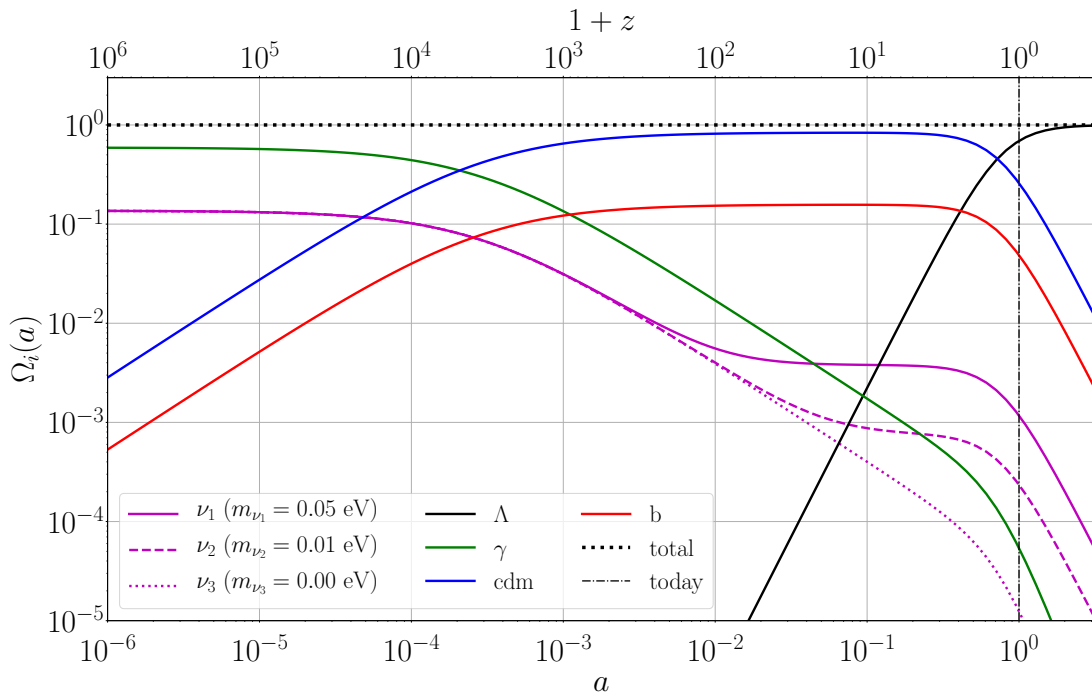


Figure 2.2: Evolution of density parameters as a function of scale factor or, equivalently, redshift for a flat Universe. The green line is the radiation density parameter that dominates at early times before dropping down, leaving the stage to a matter dominated era (with baryons in red and CDM in blue). The black line is the cosmological constant. The solid, dashed and dotted lines represent the density parameter of three different neutrino species with masses 0.05, 0.01 and 0 eV, respectively. As it can be clearly seen, the most massive species become non-relativistic first and when it occurs, they start behaving like a pressureless fluid. The total energy density (which is always equal to 1) is denoted by the dotted black line. Finally, the dot-dashed vertical line at $a = 1$ denotes present time.

2.3 Impact on density perturbations

As we saw in the previous Section, neutrinos do not change radically background quantities like density parameters and various distance measures. What they do affect in a sizeable way is the growth of density perturbations both at linear and non-linear level. In this Section we revise linear PT and non-linearities in presence of massive neutrinos, highlighting the differences with respect to the Λ CDM case.

2.3.1 Equations of motion

When dealing with neutrinos, since they behave as relativistic particles up to relatively small redshifts, we cannot make use of the Newtonian approximation of the

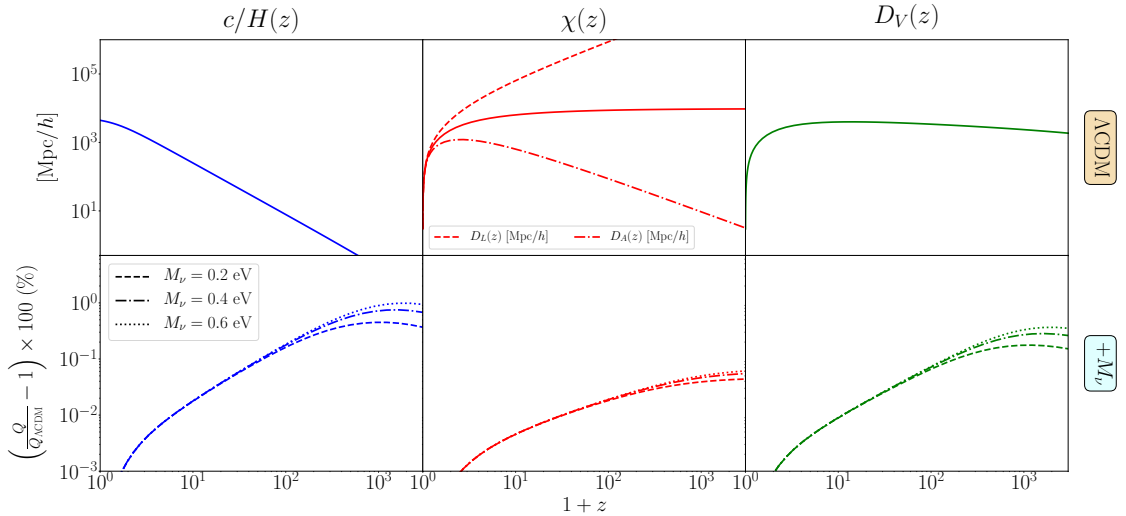


Figure 2.3: Impact of neutrino mass on various distance measures as a function of redshift. Top panels show the inverse Hubble distance measure c/H (left), the comoving distance (center, accompanied by the luminosity distance - dashed line - and the angular diameter distance - dot-dashed line) and the isotropic volume distance (right) for a Λ CDM Universe. Bottom panels show the relative differences when including one massive neutrino species with $M_\nu = 0.2, 0.4, 0.6$ eV, denoted by the dashed, dot-dashed and dotted lines respectively.

Boltzmann equation (eq. 1.18). Moreover, in this context it is better to make use of *conformal time* $d\tau = dt/a$ as time coordinate, so that the relation between the distribution function f and the total number of particle per phase-space volume is $dN = f(\mathbf{x}, \mathbf{p}, \tau) d^3\mathbf{x} d^3\mathbf{p}$. We will assume a flat Universe with metric:

$$ds^2 = a^2(\tau) [d\tau^2(1 + 2\Psi) - dx^i dx^j \delta_{ij}(1 - 2\Phi)], \quad (2.15)$$

where Ψ and Φ are two potentials responsible for time dilation and space contraction, respectively, and we set $c = 1$. The metric written in eq. 2.15 corresponds to a perturbed FLRW metric in the *Newtonian gauge*. Gauges arise when choosing a correspondence between points in the physical space-time and the background: since this choice is not unique, different gauges typically yield different values for the same perturbation quantities and different growth. This in principle is not a problem, since each observable is defined with respect to a precise coordinate system specified by the corresponding measurement. Choosing the Newtonian gauge simplifies calculations for the scalar perturbations that we are after, but for instance cannot be used to treat vector or tensor perturbations.

To derive Boltzmann equation for a relativistic fluid we have to make a couple of considerations. Despite the distribution function is written as a function of x^μ and

p^μ , it is better to work with other quantities. We define the proper momentum $P_i = P^i$ from the canonical one as $p_i = a(1 - \Phi)P_i$ and introduce $q_i = aP_i = (1 - \Phi)p_i$. We also renormalize the energy $E^2 = p^2 + m^2$ to $\epsilon^2 = a^2(P^2 + m^2) = q^2 + a^2m^2$. Finally, from momentum conservation $p_\mu p^\mu = m^2$ we get $p_0 = (1 + \Psi)\epsilon$.

Expanding the (conformal) time derivative in all its contribution, one gets:

$$\frac{\partial f}{\partial \tau} + \frac{dx^i}{d\tau} \frac{\partial f}{\partial x^i} + \frac{dq}{d\tau} \frac{\partial f}{\partial q} + \frac{d\gamma^i}{d\tau} \frac{\partial f}{\partial \gamma^i} = \left(\frac{\partial f}{\partial \tau} \right)_c, \quad (2.16)$$

where we have expanded q in its direction cosines $q_i = q\gamma_i$. It is easy to show that at zero-th order $dx^i/d\tau = p^i/p^0 \approx q\gamma^i/\epsilon$ and that $dq/d\tau \approx q\dot{\Phi} - \epsilon\gamma^i\partial_i\Psi$, where the dot here represents a derivative with respect to conformal time. Moreover, the product involving the direction cosines is already a second order contribution and can be discarded in linear PT.

In a FLRW Universe, the phase-space distribution of neutrinos is perfectly isotropic and given by a Fermi-Dirac distribution:

$$f_0(q) = \frac{g/h_P^3}{e^{q/(ak_B T_\nu)} + 1}, \quad (2.17)$$

only dependent on the modulus of q . We want to perturb eq. 2.17 by adding a fluctuation f_1 , namely we substitute $f = f_0 + f_1$ in eq. 2.16 and keep only the first order contributions. The result in Fourier space can be written as:

$$\dot{f}_1 + ik\mu \frac{q}{\epsilon} f_1 = -q \frac{\partial f_0}{\partial q} \left(\dot{\Phi} - ik\mu \frac{\epsilon}{q} \Psi \right) + \left(\frac{\partial f_1}{\partial \tau} \right)_c, \quad (2.18)$$

where $\mu = \mathbf{k} \cdot \mathbf{q}/kq$. It is easy to verify that this equation is the relativistic equivalent of eq. 1.18.

2.3.2 Free-streaming and linear power spectrum

The solution to eq. 2.18 can be written as:

$$f_1(\mathbf{k}, \tau) = f_1(\mathbf{k}, \tau_{\text{ini}}) e^{-ik\mu \frac{q}{\epsilon} (\tau - \tau_{\text{ini}})} + \frac{\epsilon}{q} \int_{\tau_{\text{ini}}}^{\tau} d\tau' \left[-q \frac{\partial f_0}{\partial q} \left(\dot{\Phi} - ik\mu \frac{\epsilon}{q} \Psi \right) + \left(\frac{\partial f_1}{\partial \tau} \right)_c \right] e^{-ik\mu \frac{q}{\epsilon} (\tau - \tau')}, \quad (2.19)$$

which can be solved iteratively (see e.g. Mo et al. (2010)). The first term represents the propagation of initial conditions, while the second term describes the dynamical evolution of the perturbations due to gravitational interactions. We can easily relate f_1 to the neutrino density perturbation since $\delta_\nu(\mathbf{k}, \tau) \propto \int d^3\mathbf{q} f_1 \propto \int dq d\mu q^2 f_1$.

To answer the question about how δ_ν evolves with time, let us consider the quantity $kq\mu/\epsilon$. When this is large, the integrand function oscillates quickly, making it impossible for δ_ν to grow. There exists therefore a scale λ_{fs} below which neutrinos cannot cluster. This is called *free-streaming length* and it is straightforward to show that:

$$\lambda_{\text{fs}} = \int_0^t dt' \frac{v(t')}{a(t')}. \quad (2.20)$$

Its value can be either written in configuration or in Fourier space for each neutrino species (e.g. Lesgourgues & Pastor (2006)):

$$\lambda_{\text{fs}}(z) = 7.7 \frac{1+z}{E(z)} \frac{1 \text{ eV}}{m_\nu} \text{ Mpc}/h \quad (2.21)$$

$$k_{\text{fs}}(z) = 0.82 \frac{E(z)}{(1+z)^2} \frac{m_\nu}{1 \text{ eV}} h/\text{Mpc}. \quad (2.22)$$

After non-relativistic transition (eq. 2.12) the proper free-streaming scale increases as $\propto t^{1/3}$, i.e. slower than the expansion rate ($\propto t^{2/3}$). As a consequence, for neutrinos becoming non-relativistic during the matter dominated epoch, k_{fs} passes through a minimum k_{nr} at the time when this transition occurs:

$$k_{\text{nr}} = 0.018 \Omega_{\text{m}}^{1/2} \left(\frac{m_\nu}{1 \text{ eV}} \right)^{1/2}. \quad (2.23)$$

The net effect of free-streaming is the following. Small-scale neutrino density perturbations are damped because neutrinos cannot be confined in regions smaller than the free-streaming length; on the other hand, at large scales and at late times, neutrinos can be considered “cold” and therefore behave like CDM. In particular, modes with $k < k_{\text{nr}}$ are never affected by free-streaming and evolve identically to the Λ CDM case. The growth of neutrino overdensities affect directly also the growth in CDM perturbations. In fact, on scales $k \gg k_{\text{nr}}$ the neutrino overdensity does not contribute to the Poisson equation and consequently the source term in eq. 1.25 is smaller by a factor $(1 - f_\nu)$. It can be shown (see e.g. Lesgourgues & Pastor (2006)) that, while in a massless neutrino Universe $\delta_{\text{c}} \propto a$ in the matter dominated epoch, when neutrinos have mass this becomes $\delta_{\text{c}} \propto a^{1-\frac{3}{5}f_\nu}$.

Therefore, neutrino free-streaming introduces a scale-dependent linear growth factor for all components. Eisenstein & Hu (1998) found an approximate formula (accurate to better than 1%) for the growth factors of CDM+b and total matter:

$$D_{1,\text{cb}}(k, z) = \left[1 + \left(\frac{D_1(z)}{1 + y_{\text{fs}}(\chi, f_\nu)} \right)^{0.7} \right]^{p_{\text{cb}}/0.7} D_1(z)^{1-p_{\text{cb}}}, \quad (2.24)$$

$$D_{1,\text{cb}\nu}(k, z) = \left[f_{\text{cb}}^{0.7/p_{\text{cb}}} + \left(\frac{D_1(z)}{1 + y_{\text{fs}}(\chi, f_\nu)} \right)^{0.7} \right]^{p_{\text{cb}}/0.7} D_1(z)^{1-p_{\text{cb}}}, \quad (2.25)$$

where $D_1(z)$ is given by eq. 1.26, $f_i = \Omega_i/\Omega_m$,

$$p_{\text{cb}} = \frac{1}{4} \left[5 - \sqrt{1 + 24 f_{\text{cb}}} \right] \geq 0, \quad (2.26)$$

$$y_{\text{fs}}(\chi, f_\nu) = 17.2 f_\nu (1 + 0.488 f_\nu^{-7/6}) \left(\frac{N_{\text{massive}} \chi}{f_\nu} \right)^2, \quad (2.27)$$

$$\chi = \frac{k}{h/\text{Mpc}} \frac{T_\gamma}{2.7 \text{ K}} \Omega_m^{-1}, \quad (2.28)$$

and N_{massive} is the number of massive neutrinos.

Of course, the matter power spectrum reflects the scale-dependence of the growth factor. When adding massive neutrinos to the recipe, the total matter density perturbation (at redshifts relevant for large-scale structure) is given by:

$$\delta = f_c \delta_c + f_\nu \delta_\nu, \quad (2.29)$$

where for ‘‘c’’ we mean CDM+b. The linear total matter power spectrum is therefore given by:

$$P^{\text{lin}}(k) = f_c^2 P_{\text{cc}}^{\text{lin}}(k) + 2f_c f_\nu P_{\text{c}\nu}^{\text{lin}}(k) + f_\nu^2 P_{\nu\nu}^{\text{lin}}(k). \quad (2.30)$$

On scales larger than k_{nr} neutrinos and CDM are indistinguishable from each other, both contribute to the background expansion and to Poisson equation. Therefore we expect the power spectra in Λ CDM and massive neutrino cosmologies to be equal. The differences arise at small scales for several reasons. The first is related to the fact that the radiation-matter equality takes place at different epochs. In fact, at this time neutrinos are effectively relativistic and therefore enhance the amount of radiation at the expenses of non-relativistic matter. In a Universe with massive neutrinos with fixed Ω_γ and Ω_m , the radiation-matter equality occurs later, the shift being given by $a_{\text{eq}}/a_{\text{eq}}^{\Lambda\text{CDM}} = (1 - f_\nu)^{-1}$. At any time before neutrinos become non-relativistic, the two models are still equivalent apart from a shift in the scale factor $\delta_c[a] = \delta_c^{\Lambda\text{CDM}}[(1 - f_\nu)a]$.

After the non-relativistic transition, neutrinos anyway suffer from free-streaming on small-scales: in this configuration, they contribute to the expansion rate but not to gravitational clustering, therefore slowing down the growth of perturbations of CDM and baryons. All in all, it can be shown that for scales $k \gg k_{\text{fs}}$ the suppression to the linear total matter power spectrum in massive neutrino cosmologies is approximately given by:

$$\frac{P^{\text{lin}}(k)}{P^{\Lambda\text{CDM,lin}}(k)} \approx 1 - 8f_\nu. \quad (2.31)$$

If one repeats the same calculation considering only the the CDM part, the result is (Castorina et al. (2015)):

$$\frac{P_{cc}^{\text{lin}}(k)}{P_c^{\Lambda\text{CDM,lin}}(k)} \approx 1 - 6f_\nu. \quad (2.32)$$

2.3.3 Non-linear growth

Investigating non-linearities in presence of massive neutrinos is a harder task than it was in the Λ CDM case. In general, using PT yields similar if not slightly worse results, because the condition under which the various kernels and growth factors are computed is an EdS Universe. Therefore one usually relies on N -body simulations.

Adding neutrinos in simulations is a non-trivial task for several reasons. First of all, because of initial conditions. What one would do in Λ CDM is to rescale a low-redshift linear power spectrum to a high redshift using the linear growth factor (eq. 1.26). Unfortunately this cannot be done in massive neutrino cosmologies, where the growth factor is scale-dependent and only approximate formulae are known. Moreover, simulations are often started at epochs where neutrinos are still relativistic ($z \sim 10^2$) and therefore contribute to the background expansion in a different way with respect to the Λ CDM framework. Zennaro et al. (2017) proposed a way to keep these inconsistencies under control, with a method that can return initial conditions as accurate as $\sim 1\%$ at $z = 99$. Always related to initial conditions: thermal velocities of neutrinos must be accurately implemented or non-convergent results will be found (Klypin et al. (1993); Primack et al. (1995)).

Following the evolution of two different fluids is much more expensive in terms of computational cost. For this latter problem, several approaches have been followed. The quickest and less accurate way to include neutrinos in N -body simulations was proposed by Brandbyge & Hannestad (2009): here neutrino perturbations are evolved by solving the linear Boltzmann equation on a grid. Particle-based methods, where neutrinos are treated as CDM particles with a large thermal velocity drawn from the Fermi-Dirac distribution, were employed in a number of following works (Brandbyge et al. (2008); Viel et al. (2010); Villaescusa-Navarro et al. (2013); Castorina et al. (2015); Carbone et al. (2016)), also combined with techniques aiming at reducing shot noise (Banerjee & Dalal (2016); Banerjee et al. (2018); Brandbyge et al. (2019)) and cosmic variance (Villaescusa-Navarro et al. (2019)). A hybrid method that combines grid-based and particle-based methods (used at early and late times, respectively) was also proposed by Brandbyge & Hannestad (2010). An alternative approach by Ali-Haïmoud & Bird (2013) consists of following the evolution of CDM particles through

N -body equations and neutrinos through Boltzmann equation but still accounting for the mutual gravitational interaction. A final implementation worth mentioning is the one by Dakin et al. (2019), where neutrinos are evolved according to the non-linear Boltzmann equation in real space.

All in all, these models agree on a wide range of scales to a few percent. A peculiar prediction that all these methods share is that, when taking the ratio of the non-linear power spectrum in massive neutrino cosmologies with respect to the Λ CDM counterpart, this acquires a spoon-like shape. This is visible in fig. 2.4. For three different neutrino masses (0.2 eV in blue, 0.4 eV in red, 0.6 eV in green), we plot the aforementioned ratio in the non-linear total matter case (solid lines), linear total matter case (dashed lines) and linear CDM(+b) only case (dotted lines). The latter two ratios reflect what we said in the previous Section in eqs. 2.31-2.32, respectively. An analytical explanation of why the spoon-like feature appears in the non-linear matter power spectrum was given by Hannestad et al. (2020) in terms of the halo model. The spoon shape is generated in the transition region between the 2-halo term and the 1-halo term: while the former is suppressed due to free-streaming, the latter reflects the fact that neutrinos, once become non-relativistic, fall into CDM halos, therefore relieving the difference with respect to Λ CDM. At higher redshifts, the depth of the spoon increases, because neutrinos have larger thermal velocities, and moves to smaller scales, since halos are on average less extended. Always Hannestad et al. (2020) showed that the presence of this feature is robust with respect to the choice of halo mass functions and halo profiles and that a simple halo model is able to predict the shape of the spoon (both in depth and width) with an accuracy of $\sim 1\%$ on scales of $k \lesssim 15 h/\text{Mpc}$.

The modelling of the results of N -body simulations with massive neutrinos requires a couple of clarifications. In the Λ CDM framework, halo/galaxy biases and halo mass functions are defined with respect to the total matter density field. It has been shown in a series of papers (Ichiki & Takada (2012); Villaescusa-Navarro et al. (2014); Castorina et al. (2014)) that opting for doing the same in the context of massive neutrino cosmologies spoils the universality of the mass function. These deviations completely disappear if one assumes that the relevant field for the description of clustering is the CDM+b one (δ_c): we refer to this feature as CDM prescription.

This has a consequence on how the non-linear matter power spectrum is computed when using fitting formulae. Since the main density field in clustering is the CDM+b one, the operator \mathcal{H} (like HALOFIT) that transforms a linear power spectrum into its non-linear counterpart should act only on the linear CDM+b one. Furthermore, as

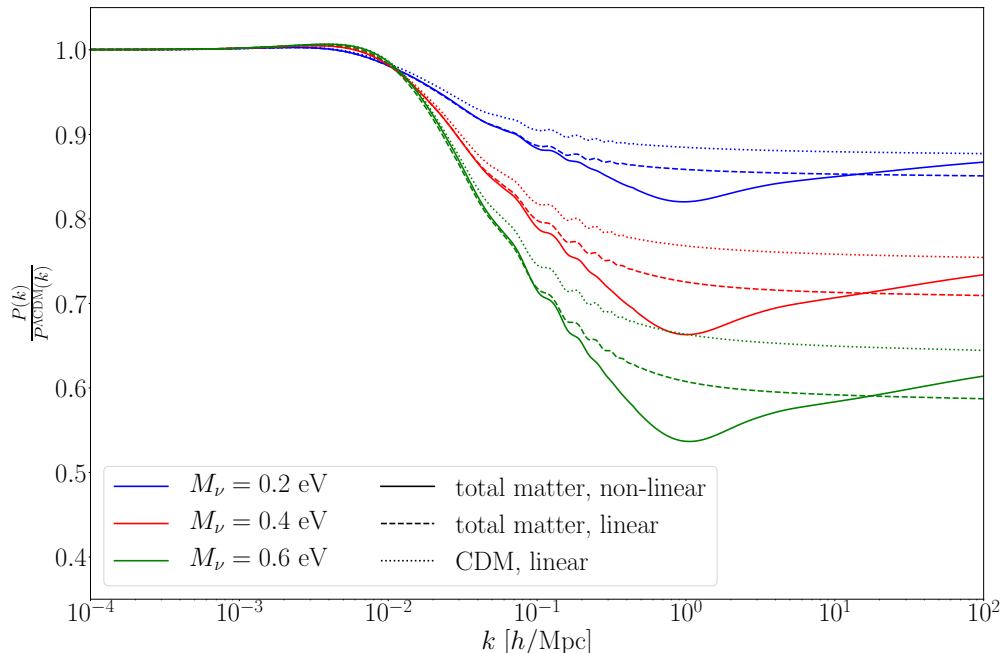


Figure 2.4: Suppression due to massive neutrinos in various power spectra at $z = 0$. Different colors label different M_ν (a single massive species is assumed): blue for 0.2 eV, red for 0.4 eV, green for 0.6 eV. Solid lines represent the non-linear suppression on the total matter power spectrum according to eq. 2.33, whereas dashed and dotted lines do the same for the linear total matter and CDM plus baryons power spectra, respectively.

was shown by Castorina et al. (2015), non-linearities in the cross ($P_{c\nu}$) and neutrino power spectra ($P_{\nu\nu}$) are expected to be sub-percent effects. Therefore, the non-linear total matter power spectrum in neutrino cosmologies can be written as:

$$P^{\text{nl}}(k) = f_c^2 \mathcal{H} [P_{cc}^{\text{lin}}(k)] + 2f_c f_\nu P_{c\nu}^{\text{lin}}(k) + f_\nu^2 P_{\nu\nu}^{\text{lin}}(k). \quad (2.33)$$

Notice that this procedure is different from the one proposed by Mead et al. (2016). The parameters proposed in their Section 3.3 are the values that best suit the massive neutrino simulations by Massara et al. (2014). If one instead wants to follow CDM prescription and use eq. 2.33, the operator \mathcal{H} must be used with the parameters that best fit CDM only simulations, i.e. the ones given in their Table 1.

The CDM prescription was used in Massara et al. (2014) to perform an interesting extension of the halo model in order to include massive neutrinos. In this picture, all the three spectra (cc , $c\nu$ and $\nu\nu$) are split into 1-halo and 2-halo terms, with neutrinos that are divided into a linear component that free-streams and a clustered component with its own universal density profile. All in all, the neutrino halo model

can reproduce the total matter power spectrum with an agreement of $\sim 10\%$ at large and small scales, but still suffers from problems in the transition scales, where the accuracy only reaches 20 – 30%.

2.4 Impact on large-scale structure observables

We turn now our attention to the impact of neutrinos on the observable we will deal with in this work. In particular, we will limit ourselves to the cases of clustering of biased tracers (halos or galaxies) in Fourier space, of the BAOs in the 2PCF and of cosmic shear.

2.4.1 Clustering of biased tracers

As we mentioned in the last Chapter, describing the clustering of a given tracer g consists of finding a functional, depending on some bias parameters, that relates the underlying density field to the one of the tracer chosen. We also said that in massive neutrino cosmologies the fundamental field for clustering is no longer total matter, but rather the CDM+b one. Therefore, assuming a linear constant bias relation, eq. 1.50 transforms into:

$$\delta_g = b_1 \delta_c. \quad (2.34)$$

However, dealing with biases in this new context is much more subtle than in the Λ CDM case: the reason is once again neutrino free-streaming. In fact, in the Λ CDM model halo formation is a completely local process (Kaiser (1984); Bardeen et al. (1986); Coles (1993); Mann et al. (1998)). On the contrary, in the massive neutrino picture, neutrinos can cover cosmological distances in relatively short time-scales, modifying the gravitational dynamics at different times up to large scales and thus making structure formation a non-local process. Therefore, the halo bias can become scale-dependent already at linear order. This feature was first predicted in the general case of hot DM (Hui & Parfrey (2008); Parfrey et al. (2011)) and then applied to the massive neutrino case (LoVerde (2014a); Chiang et al. (2018)). Qualitatively speaking, the bias of a DM halo of a given mass M can be predicted through the peak-background split (see Desjacques et al. (2018); LoVerde (2014b)):

$$b_1(M, k) = 1 + \frac{\partial \ln \left(\frac{dn}{dM} \right)}{\partial \delta_{sc}} \frac{\partial \delta_{sc}}{\partial \delta_{c,\ell}(k)}, \quad (2.35)$$

where dn/dM is the halo mass function, $\delta_{sc} \approx 1.686$ is the overdensity for spherical collapse and $\delta_{c,\ell}$ is a long-wavelength perturbation in the CDM+b fluid. The latter

derivative can be computed by following a two-fluid spherical collapse calculation in which neutrino perturbations are treated linearly while a spherical top-hat shell of CDM+b is collapsing. Of course, this term is responsible for the scale-dependence of the linear bias. Putting all this information together, the tracer power spectrum stopping at leading order in bias in massive neutrino cosmologies can be written as:

$$P_g(k) = b_1^2(k)P_{cc}(k), \quad (2.36)$$

where now the bias function can be expanded in even powers of k (for parity reasons): $b_1(k) = A + Bk^2 + \dots$

The very first confirmation of this feature from N -body simulations came from Chiang et al. (2019), where a scale-dependent linear bias was modelled through a redshift- and cosmology-dependent function $f(k)$ taken from the separate Universe prediction (Wagner et al. (2015)). However, despite the importance of these results, this effect is extremely hard to detect in real data: to obtain a significant result with a small amount of simulations, f_ν was enhanced to 0.1 with 28 degenerate massive neutrino species each with $m_\nu = 0.05$ eV.

2.4.2 BAOs in the 2PCF

Another relevant and sizeable effect of neutrinos on large-scale structure observables is the one on the 2PCF at BAO scales and its evolution in the non-linear regime. At a fixed redshift, this is expected not much because of free-streaming, that barely affects these large scales, but rather because keeping Ω_m fixed while increasing M_ν makes Ω_b/Ω_c change as well. We will dig more in detail the aspect of redshift evolution in Chapter 3: here we just want to give a qualitative explanation of the main differences in the 2PCFs in Λ CDM and in massive neutrino cosmologies. In the top panel of fig. 2.5 we plot the linear CDM+b 2PCFs for a Λ CDM model (black dashed lines) and for three different neutrino masses (one single massive species of masses 0.2, 0.4, 0.6 eV in blue, red and green, respectively) at $z = 0$. Their non-linear counterparts are represented by the solid lines and have been computed applying the HALOFIT operator by Mead et al. (2015) and the BAO smoothing like in Tegmark et al. (2006). The bottom panel shows, with the same color code, the ratio of the 2PCFs with massive neutrinos with respect to the Λ CDM one. Of course everything that will be said here holds true for the 2PCF of biased tracers as long as we keep our simple linear bias model of eq. 2.34.

Let us start from the linear 2PCF: the different baryon-to-CDM density ratio causes a shift in the peak of the BAOs. This effect is however small, $\lesssim 0.3\%$ for $M_\nu < 0.6$

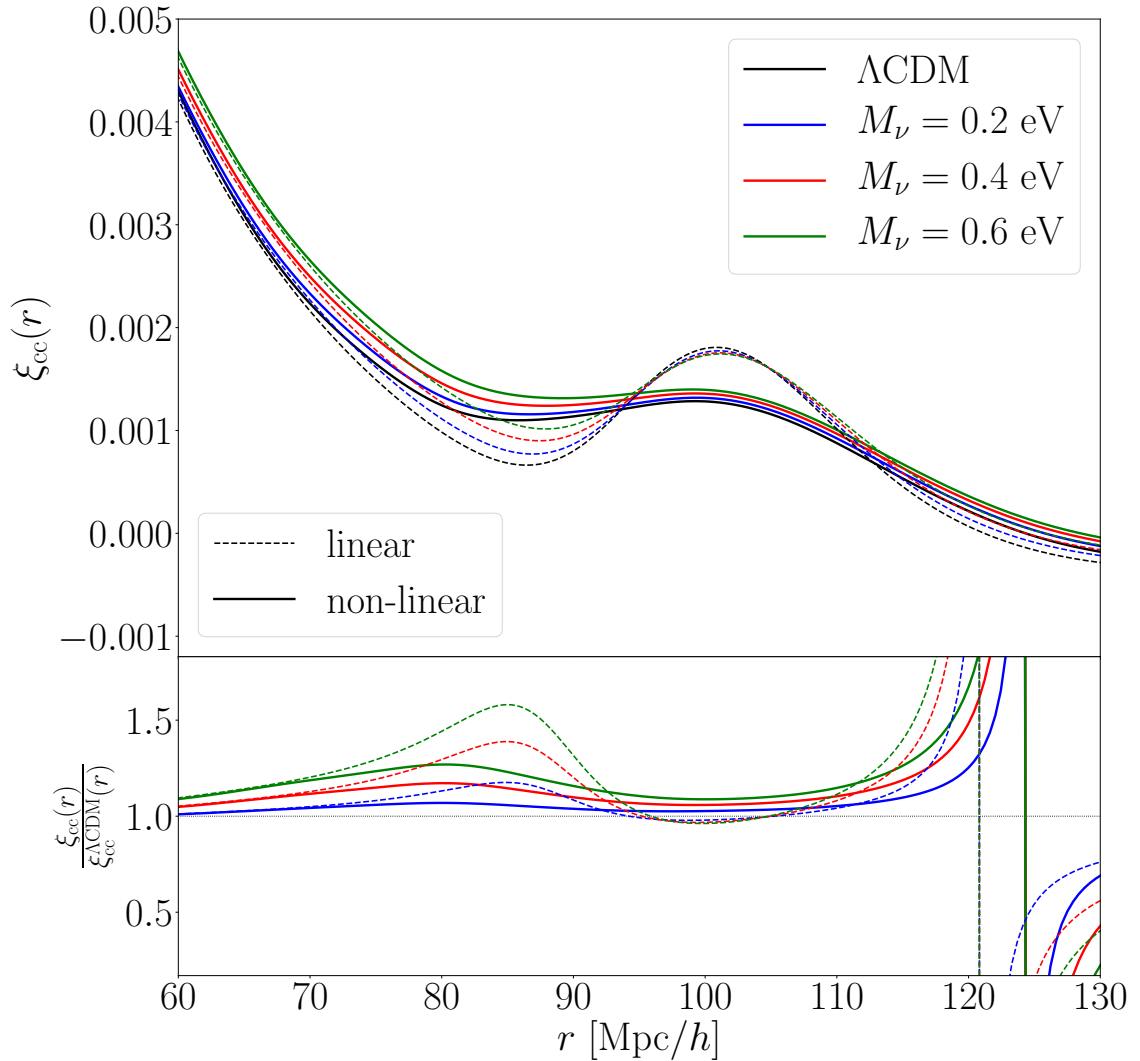


Figure 2.5: Impact of neutrino mass on the 2PCF of CDM+b at $z = 0$. The top panel shows both the linear (dashed lines) and the non-linear (solid lines) 2PCFs for different neutrino masses: ΛCDM in black, 0.2 eV in blue, 0.4 eV in red, 0.6 eV in green. A single massive neutrino species is assumed. The bottom panel shows the ratios of all the above said 2PCFs with respect to the ΛCDM case.

eV. The largest difference comes in the region of the dip, where we have amplitude discrepancies that can get as large as 50% for $M_\nu = 0.6 \text{ eV}$.

As far as the non-linear 2PCF is concerned, the differences here come from the fact that the damping factor that smooths the BAO feature is different. We can estimate this as follows. While in the plot the non-linear 2PCF is computed as the Fourier transform of the non-linear CDM+b power spectrum with smoothed BAO, a fair

approximation in the BAO region, motivated by RPT: (Crocco & Scoccimarro (2006)), can be written as (e.g. Peloso et al. (2015); Noda et al. (2017))

$$\xi_{cc}^{\text{RPT}}(r) \approx \int_0^\infty dk \frac{k^2 P_{cc}^{\text{lin}}(k)}{2\pi^2} e^{-k^2 \sigma_v^2} j_0(kr), \quad (2.37)$$

where σ_v^2 is given by eq. 1.47. We see therefore that when adding massive neutrinos, the damping factor and therefore the BAO smoothing is smaller. Moreover, the differences with respect to Λ CDM become more scale-independent, even though still of the order $\sim 10 - 25\%$ for $M_\nu = 0.6$ eV.

The differences just described will constitute the base of the analysis we will perform in Chapter 3. There, rather than on amplitudes, we will focus on the shifts induced by the scale-dependent growth on the BAO peak and dip scales and in turn to the mid-point between them, dubbed the *linear point*.

2.4.3 Cosmic shear

Another observable we turn our attention to is cosmic shear. The shear power spectrum in the Limber's and flat sky approximations is given by eq. 1.60. From that formula we see that there are several points where neutrino effects can enter.

The first is the Hubble factor $H(z)$, whose impact is however very small. From the bottom left panel of fig. 2.3 we can see that the impact of massive neutrinos on c/H is well below 0.01% for all the redshifts relevant for current and future weak lensing surveys ($z \lesssim 3$) for any neutrino mass. The reason is because massive neutrinos at these small redshifts are indistinguishable from CDM or baryons, since their parameter of state w_ν is close to zero. The same is true for the comoving distance $\chi(z)$, where the impact of massive neutrinos is even smaller (bottom center panel of fig. 2.3) and for the window functions (eq. 1.61). Assuming that only these 3 quantities vary when switching to massive neutrino cosmologies, the difference with respect to Λ CDM is well below 0.1% for future surveys.

Once again what changes completely is the power spectrum. In cosmic shear the total matter power spectrum is involved, computed with the prescription of eq. 2.33. The spoon-shape suppression we discussed in Section 2.3.3, integrated along the line of sight, damps the shear power spectrum that can reach 40 % for $M_\nu = 0.6$ eV. This is visible from fig. 2.6, where in each panel we plot the ratio of the shear power spectrum of a given pair of redshift bins with respect to the Λ CDM one. Different colors label the different contribution to the measured shear (eq. 1.62): blue for the cosmological signal GG , red for the pure intrinsic alignment signal II and green for

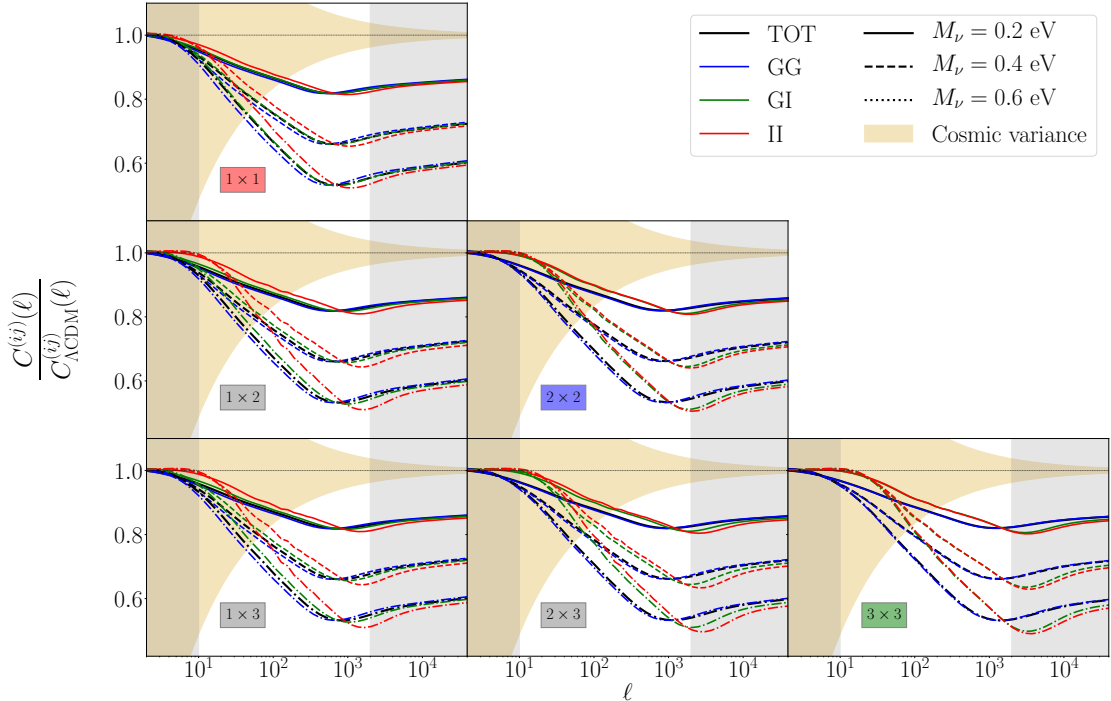


Figure 2.6: Impact of massive neutrinos on the shear power spectrum. The same settings of fig. 1.3 (redshift bins, galaxy distribution and cosmological parameters except for neutrino mass) have been used here. In each panel we show the suppression on the measured shear power spectrum (black lines), split in its contributions (GG in blue, GI in green, II in red), with respect to the ΛCDM case. Solid lines show such suppression for $M_\nu = 0.2$ eV, dashed lines for 0.4 eV and dotted lines for 0.6 eV. Grey bands show multipole regions likely excluded in upcoming surveys. Gold shaded areas represent cosmic variance for a survey with $f_{\text{sky}} = 0.366$.

the cross contribution GI , black for the sum of all of them. Different line styles instead refer to different neutrino masses: solid for 0.2 eV, dashed for 0.4 eV and dotted for 0.6 eV. The galaxy distributions, bins and cosmology used are the same of fig. 1.3; like always, every time we increase M_ν , we decrease Ω_c . Also here the grey bands are the multipole ranges which will likely be excluded by future surveys. The gold regions represent cosmic variance for a survey with $f_{\text{sky}} = 0.366$: every time a line falls outside this region, a neutrino mass detection is in principle possible. We will deal more in detail with this plot in Chapter 4, when we investigate whether this effect on the shear power spectrum can be disentangled from baryonic processes which can modify matter distribution on halo scales and which go under the name of *baryon feedback*.

2.4.4 Other large-scale structure observables

We briefly report here the impact of neutrino mass on the observables mentioned in Section 1.5.3. There we said that the tightest constraints on neutrino mass come from the combination of Planck with Ly- α forest data. The main reason is that the flux power spectrum can probe the smallest scales, where the impact of neutrinos is large. The combination of CMB and Ly- α forest can provide constraints in a very efficient way on all cosmological parameters, but especially on M_ν , because of the complementary degeneracy patterns in the $M_\nu - \Omega_m$ and $M_\nu - \sigma_8$ planes (Palanque-DeLabrouille et al. (2015b)).

On the other hand, also intensity mapping constitutes a promising new cosmological probe for constraining neutrino mass (e.g. Loeb & Wyithe (2008); Pritchard & Pierpaoli (2008)), because of its trivial dependence on the total matter power spectrum (see eq. 1.65). The impact of massive neutrinos on this observable was studied with N -body simulations by Villaescusa-Navarro et al. (2015), focusing on the post-reionization Universe and in both linear and non-linear regimes. A Fisher matrix forecast analysis was also performed: in particular, combining a deep ($3 < z < 6$) and narrow survey with SKA1-LOW, a wider and deep survey ($z < 3$) with SKA1-MID, Planck data and priors from stage IV spectroscopic galaxy surveys, the predicted uncertainty on the sum of neutrino mass is of order 0.06 eV at 95 % confidence level, yielding at least a $2\text{-}\sigma$ detection if neutrinos are distributed in the NH.

This Chapter is based on

G. Parimbelli, S. Anselmi, M. Viel, C. Carbone, F. Villaescusa-Navarro, P.S. Corasaniti, Y. Rasera, R. Sheth, G.D. Starkman and I. Zehavi,

The effects of massive neutrinos on the linear point of the correlation function

arXiv:2007.10345

3

The effects of massive neutrinos on the linear point of the correlation function

3.1 BAOs, linear point and massive neutrinos

As we saw in previous Chapters, the competing effects of gravity and radiation pressure in the primordial plasma, where photons and baryons were coupled through Thomson scattering, gave rise to acoustic waves that propagated until the epoch of recombination. Today we observe the leftover of this interaction, the BAOs, either in Fourier space, as wiggles in the power spectrum of matter or its tracers, or in configuration space as a peak in the 2-point clustering correlation function (2PCF) (Cole et al. (2005); Eisenstein et al. (2005)). More recently, full-shape analyses of the 2PCF have been performed for cosmological parameter estimation (Sánchez et al. (2009, 2012, 2013, 2017); Ivanov et al. (2019); Philcox et al. (2020)).

BAOs became an important tool in cosmology because in principle they provide a powerful standard ruler: they have been shown to be very robust against systematics (see e.g. Ross et al. (2017)) that critically affect other observables, like the full-shape power spectrum. They allow us to measure the acoustic scale, a quantity that is independent of the spatial geometry of the Universe, the primordial fluctuation parameters, late-time acceleration and the choice of observed tracers (e.g. galaxies) of the underlying density field. In other words, BAOs can be used to map the ex-

pansion history of the Universe through estimates of the Hubble parameter and the angular-diameter distance, exploiting the Alcock-Paczynski (AP) distortions (Alcock & Paczynski (1979)). Unfortunately, there are a few effects that complicate the use of BAOs: non-linearities in the late Universe affect the 2PCF and in particular the position of the BAO peak (Desjacques et al. (2010); Baldauf & Desjacques (2017); Bardeen et al. (1986)), that is the originally proposed BAO standard ruler (Eisenstein et al. (2005)). This spoils the standard ruler nature of the peak (Smith et al. (2008); Sánchez et al. (2008)).

Current analyses circumvent this problem by fitting the data with a theoretical template of the 2PCF parametrized in terms of the linear 2PCF and some nuisance parameters catching the smaller scale behavior. The most widely used method to estimate cosmic distances from the 2PCF in the BAO region (see e.g. Seo et al. (2008); Xu et al. (2012); Anderson et al. (2014)) consists of fixing the cosmological parameters to the fiducial Λ CDM values used to generate the mock catalogs from which the covariance matrix is computed. The non-linear damping parameter, which smooths the BAO feature at low redshift, is also estimated from the mocks and kept fixed in the MCMC analysis, checking *a posteriori* that it does not affect the measurement of the AP distortion parameters. This method has been shown to accurately fit the 2PCF and to return unbiased distance measures. Unfortunately, it might suffer from some drawbacks. First, the value of the damping parameter is tracer dependent (Bardeen et al. (1986); Veropalumbo et al. (2016)), and fixing it leads to unjustified claims for precision and accuracy. These assumptions could result in an underestimate of the distance error. Second, mock catalogs are typically generated using a Λ CDM model, therefore it is also not precisely clear how these measurements apply to non-standard cosmology scenarios (e.g. non-flat geometries and evolving dark energy). Putting together all these effects, employing this method might underestimate the distance errors by up to a factor of 2 (Anselmi et al. (2018a)).

In recent years, a new potential standard ruler has been proposed: the *linear point* (LP), defined as the mid-point between the BAO peak and the dip of the 2PCF (Anselmi et al. (2016, 2018c,b,a); O’Dwyer et al. (2020)). The LP has been shown to be weakly affected by gravitational processes. First of all, it is insensitive to the primordial fluctuation amplitude A_s and the scalar spectral index n_s (Anselmi et al. (2016); O’Dwyer et al. (2020)). Second, the original analysis of Anselmi et al. (2016) found that late-time non-linearities move the BAO peak towards smaller scales and the dip in the opposite direction, thus leaving the LP nearly in the same position. Similarly, redshift-space distortions (RSD) do not influence the position of the LP,

as their effect on the peak and the dip nearly cancels. Finally, the position of the LP is also nearly unaffected by scale-dependent halo bias. The stability of the LP can be ascribed to the near-antisymmetry of the 2PCF with respect to the LP itself, limiting the downward drift of the LP to $\sim 1\%$ through cosmic ages. Given the secular nature of that shift, to partially remove this non-linear effect, Anselmi et al. (2016) introduced a simple redshift-independent 0.5% correction to the LP estimated from real or simulated data:

$$r_{\text{LP}} = \frac{r_{\text{d}} + r_{\text{p}}}{2} \times 1.005. \quad (3.1)$$

The LP is identified by first finding the dip and the peak (by solving $\frac{d\xi}{dr} = 0$) and it is subsequently used to estimate the isotropic volume distance to the redshift considered. Finally, the value of such distance is compared to the theoretical predictions from different models in order to constrain the cosmological parameters.

Given what said above, a cosmological-model-independent fit is sufficient to recover the LP position without introducing systematic biases. LP analyses thus employ a model-independent approach to estimate the LP position from real or simulated clustering data. In particular, it has been shown that a simple polynomial is enough to obtain an unbiased estimate for the LP (Anselmi et al. (2018b)), with a correct and straightforward propagation of the uncertainties.

So far, the LP has been tested only in the Λ CDM framework, with no investigation of the possible impact of massive neutrinos. As already shown in detail in Chapter 2, massive neutrinos affect the clustering of matter both at the linear and non-linear levels. They decouple from the baryon-photon plasma in the very early Universe, when they are still relativistic. Due to their high thermal velocities, they cannot cluster, at linear order, on regions smaller than their so-called free-streaming scale (eq. 2.21). From flavor oscillation data, we know that at least two of them are massive enough to become non-relativistic during matter domination. In this regime, the free-streaming scale passes through a minimum, given by eq. 2.23, a scale which is larger than the ones where non-linear effects show up even at present time. All in all, the growth of structures proceeds like in the Λ CDM case for $k < k_{\text{nr}}$, but it is greatly affected by neutrino free-streaming at smaller scales, where the density perturbations grow more slowly. The net result is that the growth of perturbations becomes scale-dependent, with a substantial impact on the matter power spectrum and the 2PCF. Therefore, the position of the peak, dip and LP in the 2PCF could be affected by the value of the neutrino masses, even before the onset of gravitational non-linearities.

In a similar fashion, Baumann et al. (2019) made the first claim of a neutrino-induced phase shift of the BAO in the BOSS DR12 galaxy power spectrum. However, in this and a related analysis (Baumann et al. (2018)) several non-linear effects are incorporated using phenomenological models of the non-linear 2PCF, with the inherent risk of being subject to the limitations of template-based BAO analyses (see e.g Anselmi et al. (2018a); O’Dwyer et al. (2020)). In this regard the LP could provide a different route to detecting the neutrino mass.

This Chapter reports the work exposed in Parimbelli et al. (2020), where the impact of massive neutrinos on the LP is investigated. We start by studying how the scale-dependence clustering induced by massive neutrinos impacts the peak, dip and LP positions in linear theory. We then investigate the effects of non-linearities by using state-of-the-art N -body simulations. We focus on the behavior of the LP in the 2PCF for both cold dark matter (CDM) and halos in real space, leaving the analysis of RSD for future work. The main goal of this work is to investigate whether the neutrino mass retains or spoils the features of the LP that are crucial when employing it as a standard ruler. We discuss in the end how the LP could be applied to constrain the cosmological energy densities and the neutrino masses.

We organize the discussion in the following way. In Section 3.2 we describe the methodology we employ, i.e. the simulation sets and the LP estimation procedure in all its details. In Section 3.3 we present and discuss our results.

3.2 Methodology

The goal of this work is to study the evolution of the LP through cosmic ages, in particular assessing whether the impact of massive neutrinos spoils its nature of standard ruler. To this end, we first investigate the effect of the scale-dependent growth in linear theory. We then move to the non-linear analysis, employing N -body simulations that incorporate massive neutrinos as an extra set of particles. The observables we use are the CDM and halo 2PCF in real space, while we leave the impact of RSD for future work. To estimate the LP position, we fit the 2PCFs with a cosmology-independent polynomial function. Note that we do not consider the CDM-plus-neutrinos (i.e. total matter) 2PCF as an observable; because of neutrino free-streaming scale, it was shown (Ichiki & Takada (2012); Villaescusa-Navarro et al. (2014); Castorina et al. (2014)) that the main driver of galaxy formation is the CDM+b component rather than total matter. Using the total matter density as the fundamental field would spoil the universality of the mass function (proven by Jenkins et al. (2001); Reed

et al. (2003)) and would give rise to a strongly scale-dependent halo bias at the largest scales. Therefore the CDM+b field is expected to be the closest underlying field of the tracers we observe in the Universe¹. Furthermore, Vagnozzi et al. (2018) showed that, in upcoming surveys, not accounting for a scale-dependent bias when using total matter as fundamental field will lead to substantial shifts in the posterior of M_ν as well as of other cosmological parameters which are correlated with it.

In this Section, we first explain how we perform the linear analysis, then we present the adopted simulation sets, together with the method used to measure the correlation functions for both CDM and halos. We next describe the procedure we follow to estimate the LP best fit and uncertainty, fitting a model-independent differentiable function to the 2PCF data and errors. We also compare the 2PCF covariance matrix estimated from N -body to its linear Gaussian prediction.

3.2.1 Effects of massive neutrinos in linear theory

The fundamental feature that makes the LP a standard ruler is that its position is nearly redshift-independent in comoving coordinates (Anselmi et al. (2016, 2018a)). Anselmi et al. (2018a) explained that the LP can be used to estimate cosmological distances for Λ CDM and for cosmological models that do not introduce a scale-dependent growth, i.e. cosmologies that retain the LP redshift-independence. In order to understand whether the LP is a standard ruler for massive neutrino cosmologies we must assess the impact of massive neutrinos on the LP position, first in linear theory and then taking into account late-time non-linearities.

To investigate the redshift-dependence of the LP in linear theory for different neutrino masses, we use the Boltzmann solver CLASS (Lesgourgues (2011); Blas et al. (2011); Lesgourgues & Tram (2011)). We obtain the linear CDM power spectrum $P_{cc}^{\text{lin}}(k, z)$ at redshift z and compute the spatial derivative of the real-space 2PCF through:

$$\frac{d\xi^{\text{lin}}}{dr}(r, z) = -\frac{1}{2\pi^2} \int dk k^3 P_{cc}^{\text{lin}}(k, z) j_1(kr), \quad (3.2)$$

where $j_1(x) = (-x \cos(x) + \sin(x))/x^2$ is the first-order spherical Bessel function. We calculate the dip, peak and linear point positions by applying a root-finding routine to the condition $\frac{d\xi^{\text{lin}}}{dr}(r, z) = 0$ (without the 0.5% correction mentioned in eq. 3.1). Notice that the same procedure is used to compute dip and peak for the non-linear 2PCF.

¹From here on in this Chapter, when mentioning the CDM field, we will refer to the CDM+b one.

3.2.2 Simulations

In this work, we employ two sets of N -body simulations with massive neutrinos. As usual in N -body simulations, baryons are treated as cold dark matter, hence the CDM N -body particles are meant to describe the cold dark matter plus baryons component. The first simulation suite is a new subset of the “Dark Energy and Massive Neutrino Universe” (DEMNUi) simulations, first presented in Castorina et al. (2015) and Carbone et al. (2016). The complete DEMNUi set encloses simulations with different cosmologies, volume and mass resolution (Schuster et al. (2019); Verza et al. (2019); Kreisch et al. (2019); Bel et al. (2019)) and can be regarded as the state-of-the-art simulations in terms of the latter (Ruggeri et al. (2018)). This new suite consists of 50 realizations of two different models, a Λ CDM and a $\nu\Lambda$ CDM with three degenerate neutrino species of total mass $M_\nu = 0.16$ eV. The other parameters are set to $\Omega_m = 0.32$, $\Omega_b = 0.05$, $h = 0.67$, $n_s = 0.96$, $A_s = 2.1265 \times 10^{-9}$. The latter parameter implies a value for $\sigma_8 = 0.833$ and 0.792 for the Λ CDM and for the massive neutrino cases, respectively.

The new DEMNUi set, considered in this work, has been run using the tree-particle mesh-smoothed particle hydrodynamics (TreePM-SPH) code Gadget-III, a modification of Springel (2005) and Viel et al. (2010) that accounts for the presence of massive neutrinos. The simulation follows the evolution of $N_c = 1024^3$ CDM particles and, when present, $N_\nu = 1024^3$ neutrino particles, in a cubic box of size $L = 1000$ Mpc/ h , from $z = 99$ to present age. Initial conditions for models with massive neutrinos are obtained via the rescaling method developed in Zennaro et al. (2017). With the cosmological parameters above, the mass of a CDM particle is $M_p^c \approx 8.2 \times 10^{10} M_\odot/h$, while when neutrinos are present each particle has a mass of $M_p^\nu \approx 9.9 \times 10^8 M_\odot/h$. The softening length has been set to $\varepsilon = 20 h^{-1}$ kpc. With these features, DEMNUi are suitable for the analysis of several cosmological probes, from galaxy clustering to weak lensing. Halos and sub-halos are identified via the Friends-of-Friends (FoF) and the SUBFIND algorithms respectively, both included in Gadget-III (Springel et al. (2001); Dolag et al. (2009)), setting the linking length to $1/5$ of the mean inter-particle separation. The minimum number of particles to identify a parent halo is 32, so that the minimum halo mass is $2.6 \times 10^{12} M_\odot/h$. In this work we consider 5 snapshots at $z = 0, 0.5, 1, 1.5, 2$.

We also employ a part of the new Quijote set (Villaescusa-Navarro et al. (2019)). Like the DEMNUi, these simulations are run with the TreePM code Gadget-III. However, the initial conditions are set at $z_{\text{in}} = 127$ (also here using the prescription by Zennaro

	DEMNUni	Quijote
Realizations fiducial analysis (per model)	50	100
Boxsize (Mpc/h)	1000	1000
Snapshots (z)	0, 0.5, 1, 1.5, 2	0, 0.5, 1, 2, 3
CDM particles	1024^3	512^3
Neutrino particles	1024^3	512^3
Neutrino mass (eV)	0, 0.16	0, 0.1, 0.2
Minimum halo mass (M_\odot/h)	2.6×10^{12}	1.3×10^{13}

Table 3.1: Different specifics of the two simulation sets employed in this work.

et al. (2017)), and the mass resolution is 8 times lower, with $N_c = 512^3$ CDM particles, and $N_\nu = 512^3$ neutrinos (when present), in a box of 1000 Mpc/h on each side. The fiducial cosmology of this set has $\Omega_m = 0.3175$, $\Omega_b = 0.049$, $h = 0.6711$, $n_s = 0.9624$, $\sigma_8 = 0.834$. Neutrinos are considered to be of three different species with degenerate masses. This means that a dark matter particle has a mass of $M_P^c \approx 6.5 \times 10^{11} M_\odot/h$, while neutrino particles have $M_P^\nu \approx 1.6 \times 10^{10} M_\odot/h \times M_\nu$ [eV]. Dark matter halos, with a minimum mass of $1.3 \times 10^{13} M_\odot/h$ (32 CDM particles), are identified through the FoF algorithm with linking length parameter set to 1/5 of the mean inter-particle separation. Also in this case, we use 5 different snapshots at $z = 0, 0.5, 1, 2, 3$.

Given the number of Quijote realizations available, we do not use the full set. We included just the first 500 realization of the Λ CDM model plus the 500 standard realizations corresponding to a value of M_ν of 0.1 and 0.2 eV. We do not use at all the 500 realizations with $M_\nu = 0.4$ eV. This is because in the Quijote set, the amplitude of the power spectrum is described by σ_8 (rather than A_s), which is kept fixed to 0.834. When $M_\nu = 0.4$ eV, the large-scale amplitude is so large that late-time non-linearities completely smear out the BAO peak in the 2PCF, making our analysis impossible to perform.

These 500 simulations have been used to test the accuracy of an analytic Gaussian covariance matrix for the 2PCF (see e.g. Grieb et al. (2016)), while the LP estimation procedure has been performed only on the first 100 realizations.

Tables 3.1 and 3.2 report the specifics of the two simulations sets just described and the average number of halos per realization (or equivalently per $(\text{Gpc}/h)^3$).

	# Halos: DEMNUni		# Halos: Quijote		
	Λ CDM	0.16 eV	Λ CDM	0.1 eV	0.2 eV
$z = 3$			4.9×10^3	5.0×10^3	5.5×10^3
$z = 2$	6.1×10^5	5.5×10^5	4.4×10^4	4.4×10^4	4.4×10^4
$z = 1.5$	1.1×10^6	9.9×10^5			
$z = 1$	1.4×10^6	1.3×10^6	2.0×10^5	2.0×10^5	2.0×10^5
$z = 0.5$	1.8×10^6	1.7×10^6	3.1×10^5	3.1×10^5	3.1×10^5
$z = 0$	1.9×10^6	1.9×10^6	4.1×10^5	4.1×10^5	4.1×10^5

Table 3.2: Average number of halos per realization, per snapshot and simulation set.

3.2.3 Estimating the 2PCF from simulations

For each snapshot and each realization, we compute the 2PCF for CDM and for halos. As explained at the beginning of Section 3.2, we exclude neutrino particles from the computation of the 2PCF for observational reasons. This is also convenient from the theoretical point of view – as widely explained in e.g. Villaescusa-Navarro et al. (2014); Castorina et al. (2014); Costanzi et al. (2013), in massive neutrino cosmologies, if we consider the CDM density field we obtain a universal halo mass function and an *almost* scale-independent linear halo bias. We recall that we limit ourselves to the real space 2PCF, leaving RSD analysis for future work.

The 2PCF is computed using the FFT estimator introduced in Taruya et al. (2009) and implemented in the PYLIANS codes², in which the density field is computed on a grid and convolved with itself through a double 3-dimensional Fast Fourier Transform (FFT):

$$\hat{\xi}_X^{\text{sim}}(r) = \frac{1}{N_{\text{modes}}} \sum_{r_{\min} < |\mathbf{r}| < r_{\max}} \text{FFT}^{-1} [|\delta_X(\mathbf{k})|^2](\mathbf{r}), \quad (3.3)$$

where X can be either ‘c’ for CDM or ‘h’ for halos. The density field δ_X is computed using a Cloud-In-Cell mass-assignment scheme. The bin edges r_{\min} and r_{\max} are fixed by the thickness of the grid: in this work we set the latter to 1024, corresponding to a bin size of roughly 1 Mpc/ h .

In Fig. 3.1 we plot the 2PCF of CDM as measured with the method just described. For an easy comparison, we plot the quantity $r^2\xi(r)/\sigma_8^2 D_1^2(z)$ for the first 50 realizations and for the redshifts in common between the two simulation sets. We split

²<https://github.com/franciscovillaescusa/Pylians>

the measurements for Λ CDM from the ones with massive neutrinos. Dark-red and dark-blue dots in the left-hand panels represent the 2PCF for the Λ CDM model of the DEMNUni and the Quijote simulations, respectively. In the right-hand panels we show the massive neutrino models of the DEMNUni in light red and of the Quijote in blue (for $M_\nu = 0.1$ eV) and light blue (0.2 eV). Each measurement is accompanied by the standard error on the mean as uncertainty.

We would like to underline a subtle difference between the measurements of the two sets. As already mentioned in Section 3.2.2, in the Quijote simulations the parameter ruling the overall amplitude is σ_8 and not A_s . Therefore we expect a larger flattening of the BAO feature at late times for a fixed neutrino mass. This is clearly visible in Fig. 3.1, where (for instance in the Quijote 2PCF for $M_\nu = 0.1$ eV – blue points in the right panels) the relative height between the dip and the peak is smaller than for the analogous DEMNUni 2PCF, despite in the latter the neutrino mass is even higher (0.16 eV). This has important consequences on the estimate of the LP and in particular of its uncertainty. We will discuss this in detail in Section 3.3.4.

3.2.4 Estimating the linear point from simulations

In Anselmi et al. (2018b) it was shown that the LP position can be extracted from N -body simulations, mock and real galaxy data in a cosmology model-independent way. The proposed procedure exploits a simple polynomial function to smooth the binned 2PCF data and estimate the zero-crossings of its first derivative. This polynomial function is written as:

$$\xi_X^{\text{fit}}(r) = \sum_{n=0}^N a_n r^n \quad (3.4)$$

where the degree of the polynomial N must be chosen following Anselmi et al. (2018b). The best-fit parameters are found by maximizing the log-likelihood function given by:

$$\ln \mathcal{L} \propto -\frac{1}{2} \sum_{i,j} \left[\xi_X^{\text{fit}}(r_i) - \hat{\xi}_X^{\text{sim}}(r_i) \right] [\text{Cov}_X^{-1}]_{ij} \left[\xi_X^{\text{fit}}(r_j) - \hat{\xi}_X^{\text{sim}}(r_j) \right], \quad (3.5)$$

where $\hat{\xi}_X^{\text{sim}}(r)$ is the correlation function estimated from the simulation for either CDM or halos ($X = c, h$), eq. 3.3, $\text{Cov}_{X,ij}$ is the corresponding covariance matrix, and $\xi_X^{\text{fit}}(r)$ is the polynomial employed to estimate the LP.

We recall that, following eq. 3.1, the LP is defined as the mid-point between the peak and the dip in the 2PCF plus a 0.5% correction. We need to propagate the uncertainty from the fitted parameters of the 2PCF to the position of the peak and the dip, and finally to the LP. To do so, we write the LP position as a function of the

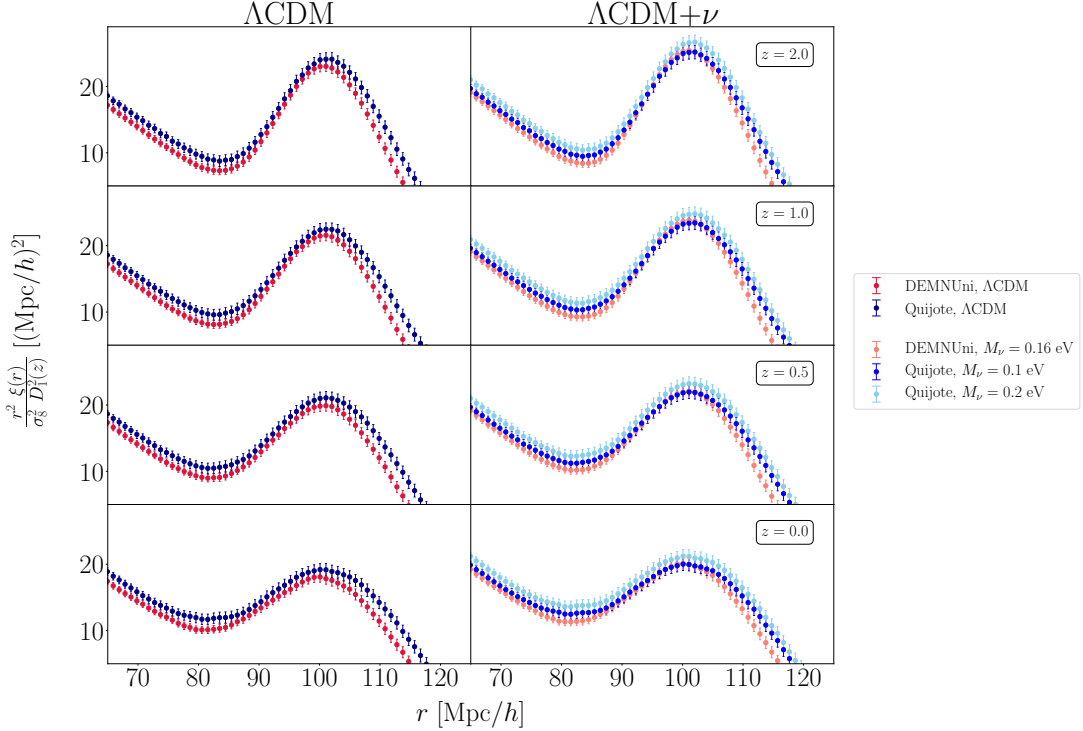


Figure 3.1: 2PCF of CDM from the DEMNUni and the Quijote sets, as measured with eq. 3.3. We show here, only for the common redshift between the two sets, the 2PCF multiplied by r^2 and divided by the σ_δ^2 and the growth factor for Λ CDM squared in order to make it easier a comparison between different sets. To facilitate the comparison, we plot the mean of the 50 DEMNUni and of the first 50 Quijote realizations, each with an uncertainty corresponding to the standard error on the mean. In the left panels we display the two Λ CDM cases, with the DEMNUni in dark red and the Quijote in dark blue; the right panels are left for the massive neutrino models, with the DEMNUni in light red and the Quijote with 0.1 eV (0.2 eV) in blue (light blue).

polynomial coefficients of eq. 3.4 and expand the result in the vicinity of the best-fit parameters. Assuming that the uncertainties in the a_i 's are small (as we verify numerically *a posteriori*), we can stop at first order:

$$r_{\text{LP}}(\mathbf{a}) \approx r_{\text{LP}}(\bar{\mathbf{a}}) + \sum_i \frac{\partial r_{\text{LP}}(\bar{\mathbf{a}})}{\partial a_i} (a_i - \bar{a}_i). \quad (3.6)$$

The error on the LP is the variance of the first-order term, namely

$$\sigma_{\text{LP}} = \left\{ \sum_{i,j} \frac{\partial r_{\text{LP}}}{\partial a_i} [\text{Cov}(\bar{\mathbf{a}})]_{ij} \frac{\partial r_{\text{LP}}}{\partial a_j} \right\}^{1/2}, \quad (3.7)$$

where $\text{Cov}(\bar{\mathbf{a}}) = \langle (a_i - \langle a_i \rangle)(a_j - \langle a_j \rangle) \rangle$ is the covariance matrix of the parameters. The derivative of the LP position with respect to the parameters is computed with

the 5-point stencil method, namely:

$$\frac{\partial r_{\text{LP}}}{\partial a_i} \approx \frac{-r_{\text{LP}}(a_i + 2\epsilon) + 8r_{\text{LP}}(a_i + \epsilon) - 8r_{\text{LP}}(a_i - \epsilon) + r_{\text{LP}}(a_i - 2\epsilon)}{12\epsilon}. \quad (3.8)$$

The step ϵ must be taken in such a way as to guarantee numerical convergence of the derivative. For every case, we choose $\epsilon = \{10^{-6}, 10^{-7}, 10^{-8}\} a_i$ as step sizes and compare the resulting errors on the LP. If, for each choice of ϵ , the computed numerical derivatives agree within 1%, we say that the derivative has converged and we take the value for σ_{LP} corresponding to $\epsilon = 10^{-7} a_i$. When performing this operation, $\text{Cov}(\bar{\mathbf{a}})$ is kept fixed, since the mean values of the a_i do not change in this procedure.

The 2PCF covariance matrix, needed to minimize the log-likelihood defined by eq. 3.5, is computed analytically, to avoid nuisances coming from the one computed directly from either set of simulations. Since the scales we are interested in are just mildly non-linear, we can still use a Gaussian-density-field approximation to build the 2PCF covariance matrix. We follow the treatment developed, employed, and tested in previous works (Smith et al. (2008); Sánchez et al. (2008); Smith (2009); Xu et al. (2012); Grieb et al. (2016); Lippich et al. (2019); Anselmi et al. (2018a)) to obtain a smoothed binned covariance matrix:

$$\text{Cov}_{X,ij} = \frac{2}{N_{\text{real}} L^3} \int_0^\infty \frac{dk k^2}{2\pi^2} \bar{j}_0(kr_i) \bar{j}_0(kr_j) \left[P_X(k) + \frac{1}{\bar{n}} \right]^2, \quad (3.9)$$

where $1/\bar{n}$ is the Poisson shot-noise term, L is the box size of the simulations, N_{real} is the number of realizations (since our observed points are the mean correlation functions) and $\bar{j}_0(x)$ is a band-averaged spherical Bessel function. In particular, if a bin is centered on r and its edges are (r_1, r_2) :

$$\bar{j}_0(kr) = \frac{r^2 j_1(kr)|_{r_1}^{r_2}}{r^2 k \Delta r \left[1 + \frac{1}{12} \left(\frac{\Delta r}{r} \right)^2 \right]} \quad (3.10)$$

with $\Delta r = r_2 - r_1$, and $j_1(x)$ is the 1st-order spherical Bessel function.

The shot-noise term is equal to L^3/N_c in the case of CDM, while for halos it is taken to be L^3/\bar{N}_h , where \bar{N}_h is the average number of halos at the single snapshot considered (see Table 3.2). On the other hand, eq. 3.9 contains the power spectrum of the tracer $P_X(k)$, which is *a priori* unknown. To avoid recomputing the covariance matrix at each step, we adopt the following prescription. The only parameter that plays an important role in the covariance is the bias factor. Therefore, when $X = c$ we use the linear CDM power spectrum, while for $X = h$ we assume a simple linear-bias model $P_{\text{hh}}(k) = b^2 P_{\text{cc}}^{\text{lin}}(k)$. The bias factor is then found by fitting the halo power spectrum

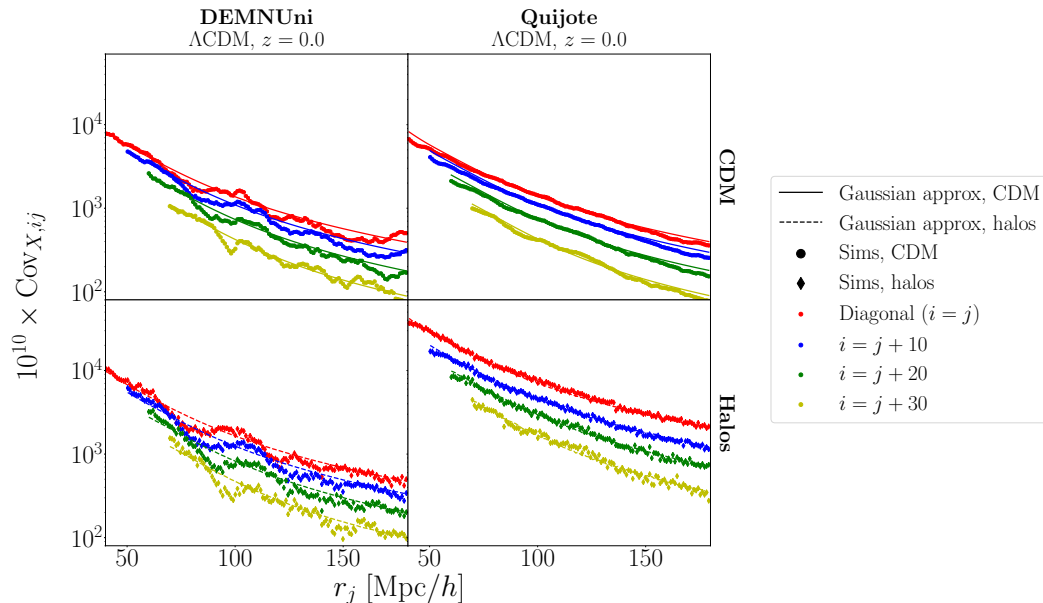


Figure 3.2: Covariance of the 2PCF in our simulations for the Λ CDM at $z = 0$. The left panels refer to the DEMNUni set, while the right panels show the same but for the Quijote simulations. Here we rescale the covariance by the number of realizations, i.e. we represent the covariance of the 2PCF in a cubic box of side $1000 \text{ Mpc}/h$. Dots and diamonds represent the measured covariance of CDM (top panels) and halos (bottom), respectively, while solid and dashed lines are the analytical equivalent under the assumption of a Gaussian density field (see eq. 3.9). Different colors label different elements of the covariance matrix: red is for the diagonal elements (i.e. the variance of the 2PCF), while blue, green and yellow show respectively the 10-th, 20-th and 30-th off-diagonal elements (with an offset introduced for sake of clarity).

up to scales of $k = 0.1 h \text{ Mpc}^{-1}$. To perform the fit we assumed an analytical diagonal covariance matrix considering both cosmic variance and shot noise, even though we checked that using the power spectrum full covariance matrix from simulations yields identical results for b .

In Fig. 3.2 we compare the covariance (relative to a cubic box of side $1000 \text{ Mpc}/h$), measured from the DEMNUni (left) and Quijote (right) simulations, and our prescription as described above, eq. 3.9. We show here both the CDM (top) and halos (bottom) measurements only for the Λ CDM case, but we find similar agreement also for the massive neutrino case. Confirming previous results (Sánchez et al. (2008); Smith (2009); Grieb et al. (2016); Lippich et al. (2019)), we find that the Gaussian-density-field approximation reproduces remarkably well not only the diagonal terms, i.e. the variances (red dots and diamonds for CDM and halos, respectively), but also the off-diagonal ones (blue, green and yellow points) down to scales of $40 \text{ Mpc}/h$.

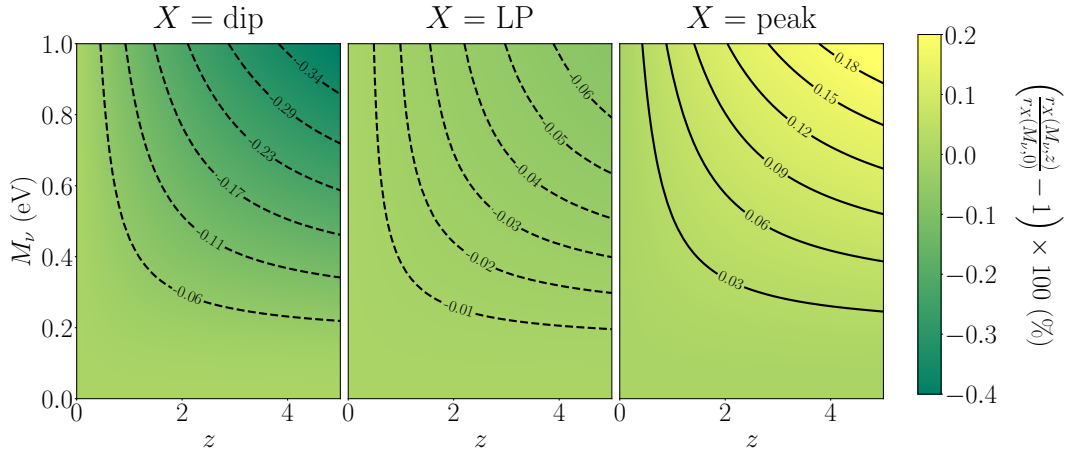


Figure 3.3: The evolution of the dip (left), LP (center) and peak (right) positions of the cold dark matter plus baryons 2PCF in the $z - M_\nu$ plane, according to linear theory. For each neutrino mass, the percentage difference between the quantity considered and its value at $z = 0$ is plotted. Solid contour lines denote positive differences, whereas dashed lines denote negative values. Here we keep σ_8 fixed for different neutrino masses, but the result for fixed A_s is almost identical.

Finally, the fitting setup employed to estimate the LP, which minimizes biases and systematics (for both the DEMNUni and the Quijote simulations), is selected by following the procedure developed in Anselmi et al. (2018b,a).

3.3 Results

In this Section we report and discuss in detail the main results of this work, obtained following the procedure presented in the previous Section. We first assess the impact of neutrino masses on the redshift-dependence position of the LP in linear theory. Next we focus on the redshift evolution of the LP position under the effects of non-linear gravitational evolution: we measure the LP position from simulations and also compare it against an approximate cosmology-dependent analytic model. We then discuss the implications of our findings when employing the LP as standard ruler for massive neutrino cosmologies. Finally, we examine the impact of massive neutrinos on the LP position, quantifying the shift in the LP with respect to the Λ CDM case. We study whether that shift can potentially be used to constrain M_ν . We also discuss the scaling of the uncertainty of the LP with the survey volume and redshift, using the set-up employed in Anselmi et al. (2018b) to estimate the LP positions and its error.

3.3.1 Linear perturbation theory: linear point redshift evolution

To illustrate the impact that massive neutrinos already have at linear level, in Fig. 3.3 we plot the percentage difference on the position of the dip (left panel), LP (central panel) and peak (right panel) for CDM+b 2PCF compared to the same quantity computed at $z = 0$ for different neutrino masses, assuming linear theory. Different cosmologies have the same σ_8 , but an almost identical result would have been obtained by fixing A_s . Solid and dashed contour lines represent positive and negative differences, respectively. We stress that in absence of massive neutrinos, i.e. with a scale-independent growth factor, the peak, dip and LP positions would have been redshift-independent. A second very important thing to notice is that the LP position is much more stable than the positions of the dip and the peak, so it is indeed a better standard ruler. Overall, the LP shift is much smaller than the 0.5% intrinsic uncertainty found in Anselmi et al. (2016).

3.3.2 Non-linear gravity: linear point redshift evolution

Let us start analyzing our results from Fig. 3.4. For each simulation set (DEMNUi in the top panels; Quijote in the bottom panels) and for each model (Λ CDM in the left panels and massive neutrinos in the central and right panels) we plot the position of the dip on the left, the peak on the right, and the LP in the center as a function of redshift, with their 68% relative uncertainty. In order to minimize the numerical systematics, the LP estimation was performed on all the DEMNUi realizations and on the first 100 Quijote ones, fitting an 8-th degree polynomial on a range of scales spanning from 77 to 107 Mpc/ h for CDM and from 75 to 115 Mpc/ h for halos. Blue crosses correspond to the measurement carried out on CDM field, while red ones refer to halos. For the sake of clarity, we introduce a little offset with respect to the actual redshift of the snapshot. In the Quijote set, red crosses at $z = 3$ are missing because the low number density of halos (and the consequent high value of the shot noise) prevents us from obtaining an accurate measurement of the LP and its uncertainty. In each subplot, the vertical dotted line represents the LP position according to linear theory. We also compare our measurements to the values predicted by a simple non-linear model. The non-linear 2PCF can be modelled through Lagrangian PT, where the dominant effect is given by the smoothing due to the displacements from the initial positions. This approximation was already used in previous works (Peloso et al. (2015); Noda et al. (2017); Vlah et al. (2015)) and shown to reproduce well the 2PCF from N -body simulations:

$$\xi_{\text{cc}}^{\text{nl}}(r, z) = \int_0^\infty dk \frac{k^2 P_{\text{cc}}^{\text{lin}}(k, z)}{2\pi^2} e^{-k^2 \sigma_v^2(z)} j_0(kr), \quad (3.11)$$

where $P_{\text{cc}}^{\text{lin}}(k)$ is the CDM linear power spectrum and $\sigma_v^2(z)$ is the variance of the displacement field or, equivalently, the one-dimensional velocity dispersion in linear theory, given by eq. 1.47. Notice that, for our purposes, the prediction of the LP motion for CDM and halos does not change, as the substitution $P_{\text{cc}}^{\text{lin}}(k) \rightarrow P_{\text{hh}}^{\text{lin}}(k) = b^2 P_{\text{cc}}^{\text{lin}}(k)$ only rescales the amplitude of the 2PCF without shifting any scale. Thus, the solid lines in Fig. 3.4 represent the prediction of the redshift evolution of the LP according to eq. 3.11, while the dashed lines do the same for the dip and the peak. The gray area shows the $\pm 0.5\%$ LP intrinsic-bias range identified in Anselmi et al. (2016), i.e. the maximum shift of the LP with respect to its linear-theory value, and the motivation for the 0.5% shift in equation (3.1).

Fig. 3.4 indicates that, within $1-\sigma$, the LP position agrees at the 0.5% level with the linear-theory prediction. Hence, for the Λ CDM model, we confirm the findings of Anselmi et al. (2016), which were derived with a less rigorous analysis. More importantly, for the first time, we show that the LP position remains in good agreement with the linear prediction when neutrinos are assumed to be massive. We also notice that the LP position agrees, within $1-\sigma$, with eq. 3.11. Therefore, if needed, Lagrangian PT could be conveniently employed to predict the LP position.

At low redshifts, the Λ CDM dip and peak non-linear shifts are different in the DEMNUni and Quijote sets, especially for the CDM. Given that the cosmological-parameter values are very similar for the two sets this behavior is unlikely to be physical. A statistical fluke also seems unlikely given the agreement between the sets at high-redshift. Therefore this difference is likely due to simulation systematics: different mass resolution of the simulations, use of the approximated analytical covariance for the 2PCF (i.e. eq. 3.9) and possible numerical systematics related to the FFT-2PCF estimator. A similar trend is present also for the $\nu\Lambda$ CDM case. Nevertheless, if there is a systematic difference between the DEMNUni and Quijote results, it seems to largely cancel out for the LP.

Interestingly, we find that the uncertainty on the LP position is smaller than just the average of the uncertainties on the peak and the dip: this reflects a significant anti-correlation between the latter two. We notice that such anti-correlation almost completely disappears if we use only the diagonal part of the covariance matrix. Therefore the strong cross-correlation between different 2PCF bins is responsible for the smaller uncertainty of the LP than of the peak and dip positions.

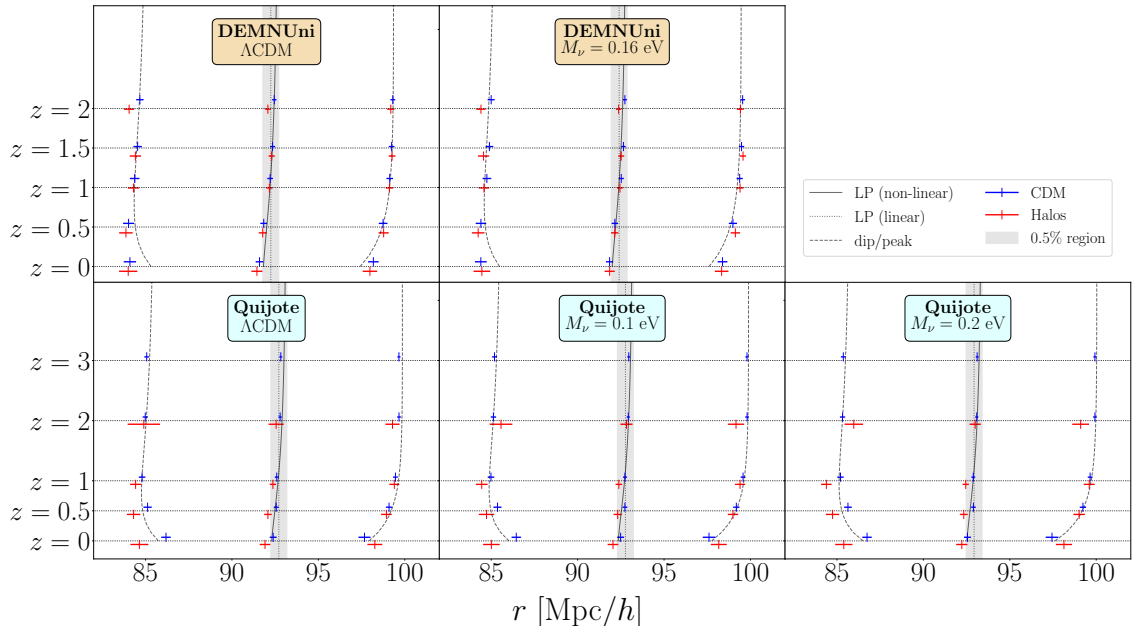


Figure 3.4: We plot 68% confidence limits on the position of the dip, the peak and the LP of the 2PCF for every snapshot of our simulation sets. The top panels refer to the DEMNUni set, for which we have the Λ CDM model (top left) and the massive neutrino model (top center). The bottom panels refer to the Quijote set with its three different models: Λ CDM (bottom left), $M_\nu = 0.1$ eV (bottom center) and $M_\nu = 0.2$ eV (bottom right). For each subpanel, dotted vertical lines represent the linear-theory prediction of the LP. The gray area shows the $\pm 0.5\%$ LP intrinsic-bias range identified in Anselmi et al. (2016) (see main text). The remaining solid and dashed lines show the evolution in redshift of the LP, the dip and the peak, respectively, according to eq. 3.11. Blue and red bars refer to the results for CDM and halos, respectively. Small offsets with respect to the snapshot redshifts have been introduced for the sake of clarity. In the Quijote sector, the red bars relative to the $z = 3$ snapshot are missing because the high shot noise made it impossible to have a clear estimate of the LP. It can be noticed that the LP is particularly stable and always in agreement with the linear prediction at the 0.5% level both for Λ CDM and when massive neutrinos are included.

Finally, we summarize in Table 3.3 the full results concerning the LP measurements obtained for all the simulation sets we used.

3.3.3 The linear point as a standard ruler

In the previous Sections, we found that the CDM and halo LP positions are nearly insensitive to non-linear gravitational evolution. It is crucial to also verify that RSD do not spoil the weakness of the redshift-dependence of the LP. If that turns out to be the case, the LP can be employed as a BAO standard ruler for cosmologies where neutrinos are massive. In fact, as explained in Anselmi et al. (2018a), the standard-

DEMNUni

Λ CDM		
Linear prediction: 92.25 Mpc/h		
redshift	CDM	Halos
$z = 2$	92.45 ± 0.12	92.08 ± 0.16
$z = 1.5$	92.35 ± 0.14	92.30 ± 0.18
$z = 1$	92.21 ± 0.16	92.17 ± 0.18
$z = 0.5$	91.84 ± 0.20	91.78 ± 0.23
$z = 0$	91.60 ± 0.22	91.45 ± 0.32

$\nu\Lambda$ CDM ($M_\nu = 0.16$ eV)
Linear prediction: 92.40 Mpc/h

redshift	CDM	Halos
$z = 2$	92.73 ± 0.12	92.37 ± 0.15
$z = 1.5$	92.65 ± 0.13	92.52 ± 0.17
$z = 1$	92.52 ± 0.15	92.45 ± 0.17
$z = 0.5$	92.15 ± 0.18	92.14 ± 0.21
$z = 0$	91.85 ± 0.21	91.85 ± 0.29

Quijote

Λ CDM		
Linear prediction: 92.71 Mpc/h		
redshift	CDM	Halos
$z = 3$	92.83 ± 0.08	X
$z = 2$	92.79 ± 0.09	92.56 ± 0.44
$z = 1$	92.59 ± 0.11	92.37 ± 0.18
$z = 0.5$	92.57 ± 0.15	92.08 ± 0.22
$z = 0$	92.39 ± 0.20	91.91 ± 0.31

$\nu\Lambda$ CDM ($M_\nu = 0.1$ eV)
Linear prediction: 92.77 Mpc/h

redshift	CDM	Halos
$z = 3$	92.96 ± 0.08	X
$z = 2$	92.93 ± 0.09	92.83 ± 0.35
$z = 1$	92.74 ± 0.11	92.38 ± 0.19
$z = 0.5$	92.73 ± 0.14	92.32 ± 0.24
$z = 0$	92.49 ± 0.20	92.05 ± 0.31

$\nu\Lambda$ CDM ($M_\nu = 0.2$ eV)
Linear prediction: 92.93 Mpc/h

redshift	CDM	Halos
$z = 3$	93.11 ± 0.08	X
$z = 2$	93.09 ± 0.09	93.00 ± 0.33
$z = 1$	92.89 ± 0.11	92.45 ± 0.18
$z = 0.5$	92.90 ± 0.14	92.34 ± 0.23
$z = 0$	92.55 ± 0.20	92.22 ± 0.32

Table 3.3: The table summarizes the results for the LP (including the 0.5% correction) for the DEMNUni (left) and the Quijote (right) simulations. We show the LP position with $1\text{-}\sigma$ uncertainty.

ruler properties of the LP imply that it can be used to perform Purely-Geometric-BAO (PG-BAO) distance measurements.

BAO measurements are one of the main motivations for cosmologists to perform galaxy surveys. As detailed in Anselmi et al. (2018a), the PG-BAO approach allows one to estimate cosmic distances without assuming neither spatial flatness nor a spe-

cific model for the late-time acceleration of the Universe. Furthermore the estimated distances are independent of the primordial-fluctuation parameters.

One of the consequences of our findings is that the set of cosmological models for which a PG-BAO approach has been demonstrated now includes massive neutrinos. Note that, while this holds true for the LP, it has not yet been proven for the correlation-function model-fitting approach to PG-BAO, as defined in Anselmi et al. (2018a). Finally, since in this work we have demonstrated the nearly redshift-independence of the LP, the next natural step will be to investigate its neutrino mass dependence. This will inform us of its power to constrain the neutrino mass. Hence the investigation presented in O’Dwyer et al. (2020) should be extended to the massive neutrino case.

3.3.4 Detecting the neutrino mass with the linear point

In the real Universe, we do not know the true value of the cosmological parameters and neutrino masses. It is, however, interesting to ask whether, assuming the Λ CDM model, the LP could be used to detect the non-zero neutrino mass, if we know perfectly all the remaining cosmological parameters. One way to answer this question is to estimate the LP position from both real observed galaxy data and from the “equivalent” mock galaxy distribution where neutrinos are massless³. We then ask if the two LP detections are different enough to provide a neutrino-mass detection. In the following, we mimic this procedure using our N -body simulations. We highlight that we do not aim at a very accurate answer, for which we should investigate the RSD effects, carefully analyze how to fix all the cosmological parameters, populate our simulations with galaxies, dealing with the cross-correlation between different simulations and matching the number densities and volume of the selected galaxy surveys. Since in this context we are not after a very accurate investigation, for simplicity in this part we choose to perform the analysis using a single setup which minimizes the biases for all the configurations (volumes, tracers and redshifts) we consider, always following the prescription by Anselmi et al. (2018c). It turns out that a 5-th order polynomial fit between 75 and 115 Mpc/ h is enough for our purposes. Notice finally that this exercise does not require the LP to be a BAO standard ruler. Nevertheless it has convenient properties to this end: it is weakly sensitive to non-linearities, it can be estimated in a model-independent way, it has a small uncertainty and it is independent of the fixed value of the scalar amplitude and index.

³From observed galaxy data we measure the LP in fiducial comoving coordinate (Anselmi et al. (2018c,a)). Therefore, before using the LP to detect the neutrino mass, it is required to use a fiducial cosmology close enough to the true cosmology.

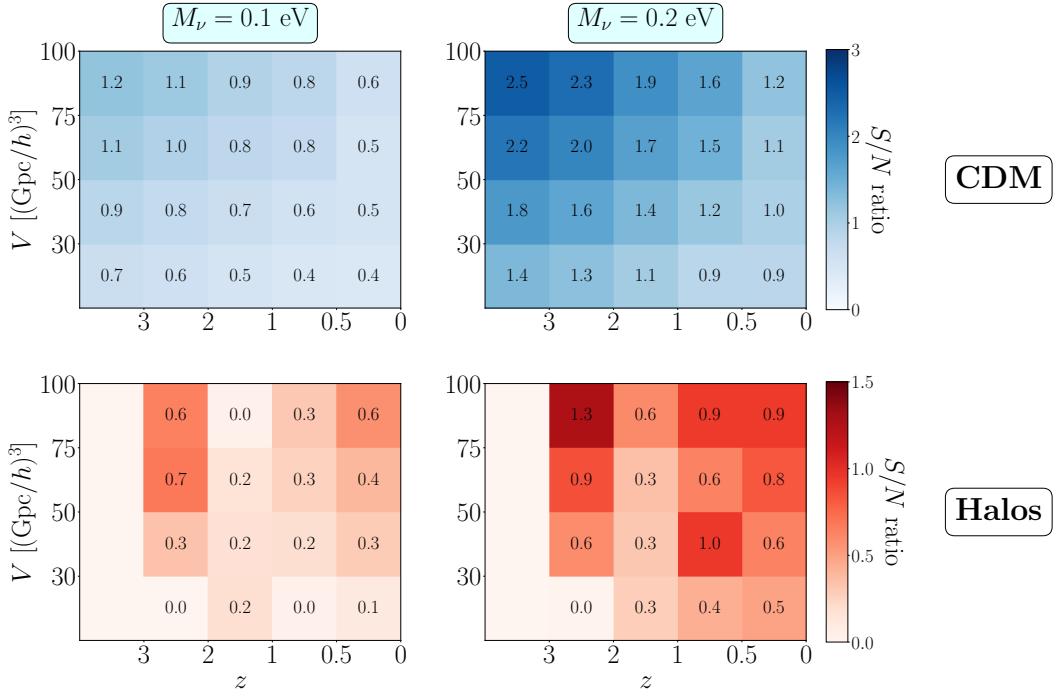


Figure 3.5: Signal-to-noise ratio, computed with eq. 3.12, for a possible neutrino mass detection using the LP shift with respect to the Λ CDM case. The S/N caused by a neutrino mass of 0.1 (0.2) eV is displayed on the left (right) panels. Top panels show the results for CDM only, while the bottom ones show the same for halos. The left columns of the bottom panels are missing because we do not perform the analysis for halos at $z = 3$.

Our neutrino mass detector is defined by a signal-to-noise ratio (SNR) for every redshift and survey volume as the ratio between the difference of the LP position, in massive neutrino cosmologies and the massless case, and the sum in quadrature of the uncertainties in the two models. Mathematically:

$$\frac{S}{N} \Big|_{z,V} = \frac{r_{\text{LP}}(M_\nu) - r_{\text{LP}}(0)}{[\sigma_{\text{LP}}^2(M_\nu) + \sigma_{\text{LP}}^2(0)]^{1/2}} \quad (3.12)$$

For both the Λ CDM and the $\nu\Lambda$ CDM cases, we use the LP position and error measured from N -body simulations.

The colormaps in Fig. 3.5 show the SNR computed with eq. 3.12 for the different models and survey volumes. The various columns label different neutrino masses (0.1 eV on the left, 0.2 eV on the right); different rows – and different colors – label the two different tracers, CDM and halos, respectively. Once again, we notice for CDM a clear trend, with the SNR increasing for increasing neutrino mass, volume and redshift, for the following reasons. First, since in the simulations Ω_m is kept fixed, a

larger neutrino mass means a smaller Ω_c . This affects the shape of the CDM power spectrum, and in turn of the 2PCF in a significant way at the linear level, in particular shifting the peak, the dip and the LP towards larger scales (see Fig. 3.1). Second, increasing the survey volume shrinks the uncertainty on the LP but does not affect its mean value: we therefore expect the denominator of eq. 3.12 to decrease for large volumes and consequently the SNR to rise. Third, also related to the previous point, a boost of the SNR for increasing redshift is also expected. While the LP remains stable, late-time non-linearities smear out the BAO feature; we therefore expect the uncertainty in the zero-crossings of the first derivative of the 2PCF, and thus the uncertainty in the LP, to be larger at low redshift. All in all, for $M_\nu = 0.1$ eV we find the SNR to be larger than 1 when $V > 30$ Gpc/h and $z > 1$; for $M_\nu = 0.2$ eV the SNR is larger than 1 for most of the volumes and redshifts considered in Fig. 3.5.

For halos the situation is different: the absence of a clear trend suggests that our SNR is dominated by the statistical error on the LP. Quantitatively, for 0.1 eV neutrino mass the SNR is never greater than 1, while we only find a few cases for which this is true for $M_\nu = 0.2$ eV. On the other hand, the additivity of eq. 3.12 ensures that having more redshift bins can help in increasing the SNR. For instance, from the bottom-right panel of Fig. 3.5, we can see that four bins at $z = 2, 1, 0.5, 0$, each of 75 (Gpc/h)³ would be sufficient to detect the LP shift due to a neutrino mass of 0.2 eV with SNR = 2.6.

An important point to stress is the following. In Section 3.3.2 we pointed out how the uncertainty on the LP is smaller than the average of the uncertainties of the peak and the dip. This translates to the fact that, if we reproduced Fig. 3.5 using the peak as our observable to detect the neutrino mass (instead of the LP), we would obtain a lower SNR because the numerical value of the denominator in eq. 3.12 will be larger than the LP case. As a consequence using the LP position to detect the neutrino mass works better than using the peak: the LP position is found to be extremely well measured due to the high degree of anti-correlation of the peak and the dip positions. We wish now to compare the SNR for the two simulation sets. In Fig. 3.6 we show the SNR as a function of redshift. The light-blue and pink squares are relative to the SNR as measured from the 50 DEMNUni realizations, for CDM and halos, respectively. For the Quijote we also plot the SNR relative to 50 realizations. As in previous plots, CDM is depicted in blue, whereas halos are in red. Different models are represented with different line styles: dotted for $M_\nu = 0.1$ eV, solid for $M_\nu = 0.2$ eV.

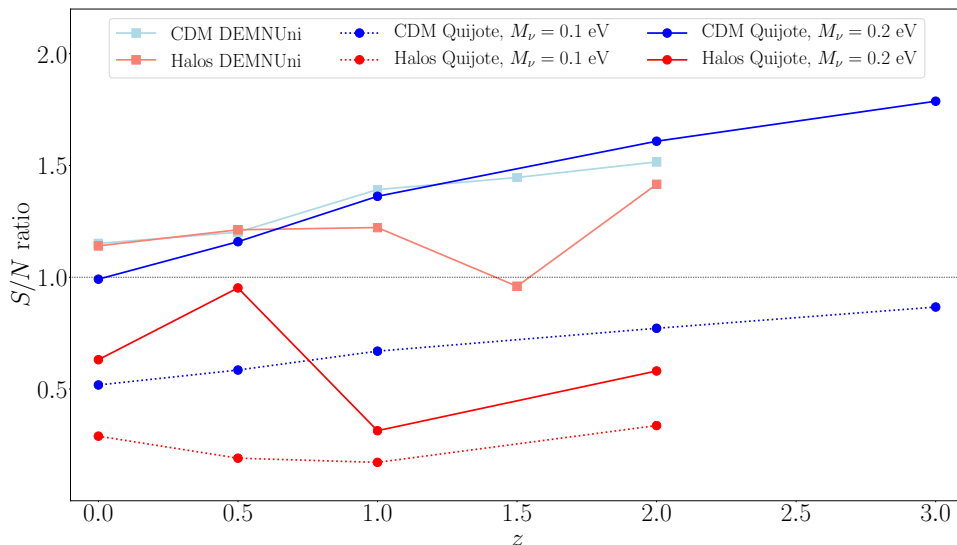


Figure 3.6: The figure shows the signal-to-noise ratio for a possible neutrino-mass detection using the LP shift with respect to the Λ CDM case. Here we compare the signal-to-noise for the 50 realizations of the DEMNUni set with the 50 of the Quijote (i.e. our reference volume). Squares represent the ratio for the DEMNUni set, light-blue and pink for CDM and halos respectively. Circles refer to the Quijote set, where we distinguish the model with $M_\nu = 0.1$ eV (dashed line) and the one with $M_\nu = 0.2$ eV (dotted line). Like in the previous figures, CDM is represented in blue, whereas halos are in red. Finally, the dotted black horizontal line symbolizes a S/N ratio equal to 1.

Let us focus on CDM first. Before comparing the two sets, it must be stressed that although they share the same volume, there are two fundamental differences. First, in the DEMNUni simulations neutrinos have a total mass of 0.16 eV, while in the Quijote M_ν is either 0.1 or 0.2 eV. Second, as already mentioned, the amplitude of fluctuations in the two sets is regulated by two different parameters: while in the DEMNUni the amplitude of the primordial scalar perturbations, A_s , is constant and σ_8 decreases for increasing neutrino mass, in the Quijote σ_8 is kept fixed. Therefore, for fixed M_ν , in the latter set we expect a higher damping of the BAO feature due to non-linearities (see Fig. 3.1 and, consequently, a higher uncertainty in the LP and a smaller SNR. This explains why the SNR in the Quijote is much smaller than the DEMNUni for $M_\nu = 0.1$ eV but comparable with it for $M_\nu = 0.2$ eV, i.e. for a larger neutrino mass.

We turn now our attention to halos, again underlining that there are relevant differences between the halo populations. The different mass resolutions of the two sets imply a different minimum halo mass (see Table 3.1. Table 3.2 shows how halos in the

DEMNUi outnumber the ones in the Quijote by a factor that ranges from $\sim 4 - 5$ at $z = 0$ to $\sim 12 - 14$ at $z = 2$. From Fig. 3.6, it is evident how in the DEMNUi, despite a lower neutrino mass, the SNR for a detection is substantially larger than in the Quijote, even for $M_\nu = 0.2$ eV. This suggests that shot noise plays a crucial role in reducing the SNR, more than neutrino mass itself. To further support this conclusion, we notice how the evolution of the SNR in the Quijote is almost identical for different neutrino masses. In fact, if we crudely estimate the standard deviation of the error on LP by assuming that the LP position is normally distributed (Kenney & Keeping (1951)):

$$\sigma_{\sigma_{\text{LP}}} = \sigma_{\text{LP}} \frac{\Gamma[(N_{\text{real}} - 1)/2]}{\Gamma[N_{\text{real}}/2]} \sqrt{\frac{N_{\text{real}} - 1}{2} - \left(\frac{\Gamma[N_{\text{real}}/2]}{\Gamma[(N_{\text{real}} - 1)/2]} \right)^2}, \quad (3.13)$$

where N_{real} is the number of realizations considered, we see that the spike at $z = 0.5$ for the 0.2 eV case is just a $2\text{-}\sigma$ statistical fluctuation. We also point out that shot noise and the bias of the tracer are tightly related to one another – imposing a fixed-mass cut in simulations corresponds to selecting fewer halos at high redshifts, with the latter being the most massive and the most biased.

In conclusion, two different things are needed in future surveys in order to be able to detect neutrino mass using the LP: a large volume and a densely populated galaxy sample to pull down cosmic variance and shot noise. To quote some numbers reflecting the current status, we can forecast the SNR in past and upcoming surveys. One promising avenue to use the LP as a neutrino mass probe would be to rely on intensity mapping surveys: in this case very large volumes can be covered and the shot-noise contribution to the overall signal is expected to be small (Villaescusa-Navarro et al. (2017, 2018b)).

In order to forecast the capability of galaxy surveys to detect the neutrino mass with the LP, we need to investigate its uncertainty and how it scales with redshift, volume and number density. In Fig. 3.7 we plot the 68% error on the LP position as a function of redshift and volume in the Quijote simulations. The three different columns refer to the three different neutrino masses we consider (0 eV, 0.1 eV, and 0.2 eV in the left, center and right panels, respectively). The blue surfaces show the uncertainty in the LP as measured from the 2PCF of the CDM, whereas the red ones represent the same for halos. As expected, we find a decreasing uncertainty for increasing volume, scaling as $V^{-1/2}$. However, concerning the evolution in redshift, we notice different trends for the two tracers. On the one hand, σ_{LP} for CDM monotonically increases with time due to the larger BAO smoothing caused by late-time non-linearities. On the other

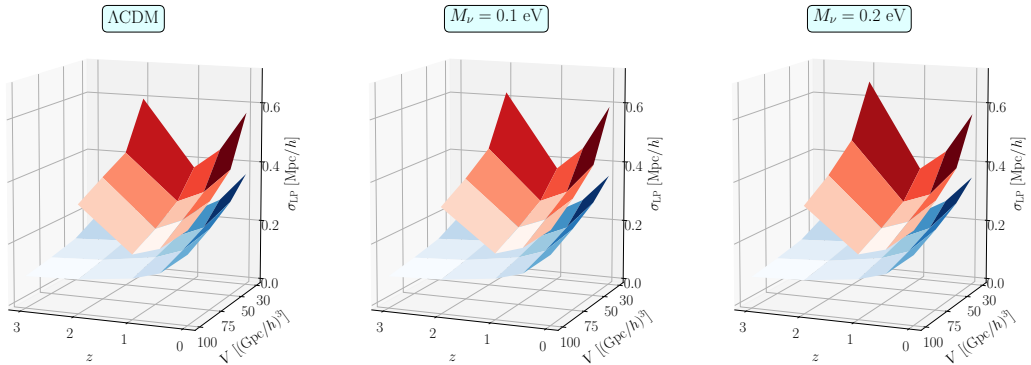


Figure 3.7: LP position uncertainty as a function of redshift and volume (i.e. number of realizations) in the Quijote set. We show the case for the Λ CDM (left) and the two massive neutrino models (center and right). The blue surfaces show the 68% uncertainty on the LP in the 2PCF of the CDM, while the red ones are the equivalent for halos.

hand, while we find an analogous trend also for halos at late times, this tendency abruptly reverses at around $z \approx 1$. The reason is the decreasing number density of halos at early times and the consequent rise of shot noise, whose contribution becomes more and more important in the covariance matrix, eq. 3.9.

By fitting to our simulations, we obtained an empirical formula that can be used to predict the uncertainty on the LP for the tracer X :

$$\sigma_{\text{LP},X}(z, V) \approx \left[\frac{2 (\text{Gpc}/h)^3}{V} \right]^{1/2} \left[(1 + \alpha_X) b^{1/2} D_1^2(z) + (1 + \beta_X) \frac{\bar{n}_c}{\bar{n}_X(z)} \right] \text{Mpc}/h. \quad (3.14)$$

Here we have normalized the shot-noise term with respect to the (constant) average CDM number density \bar{n}_c ; b is the bias factor; $D_1(z)$ is the scale-independent linear growth factor; and α_X and β_X are two free parameters that represent respectively deviations from the standard growth, and the shot noise $1/\bar{n}_X(z)$. The values of the parameters we obtain are quite independent of the neutrino mass, but do depend on the tracer: in particular, we find $\alpha_h \approx 0.7$, $(1 + \beta_h) \sim 10^{-4}$ for halos, and $\alpha_c \approx 0$, $(1 + \beta_c) \approx 0.52$ for CDM. To find the numerical value of α_h and β_h we use the approximation introduced in eq. 3.13 to estimate the uncertainty on the uncertainty on the LP. Notice that to forecast the galaxy-survey SNR we will use eq. 3.14 in parameter regions where it has not been validated. We are aware of the potential systematic error introduced by this extrapolation. However, this is adequate for our purposes here of conducting a preliminary investigation of the utility of the LP for neutrino mass detection. For the same reason, to compute the numerator of eq. 3.12

we always use the value of the LP estimated from 50 simulation boxes. In fact we found that, as expected, the LP best fit is weakly sensitive to the simulation volume considered.

Using the first and third bins of the BOSS DR-12 data (Alam et al. (2017)) we obtain a SNR of 0.8 for $M_\nu = 0.1$ eV and of 1.9 for $M_\nu = 0.2$ eV. Concerning future surveys, by assuming the 4 redshift bins, number densities, volumes and biases reported in Euclid Collaboration et al. (2019a), and using the fitted values for α_h and β_h , we forecast an overall SNR ≈ 3.9 for $M_\nu = 0.1$ eV, and SNR ≈ 5.2 for $M_\nu = 0.2$ eV. We should finally remark that comparing the outcomes of eq. 3.14 to the accurate LP error estimates found for BOSS (Anselmi et al. (2018b)) and Euclid (Anselmi et al. (2018a)) we notice that eq. 3.14 consistently underestimates the LP uncertainties. We warn the reader that the SNR we found for BOSS and Euclid is probably an upper limit on the results of a dedicated analysis.

As a final remark, we would like to stress that these results were obtained by assuming perfect knowledge of the underlying cosmology. When allowing cosmological parameters to vary, the SNR analysis just exposed may drastically change due to the possible degeneracies among parameters that would come into play. Further work is the needed to provide more accurate results, also including the effect of RSD and using galaxies instead of halos.

This Chapter is based on

G. Parimbelli, M. Viel, E. Sefusatti,

On the degeneracy between baryon feedback and massive neutrinos as probed by matter clustering and weak lensing

JCAP01(2019)010, [arXiv:1809.06634](https://arxiv.org/abs/1809.06634)

4

Degeneracies between massive neutrinos and nuisances in matter clustering and weak lensing

4.1 Motivation

Upcoming galaxy surveys like Euclid¹, the Large Synoptic Survey Telescope (LSST)², the Dark Energy Spectroscopic Instrument (DESI)³ and the Square Kilometer Array (SKA)⁴ will become operative in the next few years. Other ambitious projects like DES⁵ are indeed already happening (Abbott et al. (2018, 2019)). These probes will allow us to study the evolution of the Universe through cosmic ages with unprecedented accuracy, using as observables galaxy clustering (baryon acoustic oscillations, BAO, and redshift-space distortions, RSD) and weak lensing. With these improvements we will be able to put tighter constraints on the cosmological parameters and assess possible deviations from the standard flat Λ CDM paradigm. As mentioned in previous Chapters, these new experiments will almost certainly be able to measure

¹<https://www.euclid-ec.org/>

²<https://www.lsst.org/>

³<http://desi.lbl.gov/>

⁴<https://www.skatelescope.org/>

⁵<https://www.darkenergysurvey.org/>

for the first time the total neutrino mass M_ν (Audren et al. (2013); Sprenger et al. (2019); Euclid Collaboration et al. (2019a)).

Particle physics experiments on neutrino oscillations have put a lower bound to $M_\nu \approx 0.06$ eV (see e.g. Lesgourgues & Pastor (2006)). On the other hand, cosmology has been able to place either upper limits (Giusarma et al. (2016)) or marginal preference (Beutler et al. (2014); Battye & Moss (2014); Di Valentino et al. (2017)) for a non-zero total neutrino mass. The current tightest constraints come from combining Planck (Planck Collaboration et al. (2016)) with BOSS Lyman- α forest data, providing $M_\nu < 0.12$ eV at 95% confidence level (Palanque-Delabrouille et al. (2015a)).

To reach percent accuracy in the constraints of cosmological parameters, a huge effort must be carried out in the theoretical modelling of the observables and of the systematic errors that may affect our predictions for RSD and galaxy bias in clustering observations and shape-noise in shear surveys. One of the most important aspects when including massive neutrinos in the cosmological model is the fact that their effect on the matter power spectrum may mimic what goes under the name of *baryon feedback*. Baryon feedback can be defined as a set of astrophysical processes capable of modifying the matter distribution on the scales comparable to the halo sizes. Such processes include Active Galactic Nuclei (AGN) feedback, galactic winds and hot X-ray emitting gas physics. Usually their description relies on hydrodynamical N -body simulations (Schaye et al. (2010); van Daalen et al. (2011); Semboloni et al. (2011); Mummery et al. (2017)), since the observational constraints are still poor. However, it is well known that baryon effects are underestimated in simulations: while observations have shown that even massive halos are missing significant amounts of gas (Sun et al. (2009); Lovisari et al. (2015); Eckert et al. (2016)), simulations tend to overpredict the baryon fraction in clusters. BAHAMAS and FABLE simulations make the only exceptions, as they are calibrated to reproduce the observed baryon fractions (McCarthy et al. (2017); Henden et al. (2018)). Interestingly, despite these mechanisms are different in nature, their net effect on the matter power spectrum is similar: a suppression starting from $k \sim 0.5$ h/Mpc is expected, reaching 10-25 % around $k \sim 2$ h/Mpc (Schneider & Teyssier (2015)). In recent years, several analytical approaches have been proposed to model this effect: some approaches propose fitting functions with parameters depending on the feedback model implemented in the simulation (Harnois-Déraps et al. (2015); Chisari et al. (2018)), others treat feedback as the consequence of a modification of the universal density profile of dark matter halos (Mead et al. (2015); Schneider & Teyssier (2015)).

Previous and current works have always treated baryon feedback as a nuisance to the cosmological signal (Abbott et al. (2018); Köhlinger et al. (2017)), without quantifying a possible bias on the estimate of M_ν . In this paper we show that the degeneracy between baryon feedback and massive neutrinos is not significant and the two effects can be disentangled. The main reason why this can be done is that, besides involving different ranges of scales, the redshift evolution of the two phenomena are rather different from each other: thus, performing a tomographic analysis is expected to be the best way to achieve our goal.

Our work is based on the formalism developed in Audren et al. (2013), where a Markov Chain Monte Carlo (MCMC) method to forecast errors on cosmological parameters for a Euclid-like survey combined with Planck is used. More recently, (Sprenger et al. (2019)) have carried out the same analysis including also 21cm galaxy clustering and intensity mapping as will be probed by SKA. The reason why we chose to perform MCMC instead of simple Fisher matrix analysis is that the former has been shown to return more realistic results than the latter, which has well-known limits when exploring the cosmological parameters *full* likelihood function. An official Fisher matrix forecast for Euclid has been anyway performed (Euclid Collaboration et al. (2019a)) one year after the publication of Paribelli et al. (2019) and Sprenger et al. (2019).

In this Chapter we consider as our “observables” the 3-D, *cold dark matter-plus-baryons* (CDM+b) power spectrum and the cosmic shear power spectrum. Clearly the former is not a real observable and, in fact, in this paper we limit ourselves to a study of the degeneracy between neutrino mass and baryon feedback *at the level of the matter distribution*, leaving any complication due to galaxy bias (and redshift-space distortions) for a future work. Furthermore, for clustering we apply the so-called *cold dark matter prescription* (Ichiki & Takada (2012); Villaescusa-Navarro et al. (2014); Castorina et al. (2014); Costanzi et al. (2013)): in massive neutrino cosmologies, the relevant field for the description of galaxy clustering is the CDM+b one rather than the total matter, since we can recover the expected constant linear bias at large scales only with respect to the former (see Section 2.4.1 for a more detailed discussion).

Weak lensing is surely one of the most promising cosmological tools for the next decade, as it probes the deep non-linear regime: in fact, while non-linearities already arise at relatively small multipoles ($\ell \sim 100$, see e.g. Takada & Jain (2004)), future surveys are expected to reach much smaller angular scales ($\ell_{\max} \sim 2000 - 5000$). Despite it results from an integration along the line-of-sight, 3-dimensionality can be

restored by performing a tomographic analysis, i.e. dividing galaxies in redshift bins and for each pair measure the shear power spectrum.

Latest results from the KiDS survey (Köhlinger et al. (2017)) and DES (Abbott et al. (2018, 2019)) highlight some tensions between each other. In addition, KiDS data seem to underpredict the overall amplitude of primordial fluctuations with respect to Planck (Leauthaud et al. (2017); Efstathiou & Lemos (2018)), while McCarthy et al. (2018) has demonstrated that baryon feedback alone is not enough to reconcile the tension in the $\Omega_m - \sigma_8$ plane and a non-minimal neutrino mass can resolve it. Therefore a detailed study of the possible degeneracies between the two effects becomes of primary importance.

For both clustering and shear we incorporate non-linearities using the HALOFIT version by (Mead et al. (2015)). These fitting formulae can reproduce the cold matter power spectrum with an accuracy better than $\sim 5\%$ even in the deeply non-linear regime ($k \lesssim 10 h/\text{Mpc}$). With this approach we essentially assume that any prediction adopted in the analysis of future data set is the direct results of investigations based on N -body simulations and we therefore include as theoretical uncertainties those affecting numerical methods. How this and other error sources are computed can be found explicitly in Section 4.3.

This Chapter is organized as follows: in Section 4.2 we briefly introduce the observables we employ as well as the impact that the phenomena we are after have on the latter; in Section 4.3 we describe in detail the procedure we follow; in Section 4.4 we present our main results; in Section 4.5 we report our conclusions; finally in Section 4.6 we discuss some possible interesting follow-up work.

Throughout this work we assume a flat Λ CDM model with one single massive neutrino species with parameters $\Omega_b = 0.0486$, $\Omega_m = \Omega_c + \Omega_\nu + \Omega_b = 0.3089$, $h = 0.6774$, $A_s = 2.14 \times 10^{-9}$, $n_s = 0.9667$, i.e. the best-fit values found by Planck Collaboration et al. (2016).

4.2 Theoretical framework

This Section summarizes the observables we are going to use in our analysis, namely the CDM+b power spectrum and the cosmic shear spectrum. We will report some of the equations already derived in Chapters 1 and 2. In the second part of this Section we will also discuss in detail the phenomenon of baryon feedback and its impact on the aforementioned observables. In particular, we will focus on the baryon feedback model of Schneider & Teyssier (2015).

4.2.1 Observables: CDM+b power spectrum and cosmic shear

The large-scale structure of the Universe is the result of the growth of small density perturbations that evolved through cosmic ages. In massive neutrino cosmologies, at the redshifts relevant for large-scale structure observations, we can identify two contributions to the total matter density ρ_m given by the cold matter (including baryons), ρ_c , and neutrinos, ρ_ν . Total matter perturbations can then be written as (see also eq. 2.29):

$$\delta_m = (1 - f_\nu) \delta_c + f_\nu \delta_\nu, \quad (4.1)$$

where $f_\nu \equiv \Omega_\nu/\Omega_m$ is the fraction of the neutrino contribution to the total matter density. From here on, the subscript ‘c’ will label the CDM+b fluid, while ‘m’ will denote total matter quantities. Numerical investigations (Villaescusa-Navarro et al. (2014); Castorina et al. (2014); Costanzi et al. (2013); Castorina et al. (2015); Villaescusa-Navarro et al. (2018a); Ruggeri et al. (2018)), along with earlier theoretical descriptions of spherical collapse in the massive neutrino scenario (Ichiki & Takada (2012)), have shown that halo formation is driven by the CDM+b component alone. This assumption allows to recover universality for the halo mass function and halo bias, otherwise apparently lost in a description based on total matter perturbations. The quantity of interest for halo (and galaxy) clustering is therefore the CDM+b power spectrum, $P_{cc}(k)$. We will focus on this quantity leaving aside the actual observable, i.e. the galaxy power spectrum. In fact, the aim of this work is just to quantitatively address the putative degeneracies between the suppressions of power induced by feedback effects and neutrinos *at the level of matter perturbations alone*, without focusing on the most realistic errors on M_ν .

Our second quantity of interest is the shear power spectrum from gravitational lensing (Bartelmann & Schneider (2001); Hoekstra & Jain (2008)). We will work in the weak regime, where distortions of the shapes of galaxies are much smaller than their intrinsic ellipticity and the power spectra of convergence and shear are statistically equivalent. The lensing effect depends on the gravitational potential along the line-of-sight, directly related through Poisson equation, to the total matter perturbations. Our predictions for this observable will then be derived in terms of the total matter power spectrum $P_{mm}(k)$.

Dividing source galaxies into N redshift bins, i.e. performing a tomographic analysis, allows to improve the constraints on cosmological parameters (Takada & Jain (2004)), as this will result in $N(N + 1)/2$ nearly independent observables. We assume the flat-sky Limber’s approximation, which is valid for small angles or, equivalently, for

high ℓ values ($\ell \gtrsim 10 - 20$) (see Kilbinger et al. (2017) for a derivation of the shear and convergence spectra without these approximations). We report here the formula already exposed in Chapter 1:

$$C^{(ij)}(\ell) = \int_0^\infty dz \frac{c}{H(z)} \frac{W^{(i)}(z) W^{(j)}(z)}{\chi^2(z)} P_{\text{mm}} \left(k = \frac{\ell}{\chi(z)}, z \right), \quad (4.2)$$

where $P_{\text{mm}}(k, z)$ is the non-linear total matter power spectrum and $\chi(z)$ is the co-moving distance to redshift z (eq. 1.11). $W^{(i)}$ is the window function describing the (normalised) distribution of sources $\mathcal{P}(z)$ in the redshift bin $[z_i, z_{i+1}]$, given by eq. 1.61 and is a measurement of the lensing efficiency in the i -th tomographic bin.

4.2.2 Impact of massive neutrinos

We saw in Chapter 2 that massive neutrinos affect the cold and total matter power spectra (and in turn the cosmic shear one) both in the linear and non-linear regimes. The large thermal velocities that neutrinos possess at their decoupling prevent them from clustering, at linear order, in regions smaller than the free-streaming scale (e.g. Lesgourgues & Pastor (2006)):

$$k_{\text{fs}} = 0.82 \frac{E(z)}{(1+z)^2} \frac{M_\nu}{1 \text{ eV}} h/\text{Mpc}. \quad (4.3)$$

This results in a suppression in the linear CDM+b power spectrum $P_{\text{cc}}(k)$ and total matter power spectrum $P_{\text{mm}}(k)$ at scales smaller than k_{fs} of $-6f_\nu - 8f_\nu$ (Lesgourgues & Pastor (2006); Castorina et al. (2015), Eqs. 2.32 and 2.31, respectively) as long as $f_\nu \lesssim 0.07$. Clearly we expect a larger suppression in the total matter power spectrum since this is given by the combination:

$$P_{\text{mm}}(k) = (1 - f_\nu)^2 P_{\text{cc}}(k) + 2 f_\nu (1 - f_\nu) P_{\text{c}\nu}(k) + f_\nu^2 P_{\nu\nu}(k), \quad (4.4)$$

and the cross cold matter-neutrinos power spectrum $P_{\text{c}\nu}(k)$ and neutrinos power spectrum $P_{\nu\nu}(k)$ rapidly decay for $k > k_{\text{fs}}$.

At lower redshift, neutrinos become non-relativistic and eventually fall into dark matter potential wells. This “neutrino drag” relieves the small-scale suppression, so that plotting the ratio between the power spectra in a massive neutrino cosmology with respect to the Λ CDM one with the same amplitude in the large-scale perturbations gives rise to the well-known spoon-shape curve around $k \sim 1 h/\text{Mpc}$ (see the continuous lines in the top left panel of fig. 4.1). Quantitatively, in the non-linear regime, the suppression becomes of order $\Delta P_{\text{mm}}/P_{\text{mm}} \approx -10 f_\nu$ with a stronger scale-dependence (Brandbyge & Hannestad (2009); Viel et al. (2010); Hannestad et al. (2020)).

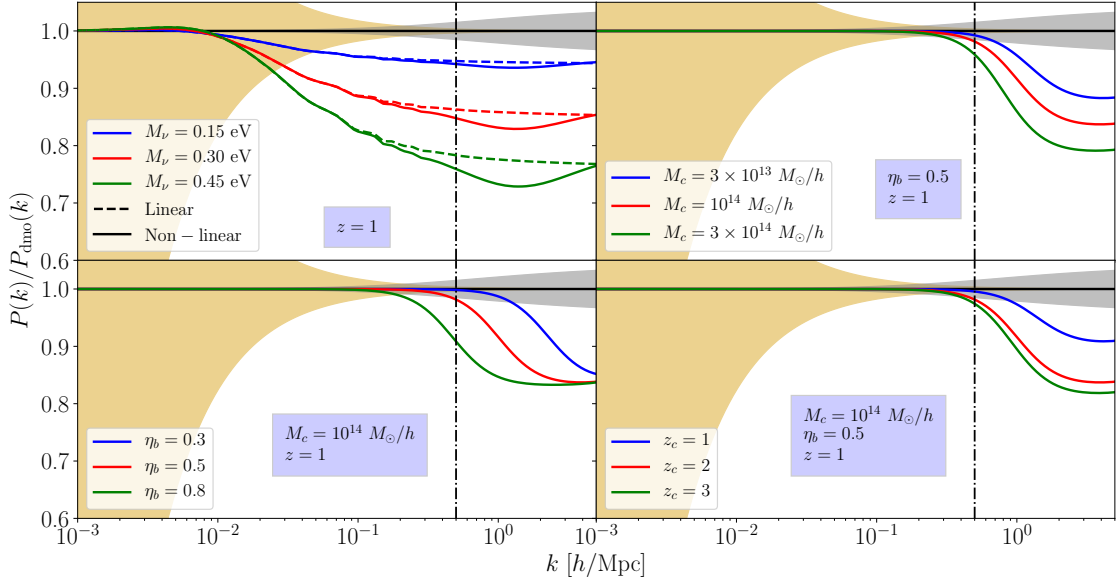


Figure 4.1: The four panels show the effect of the neutrino mass and of the three different feedback parameters of the BCM on the matter power spectrum at $z = 1$ (approximately the median redshift of future surveys). All the ratios are taken with respect to a CDM+b power spectrum model (linear with respect to the linear, non-linear w.r.t. the non-linear) in a cosmology with minimum-allowed neutrino mass $M_\nu = 0.056$ eV and no baryon feedback. In the top left panel the neutrino mass is varied while the ratio in both linear and non-linear regime are shown. The top right panel shows the effect of increasing $\log M_c$, in the bottom left panel we change the parameter η_b , while in the bottom right we display how the redshift parameter affects the feedback fitting function. The gold shaded areas represent cosmic variance for a survey like in Audren et al. (2013) in a redshift bin of $\Delta z = 0.1$ centered at $\bar{z} = 1$. The grey shaded areas represent the theoretical uncertainty on the matter power spectrum due to the HALOFIT fitting formulae, 4.14. In all the panels a vertical line at $k = 0.5$ h/Mpc is drawn, to mark the maximum k at which our analysis is extended.

On the other hand, because of the line-of-sight integration of eq. 4.2, the suppression of the matter power spectrum translates into a suppression in the shear power spectrum that affects almost all multipoles, with a milder dependence on scale (see fig. 2.6 and top-right panel of fig. 4.2).

4.2.3 Impact of baryon feedback

In addition to massive neutrinos, baryonic feedback processes, comprising violent events such as supernova explosions and the accretion onto the central black hole in AGNs, are also responsible for a small-scale drop in power. The theoretical modelling of these effects is affected by large systematic uncertainties because of the difficulty in properly capture baryonic physics in simulations and because of the looseness of

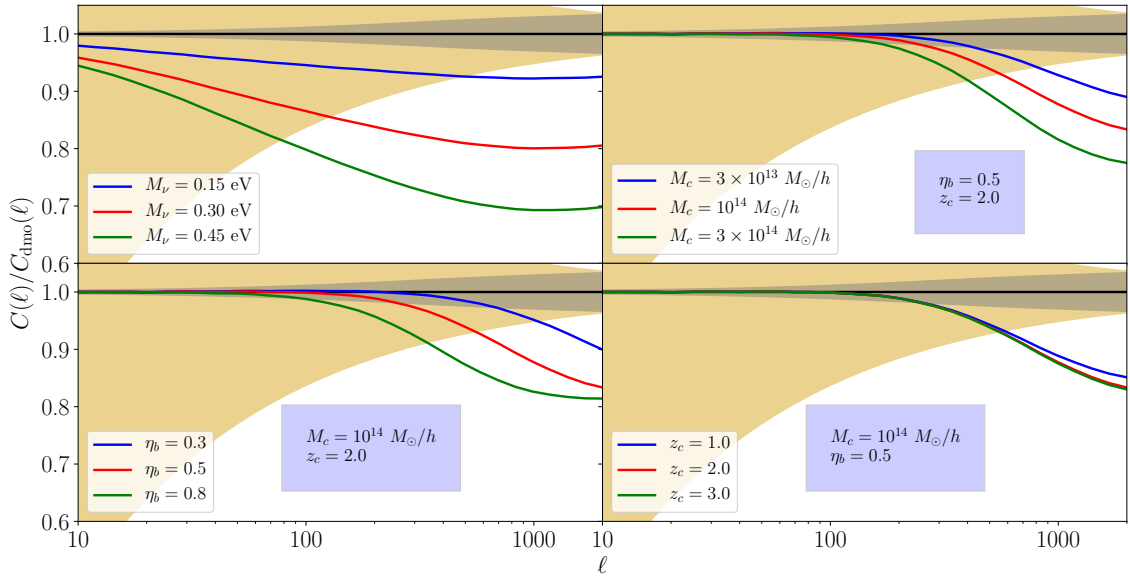


Figure 4.2: This picture is the same of fig. 4.1 but here the cosmic shear power spectrum is shown, with a source distribution like in Audren et al. (2013), a sky coverage of $f_{\text{sky}} = 0.375$ and with all galaxies in a single bin, i.e. no tomography has been performed.

the constraints offered by observations. In general, baryon feedback is expected to cause a suppression to the matter power spectrum of $\sim 25\%$ at scales of $k \sim 2 h/\text{Mpc}$ (Schneider & Teyssier (2015)), but the uncertainty on different AGN feedback models could reach 50% for scales $k \lesssim 1 h/\text{Mpc}$ (Harnois-Déraps et al. (2015)).

Nevertheless, in the last few years several analytical descriptions, relying on fits to numerical simulations, have been proposed. We will make use here of the *baryon correction model* (BCM) by Schneider & Teyssier (2015). As opposed to other similar proposals (see for instance Harnois-Déraps et al. (2015); Chisari et al. (2018)) this model has the advantage of employing parameters with a well-established physical meaning. The BCM assumes that X-ray emitting gas, AGN activity and more in general the complex intracluster physics smoothly modify the profile of the dark matter halo, assumed to be NFW. It must be stressed however, that this model is obtained from a set of hydrodynamical simulations that do not incorporate other mechanisms such as galactic winds, which could produce different scale and redshift dependencies for the suppression. Although the suppression of power depends on different sets of parameters, the shape of the predicted damping, as obtained from simulations, is similar for most of the feedback mechanisms. This is the main motivation to relax the priors on the BCM feedback parameters even outside their physical range in order to be conservative and probe a wider range of feedback-induced suppressions.

The BCM assumes that a halo is composed by a relaxed DM profile plus a number of baryonic components: a fraction of gas which is bound to the halo, a fraction of gas that is ejected and a stellar component which enhances the density at the very center of the halo. Each of these components has its own density profile (the model also includes a back-reaction of baryons on the NFW profile), regulated by some free parameters. The latter are used to actually kick the particles in CDM-only simulations to mimic the effect of the baryons. Depending on the strength of these parameters the halo profile is modified more or less, affecting the matter distribution in the Universe on scales comparable to halo sizes. These modifications are reflected on the matter power spectrum in a way that can be described by a fitting function: it can be shown that out of the dozen free parameters used to modify halo profiles, only three of them are sufficient to grasp the relevant modification to the power spectrum. Said function describes the ratio between the total matter power spectrum accounting for baryon feedback to the power spectrum of the dark-matter-only (dmo) scenario and reads:

$$F_{\text{feed}}(k, z | M_c, \eta_b, z_c) \equiv \frac{P_{\text{feed}}(k)}{P_{\text{dmo}}(k)} = \left\{ \frac{B(z)}{1 + (k/k_g)^3} + [1 - B(z)] \right\} S(k), \quad (4.5)$$

where

$$B(z) = \frac{0.105 \log \left(\frac{M_c}{M_\odot/h} \right) - 1.27}{1 + (z/z_c)^{2.5}} \quad (4.6)$$

for $M_c \geq 10^{12} M_\odot/h$ and zero otherwise,

$$k_g(z) = 0.7 [1 - B(z)]^4 \eta_b^{-1.6} h/\text{Mpc}, \quad (4.7)$$

while the term outside the bracket is the stellar component of the central galaxy,

$$S(k) = 1 + \left(\frac{k}{55 h/\text{Mpc}} \right)^2. \quad (4.8)$$

As already said, the expressions above depend on three parameters: M_c , η_b and z_c . The critical mass M_c is related to the bound gas fraction in a halo. Hydrodynamical simulations show that part of this gas is ejected and such ejection is stronger in low mass halos. So we expect low mass halos to have their gas almost completely stripped. In this picture, M_c represents the typical halo mass scale below which most of the gas is ejected. This parameter regulates the prominence of the suppression: the higher M_c , the smaller $P_{\text{feed}}(k)$ will be. The parameter η_b controls the scale at which the suppression becomes relevant. Such parameter is related to the ejected gas fraction: it may be viewed as the ratio between the thermal velocity of the gas in the

intracluster medium and the halo escape velocity. As such, the higher η_b , the more the suppression occurs at larger scales. Finally, the last parameter z_c accounts for the time dependence of the suppression, which is growing with decreasing redshift as the signal is dominated by larger and larger halos.

To prove the goodness of their formula, Schneider & Teyssier (2015) tested the BCM on the hydrodynamical simulations by Jing et al. (2006) which include radiative cooling and star formation but no AGN feedback. They obtained a best fit of $\eta_b \sim 1.0$ and $M_c \sim 2 \times 10^{12} M_\odot/h$: such a low value for the latter parameter is in very good agreement with the lack of AGN feedback set in the simulations. BCM was also applied to the OWLs simulations (van Daalen et al. (2011)) obtaining values of $M_c \sim 5 \times 10^{14} M_\odot/h$ and $\eta_b \sim 0.4$, indicating a high AGN activity. The systematic error affecting 4.5 is of order 2–3% at all scales up to $k \lesssim 10 h/\text{Mpc}$. This uncertainty will be included in the error on the HALOFIT formulae that we will introduce in the next Section.

A follow-up work of the BCM model (Schneider et al. (2019)) was published few years later of the analysis presented in this Chapter. With respect to the former, the new proposed suppression is shallower with a milder scale-dependence. However, this latest work does not provide a fitting formula for the suppression of the power spectrum, but only evaluates it by displacing the CDM particles in the simulation according to the various baryonic components inside halos.

Figs. 4.1 and 4.2 show separately the effects of massive neutrinos and the original BCM, respectively on the matter power spectrum and the shear power spectrum. The top left panel of fig. 4.1 shows how increasing the neutrino mass suppresses more and more the matter power spectrum (both in the linear and non-linear regimes). A crucial point to stress is that the scale at which neutrino suppression starts is almost constant (i.e. k_{nr} is only weakly-sensitive to M_ν) and much larger than the scales involved by baryon feedback (see the other three panels).

Fig. 4.2 shows the same effect but on cosmic shear. Here feedback only affects high multipoles ($\ell \gtrsim 80$), while massive neutrinos damp the shear spectrum even at low ones. For neutrino masses greater than 0.3 eV, the suppression is so high that, in order for baryon feedback to mimic it, all halos with mass smaller than $\sim 10^{14} M_\odot/h$ should expel their gas, implying an extraordinarily strong AGN activity.

4.3 Method

The goal of this Chapter is to investigate potential degeneracies between the effects of massive neutrinos and baryon feedback on CDM+b and shear power spectra. To do so, we follow a procedure similar to Audren et al. (2013). In that work, a forecast of the errors on cosmological parameters was presented, as expected from a Euclid-like galaxy clustering and weak lensing survey. They performed a MCMC likelihood analysis assuming as fiducial, “mock” data the theoretical prediction (i.e. without statistical scatter). This had been shown to lead to the same forecast errors as employing more realistic measurements from N -body simulations (Perotto et al. (2006)). In particular, they used the prescription by Bird et al. (2012), available at that time, to account for non-linearities both in the galaxy and shear spectra. The systematic uncertainty affecting the HALOFIT prescription was also accounted for in the error budget.

In the following subsections we describe in detail the similar analysis we perform for the clustering and shear survey along with the specific characteristics assumed for the surveys, borrowed as well from Audren et al. (2013).

4.3.1 Clustering survey

As already mentioned, we are limiting the scope of our analysis to exploring degeneracies at the level of the matter density field. For our CDM+b clustering survey we consider the volume probed by a spectroscopic redshift survey covering a sky fraction of $f_{\text{sky}} = 0.375$, spanning a redshift range from $z = 0.5$ to $z = 2.0$ subdivided in 16 redshift bins. The volume of each shell is given by:

$$V_s(z) = 4\pi f_{\text{sky}} \chi^2(z) \frac{\Delta z}{(1+z)^3} \frac{d\chi}{dz}, \quad (4.9)$$

where $\Delta z = 0.1$ is the bin width in redshift. Since our “observable” is the 3-D CDM+b power spectrum, additional, relevant survey characteristic such as the expected galaxy number density will not play a role in our analysis.

We assume a Gaussian likelihood function for cold matter power spectrum P_{cc} given by:

$$\ln \mathcal{L}_C \propto -\frac{1}{2} \sum_{z \text{ bins}} \sum_{i,j} [P_{\text{cc}}^{\text{th}}(k_i, z) - P_{\text{cc}}^{\text{obs}}(k_i, z)] [\text{Cov}(z)^{-1}]_{ij} [P_{\text{cc}}^{\text{th}}(k_j, z) - P_{\text{cc}}^{\text{obs}}(k_j, z)], \quad (4.10)$$

where $P_{\text{cc}}^{\text{th}}(k, z)$ and $P_{\text{cc}}^{\text{obs}}(k, z)$ are respectively the theoretical and “observed” cold matter power spectra while Cov_{ij} is the covariance matrix. All power spectra are

evaluated in wavenumber bins of size $\Delta k = 0.0163 h/\text{Mpc}$ from a minimal value of $k_{\min} = 0.01 h/\text{Mpc}$ to a maximum of $k_{\max} = 0.5 h/\text{Mpc}$. The chosen value of Δk is always larger than the effective fundamental frequency $k_{\text{f}}^{\text{eff}}(z) \equiv 2\pi/[V_{\text{s}}(z)]^{1/3}$ of each subvolume $V_{\text{s}}(z)$ defined by the binning in redshift. The value for k_{\max} is a rather optimistic estimate for the maximum scale that future surveys will reach. In fact, most spectroscopic surveys targeting baryonic oscillations as one of the main cosmological probes are, by design, limited by shot-noise to $k_{\max} = 0.3 - 0.4 h/\text{Mpc}$. All power spectra are generated using CAMB (Lewis et al. (2000)). Non-linearities are modelled through the version of the HALOFIT module by Mead et al. (2015), applied to the CDM+b power spectrum only.

In addition, neutrino effects on matter power spectrum have been shown to be separable from the baryon feedback ones (Mummery et al. (2017)), so we implement baryonic effects by means of 4.5 as a multiplicative factor F_{bf} to the non-linear cold matter power spectrum alone. Therefore, the HALOFIT module parameters providing the nonlinear mapping $P_{\text{cc}} = \mathcal{H}(P_{\text{cc}}^{\text{lin}})$ will correspond to the ‘‘DM only’’ case (see Table 4 in Mead et al. (2015)) as we are treating the baryonic suppression separately. In short, our model for the nonlinear cold matter power spectrum will be given by:

$$P_{\text{cc}}^{\text{obs/th}}(k, z) = \mathcal{H} [P_{\text{cc}}^{\text{lin}}(k, z)] F_{\text{bf}}(k, z | M_{\text{c}}, \eta_{\text{b}}, z_{\text{c}}). \quad (4.11)$$

The accuracy of these fitting formulae will be taken into account in the error budget as we will discuss shortly.

In fact, the covariance matrix Cov_{ij} in eq. 4.10 accounts for both statistical and systematic errors, as:

$$\text{Cov}_{ij}(z) = \text{Cov}_{ij}^{\text{CV}}(z) + \text{Cov}_{ij}^{\text{sys}}(z), \quad (4.12)$$

where the statistical contribution from cosmic variance is simply given by:

$$\text{Cov}_{ij}^{\text{CV}}(z) = \frac{(2\pi)^2}{k_i^2 \Delta k V_{\text{s}}(z)} P_{\text{cc}}^2(k_i, z) \delta_{ij} \quad (4.13)$$

and therefore neglects any non-Gaussian component along with any beat-coupling or super-sample covariance term from the finite observed volume (Sefusatti et al. (2006); Hamilton et al. (2006); Takada & Hu (2013)).

For what concerns the systematic uncertainty affecting the theoretical predictions for the matter power spectra, our standpoint assumes that such predictions are the outcome of state-of-art numerical simulations (we do *not* consider here approaches based on PT). As such they will suffer from systematic uncertainties related to the

choice of the N -body code, the resolution, etc. but also on the accuracy of the fitting function or the emulator built to exploit the numerical results in an efficient MC-based likelihood analysis of future data-sets.

The code comparison by Schneider et al. (2016) estimates the systematic difference among different codes at the 1% and 3% level respectively at $k = 1$ and $10 h/\text{Mpc}$, while suggesting a minimum box size and maximum particle mass in order to avoid errors due to finite-volume effects and resolution beyond the percent level. Similar comparisons are not available for numerical simulations of massive neutrino cosmologies although one can expect additional errors of the order of 1% related to the problem of the proper setting of initial conditions (Zennaro et al. (2017)). Clearly, we do not include in this budget the error on the numerical description of baryonic effects since we deal with it explicitly: the evaluation of its impact is precisely the goal of this work.

In addition to the systematic error intrinsic to the numerical approach, fitting functions such as the various versions of HALOFIT (Smith et al. (2003); Bird et al. (2012); Takahashi et al. (2012)) are also affected by their own uncertainty in reproducing the N -body results on which they are based. Here, for instance, we use the newest version of HALOFIT (Mead et al. (2015)). The latter is expected to provide an accuracy of a few percent at $k < 10 h/\text{Mpc}$ for the most common extensions to the Standard Model only worsening to 10% for specific modified gravity models with chameleon screening. On the other hand, another viable approach is given by cosmic emulators. The CosmicEmu code (Heitmann et al. (2010, 2009); Lawrence et al. (2010b,a)), in its latest version, is claimed to predict the power spectrum at the 1% level up to $k = 8 h/\text{Mpc}$ over a significant region of the allowed parameter space. The accuracy of the new Euclid Emulator (Euclid Collaboration et al. (2019b)) is approximately $\sim 1\%$ at $k < 1 h/\text{Mpc}$, therefore comparable to the one obtained with N -body simulations. Finally, an alternative method, combining PT results at large scales and fitting functions from high-resolution simulations at small scales, has recently been proposed by Smith & Angulo (2019) and implemented in the NG-HALOFIT code, characterised by an expected accuracy of 1% up to $k = 0.9 h/\text{Mpc}$.

In light of these results, we will take a conservative stand assuming that N -body-based methods providing predictions for the nonlinear power spectrum, including massive neutrino effects and common extensions to the Standard Model, are affected by a systematic uncertainty of 3% at $k = 1 h/\text{Mpc}$ and 4% at $k = 10 h/\text{Mpc}$ for our Planck fiducial cosmology at $z = 0$. In particular, following Audren et al. (2013),

we describe the scale and redshift dependence of the relative, systematic error on the cold matter power spectrum as:

$$\alpha(k, z) \equiv \frac{\Delta P_{\text{cc}}(k, z)}{P_{\text{cc}}(k, z)} = \frac{\ln[1 + k/k_{\sigma}(z)]}{1 + \ln[1 + k/k_{\sigma}(z)]} 5\%, \quad (4.14)$$

where $k_{\sigma}(z)$ is the non-linear scale at which the mass fluctuations, smoothed by a Gaussian filter, are equal to unity, that is $\sigma_R = 1$ for $R = 1/k_{\sigma}$. This functional form for $\alpha(k, z)$ was also used by Audren et al. (2013), while a different form for the same quantity has been adopted by Sprenger et al. (2019). At the value of $k_{\text{max}} = 0.5 h/\text{Mpc}$ adopted for the clustering analysis we have $\alpha \simeq 2\%$ at redshift zero, which is a conservative choice.

We expect any systematic error to correlate different wavenumbers. Following Baldauf et al. (2016), we account for the systematic uncertainty with a contribution to the covariance matrix C_{ij} of the form:

$$\text{Cov}_{ij}^{\text{sys}}(z) = \alpha(k_i, z) \alpha(k_j, z) P_{\text{cc}}(k_i, z) P_{\text{cc}}(k_j, z) \exp\left[-\frac{\log^2(k_i/k_j)}{2\sigma_{\alpha}^2}\right], \quad (4.15)$$

where the log-exponential term represents the correlation kernel. We choose $\sigma_{\alpha} = \log 5$ as the log-scale correlation length. This choice is motivated by the fact that the typical scale over which HALOFIT overestimates/underestimates the power spectrum of a simulation is roughly half a decade (see for example fig. 1 of Mead et al. (2015)). In this work we use the EMCEE⁶ package for the likelihood sampling.

4.3.2 Cosmic shear survey

For the shear survey we assume the same sky coverage of the clustering survey ($f_{\text{sky}} = 0.375$). The distribution of source galaxies is taken to be:

$$\mathcal{P}(z) \propto z^{\alpha} \exp\left[-\left(\frac{z}{z_0}\right)^{\beta}\right], \quad (4.16)$$

normalized so that the integral over all redshifts is equal to unity. We set $\alpha = 2$, $\beta = 1.5$ and $z_{\text{mean}} = 1.412 z_0 = 0.9$. We fit a multipole range going from $\ell = 10$ up to $\ell = 2000$, corresponding to an angle of 5 arcseconds or, equivalently, a scale of $\sim 0.7 h/\text{Mpc}$ at the median redshift. We divide the sources into $N = 3$ redshift bins, in such a way that each of them contains the same number of galaxies. We assume a galaxy density of $d = 30 \text{ arcmin}^{-2}$ with a root mean square intrinsic shear

⁶<http://dfm.io/emcee/current/>

of $\langle \gamma_{\text{rms}}^2 \rangle^{1/2} = 0.30$. All the values and functional forms employed here are likely to be in broad agreement with future surveys specifics like Euclid. We can easily estimate the expected shot noise as:

$$N^{(ij)}(\ell) = \delta_{ij} \langle \gamma_{\text{rms}}^2 \rangle n_i^{-1}, \quad (4.17)$$

where $n_i = 3600 d (180/\pi)^2 / N$ is the number of galaxies per steradian in the i -th bin. We assume a Gaussian likelihood also for the shear power spectrum $C_\ell^{(ij)}$, given by:

$$\ln \mathcal{L}_S \propto -\frac{1}{2} \sum_{i,j} \sum_{\ell,\ell'} \left(C_{\text{obs}}^{(ij)} - C_{\text{th}}^{(ij)} \right)_\ell \left[\text{Cov}^{(ij)} \right]_{\ell\ell'}^{-1} \left(C_{\text{obs}}^{(ij)} - C_{\text{th}}^{(ij)} \right)_{\ell'}, \quad (4.18)$$

where $\text{Cov}_{\ell\ell'}^{(ij)}$ represents the power spectra covariance matrix with the indices i, j running from 1 to 3 labelling the redshift bins and ℓ, ℓ' labelling the multipoles.

Consistently with the discussion in the previous Section, the total matter power spectrum, relevant for weak lensing observables, is obtained as:

$$\begin{aligned} P_{\text{mm}}(k, z) &= (1 - f_\nu)^2 \mathcal{H} [P_{\text{cc}}^{\text{lin}}(k, z)] F_{\text{bf}}(k, z | M_c, \eta_b, z_c) \\ &\quad + 2 (1 - f_\nu) f_\nu P_{\text{cv}}^{\text{lin}}(k, z) + f_\nu^2 P_{\nu\nu}^{\text{lin}}(k, z), \end{aligned} \quad (4.19)$$

where again the HALOFIT operator only acts on the CDM+b auto-spectrum. For the cross and neutrino spectra we use linear theory as their non-linear counterpart is expected to give sub-percent contribution (Castorina et al. (2015)).

The error sources we consider here are cosmic variance, shape noise and the theoretical error on the matter power spectrum propagated in the cosmic shear spectrum (4.23), so that the total covariance matrix reads:

$$\text{Cov}_{\ell\ell'}^{(ij)}(z) = \text{Cov}_{\ell\ell'}^{(ij),\text{CV-SN}}(z) + \text{Cov}_{\ell\ell'}^{(ij),\text{sys}}(z). \quad (4.20)$$

The cosmic variance, in the Gaussian approximation, and shape noise contributions is given by:

$$\text{Cov}_{\ell\ell'}^{(ij),\text{CV-SN}} = \frac{2}{2\ell + 1} f_{\text{sky}}^{-1} [C^{(ij)}(\ell) + Nl^{(ij)}(\ell)]^2 \delta_{\ell\ell'}. \quad (4.21)$$

The systematic component is given instead by:

$$\text{Cov}_{\ell\ell'}^{(ij),\text{sys}} = E_\ell^{(ij)} E_{\ell'}^{(ij)} \exp \left[-\frac{\log^2(\ell/\ell')}{2 \sigma_E^2} \right]. \quad (4.22)$$

where the relative uncertainty on the shear power spectrum is obtained by propagating the uncertainty on the matter power spectrum through eq. 4.2 as:

$$\begin{aligned} E^{(ij)}(\ell) &\equiv \frac{\Delta C^{(ij)}(\ell)}{C^{(ij)}(\ell)} = \\ &= \int_0^\infty dz \frac{c}{H(z)} \frac{W^{(i)}(z) W^{(j)}(z)}{\chi^2(z)} \alpha \left(\frac{\ell}{\chi(z)}, z \right) P_{\text{mm}} \left(\frac{\ell}{\chi(z)}, z \right). \end{aligned} \quad (4.23)$$

Here we have implicitly assumed that the error on P_{mm} is the same of that on P_{cc} , since the other quantities are involved at the linear level and are therefore known with high precision ($\sim 0.1\%$).

The value for the correlation length σ_{E} for the uncertainty on the shear power spectrum is chosen consistently with the one on the matter power spectrum. To estimate it we introduce a logarithmic modulation of period $\sigma_{\alpha} = \log 5$ in the matter power spectra and computed the shear spectra integrating them. This is checked to be translated in a modulation of period approximately one third of a decade in the shear spectra: hence we set $\sigma_{\text{E}} = \log 3$.

As a final remark, we should stress that, despite a mission like Euclid will measure clustering and shear in the same patch of the sky, we never perform a combined analysis of the two quantities. We will leave this for future work.

4.4 Results

In this Section we present our results. We divide it into three parts: in the first, we verify if a properly chosen set of feedback parameters is able to reproduce a suppression in the matter spectra similar to the effect of massive neutrinos; in the second, we address the possible degeneracies between the neutrino mass and the three feedback parameter; in the third, we investigate additional, possible degeneracies between M_{ν} and the intrinsic alignment parameter as it could be measured in weak lensing surveys.

4.4.1 Fitting baryon feedback on massive neutrino cosmologies

The goal of this Section is to check whether there exists a set of reasonable feedback parameters able to reproduce the same effects of massive neutrinos. We first generate data for three fiducial cosmologies with a single massive neutrino species of mass $M_{\nu} = 0.15, 0.30, 0.45$ eV. Then we fit each of these synthetic data with a model that assumes a constant neutrino mass corresponding to the minimum allowed value $M_{\nu} = 0.056$ eV (Lesgourgues & Pastor (2006)) but with varying baryon feedback parameters.

The results of this test are summarised in Table 4.1, which reports the best-fit values for the parameters, along with their 68% confidence level errors. The table also shows the shift in the reduced chi-square with respect to the one obtained by fitting the true model on the mock data. The first thing to notice is that clustering can better distinguish between the two effects – massive neutrinos and baryon feedback

M_ν	Clustering				Cosmic shear			
	$\log M_c$	η_b	z_c	$\Delta\chi_{\text{red}}^2$	$\log M_c$	η_b	z_c	$\Delta\chi_{\text{red}}^2$
0.15 eV	$12.56^{+0.02}_{-0.02}$	$5.5^{+2.3}_{-0.8}$	> 8.3	+0.03	$12.77^{+0.11}_{-0.11}$	$14.0^{+10.8}_{-8.9}$	> 4.8	+0.005
0.30 eV	$13.33^{+0.02}_{-0.02}$	$3.6^{+0.1}_{-0.1}$	> 10.0	+0.27	$13.85^{+0.11}_{-0.11}$	$3.3^{+2.9}_{-0.9}$	> 5.2	+0.009
0.45 eV	$14.08^{+0.01}_{-0.01}$	$2.6^{+0.1}_{-0.1}$	> 12.3	+0.95	$14.86^{+0.09}_{-0.09}$	$1.8^{+0.4}_{-0.3}$	> 5.1	+0.019

Table 4.1: Best-fit values of the baryon parameters obtained from the analysis of Section 4.4.1, where we fitted spectra with baryonic features onto spectra containing massive neutrinos. We also report the difference in the reduced chi-squared $\Delta\chi_{\text{red}}^2$ with respect to the one obtained using the “true” model. M_c is in units of M_\odot/h while the errors or lower limits represent the 68% confidence level. The priors are $\log M_c [M_\odot/h] \in [12, 30]$, $\eta_b \in [0, 30]$, $z_c \in [0, 30]$.

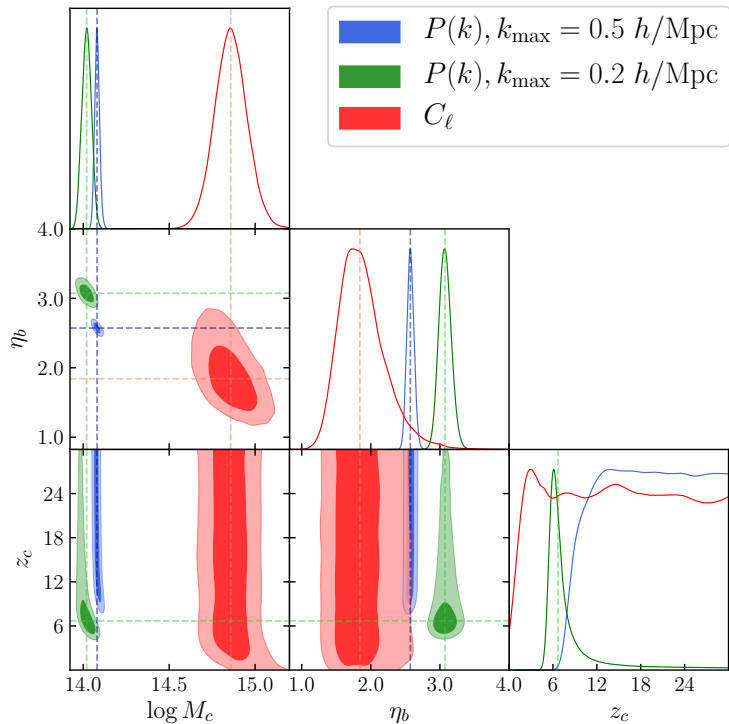


Figure 4.3: Contour plots showing the posterior probability distribution for the three feedback parameters. These are obtained when matter (blue and green, where we stop at 2 different k_{max}) and shear (red) spectra for cosmologies with minimal neutrino mass ($M_\nu = 0.056$ eV) and baryon feedback are fitted on spectra in massive neutrino cosmologies ($M_\nu = 0.45$ eV in this plot) with no baryon feedback.

– even for the lowest neutrino masses. This can be addressed to the larger cosmic variance that one has in weak lensing surveys, that dominates the total error at almost all multipoles (see fig. 4.2). Furthermore, the characteristic scales are more clearly defined for the three-dimensional power spectrum than for the shear one.

Interestingly, we find some discrepancies in the contour plots in fig. 4.3: it seems not possible to find a single set of feedback parameters able to describe the neutrino-induced suppression in both the observables. In fact, the picture shows the allowed (1- and 2- σ) regions for the feedback parameters inferred by cosmic shear (red) and clustering when stopping the analysis at $k_{\text{max}} = 0.5 h/\text{Mpc}$ (blue) or at $k_{\text{max}} = 0.2 h/\text{Mpc}$ (green), for the case $M_\nu = 0.45 \text{ eV}$. Not only the clustering contours do not match their counterpart from cosmic shear, but there is a significant dependence on the maximum wavenumber, k_{max} assumed for the analysis. Despite the three degrees of freedom describing the baryonic effects, the fit is even more inaccurate at the intermediate scales between 0.2 and 0.5 h/Mpc : for instance, when stopping at $k = 0.2 h/\text{Mpc}$ for $M_\nu = 0.45 \text{ eV}$ we obtained $\Delta\chi_{\text{red}}^2 = 0.73$, versus a $\Delta\chi_{\text{red}}^2 = 0.95$ when pushing up to $k = 0.5 h/\text{Mpc}$. This provides some first clue that a combined analysis should be able to disentangle baryonic and neutrinos effects. However, since we expect a high degree of correlation between the two observables, a detailed and careful study of their covariance matrices must be carried out.

The redshift parameter z_c remains largely unconstrained for any the neutrino mass. Looking at the bottom right panel of fig. 4.1 can help realize how this happens. At $z = 1$ (a characteristic redshift for future galaxy surveys) and at scales of 0.5 h/Mpc (that is the maximum we consider for our analysis) the dependence of the power spectrum on z_c is very weak: the difference with respect to the “base” model lies well within the theoretical uncertainty. Besides, the suppression almost saturates for $z_c \gtrsim 3$, meaning that any value for this parameter is equivalent. The same holds true also for the shear power spectrum (see the bottom right panel of figure 4.2): z_c does not play an important role, as the variation in the range $z_c = 1 - 3$ is of the order of 2% versus a theoretical uncertainty of $\sim 3\%$ even at the highest multipoles.

The η_b parameter sets the scale at which the suppression occurs, so we expect it to be degenerate with neutrino mass to some extent. In fact Table 4.1 shows this effect: a higher neutrino mass implies a lower value for η_b . Moreover, the constraints on this parameter get tighter with increasing neutrino mass. The reason is two-fold: first, because of the strong power-law dependence of the feedback suppression on η_b (see 4.5); second, a small neutrino mass implies a lower suppression at large scales, where cosmic variance is larger.

4.4.2 Baryonic feedback and massive neutrinos degeneracies

We now address directly the degeneracy between the neutrino mass and the parameters of the BCM by considering a likelihood analysis where all relevant parameters

Input parameters				Clustering			Cosmic shear		
M_ν	$\log M_c$	η_b	z_c	M_ν	$\log M_c$	η_b	M_ν	$\log M_c$	η_b
0.15	13	0.5	1.0	$0.150^{+0.006}_{-0.009}$	< 14.6	\times	$0.147^{+0.030}_{-0.045}$	< 13.3	< 5.6
0.15	13	0.5	2.0	$0.150^{+0.004}_{-0.004}$	\times	\times	$0.148^{+0.033}_{-0.041}$	< 13.4	< 8.3
0.15	13	1.0	1.0	$0.150^{+0.003}_{-0.003}$	$13.2^{+0.6}_{-0.3}$	$0.9^{+0.2}_{-0.3}$	$0.167^{+0.048}_{-0.058}$	< 13.2	< 5.5
0.15	13	1.0	2.0	$0.150^{+0.003}_{-0.003}$	$13.0^{+0.1}_{-0.1}$	$1.0^{+0.1}_{-0.1}$	$0.156^{+0.050}_{-0.054}$	< 13.3	< 2.3
0.15	14	0.5	1.0	$0.150^{+0.003}_{-0.003}$	< 16.9	< 1.0	$0.152^{+0.034}_{-0.037}$	$13.9^{+0.3}_{-0.3}$	$0.5^{+0.1}_{-0.1}$
0.15	14	0.5	2.0	$0.150^{+0.003}_{-0.003}$	$14.4^{+1.9}_{-1.1}$	$0.4^{+0.3}_{-0.2}$	$0.150^{+0.034}_{-0.037}$	$14.0^{+0.3}_{-0.3}$	$0.5^{+0.1}_{-0.1}$
0.15	14	1.0	1.0	$0.150^{+0.003}_{-0.003}$	$14.0^{+0.1}_{-0.1}$	$1.0^{+0.1}_{-0.1}$	$0.166^{+0.061}_{-0.059}$	$13.8^{+0.4}_{-0.4}$	$1.0^{+0.2}_{-0.2}$
0.15	14	1.0	2.0	$0.150^{+0.003}_{-0.003}$	$14.0^{+0.1}_{-0.1}$	$1.0^{+0.1}_{-0.1}$	$0.165^{+0.062}_{-0.062}$	$13.9^{+0.4}_{-0.5}$	$1.0^{+0.2}_{-0.2}$
0.30	13	0.5	1.0	$0.300^{+0.005}_{-0.005}$	< 16.4	\times	$0.300^{+0.031}_{-0.051}$	< 13.5	< 8.3
0.30	13	0.5	2.0	$0.300^{+0.007}_{-0.004}$	< 18.3	\times	$0.303^{+0.033}_{-0.055}$	< 13.4	< 11.3
0.30	13	1.0	1.0	$0.300^{+0.003}_{-0.003}$	$13.1^{+0.6}_{-0.3}$	$0.9^{+0.2}_{-0.3}$	$0.310^{+0.054}_{-0.080}$	< 13.4	< 6.9
0.30	13	1.0	2.0	$0.300^{+0.003}_{-0.003}$	$13.0^{+0.1}_{-0.1}$	$1.0^{+0.1}_{-0.1}$	$0.317^{+0.051}_{-0.084}$	< 13.7	< 5.1
0.30	14	0.5	1.0	$0.300^{+0.003}_{-0.003}$	< 16.6	< 0.9	$0.301^{+0.035}_{-0.040}$	$13.9^{+0.3}_{-0.3}$	$0.5^{+0.1}_{-0.1}$
0.30	14	0.5	2.0	$0.300^{+0.003}_{-0.003}$	$14.4^{+1.7}_{-1.1}$	$0.4^{+0.3}_{-0.2}$	$0.299^{+0.036}_{-0.041}$	$14.0^{+0.3}_{-0.3}$	$0.5^{+0.1}_{-0.1}$
0.30	14	1.0	1.0	$0.300^{+0.003}_{-0.003}$	$14.0^{+0.1}_{-0.1}$	$1.0^{+0.1}_{-0.1}$	$0.322^{+0.068}_{-0.086}$	$13.7^{+0.6}_{-0.5}$	$1.0^{+0.2}_{-0.2}$
0.30	14	1.0	1.0	$0.300^{+0.003}_{-0.003}$	$14.0^{+0.1}_{-0.1}$	$1.0^{+0.1}_{-0.1}$	$0.318^{+0.070}_{-0.085}$	$13.9^{+0.6}_{-0.5}$	$1.0^{+0.2}_{-0.2}$

Table 4.2: Best-fit values and 68% confidence level intervals for the parameters obtained from the power spectrum, $P(k)$, as well as from the cosmic shear, $C(\ell)$, analysis. The mark \times means that such parameter is not constrained at all. See Section 4.4.2 for details.

are allowed to vary simultaneously.

We consider 16 distinct fiducial models corresponding to all possible combinations for each of the four parameters taking two values given by $M_\nu = (0.15, 0.3)$ eV, $\log M_c [M_\odot/h] = (13, 14)$, $\eta_b = (0.5, 1)$, $z_c = (1, 2)$. We then run the MCMC likelihood analysis over the 4 parameters with a two-fold goal: check whether we are able to recover the fiducial values, with special attention to the neutrino mass, and examine the degeneracies among the parameters.

The values obtained for the parameters of major interest are listed in Table 4.2, while the results relative to the neutrino mass are shown in fig. 4.4. The blue and red data points with error bars mark the 68% confidence level on the neutrino mass as determined, respectively, by matter clustering and cosmic shear. We see that we can recover the right input M_ν^{real} within $1\text{-}\sigma$ in all cases. The value of M_ν found with weak lensing is always within $\sim 0.25 \sigma$ from the correct one. Moreover, the values

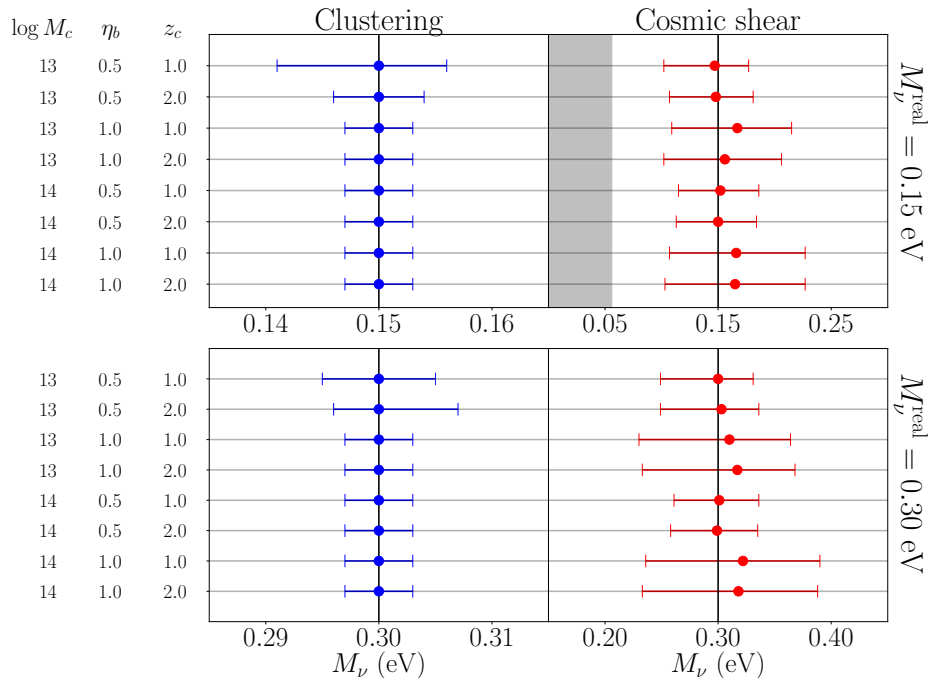


Figure 4.4: 1-D posterior probability distributions for neutrino mass for all the cases analysed in Section 4.4.2. The error-bars represent the 68% confidence level on M_ν using clustering (blue) and weak lensing (red). The left columns show the feedback parameters used to generate the mock data. The top panels show the results when $M_\nu = 0.15$ eV, while the bottom ones do the same for the case $M_\nu = 0.30$ eV. The grey shaded area in the top panels mark the region $M_\nu < 0.056$ eV, forbidden by particle physics experiments.

of neutrino mass obtained through clustering are basically perfect (see Table 4.2). The reasons are multiple. First of all, the matter power spectrum describes the 3-D distribution of inhomogeneities, while the shear one is a 2-D projection of a 3-D field. Thus, while the features of the matter power spectrum are well defined at each scale, the scale mixing of 4.2 makes it difficult to associate a range of multipoles to a single effect. Second, neutrinos affect all multipoles in the shear power spectrum, but only the smallest scales in the matter one. Third, the redshift dependence of the two effects is very different. The neutrino suppression in the CDM+b power spectrum is insensitive to redshift: while the scale at which the “turnaround” of the spoon shape damping slightly moves towards low- k values, the amplitude of such suppression stays almost constant in time. On the other hand, Mummery et al. (2017) shows that the suppression due to baryon feedback increases significantly at late times. Therefore tomography plays a crucial role in this kind of analysis. Fourth, here we are assuming perfect knowledge on of the functional forms both for neutrinos and baryon feedback and that helps in recovering the correct input values with a very low level of bias.

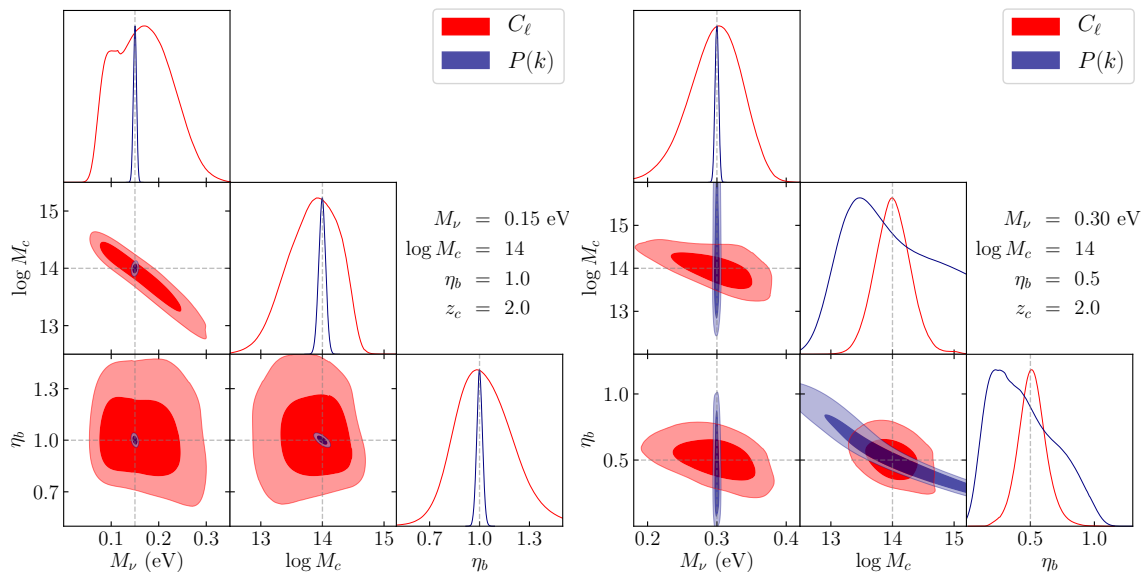


Figure 4.5: 1-D and 2-D posterior PDFs for M_ν , $\log M_c$ and η_b for 2 of the 16 runs described in Sections 4.4.2 whose parameters are displayed in the plot. The blue contours show the results for clustering, while the red contours represent the results from the cosmic shear survey. The grey dashed lines show the “true” values, used to generate the mock data.

The absence of neutrino-baryon degeneracy in the 3D clustering case is evident in fig. 4.5. There we show the contour plot for 2 of the 16 runs mentioned above. The blue contours represent the 2-D posteriors on the parameters M_ν , $\log M_c$ and η_b , marginalized over z_c : the contours in the planes $M_\nu - \log M_c$ and $M_\nu - \eta_b$ are clearly parallel to the parameter axes, implying that neutrino mass is not degenerate with the BCM parameters. However, there exists a degeneracy intrinsic to the feedback parameters, in particular in the $\log M_c - \eta_b$ plane, that is very clear in the bottom panel of fig. 4.5. On the other hand, the red contours, representing the results obtained from weak lensing, show that a degeneracy is indeed present, i.e. the one between $M_\nu - \log M_c$. However, it is still weak enough not to affect the measurement on neutrino mass, which, as we mentioned above, is recovered well within the error-bars.

Interestingly, there are some fixed triads of fiducial BCM parameters that cannot be properly constrained neither by clustering nor by weak lensing (see Table 4.2). For instance, when $\log M_c = 13$ weak lensing can only return upper limits for the feedback parameters; or again low feedback activity (i.e. low $\log M_c$ and low η_b) is not constrained by clustering, since the scales affected by baryon feedback are mostly left out from the analysis.

The error-bars from weak lensing are typically much larger than the ones for clus-

tering, especially those on neutrino mass. This is expected for many reasons. First, despite performing tomography, the integration along the line-of-sight causes the loss of information on the z -direction. Second, cosmic variance limits the constraining power more than in the clustering case (see figs. 4.1 and 4.2). Moreover, for the clustering case we only considered the CDM+b power spectrum as observable: introducing galaxy bias, Alcock-Paczynski effect and RSD would considerably enlarge them.

4.4.3 Degeneracy with intrinsic alignment

In the last part of this work we want to investigate the possible degeneracy between neutrino mass and intrinsic alignment in weak lensing measurements. Intrinsic alignment (IA) is one of the most significant astrophysical systematics in cosmic shear surveys, as it can enhance the signal up to 10% at all multipoles (Troxel & Ishak (2015)). It is due to the fact that orientations of nearby galaxies can be correlated when they form and evolve in the same gravitational environment. As a result, in a shear survey one observes not only the cosmological signal due to the large-scale gravitational lensing potential, but, in addition, an intrinsic ellipticity term, so that:

$$\gamma_{\text{obs}} = \gamma_G + \gamma_I. \quad (4.24)$$

Thus, when computing the power spectrum of this quantity, one obtains different contributions (see also eq. 1.62):

$$C_{\text{obs}}^{ij}(\ell) = C_{GG}^{ij}(\ell) + C_{GI}^{ij}(\ell) + C_{II}^{ij}(\ell) + N^{(ij)}(\ell), \quad (4.25)$$

where we also included the shape-noise term $N^{(ij)}(\ell)$. The GG term is just eq. 4.2, i.e. the cosmological signal. The latter two terms represent the correlation of shapes between physically nearby galaxy pairs (II) (Heavens et al. (2000); Croft & Metzler (2000)) and the correlation of galaxies that are aligned with those that are lensed by the same structure (GI) (Hirata & Seljak (2004)).

To describe this systematic we use the linear alignment model of Hirata & Seljak (2004): large-scale correlations or fluctuations in the mean intrinsic ellipticity field of triaxial elliptical galaxies is to ascribe to large-scale fluctuations in the primordial potential in which the galaxy formed during the matter dominated epoch. Thus we expect a linear relation between IA and the matter power spectrum. Within this

paradigm, the IA terms read:

$$C_{GI}^{(ij)}(\ell) = \int_0^\infty dz \frac{c}{H(z)} \frac{W^{(j)}(z) N^{(i)}(z) + W^{(i)}(z) N^{(j)}(z)}{\chi^2(z)} \times \\ \times F_{\text{IA}} \left(\frac{\ell}{\chi(z)}, z \right) P_{\text{mm}} \left(\frac{\ell}{\chi(z)}, z \right) \quad (4.26)$$

$$C_{II}^{(ij)}(\ell) = \int_0^\infty dz \frac{c}{H(z)} \frac{N^{(i)}(z) N^{(j)}(z)}{\chi^2(z)} \times \\ \times F_{\text{IA}}^2 \left(\frac{\ell}{\chi(z)}, z \right) P_{\text{mm}} \left(\frac{\ell}{\chi(z)}, z \right), \quad (4.27)$$

with

$$N^{(i)}(z) = \mathcal{P}^{(i)}(z) \frac{dz}{d\chi} = \mathcal{P}^{(i)}(z) \frac{H(z)}{c} \quad (4.28)$$

$$F_{\text{IA}}(k, z) = -A_{\text{IA}} C_1 \rho_c \frac{\Omega_m}{D_m(k, z)}, \quad (4.29)$$

where ρ_c and Ω_m are the critical density and the matter density parameter today, $D_m(k, z)$ is the total matter, scale-dependent linear growth factor, while $C_1 = 5 \times 10^{-14} h^{-2} M_\odot^{-1} \text{Mpc}^3$ is a normalization constant chosen such that the free parameter A_{IA} takes values around unity. For instance, Köhlinger et al. (2017) found $A_{\text{IA}} = -1.81_{-1.21}^{+1.61}$ and $A_{\text{IA}} = -1.72_{-1.25}^{+1.49}$ for the analyses using 3- z and 2- z bins respectively, while Troxel et al. (2018), although using another model, obtained $A_{\text{IA}} = 1.3_{-0.6}^{+0.5}$.

In fig. 4.6 we plot the relative difference on the shear power spectrum (we consider a single tomographic bin for simplicity) of models with different neutrino masses and models with different IA parameter with respect to a model with minimal neutrino mass and $A_{\text{IA}} = 0$. IA can either enhance (if $A_{\text{IA}} < 0$) or damp (if $A_{\text{IA}} > 0$) the signal at all multipoles, and this effect may in principle mimic the neutrinos and introduce a possible degeneracy with M_ν .

We perform the MCMC with the usual method but this time setting the z_c parameter to a fixed value of 2. We choose to do so because none of the runs of the previous analysis (Section 4.4.2) was able to constrain such parameter, due to the weak dependence of the shear spectra on it (see the bottom right panel of fig. 4.2). Therefore, we will have again 4 free parameters: M_ν , $\log M_c$, η_b , A_{IA} . We use the same grid of parameter values of the previous Section, plus $A_{\text{IA}} = 1.3, -1.3$.

The results for the main parameters of interest are listed in Table 4.3. For a clearer view, fig. 4.7 reports the results for what concerns neutrino mass and the IA parameter in all the 16 different parameter sets. We grouped the results according to the value of the input neutrino mass and the sign of A_{IA} . We see that once again we are

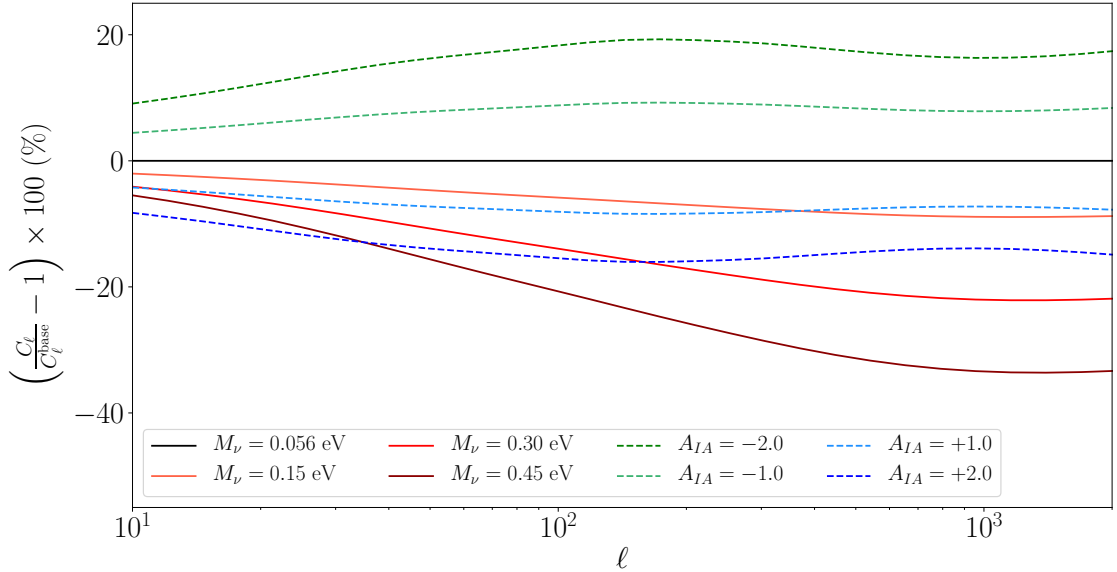


Figure 4.6: Percentage difference on the shear power spectrum $C(\ell)$ due to an increasing neutrino mass (from red to blue) or an increasing IA (from green to yellow) with respect to a model with minimal neutrino mass and no IA. We assume here a single tomographic bin.

able to recover the right input parameters. For the neutrino mass, the maximum difference with respect to the true value is $\sim 0.46 \sigma$, while for A_{IA} is $\sim 0.3 \sigma$. Again, we stress that we are assuming a perfect knowledge of the functional form and parameter values for baryonic and neutrino effects as well as the IA model, which in principle may be much more complicated than what we assumed.

Fig. 4.8 shows the contour plots for two combinations of parameters (the same of fig. 4.5). In green we show the $1\text{-}\sigma$ and $2\text{-}\sigma$ contours for the run with IA, while the red ones are the same contours of fig. 4.5 (and therefore the posterior on A_{IA} is absent). The results and in particular the degeneracy patterns are rather similar: the only particularly pronounced degeneracy lies in the $M_\nu - \log M_c$ plane, but it is essentially unaffected by IA, while those between the other feedback parameters are pretty weak. An interesting point to discuss concerns the degeneracy between M_ν and A_{IA} . Fig. 4.9 shows the $1\text{-}\sigma$ and $2\text{-}\sigma$ contour lines in the $M_\nu - A_{\text{IA}}$ plane for the 16 different parameter sets we used. There seems to be a degeneracy pattern which is weak for positive A_{IA} (odd columns) and stronger for negative A_{IA} (even columns). In particular we find an anti-correlation between the two parameters. This is expected, since M_ν lowers the signal at almost all multipoles (see fig. 4.2), while the IA parameter boosts it – if A_{IA} is negative – or damps it – if A_{IA} is positive – approximately in the same way (see for instance fig. 4 in Köhlinger et al. (2017)). We would like to stress that this degeneracy appears only as long as we use a single redshift bin, so

Input parameters				Cosmic shear with IA			
M_ν	$\log M_c$	η_b	A_{IA}	M_ν [eV]	$\log M_c$	η_b	A_{IA}
0.15	13	0.5	1.3	$0.142^{+0.041}_{-0.047}$	< 13.4	< 7.5	$1.31^{+0.11}_{-0.11}$
0.15	13	0.5	-1.3	$0.144^{+0.042}_{-0.054}$	< 13.6	< 5.0	$-1.28^{+0.22}_{-0.19}$
0.15	13	1.0	1.3	$0.166^{+0.059}_{-0.062}$	< 13.3	< 5.4	$1.27^{+0.11}_{-0.11}$
0.15	13	1.0	-1.3	$0.159^{+0.068}_{-0.070}$	< 13.3	< 5.7	$-1.31^{+0.23}_{-0.20}$
0.15	14	0.5	1.3	$0.148^{+0.046}_{-0.044}$	$14.0^{+0.3}_{-0.3}$	$0.5^{+0.1}_{-0.1}$	$1.31^{+0.11}_{-0.12}$
0.15	14	0.5	-1.3	$0.156^{+0.047}_{-0.049}$	$14.0^{+0.3}_{-0.3}$	$0.5^{+0.1}_{-0.1}$	$-1.31^{+0.19}_{-0.20}$
0.15	14	1.0	1.3	$0.165^{+0.067}_{-0.061}$	$13.9^{+0.4}_{-0.4}$	$1.0^{+0.2}_{-0.2}$	$1.28^{+0.11}_{-0.11}$
0.15	14	1.0	-1.3	$0.166^{+0.087}_{-0.065}$	$13.9^{+0.5}_{-0.5}$	$1.0^{+0.2}_{-0.4}$	$-1.32^{+0.28}_{-0.21}$
0.30	13	0.5	1.3	$0.298^{+0.044}_{-0.067}$	< 13.8	< 3.1	$1.30^{+0.12}_{-0.12}$
0.30	13	0.5	-1.3	$0.299^{+0.044}_{-0.063}$	< 13.5	< 9.6	$-1.29^{+0.19}_{-0.18}$
0.30	13	1.0	1.3	$0.324^{+0.060}_{-0.094}$	< 13.5	< 10.4	$1.26^{+0.11}_{-0.11}$
0.30	13	1.0	-1.3	$0.319^{+0.066}_{-0.097}$	< 13.5	< 3.7	$-1.34^{+0.21}_{-0.20}$
0.30	14	0.5	1.3	$0.298^{+0.047}_{-0.051}$	$14.0^{+0.3}_{-0.3}$	$0.5^{+0.1}_{-0.1}$	$1.30^{+0.11}_{-0.11}$
0.30	14	0.5	-1.3	$0.299^{+0.052}_{-0.056}$	$14.1^{+0.3}_{-0.3}$	$0.5^{+0.1}_{-0.1}$	$-1.29^{+0.19}_{-0.19}$
0.30	14	1.0	1.3	$0.320^{+0.106}_{-0.094}$	$13.9^{+0.6}_{-0.8}$	$1.0^{+0.3}_{-0.2}$	$1.28^{+0.11}_{-0.11}$
0.30	14	1.0	-1.3	$0.346^{+0.160}_{-0.099}$	$14.0^{+2.7}_{-0.6}$	$1.0^{+0.2}_{-0.9}$	$-1.37^{+0.22}_{-0.18}$

Table 4.3: This table shows the 68% confidence level intervals for the parameters obtained from the analysis of cosmic shear power spectra to which the IA contribution has been added. See Section 4.4.3 for details.

performing tomography could help in alleviating or breaking it. In fact, while neutrinos affect all the redshift bins in a similar way, IA depends much more on the source distribution and therefore has a different impact on different redshift bins. Moreover, although we do not show here the plots, another interesting point is the absence of degeneracy between the IA parameter and the other feedback parameters $\log M_c$ and η_b . All combined, these results, limited to the analysis of matter 3D clustering, yield the conclusion that in the BCM model the measurement of neutrino mass will not be affected by baryon feedback nor by IA.

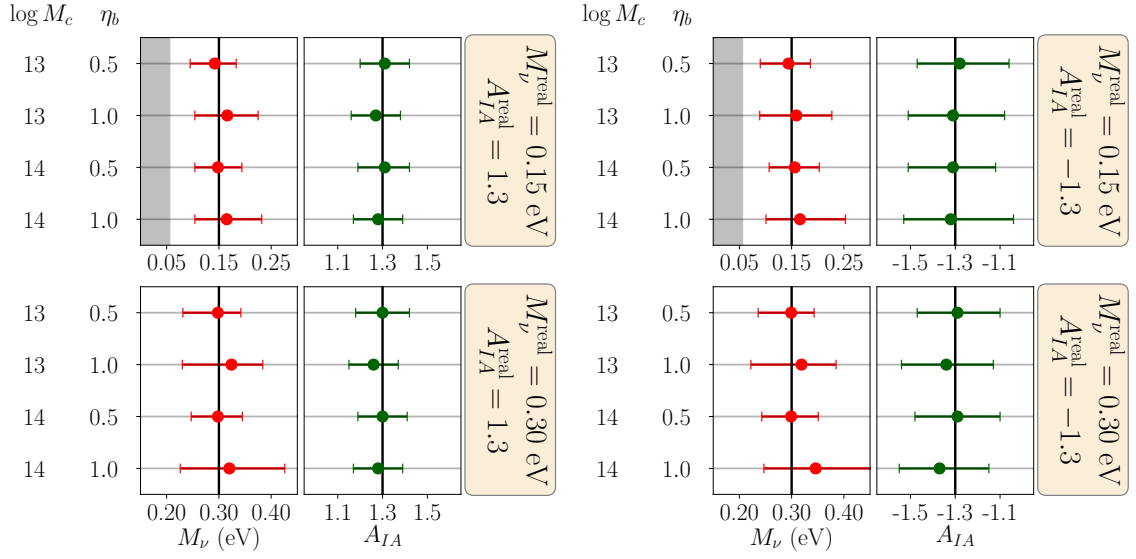


Figure 4.7: Results obtained from the 16 different runs for a cosmic shear survey including the IA effect. For clarity we have separated the runs with same neutrino mass and IA parameters. The black vertical lines represent the true input value, the error-bars mark the 68% confidence level for neutrino mass (red) and IA parameter A_{IA} (green). The left columns report the values of the feedback parameters used to generate mock data (z_c has been set to 2). The grey shaded area is forbidden by the solar neutrino experiments.

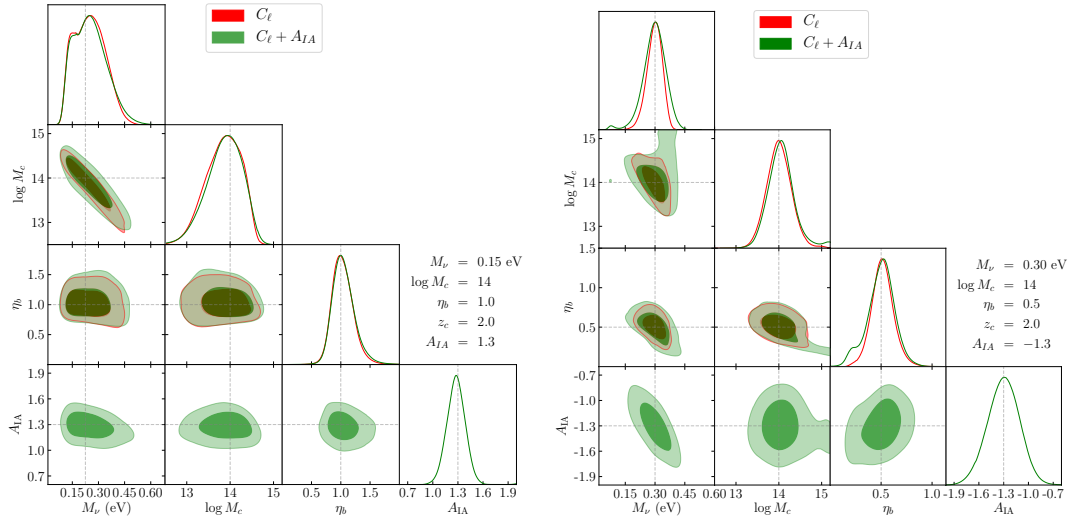


Figure 4.8: Triangle plot showing 1-D and 2-D posterior PDFs for M_ν , $\log M_c$, η_b and A_{IA} for two of the 16 runs described in Sections 4.4.2 and 4.4.3 whose parameters are displayed in the plot. The red and green contours represent the results from the cosmic shear survey with and without IA, respectively. The grey dashed lines show the “true” values, used to generate the mock data.

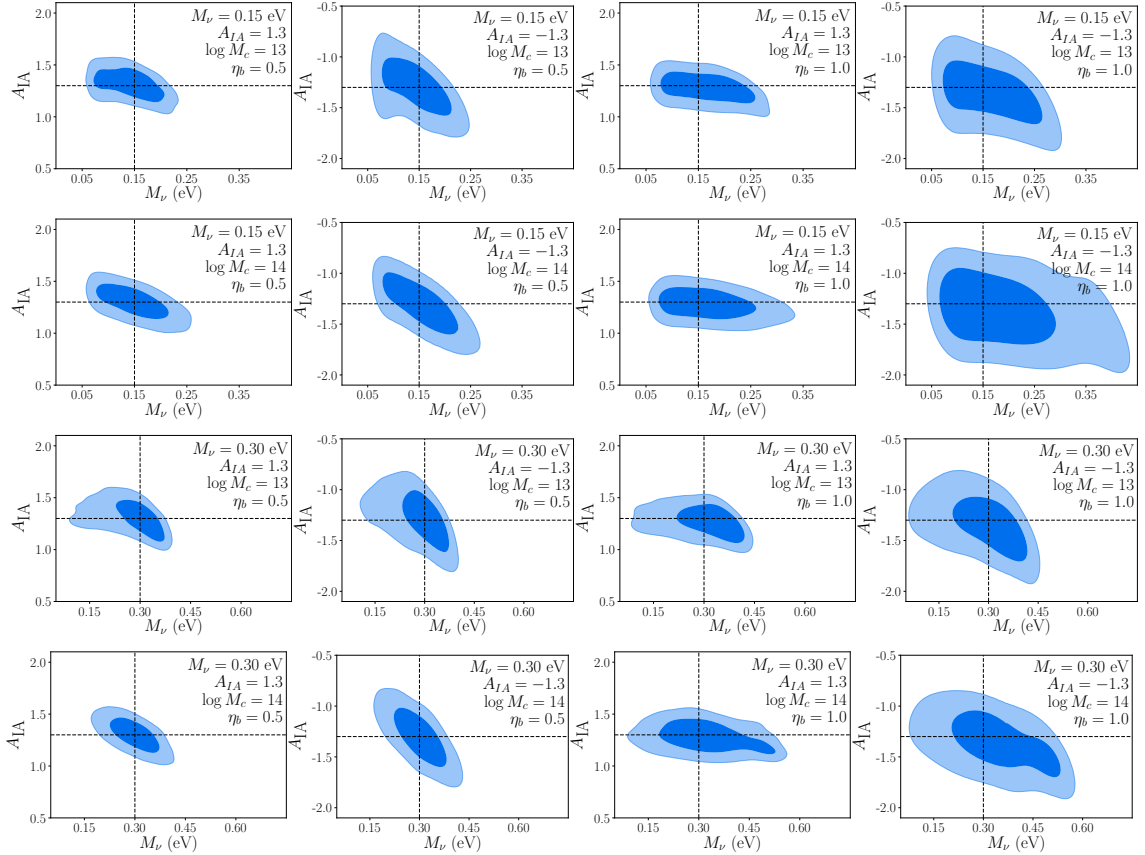


Figure 4.9: This picture shows the degeneracy between neutrino mass and the IA parameter for the 16 different cases analysed in Section 4.4.3. The top plots have $M_\nu = 0.15$ eV, while the bottom ones have $M_\nu = 0.3$ eV; odd columns have $A_{IA} = 1.3$, even columns have $A_{IA} = -1.3$ (the dashed lines help the view in marking the true value). The parameters of the set are written inside each panel. The contour lines shown are 68% and 95% confidence level, while the dashed black lines show the true values for the parameters. It is clearly visible that in some cases the degeneracy between the two parameters is totally absent, but even where is present it will be likely not to bias the measurement on neutrino mass.

4.5 Discussion

In this Chapter we have shown that the effect of baryons on the matter and shear power spectra can be disentangled *at the matter perturbation level* by using a tomographic analysis. To do so, we performed a likelihood analysis for the matter and shear power spectra using the MCMC method.

In our analysis, we accounted for both statistical error, i.e. cosmic variance, as well as the systematic error affecting the theoretical model. Assuming that all theoretical predictions are based on fitting functions or emulators based on numerical N -body simulations, the systematic uncertainty reflects the limitations of this approach in pro-

viding an accurate description of the non-linear matter power spectrum. We adopted the formula by Audren et al. (2013) to describe the scale-dependence of this systematic error, negligible at the largest, linear scales while growing monotonically until reaching a $\sim 2\%$ level at scales of $0.5 h/\text{Mpc}$ at $z = 0$. In addition we follow Baldauf et al. (2016) to account for the correlation such error induces among different wavenumbers.

We investigated directly the effect of baryon feedback, another important source of systematic error, using the BCM by Schneider & Teyssier (2015). Their fitting formula depends on three parameters (M_c , η_b , z_c) with well-established physical meanings. The main focus of our work has been the specific study of their degeneracies with neutrino masses.

As a first test, we explored the possibility that baryonic effects alone could mimic the characteristic suppression of power at small scales due to a non-vanishing neutrino mass. As expected, for both clustering and cosmic shear, we found that growing values of the parameter $\log M_c$, the mass below which halos are emptied from their gas, can reproduce, to some extent, the effect on an increasing neutrino mass. However, the two probes, matter clustering and cosmic shear, interestingly prefer quite different values of this parameter, highlighting the relevance of their combination. In addition, for matter clustering in particular, the recovered value of the $\log M_c$ parameter strongly depends on the maximum wavenumber included in the analysis. These differences can be up to $\sim 9 \sigma$ for $M_\nu = 0.45 \text{ eV}$ for the Euclid-like observational setup we considered, a clear hint that massive neutrinos and baryonic feedback effects will be indeed distinguishable in upcoming surveys.

As a second test, the central analysis carried out in this work, we studied directly the degeneracy between the two effects allowing the parameters of the baryonic feedback model and the neutrino mass to vary simultaneously. We performed this Monte-Carlo analysis for 16 different sets of fiducial parameters in order to properly explore how such degeneracy depends on the assumed baryonic feedback model, a priori unknown. In all cases, we were able to recover the input neutrino mass. In particular, in the matter clustering case, the degeneracy between neutrino mass and feedback parameters is completely absent, while an interesting correlation exists in the plane $\log M_c$ - η_b . For the weak lensing shear power spectrum, the convolution of the matter power spectrum with the lensing kernel smooths-out the different scale-dependent features of the two effects leading to a noticeable degeneracy between the neutrino mass M_ν and the baryon feedback parameter $\log M_c$. Despite this fact, the estimate

of M_ν by cosmic shear is still unbiased, with a maximum difference with respect to the true value of $\sim 0.25 \sigma$.

Finally we considered how these results are affected by the additional systematic represented by the IA effect in weak lensing survey. We employed the linear alignment model by Hirata & Seljak (2004) to introduce the IA effect on the shear spectra. For this part we fixed the z_c parameter to a value of 2: this choice is motivated by the fact that in the previous part of the analysis we were never able to constrain it, as its effects are pretty small on the spectra and scales that we consider. The MCMC analysis was therefore performed with 4 free parameters: $M_\nu, \log M_c, \eta_b, A_{\text{IA}}$. Again, we were able to recover the right input values for what concerns neutrino mass and the A_{IA} parameter. The posterior PDFs and contours for the cases with and without IA are almost identical (see fig. 4.8), while we find a degeneracy pattern in the $M_\nu - A_{\text{IA}}$ plane (fig. 4.9) that is more pronounced when A_{IA} is negative. Also, such parameter seems not to suffer from any degeneracy with the other feedback parameters.

In conclusion, if the BCM is used as a baryon feedback fiducial model, measurements on the neutrino mass from future surveys are likely not be affected by biases due to the degeneracy between neutrino masses and the feedback parameters.

4.6 Future work

It is clear that the work presented in this Chapter is a first step in tackling a quite complex problem that requires much further investigation. A complete analysis would require to allow the whole set of cosmological parameters to vary within some prior, as well as a bias model and redshift-space distortions on the galaxy clustering side. Another interesting step would of course be to explore the possibility to cross-correlate the two observables, like in Euclid Collaboration et al. (2019a), a work that would require a careful investigation of the cross-covariance.

We are currently developing a simple extension to the work just presented (Parimbelli et al. (in prep.)). In this new analysis, we include non-standard DM models such as warm dark matter (WDM) and mixed dark matter (MDM), where part of dark matter is cold and part warm. Moreover, we are planning to incorporate also the effects of isocurvature perturbations, like primordial black holes (PBH). The effect of these non-standard scenarios are estimated by taking the ratio of the power spectra from N -body simulations, specifically run varying the WDM mass and fraction and the isocurvature perturbation parameters, with respect to the Λ CDM counterpart

with the same initial conditions. Moreover, to apply this procedure to weak lensing surveys, we need several snapshots at different redshifts.

Once generated the data (following the procedure exposed in Section 4.3), we will assess the degeneracies among the parameters of the different models, evaluating the impact of using covariance matrices measured from N -body simulations in light-cones (e.g. Schneider et al. (2020)) so that it includes non-Gaussian contributions, the gain in constraints by varying the number of redshift bins and the amplitude and the shape of the systematic uncertainty in the non-linear power spectrum (eq. 4.14).

This Chapter is based on
P. Mertsch, G. Parimbelli, P.F. de Salas, S. Gariazzo, J. Lesgourgues, S. Pastor,
Neutrino clustering in the Milky Way and beyond
JCAP01(2020)015, [arXiv:1910.13388](https://arxiv.org/abs/1910.13388)

5

Neutrino clustering in the Milky Way

5.1 Detecting relic neutrinos with clustering

As already mentioned in previous Chapters, so far we only have indirect indications of the existence of a cosmic neutrino background ($C\nu B$). These mainly come from CMB experiments, that constrained the number of relativistic species in the early Universe (Planck Collaboration et al. (2018)) and found that it was very close to the expected theoretical value $N_{\text{eff}} = 3.045$ (Mangano et al. (2005); de Salas & Pastor (2016); Gariazzo et al. (2019)). The imprint of these relativistic species on the CMB spectrum is compatible with those of free-streaming relics (see e.g. Audren et al. (2015)). A direct probe of the existence of a background of relic neutrinos would of course be a major discovery and a confirmation of what we know about cosmology and neutrinos. In particular, it would rule out scenarios where neutrinos decay at some stage of cosmic time (see e.g. Beacom et al. (2004); Escudero & Fairbairn (2019); Chacko et al. (2020)) or where they are produced with unexpectedly low abundance (e.g. in low reheating scenarios, de Salas et al. (2015)), while another form of dark radiation would contribute to $N_{\text{eff}} \simeq 3$. Interestingly however, the effective sound speed and the anisotropic stress parameters, measured from CMB, are in good agreement with the values that they would have if these species were active neutrinos as described by the Standard Model of particle physics (Planck Collaboration et al. (2016)).

The most promising method for obtaining a direct detection of the $C\nu B$ is to exploit neutrino capture on β -decaying nuclei (Weinberg (1962)), in particular tritium (Cocco et al. (2007)). The detection would consist of a small peak in the electron energy spectrum of tritium due to the capture of relic neutrinos, just above the endpoint of β decay. Despite the experimental challenges represented by the required energy resolution (that must be comparable to the absolute value of the neutrino mass) and the high number of background events, coming from β decay, that must be distinguished from the signal, a project named PTOLEMY (Baracchini et al. (2018)) is nowadays starting to test innovative technology that could lead, for reasonable values of the neutrino masses, to the first direct observation of the $C\nu B$ (Betti et al. (2019)). A possible detection of the $C\nu B$ by PTOLEMY would also offer the opportunity to study for the first time the interactions of non-relativistic neutrinos ¹.

The number of events detected by an experiment scales linearly with the neutrino number density at the Earth's position; therefore it is crucial to have a precise knowledge of how many relic neutrinos are present today here. The standard cosmological model predicts an average number density of 56 cm^{-3} per family and per degree of freedom, making them the second most populous species in the Universe after photons. Relic neutrinos, however, possess a very small energy today compared to their mass (of the orders of 10^{-4} eV and 0.1 eV , respectively). Using the constraints on the mass splittings (e.g. Tanabashi et al. (2018)), we see that at least two of the three species are non-relativistic at present time. Therefore their average number density can be enhanced because of the gravitational attraction of the matter content of the Galaxy, as well as other neighbouring galaxies and galaxy clusters, provided that their masses are large enough to let them cluster at small scales. The calculation of the clustered number density of relic neutrinos was proposed for the first time in Singh & Ma (2003), using a method based on the collisionless Boltzmann equation, and in Ringwald & Wong (2004), using a method called N -one-body simulations. The latter case consists in computing the trajectories of several (N) independent test particles (one-body) in the evolving gravitational potential of the Galaxy, starting from some high redshift until today, and then reconstructing the profile of the neutrino halo according to the final positions of all the test particles. The same method has been adopted later in de Salas et al. (2017); Zhang & Zhang (2018), where an updated treatment of the DM and baryonic content of the Milky Way was considered.

¹Given the values of the mass splittings provided by neutrino oscillation experiments, the second-to-lightest neutrino mass eigenstate must be heavier than at least 8 meV (see e.g. Capozzi et al. (2018); de Salas et al. (2018); Esteban et al. (2019)), while the mean energy of relic neutrinos is of the order of 10^{-4} eV .

In this Chapter, we expose the work published in Mertsch et al. (2020), where we improve the calculation presented in de Salas et al. (2017). For the first time, nearby astrophysical objects, whose presence may play a relevant role in the clustering process, are taken into account in the computation of the gravitational potential: in particular, we consider the contributions carried by the Andromeda galaxy and the Virgo cluster. In order to perform this analysis, we need to relax the assumption of spherical symmetry that has been used in previous works. In Sections 5.2 to 5.4 we discuss the theoretical aspects of the calculation and the practical implementations in our code. The treatment of the matter content of the two galaxies and the Virgo cluster is presented in Section 5.5. This Section is accompanied by Appendix B, which explains how we solved the Poisson equation for the density profiles employed. In the final Section 5.6 we present and discuss our results on the local number density of relic neutrinos.

5.2 Neutrino gravitational clustering

The motion of the test particle is computed in a background where the gravitational potential is time-dependent and the Universe expands. On galaxy scales and at recent times, the behavior of at least the two heaviest neutrino states is well captured by Newton's theory, in which the motion equations can be obtained from the following Lagrangian:

$$\mathcal{L} = a \left(\frac{1}{2} m_\nu v^2 - m_\nu \Phi(\mathbf{x}, t) \right), \quad (5.1)$$

where a is the scale factor, m_ν is the mass of the test neutrino, v its velocity and Φ the gravitational potential. The corresponding Hamiltonian, expressed in Cartesian coordinates x, y, z and the corresponding conjugate momenta p_x, p_y, p_z , is given by:

$$\mathcal{H} = \frac{1}{2am_\nu} (p_x^2 + p_y^2 + p_z^2) + am_\nu \Phi(\mathbf{x}, t). \quad (5.2)$$

From eq. 5.2, the equations of motion are computed. Denoting with a dot the derivative with respect to conformal time $d\tau = dt/a(t)$, we find:

$$p_i = am_\nu \dot{x}_i, \quad \dot{p}_i = -am_\nu \frac{\partial \Phi(\mathbf{x}, t)}{\partial x^i}, \quad \text{with } x_i = x, y, z. \quad (5.3)$$

For a spherically symmetric potential, like the case considered in previous works, the equations of motion simplify significantly due to the conservation of angular momentum and are best expressed in spherical coordinates. A great simplification

can anyway be obtained if one rescales the momenta to eliminate the neutrino mass from the equations:

$$u_i = p_i/m_\nu, \quad (5.4)$$

thus replacing $p_i \rightarrow u_i$ and $m_\nu \rightarrow 1$ in the Hamilton equations above. Solving for u_i will allow to obtain the results for any neutrino mass, provided that the parameter space volume is rescaled appropriately (see Ringwald & Wong (2004); Zhang & Zhang (2018)).

To solve the equations, we need to find the gravitational potential Φ of the Galaxy as well as those of other nearby objects like Andromeda and Virgo. We make use of the Poisson equation to obtain the contribution to the total gravitational potential of each component described by its energy density ρ :

$$\nabla^2\Phi(\mathbf{x}, t) = 4\pi G a^2 \rho, \quad (5.5)$$

where the Laplacian operator is in comoving coordinates.

The linearity of the Poisson equation allows us to solve it separately for the different constituents of the total matter density. When assuming spherical symmetry, the potential depends only on the distance from the center of the halo, r , so that it is possible to have an analytic expression for the derivative of the potential from eq. 5.5:

$$\frac{\partial\Phi}{\partial r}(r, z) = \frac{4\pi G a^2}{r^2} \int_0^r \rho_{\text{halo}}(x, z) x^2 dx = \frac{G}{a r^2} M_{\text{halo}}(r, z). \quad (5.6)$$

When the density is instead not symmetric, the Poisson equation must be solved numerically. The most convenient way is to use Fourier transforms, as we discuss in the Appendix B. Once Φ is known, one must plug its partial derivatives in the Hamilton equations above. We discuss in detail how we perform this calculation in Section 5.5.

The N -one-body simulation method requires the solution of the equations of motion of many test particles with different initial conditions. When dealing with the spherically symmetric case, one has to sample different values for the parameter space of only three quantities: the initial distance from the center of the halo, the initial momentum of the particle, and the initial angle between the initial momentum vector and the radial direction. Moreover, the spherical symmetry of the problem ensures that the motion of each test particle will always be contained in a plane. To calculate the number density profile of the relic neutrino halo (and of its particular value at Earth) one must take into account the final position of all test particles weighted by their initial phase space, see Ringwald & Wong (2004). If one wants to relax the

spherical symmetry assumption, however, the final position will have to be computed as a function of six input variables (three spatial coordinates and three momentum coordinates). Since the number of test particles required to obtain a sufficiently precise result scales exponentially with the dimension of the phase-space, repeating the calculation without spherical symmetry would require unreasonable computational time. Moreover, the majority of the simulated test particles will end up very far from the position of the Earth, and will give very little or no contribution to the local density of relic neutrinos.

Fortunately, a simple way to overcome this problem has been known for many years in the context of cosmic ray propagation, i.e. the back-tracking technique. Instead of forward-tracking the particles starting from homogeneous and isotropic initial conditions at high redshift, it is more efficient to consider only those particles that are at Earth today. This is done by inverting the arrow of time in the equations, and back-tracking the particles from our position today. Afterwards, an initial phase-space volume and an appropriate statistical weight to each trajectory are assigned. The main advantage of this method is that one only needs to sample over the 3-momentum of the neutrinos reaching the Earth today, since their position is fixed by assumption and does not depend on the assumed symmetries of the astrophysical environment. The computational time will thus remain comparable to that of previous works assuming spherical symmetry, while allowing us to introduce a complex distribution of matter with many objects.

The drawback of this approach is that one cannot obtain the shape of the neutrino halo around the Earth, but only the local number density. To estimate the shape of the neutrino profile, multiple simulations at different positions (in three dimensions) are required. More details on the back-tracking method and on our specific implementation are discussed in the next Sections.

5.3 Forward versus backward N -one-body method

The forward-tracking technique has been used in previous works (de Salas et al. (2017)), following Appendix A.3 in Ringwald & Wong (2004) and using the kernel method of Merritt & Tremblay (1994). In this approach, the number density is reconstructed from a set of N particles which are representative of the phase-space interval $(r_a, p_{r,a}, p_{T,a})_i \rightarrow (r_b, p_{r,b}, p_{T,b})_i$. Each trajectory is given a weight w_i ($i = 1, \dots, N$):

$$w_i = \int_{(r_a, p_{r,a}, p_{T,a})_i}^{(r_b, p_{r,b}, p_{T,b})_i} \int_{\theta, \phi, \varphi} f(p) d^3\mathbf{r} d^3\mathbf{p}, \quad (5.7)$$

where $f(p)$ is assumed to be the homogeneous and isotropic Fermi-Dirac distribution (we neglect small linear perturbations far from the Milky Way), while we used $d^3\mathbf{r} = r^2 \sin\theta d\theta d\phi dr$ and $d^3\mathbf{p} = p_T dp_T dp_r d\varphi$, with p_T the transverse momentum and p_r the radial momentum. The final number density at radius r is then given by:

$$n(r) = \sum_{i=1}^N \frac{w_i}{\xi^3} K(r, r_i, \xi), \quad (5.8)$$

where the Gaussian kernel is:

$$K(r, r_i, \xi) = \frac{\xi^2}{(2\pi)^{3/2} r r_i} \exp\left(-\frac{r^2 + r_i^2}{2\xi^2}\right) \sinh\left(\frac{r r_i}{\xi^2}\right) \quad (5.9)$$

smooths the particles around the surface of a sphere in order to get a profile that is spherically symmetric. The parameter ξ is the window width (Merritt & Tremblay (1994)) and its value can be optimized for each step in the simulation.

When switching to the back-tracking method, we take the opposite perspective. We fix the initial spatial coordinates to the Earth's position and draw trajectories from samples of the neutrino momentum today. At that time and location, the phase-space distribution of neutrinos is no longer close to the Fermi-Dirac distribution of the average neutrino background, because of the non-linear dynamics inside the halo. Fortunately, we can make use of Liouville's theorem to compute the statistical weight of each phase-space volume element around the Earth to that at the other end of the trajectory, where neutrinos still obey the average homogeneous and isotropic Fermi-Dirac distribution. Liouville's theorem (Goldstein et al. (2002)) implies the conservation of phase-space density along the solutions of the equations of motions, i.e. yields the Boltzmann equation:

$$\frac{\partial f}{\partial t} + \dot{\mathbf{x}} \cdot \nabla_{\mathbf{x}} f + \dot{\mathbf{p}} \cdot \nabla_{\mathbf{p}} f = 0. \quad (5.10)$$

After tracking a particle from redshift $z = 0$, the Earth position \mathbf{x}_{\oplus} and some arbitrary momentum $\mathbf{p}_j(0)$ back to redshift z_{back} , position $\mathbf{x}_j(z_{\text{back}})$ and momentum $\mathbf{p}_j(z_{\text{back}})$, we can compute the phase-space distribution today and in the right direction by applying:

$$f[\mathbf{x}_{\oplus}, \mathbf{p}_j(0), 0] = f_{\text{back}}[\mathbf{x}_j(z_{\text{back}}), \mathbf{p}_j(z_{\text{back}}), z_{\text{back}}], \quad (5.11)$$

where f_{back} can be identified with the Fermi-Dirac distribution of the average neutrino background. This gives us f today in any direction. The final number density is then obtained by integrating over the observed momentum $\mathbf{p}_j(0)$, without any need for Gaussian smoothing.

We choose $z_{\text{back}} = 4$, after verifying that the value of z_{back} has no significant impact on the final number density, see Section 5.6. Note that this Liouville mapping is routinely used when back-tracking cosmic rays, see e.g. Mertsch (2019).

In both methods, after obtaining the local number density $n_{\nu_i}(\mathbf{x}_{\oplus}, z = 0)$ for each mass eigenstate i , one can compute the clustering factor:

$$f_i \equiv n_{\nu_i}/n_{\nu,0}, \quad (5.12)$$

where $n_{\nu,0} = 112 \text{ cm}^{-3}$ is the cosmological average number density for one family of neutrinos plus anti-neutrinos.

5.4 Computing neutrino clustering with back-tracking

To solve the equations of motion, we use a symplectic ODE solver that also conserves phase-space volume, the `symplectic_rkn_sb3a_mclachlan` solver, that is the symmetric B3A method of the Runge-Kutta-Nyström scheme of sixth order (McLachlan (1995)) from the `odeint` package of the Boost libraries² (Schäling (2014)).

The symplectic solvers of the `odeint` package require the equations of motion to be separable, that is the time-derivatives of the coordinates are functions of the conjugate momenta only and *vice versa*, and autonomous, that is all right-hand sides must not depend on time t explicitly. The latter requirement represents in principle a problem, since both the background expansion and the redshift evolution of the gravitational potential introduce a time-dependence in the Hamiltonian, eq. 5.2. A common fix consists of treating time as an extra variable to be integrated on top of $u_i(t)$ and $x_i(t)$, with a trivial derivative $\dot{t} = 1$ (cfr. e.g. Blanes & Moan (2001)). With this addition, the system is formally autonomous and still separable. Finally, we note that if we substitute time for the new variable s :

$$s(z) = - \int_0^z \frac{dz}{\dot{a}} = - \int_0^z dz \frac{(1+z)}{H(z)}, \quad (5.13)$$

the equations of motion 5.3 take on the even simpler form:

$$\frac{dx_i}{ds} = u_i, \quad \frac{du_i}{ds} = -a^2 \frac{\partial \phi}{\partial x_i}, \quad (5.14)$$

allowing to further speed up the computation.

Although back-tracking dramatically reduces the number of particles to be simulated, we still need a large number of trajectories, obtained by solving eqs. 5.14 for several

²<http://www.boost.org>

initial conditions $u_i(z = 0)$. This requirement is most efficiently fulfilled in a “Single Instruction, Multiple Data” (SIMD) architecture, modern graphic processing units (GPUs) being an example. We use the `CUDA` framework³ via the `Thrust` library⁴ which can be interfaced with `odeint`’s solvers. In order to increase speed, we pre-compute the baryonic contributions to the gravitational potential (see next Section) at redshift $z = 0$ on a grid in cylindrical coordinates R and z , load them as textures onto the GPU, bi-linearly interpolate them between grid points, and finally scale the results up to higher redshifts z . For the results below, we isotropically sample the arrival directions of neutrinos (20 points for polar angle, 20 points for azimuth) and logarithmically sampled in momentum (100 points over 3 decades), which leads to a grid of 4×10^4 velocities. We have also checked that this is sufficient for getting well-converged clustering factors even in the non-axisymmetric case (Milky Way DM plus baryons plus Andromeda and Virgo). All the computations were performed on an Nvidia Quadro P6000. Depending on the number of different contributions to the gravitational potential, back-tracking the 4×10^4 particles from redshift $z = 0$ to $z = 4$ required between 120 and 500 minutes.

5.5 Density profiles and gravitational potential

In this Section we describe how we implement the gravitational potential of the objects that we include in our analysis. For the Milky Way, we consider a spherical DM halo plus a number of baryonic components, which follow axial symmetry. Beyond the Milky Way, we consider spherical DM halos for the Andromeda galaxy and the Virgo Cluster, which are the largest objects relatively close to Earth that can have an impact on the local density of relic neutrinos. Finally, we report technical details on the discretization of the grid that we adopt in the numerical calculation for the interpolation of the derivatives.

³<http://developer.nvidia.com/cuda-zone>

⁴<http://thrust.github.io>

5.5.1 The Milky Way

For the DM halo of the Milky Way, we consider two distinct cases: a NFW (Navarro et al. (1996)) and an Einasto (Einasto (1965)) profile, which read, respectively:

$$\rho_{\text{NFW}}(r) = \frac{\rho_0}{\frac{r}{R_s} \left(1 + \frac{r}{R_s}\right)^2} \quad \text{for } r < R_{\text{vir}}, \quad (5.15)$$

$$\rho_{\text{Ein}}(r) = \rho_0 \exp[-(r/R_s)^\alpha], \quad (5.16)$$

where ρ_0 is the normalization, R_s is the scale radius, R_{vir} is the virial radius of the NFW profile (related to R_s through the concentration parameter $c = R_{\text{vir}}/R_s$), and α is an additional parameter for the Einasto profile that controls the change in the slope of the density.

As far as baryons are concerned, we follow the treatment of Misiriotis et al. (2006) and adopt five separate components: stars, warm and cold dust, atomic HI and molecular H₂ gas. The density of stars is parametrized through a disk plus a bulge. The bulge of the Milky Way has been shown to have a triaxial shape (Portail et al. (2015)). However, since we are mainly interested in the neutrino clustering at the Earth position, which is located at distances (8.2 ± 0.1 kpc, Bland-Hawthorn & Gerhard (2016)) significantly larger than the bulge size, we can safely approximate it as a sphere. In particular, again following Misiriotis et al. (2006), we assume for the bulge profile a Sersic law with index $n = 4$ (i.e. a de Vaucouleurs profile):

$$\rho_{\text{DeVauc}}(r) = \rho_0 \exp \left[-A \left(\frac{r}{R_b} \right)^{1/4} \right] \left(\frac{r}{R_b} \right)^{-7/8}, \quad (5.17)$$

where $A = 2n - 1/3 \approx 7.67$ and we take $R_b = 0.74$ kpc.

The other baryonic components are assumed to be distributed according to a double exponential disk profile:

$$\rho_{\text{exp}}(R, z) = \rho_0 e^{-R/R_s} e^{-|z|/z_s}. \quad (5.18)$$

The present day values of the parameters of the different profiles are obtained as follows. The parameters related to the DM component of the Milky Way at $z = 0$ are obtained by fitting the DM contribution to the rotation curve data as reported in Pato & Iocco (2015), following the same procedure already adopted in de Salas et al. (2017)⁵. Better estimates of the Galactic rotation curve are nowadays accessible

⁵Notice that to switch from our parametrization of the Einasto profile in eq. 5.16 to the one used by de Salas et al. (2017), one has to substitute $\rho_0 \rightarrow \rho_0 \exp(-2/\alpha)$ and $R_s \rightarrow R_s (2/\alpha)^{1/\alpha}$.

	NFW	Einasto
$M_{\text{vir}} [M_{\odot}]$	2.03×10^{12}	1.17×10^{12}
$\rho_0 [M_{\odot}/\text{kpc}^3]$	1.06×10^7	2.70×10^8
$R_s [\text{kpc}]$	19.9	0.737
$R_{\text{vir}} [\text{kpc}]$	333.5	X
α	X	0.45

Table 5.1: DM density parameters for the Milky Way at $z = 0$, obtained by fitting the data from Pato & Iocco (2015), following the same procedure as in de Salas et al. (2017).

thanks to the second data release of the ESA/Gaia mission (Brown et al. (2018)) (see e.g. de Salas et al. (2019) for an analysis of the DM contribution to the rotation curve data presented in Eilers et al. (2019)). However, given the limited radial extent of the data, instead of fixing the total DM mass to the values predicted either in Pato & Iocco (2015) or de Salas et al. (2019), we use an estimate based on orbiting Milky Way satellites up to ~ 300 kpc from the center of the Galaxy (Watkins et al. (2010)). Concerning the baryon components, we take the warm dust, cold dust, H_2 and HI profile parameters from Misiriotis et al. (2006), as well as the scale parameters of the bulge and the disk. For the central density of the bulge we use the value given by Bland-Hawthorn & Gerhard (2016). They also provide an estimate for the total stellar mass in the Galaxy ($5 \times 10^{10} M_{\odot}$). From this number we can derive the total mass of the stellar disk by subtracting the total mass of the bulge. The parameter values that we adopt are listed in Tables 5.1 and 5.2.

Regarding the HI density profile, observations (e.g. Kalberla et al. (2005); McMillan (2017)) have shown that the distribution of neutral hydrogen in the outskirts of the Galaxy follows an exponential profile, as we assume in this work; conversely, the central 2.75 kpc (McMillan (2017)) seem to be devoid of it. This feature would in principle prevent us from using an analytical formula for our potential. However, we found that neglecting the central hole in the hydrogen distribution, i.e. extrapolating the exponential profile until the origin of the coordinates, would just cause an increase of the total HI mass of 1%, which is, in turn, an overestimate of 0.01% on the total mass of the Milky Way. We then safely ignore such a feature in the HI profile, and we consider it to be also a double exponential disk, following eq. 5.18.

In order to compute the clustering factor today, we also need the time evolution of the density profiles. As we check *a posteriori* in Section 5.6, most of the clustering happens at small redshifts, so there is no need to compute the density profiles very precisely at all times. The evolution in redshift of the density profiles is accounted for

	$\rho_0 [M_\odot/\text{kpc}^3]$	$R_s [\text{kpc}]$	$z_s [\text{kpc}]$	$M_{\text{tot}} [M_\odot]$
Bulge	1.79×10^{12}	0.74	X	1.55×10^{10}
Disk	3.40×10^9	2.4	0.14	3.45×10^{10}
Warm dust	1.80×10^4	3.3	0.09	2.22×10^5
Cold dust	2.23×10^6	5.0	0.1	7.01×10^7
H ₂	2.00×10^8	2.57	0.08	1.33×10^9
HI	7.90×10^6	18.24	0.52	1.72×10^{10}

Table 5.2: Density profile parameters for the baryonic components at $z = 0$. We also provide the total mass for each component. All the components have a profile described by eq. 5.18, except for the bulge, which follows a de Vaucouleurs profile (eq. 5.17). The scale radii and heights are taken from Misiriotis et al. (2006), as specified in the main text. The redshift evolution of the total mass is found following the N -body simulation results of Marinacci et al. (2014), while we assume that R_s and z_s do not evolve in time.

as follows. We assume the total virial mass of the DM halo to be constant in redshift, while the concentration parameter changes according to Dutton & Macciò (2014):

$$\log \beta c_{\text{vir}}(z) = a(z) + b(z) \log \left(\frac{M_{\text{vir}}}{10^{12} h^{-1} M_\odot} \right), \quad (5.19)$$

where β is a parameter (assumed constant in time) which denotes the offset of the Milky Way concentration with respect to the average one. The functions $a(z)$ and $b(z)$ are different for the NFW and Einasto profiles. For the NFW they correspond to $a(z) = 0.537 + (1.025 - 0.537) \exp[-0.718 z^{1.08}]$, $b(z) = -0.097 + 0.024 z$, while for the Einasto profile $a(z) = 0.459 + (0.977 - 0.459) \exp[-0.490 z^{1.303}]$, $b(z) = -0.130 + 0.029 z$.

The time evolution of the virial radius is obtained from

$$M_{\text{vir}} = 4\pi a^3 \int_0^{R_{\text{vir}}(z)} \rho(x, z) x^2 dx, \quad (5.20)$$

$$R_{\text{vir}}(z) = \left(\frac{3M_{\text{vir}}}{4\pi \Delta_{\text{vir}}(z) \rho_{\text{crit}}(z)} \right)^{1/3}, \quad (5.21)$$

where $\rho_{\text{crit}} = 3H_0^2/(8\pi G)$ is the critical density of the Universe and $\Delta_{\text{vir}}(z) = 18\pi^2 + 82[\Omega_m(z) - 1] - 39[\Omega_m(z) - 1]^2$ (Bryan & Norman (1998)) for the NFW. For the Einasto profile it is instead fixed to $\Delta_{\text{vir}} = 200$, since this was the approach followed by Dutton & Macciò (2014) to obtain the numerical values of the corresponding $a(z)$ and $b(z)$ equations. Combining eqs. 5.19, 5.20 and 5.21 allows us to find the scale radius as a function of redshift. The cosmology used in this work has $h = 0.6766$ and $\Omega_m = 0.3111$ according to the Planck (TT,TE,EE+lowE+lensing+BAO) best-fit model (Planck Collaboration et al. (2018)).

On the other hand, reconstructing the evolution of scale radii of baryon components is a hard task. For simplicity, we assume that the radii are constant in time, while the central densities change according to the results of N -body simulations obtained by Marinacci et al. (2014). In particular we assume that the fraction of each component with respect to the total baryon mass is conserved.

The equations of motion need the derivatives of the gravitational potentials. A detailed description of the method we employ to compute the potentials and their derivatives for all the matter components of the Galaxy can be found in Appendix B. The derivative of the total Milky Way potential, with respect to a given axis x_i and split in all its contributions from the different components, is given by:

$$\begin{aligned}
\frac{\partial \Phi_{\text{tot}}}{\partial x_i}(\mathbf{x}) &= \frac{\partial \Phi_{\text{DM}}}{\partial x_i}(r, \rho_{\text{DM}}, R_{\text{DM}}, R_{\text{vir,DM}}) && \text{dark matter (eqs. 5.15/5.16)} \\
&+ \frac{\partial \Phi_{\text{b}}}{\partial x_i}(r, \rho_{\text{b}}, R_{\text{b}}) && \text{stellar bulge (eq. 5.17)} \\
&+ \frac{\partial \Phi_{\text{d}}}{\partial x_i}(R, z, \rho_{\text{d}}, R_{\text{d}}, z_{\text{d}}) && \text{stellar disk (eq. 5.18)} \\
&+ \frac{\partial \Phi_{\text{w}}}{\partial x_i}(R, z, \rho_{\text{w}}, R_{\text{w}}, z_{\text{w}}) && \text{warm dust (eq. 5.18)} \\
&+ \frac{\partial \Phi_{\text{c}}}{\partial x_i}(R, z, \rho_{\text{c}}, R_{\text{c}}, z_{\text{c}}) && \text{cold dust (eq. 5.18)} \\
&+ \frac{\partial \Phi_{\text{H}_2}}{\partial x_i}(R, z, \rho_{\text{H}_2}, R_{\text{H}_2}, z_{\text{H}_2}) && \text{H}_2 \text{ (eq. 5.18)} \\
&+ \frac{\partial \Phi_{\text{HI}}}{\partial x_i}(R, z, \rho_{\text{HI}}, R_{\text{HI}}, z_{\text{HI}}) && \text{HI (eq. 5.18)}. \tag{5.22}
\end{aligned}$$

5.5.2 Other objects: Virgo & Andromeda

We also incorporate in our system nearby objects whose presence may have a significant impact on the clustering factor of neutrinos in the Milky Way. Results from N -body simulations in Villaescusa-Navarro et al. (2011) (see their Figure 2) show that the neutrino halo of Virgo-like clusters may extend up to distances comparable to the one between the Milky Way and the Virgo cluster itself. The neutrino overdensity caused by the Virgo halo at the Milky Way distance is expected to be of a few percent, even for the minimum masses allowed by neutrino oscillations ($\Sigma m_\nu = 60$ meV). At the location of the Earth, we therefore expect the Virgo effect to be almost of the same order of magnitude as the Milky Way effect.

We assume for the Virgo Cluster a NFW profile for the DM halo, with a mass of $6.9 \times 10^{14} M_\odot$ (Fouque et al. (2001)). Its distance and position in the sky in Galactic

coordinates are taken from the NASA Extragalactic Database (NED)⁶:

$$\begin{cases} D_{\text{Virgo}} & \approx 16.5 (\pm 2.0) \text{ Mpc} \\ \text{latitude}_{\text{Virgo}} & = 74.44^\circ \\ \text{longitude}_{\text{Virgo}} & = 283.81^\circ \end{cases} \Rightarrow \begin{cases} x_{\text{Virgo}} = 1.056 \text{ Mpc} \\ y_{\text{Virgo}} = -4.299 \text{ Mpc} \\ z_{\text{Virgo}} = 15.895 \text{ Mpc} \end{cases} . \quad (5.23)$$

We also include the Andromeda galaxy, much lighter than Virgo (by a factor ~ 500) but much closer (by a factor ~ 20) to the Milky Way. Also for Andromeda we consider a NFW profile and we neglect its baryon content. The galactic latitude and longitude of Andromeda are taken from the Vizier database⁷, while its distance, mass and density profile parameters are given by Kafle et al. (2018), leading to:

$$\begin{cases} D_{\text{And}} & \approx 0.784 (\pm 0.120) \text{ Mpc} \\ \text{latitude}_{\text{And}} & = -21.573311^\circ \\ \text{longitude}_{\text{And}} & = 121.174322^\circ \end{cases} \Rightarrow \begin{cases} x_{\text{And}} = -0.377 \text{ Mpc} \\ y_{\text{And}} = 0.623 \text{ Mpc} \\ z_{\text{And}} = -0.288 \text{ Mpc} \end{cases} . \quad (5.24)$$

The density parameters at $z = 0$ are listed in Table 5.3 for both Andromeda and the Virgo cluster. The redshift-evolution of the density profile parameters for these objects is governed by the same equations as for the Milky Way halo (see Section 5.5.1).

The complete geometrical configuration of our system, with the Milky Way, Andromeda and the Virgo cluster, is shown in Figure 5.1. The size of the dots corresponds to the virial radius of the NFW halos. We can appreciate the difference in size and distance for Andromeda and Virgo. However, as N -body simulations show (Villaescusa-Navarro et al. (2011)), the neutrino halo of each object is always much more extended than the one of DM, due to the high neutrino thermal velocities. Thus, despite its high distance from the Milky Way, we expect that Virgo will also contribute to the neutrino overdensity at the Earth location.

5.5.3 Gravitational potential grid

Solving the Hamiltonian equations of motion requires the derivative of the gravitational potentials listed in eq. 5.22. For computational time reasons, it is convenient to provide these derivatives explicitly to the code in order to benefit from the use of textures in the GPU calculations.

⁶<https://ned.ipac.caltech.edu/>

⁷<http://vizier.u-strasbg.fr/viz-bin/VizieR-S?NGC%20224>

	Virgo cluster	Andromeda
$M_{\text{vir}} [M_{\odot}]$	6.9×10^{14}	8.00×10^{11}
$\rho_0 [M_{\odot}/\text{kpc}^3]$	8.08×10^5	3.89×10^6
$R_s [\text{kpc}]$	399.1	21.8
$R_{\text{vir}} [\text{kpc}]$	2328.8	244.7

Table 5.3: DM density parameters for the Andromeda galaxy and the Virgo cluster at $z = 0$. The parameters for Virgo are taken from Fouque et al. (2001), and for Andromeda from Kafle et al. (2018).

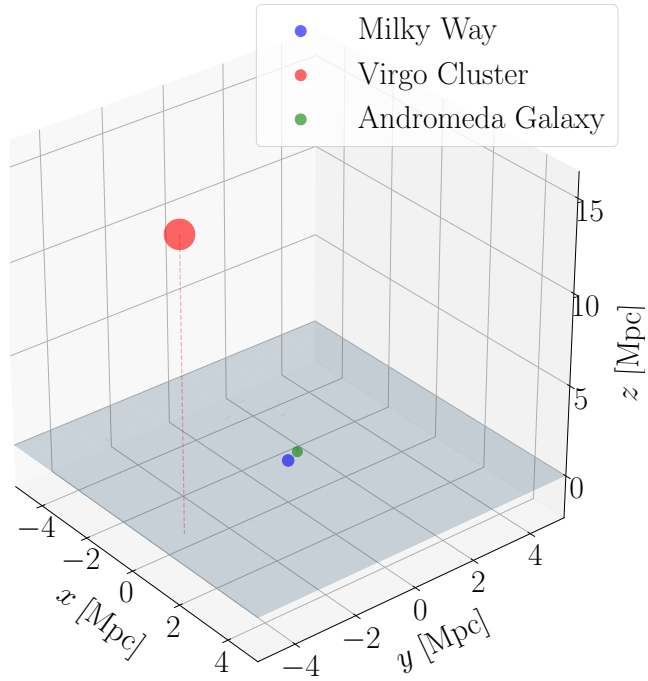


Figure 5.1: Relative position of the Milky Way, Andromeda Galaxy and the Virgo Cluster. The size of the dots matches the virial radius of the object. The grey shaded plane represents the plane of the Milky Way.

First of all, we safely assume that outside the virial radius of each DM halo, the potential is just given by Kepler’s formula. In this way we do not have to build very broad grids.

Inside the halos, the choice of the grid size depends on how much we want to characterize the halo itself. For us, the most interesting structure is of course the Milky Way. We want our grid to be much finer than the distance between the Earth and the Galactic center (≈ 8 kpc) in order to follow very accurately the trajectories of neutrinos in the regions surrounding the Earth. At the same time, the grid must extend at least to the maximum value (across the redshift range considered in our simulation) of the virial radius of the Milky Way, which is approximately 450 kpc. To fulfill all these requirements, we opt for 0.1 kpc-wide radius bins for the DM halo. Likewise, for the Andromeda galaxy we also use a binning of 0.1 kpc with an extension of 350 kpc, i.e. ~ 50 kpc more than the maximum virial radius at $z = 4$. On the other hand, despite the fact that the Virgo cluster is much more extended than the Milky Way (its virial radius reaches up to 3 Mpc), we do not need a very narrow binning there, since we are not interested in what happens on very small scales. We use a 1 kpc bin size in radius.

After computing these derivatives in spherical coordinates as a function of the radius, we get the derivatives in Cartesian coordinates by means of the chain rule (see Appendix B for more details).

The baryonic components only have cylindrical symmetry, leading to a more subtle situation. Their 2-D grid in R and z must extend at least up to a point where we can safely approximate the potential generated by a disk-like profile with the one generated by a sphere of the same mass. This depends of course on the ratio of scale radius and scale height: the larger the ratio, the further the grid needs to extend before we approach a Keplerian law. Looking at Table 5.2, we notice that in the Milky Way the maximum ratio between the scale radius and the height of the disk is 50, for cold dust. For this configuration, we compute the potential of an exponential profile as well as its Keplerian counterpart (i.e. a point-like object with the same mass) to check where the two potentials start to coincide. In Figure 5.2, we plot the iso-potential contours for these two configurations: at distances of $R \approx 25R_s$, the red and black isocontours, which refer to the cylindrical and spherical case respectively, differ approximately by just 1%. We therefore extend the grid on which we calculate the derivative of the potential to at least 30 times the largest scale radius among all the components. All in all, for the Milky Way, we compute the derivative of the potential up to ≈ 550 kpc from the Galactic center.

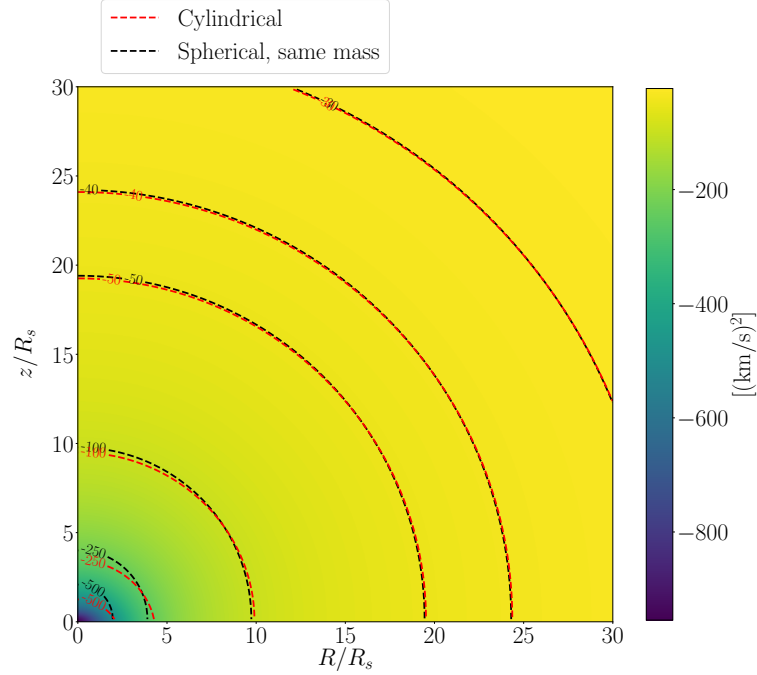


Figure 5.2: The colormap shows the potential generated by an exponential disk. The red lines denote isocontours for this potential, while the black ones denote the isocontours for the potential generated by a point-like source with the same mass. At $R/R_s \sim z/R_s \sim 25$ the difference between the spherical and cylindrical potentials is smaller than 1%.

The bin sizes must be chosen carefully, especially along the direction z orthogonal to the baryonic disks. For DM, a bin size of 0.1 kpc would be sufficient, but some of the baryonic components have a disk much thinner than that. We therefore opt for a logarithmic grid in z that spans from 10^{-4} to 550 kpc.

All the above choices are summarized in Table 5.4.

	Milky Way	Andromeda	Virgo
r / R	0.1 – 550 kpc	0.1 – 350 kpc	1 – 3000 kpc
$\Delta r / \Delta R$	0.1 kpc	0.1 kpc	1 kpc
z	10^{-4} – 550 kpc		
$\Delta \log_{10}(z)$	0.0337		

Table 5.4: Characteristics of the grid used for the derivative of the contributions to the potential.

5.6 Results

Figure 5.3 shows the clustering factor, i.e. $n_{\nu_i}/n_{\nu,0}$, computed at the Earth’s position for a given neutrino mass eigenstate as a function of m_{ν_i} , both for the case with an NFW distribution and an Einasto distribution for the DM in the Milky Way. We recall that for Virgo and Andromeda, we only consider DM with an NFW profile. We also compare our results with those of previous studies (Ringwald & Wong (2004); de Salas et al. (2017); Zhang & Zhang (2018)), denoted by squares, triangles and rhombuses.

As expected, regardless of our assumptions on the gravitational potential, the clustering factor increases with the neutrino mass. The impact of baryons in our Galaxy is found to be significant for any value of the mass. In contrast, adding the Virgo contribution leads to an enhancement at small neutrino mass, but can actually lead to less clustering at masses larger than approximately 200 meV. This phenomenon can be explained in both forward- and back-tracking scenarios. In the forward-tracking picture, this is easily explained as some of the neutrinos that would have clustered at the Earth’s position in the absence of Virgo are now clustering in the Virgo potential well instead. In the back-tracking picture, a fraction of the particles sent out from the Earth that would have lost energy by leaving the Milky Way’s gravitational potential have fallen into Virgo’s gravitational potential instead. This leads to an increase in momentum of these particles with increasing redshift. Thus the phase-space density is sampled only at large momenta for these particles (instead of all momenta), and the clustering is overall less pronounced.

We can also see in Figure 5.3 that both the effect of Andromeda and the difference between an NFW and an Einasto profile for the Milky Way’s DM are negligible. Assuming $m_\nu = 50$ meV, the overdensity is $(n_\nu/n_{\nu,0} - 1) \simeq 7\%$, 9% and 12% for the cases with DM only, DM + baryons and DM + baryons + Virgo.

Our results are overall consistent with previous studies. Our clustering factor is significantly larger than that inferred by Ringwald & Wong (2004), but with a similar dependence on the neutrino mass. The larger clustering is likely due to our updated DM profile parameters. The results are even closer to those of de Salas et al. (2017); Zhang & Zhang (2018), although slightly below in the NFW case (due to different assumptions on the NFW parameters), both for the DM only case and for the case with baryonic contributions.

Finally, we test the convergence of our results as a function of the redshift z_{back} . In the back-tracking approach, z_{back} controls the time at which we stop integrating the

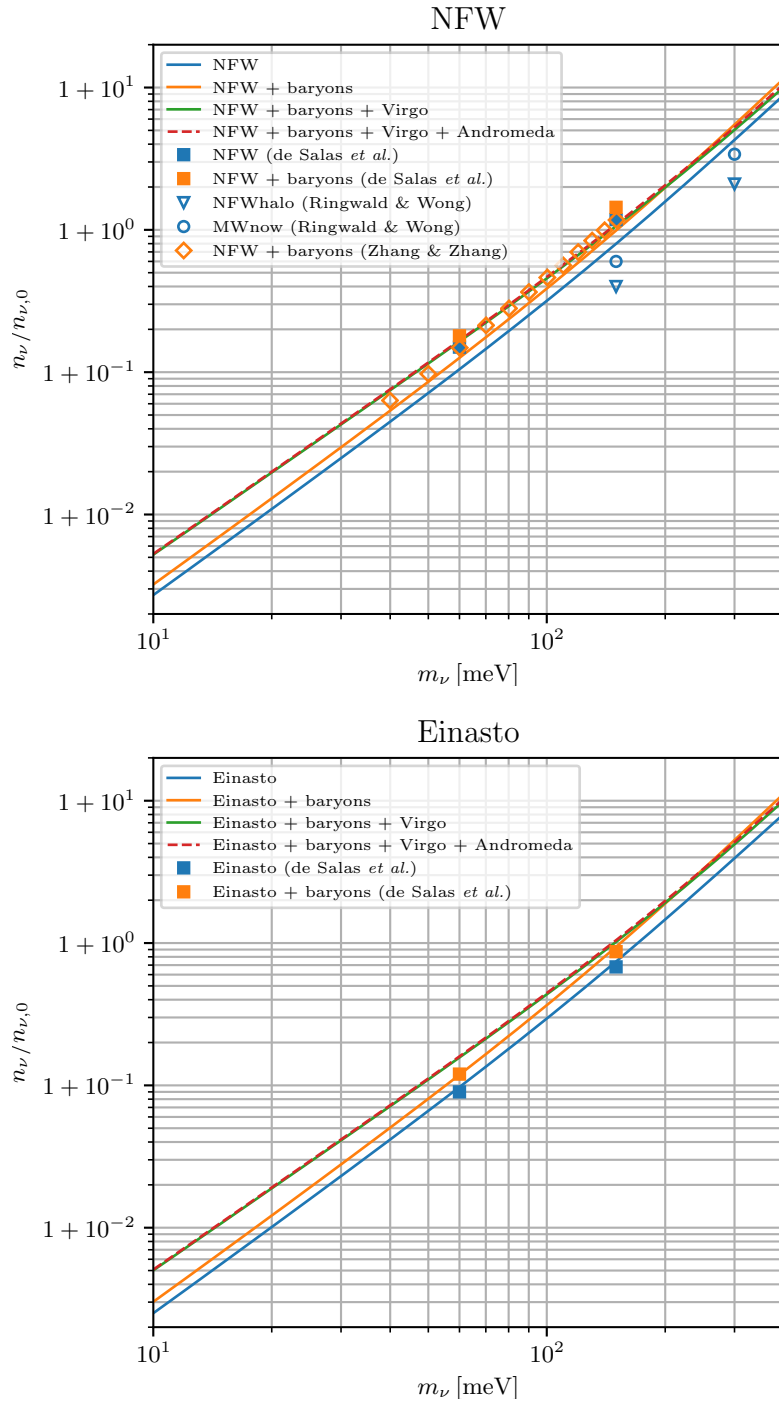


Figure 5.3: For each neutrino mass state, we plot the ratio $n_\nu/n_{\nu,0}$ at the Earth’s position as a function of the neutrino mass m_ν . We consider contributions to the gravitational potential from the Galactic DM halo (*top panel*: NFW profile, *bottom panel*: Einasto profile), from baryons in the Galaxy, from the Virgo cluster and from the Andromeda galaxy. We also compare with earlier studies (Ringwald & Wong (2004); de Salas *et al.* (2017); Zhang & Zhang (2018)).

neutrino trajectories – while with forward-tracking it would be the *initial* redshift. In both cases, z_{back} represents the time at which we assume a perfect homogeneous and isotropic Fermi-Dirac distribution for the neutrinos. Figure 5.4 shows the reconstructed value of the clustering factor today when z_{back} is floated – rather than being fixed to our baseline case of averaging $z_{\text{back}} \in [3.5, 4]$.

Figure 5.4 shows a strong variation of the clustering factor when z_{back} is in the range from 0 to 0.5, and a gradual convergence towards an asymptotic value for $z_{\text{back}} > 1$. This shows that most of the neutrino clustering takes place at very small redshift. This check is crucial for at least two reasons. First, it shows that the simplicity of our assumptions concerning the evolution of the DM and baryon density profiles at very high redshift does not affect the results significantly: what matters most is to capture the gravitational potential behavior at $z < 0.5$. Second, this convergence test proves that it is sufficient to assume a perfect homogeneous and isotropic Fermi-Dirac distribution for the neutrinos at z_{back} . Indeed, in principle, one should either push the simulation up to $z_{\text{back}} \rightarrow \infty$, or introduce some small phase-space density fluctuations $\delta f(t_{\text{back}}, \mathbf{x}, \mathbf{p})$ accounting for the amount of clustering that took place between the onset of structure formation and z_{back} . If gravitational potential wells at z_{back} were so large that such fluctuations should be taken into account, neglecting them would introduce a bias in the results that would depend on z_{back} . A non-observation of this dependence shows that the clustering between $z \rightarrow \infty$ and z_{back} can be safely neglected.

As one can see from Figure 5.4, for masses below 100 meV, the convergence of the clustering factor is achieved for $z_{\text{back}} > 2$. Instead, for growing neutrino mass, we note that the solution is slightly less converged, due to the existence of trapped orbits for some of the neutrinos around the Milky Way and Virgo halos, which originate well before the initial redshift we choose⁸. In these cases, the value of z_{back} can have an impact on the results, but the magnitude of the oscillations seen in Figure 5.4 shows that this is at most a 10% effect for $n_\nu/n_{\nu,0} - 1$. Since this effect is smaller than the uncertainties coming from the assumptions on the DM and baryon composition of the Galaxy, and that neutrino masses above 100 meV are disfavored by cosmological measurements, we simply present the results (Figure 5.3) at high masses as an average of the values $n_\nu/n_{\nu,0}$ obtained considering $z_{\text{back}} \in [3.5, 4]$.

⁸In the forward picture, it is easier to understand the phenomenon: since neutrinos are already clustering around the Milky Way and the Virgo cluster at $z = 4$, their momentum distribution function is not the homogeneous and isotropic Fermi-Dirac at such redshifts. In the backward case, one has to think that the neutrinos cannot escape the Milky Way and the Virgo cluster until higher redshifts.

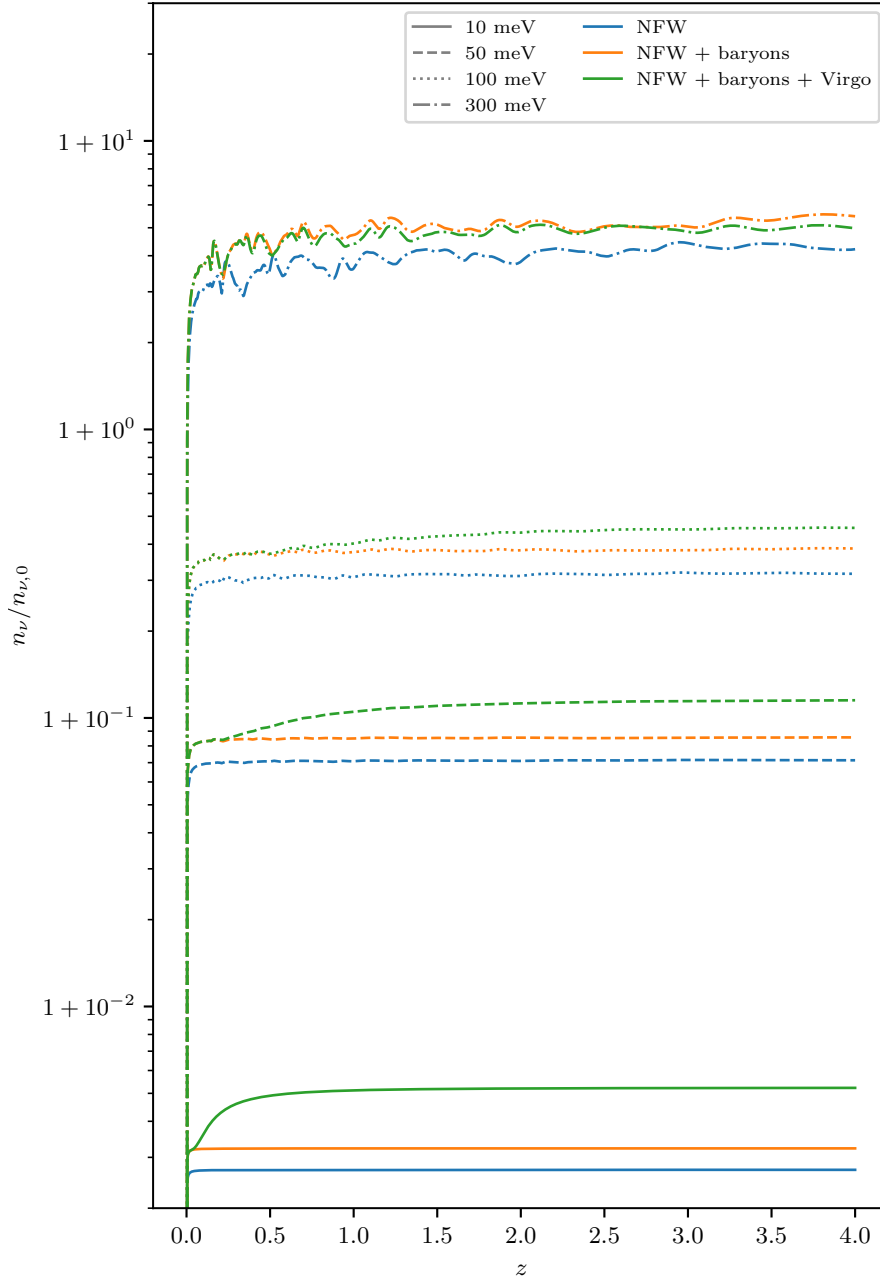


Figure 5.4: Clustering factor as a function of the earliest redshift z_{back} at which neutrino trajectories are integrated, for different values of the neutrino mass and different astrophysical configurations.

We report also our results for a few representative values of neutrino masses. The two cases $m_\nu = 10$ meV and 50 meV are particularly interesting, because they stand for plausible values of the mass of the second and third neutrino mass eigenstates in the minimal normal hierarchy scenario (that is, when the lightest neutrino is massless and the mass ordering is normal). Additionally, in the minimal inverted hierarchy scenario (when the lightest neutrino is massless and the mass ordering is inverted), the two heaviest neutrinos have a mass close to $m_\nu = 50$ meV. We also quote our results for a mass of 300 meV, in tension with recent cosmological bounds, but still well below the strong and model-independent limit currently set by KATRIN (Aker et al. (2019)).

For such masses of 10 meV, 50 meV, 100 meV and 300 meV, we obtain that the local number density of the relic neutrinos is respectively enhanced by 0.53%, 12%, 50% and 500%. with respect to the cosmological average. We therefore find that the local number density of relic neutrinos is 56.8 cm^{-3} , 63.4 cm^{-3} , 85 cm^{-3} and 300 cm^{-3} for these cases.

The clustering factor $f_{c,i}$ of each neutrino species enters linearly in the computation of the detection rate of neutrinos in future experiments like PTOLEMY, namely:

$$\Gamma_{\text{C}\nu\text{B}} = N_T \bar{\sigma} v_\nu \sum_{i=1}^{N_\nu} |U_{ei}|^2 n_{0,i} f_{c,i} \quad (5.25)$$

where N_T is the number of tritium atoms in the source, $\bar{\sigma}$ is the average cross section of neutrino capture, v_ν is the neutrino velocity, N_ν the total number of neutrino mass eigenstates, $|U_{ei}|^2$ is the mixing of the i -th neutrino mass eigenstate with the electron flavor eigenstate, $n_{0,i} = 112 \text{ cm}^{-3}$. This rate is expected to be around $\sim 4 \text{ yr}^{-1}$ when assuming Dirac neutrinos and 100 g of tritium (Cocco et al. (2007)). Using this value, together with the studies on the energy resolution Δ of PTOLEMY by Betti et al. (2019), one can conclude that a $2\text{-}\sigma$ detection of a non-vanishing neutrino mass will be possible only if $\Delta \lesssim 0.86 \frac{m_\nu}{\text{meV}} - 14 \text{ meV}$.

6

Conclusions

*A conclusion is the place where you
got tired thinking*

Martin Fischer

6.1 Summary

In the last decade the Λ CDM paradigm has settled as the standard model for cosmology. It has been extensively tested through several different observables probing the expansion history of the Universe (BAOs, SNIa) and the growth of density fluctuations through cosmic ages (CMB spectra, galaxy clustering, cosmic shear...). Although there are relevant tensions among parameters estimated with different observables (like for H_0 – Guo et al. (2019); Desmond et al. (2019); Bernal et al. (2016); Knox & Millea (2020) – or S_8 tensions – Efstathiou & Lemos (2018); Leauthaud et al. (2017)), so far no significant deviations have been detected when minimally extending the 6-dimensional parameter space by e.g. allowing a non-flat geometry or introducing a phenomenological model for the parameter of state of dark energy. However, we know that the Λ CDM model as it is cannot be completely consistent with particle physics experiments, since in its original form it does not allow neutrinos to have mass.

Neutrinos were proven to be massive in a series of experiments aimed at detecting flavor oscillations. Unfortunately, the matrix elements ruling these oscillations do

not depend on the absolute values of the single masses – $m_{\nu,i}$ – but rather on the difference of their squares, thus making it impossible to constrain the total mass scale – M_ν .

On the other hand, cosmology has the power to do so. Neutrinos, in fact, due to their high thermal velocities, substantially suppress the growth of matter density perturbations already at linear order. This leads to a scale-dependent growth factor and to a modification of the matter distribution which affects all scales larger than k_{nr} (eq. 2.23). The impact of neutrinos on the CMB spectra and on the large-scale structure observables has led to an upper limit for the sum of neutrino masses of $M_\nu < 0.12$ eV at 95 % confidence level (Palanque-Delabrouille et al. (2015a)).

Upcoming surveys (e.g. Euclid, LSST, SKA, DESI) will likely be the first to measure the absolute mass scale of neutrinos by exploiting several observables of large-scale structure, such as galaxy clustering, cosmic shear, BAOs, HI intensity mapping and Ly- α forest. Sprenger et al. (2019) discovered that combining Euclid galaxy clustering (power spectrum only), cosmic shear with SKA intensity mapping and Planck the uncertainty on M_ν could get as low as 18 meV. On the other hand, Chudaykin & Ivanov (2019) found that, with a complete analysis of galaxy clustering including 1-loop power spectrum and tree-level bispectrum in redshift space, Euclid-like surveys will measure the sum of neutrino masses with a standard deviation of 28 meV (i.e. at least a $2\text{-}\sigma$ detection), value that decreases to 13 meV when the survey is combined with Planck and to 11 meV when reducing the theoretical uncertainty on the bispectrum. All the mentioned results were obtained with the MCMC technique. The results for LSST combined with Planck yield instead a neutrino mass constraint of $\sigma_{M_\nu} \approx 0.1$ eV (Zhan & Tyson (2018)). In order not to deteriorate these forecasts, a detailed study on the possible degeneracies of the effects of neutrino mass with other physical phenomena and nuisances, together with a characterization of the systematics that may affect future surveys is made necessary. The work presented in this thesis has been carried out with these exact purposes in mind. To this end, we followed several different approaches: we tested new possible observables that could come in aid to the standard BAO analysis in future surveys, evaluating their sensitivity to neutrino mass; we assessed the degeneracies induced by nuisance signals and systematics in standard observables such as galaxy clustering and weak lensing; we predicted the clustering of relic massive neutrinos in the Milky Way in view of future direct detection experiments.

Chapter 1 consists of a general introduction to the standard cosmological model, the Λ CDM paradigm: there we presented the general framework in which we work,

together with an exhaustive description of the main observables that we use, their time evolution and their dependence on the fundamental cosmological parameters. In Chapter 2 we describe in detail the impact that neutrino mass has on the quantities previously introduced. In particular, we focused on the effect that neutrino free-streaming has on the growth of density perturbations and in turn on the halo/galaxy and cosmic shear power spectra and to the BAO feature in the two-point correlation function (2PCF). These two initial Chapters contain all the relevant information for a thorough comprehension of the work described in the following ones.

In Chapter 3 we extended previous work on the Λ CDM paradigm to address the impact of massive neutrinos on the linear point (LP). By employing state-of-art N -body simulations, the DEMNUni (Carbone et al. (2016)) and the Quijote (Villaescusa-Navarro et al. (2019)), we found the LP position to be weakly sensitive (at the 0.5% level) to gravitational non-linearities, i.e. its comoving position is nearly redshift-independent. While we still need to check whether this result is not spoiled by redshift-space distortions (RSD), what we found is the first important step to show that the LP can be employed as a cosmological standard ruler in this context. Hence, we can use the LP to measure cosmological distances (independent of the primordial cosmological parameters) without assuming a particular spatial curvature of the Universe or a specific model employed to describe late-time acceleration. Such distances can be employed to constrain not only the dark energy, dark matter and baryon energy densities but also the neutrino masses.

We also investigated whether a detection of M_ν is possible using the shift of the LP with respect to the Λ CDM case at a given redshift, survey volume and galaxy number density. Our proposal was to compare the LP as measured from real data to the one estimated with an “equivalent” mock galaxy distribution that assumes massless neutrinos. With our simulation set, we found that for underlying CDM field, the neutrino mass SNR detection increases for increasing volume, redshift and neutrino mass – as expected. On the other hand, from the halo investigation, we found that shot noise suppresses the SNR in a considerable way. Nevertheless deep tomographic redshift surveys with several redshift bins will help in increasing the SNR. Notice that this approach is similar to the one presented in Baumann et al. (2019), where a neutrino-induced phase shift of the BAO in the BOSS DR12 galaxy power spectrum was detected. However, in this work and in a related analysis (Baumann et al. (2018)) several non-linear effects are incorporated using phenomenological models of the non-linear 2PCF, with the concrete risk of being subject to the limitations of

template-based BAO analyses (see e.g. Anselmi et al. (2018a); O’Dwyer et al. (2020)). Therefore our approach could provide a different route to detecting the neutrino mass. In Chapter 4 we showed that the effect of baryons on the matter and shear power spectra can be disentangled *at the matter perturbation level* by using a tomographic analysis. In our model we used the analytical formula by Schneider & Teyssier (2015) (the Baryon Correction Model, BCM) to describe the effect of baryon feedback on the matter power spectrum, while neutrinos and non-linearities are accounted for by a Boltzmann solver and the HALOFIT algorithm. We performed a likelihood analysis for the matter and shear power spectra using the Markov Chain Monte Carlo (MCMC) method. In the error budget we considered cosmic variance, shot/shape noise and a systematic error that induces correlation among different wavenumbers (following Baldauf et al. (2016)) and that describes the uncertainties in the theoretical modelling of our observables. The results we obtained can be summarized as follows.

First, baryonic effects alone are in principle able to mimic the characteristic suppression of power at small scales due to a non-vanishing neutrino mass, but the parameters of the BCM, which have well-established physical meaning, take very unlikely values and depend strongly on the maximum wavenumber included in the analysis. This suggests that massive neutrinos and baryonic feedback effects will be indeed distinguishable in upcoming surveys.

Second, we studied the degeneracy between the two effects allowing the parameters of the baryonic feedback model and the neutrino mass to vary simultaneously. In all cases, we were able to recover the input neutrino mass. In particular, in the matter clustering case, the degeneracy between neutrino mass and feedback parameters is completely absent. For the shear power spectrum, we highlight a noticeable degeneracy between the neutrino mass M_ν and the BCM parameter $\log M_c$, which controls the minimum mass of halos that are not deployed of their gas.

Third, we considered how these results are affected by the additional systematic represented by the intrinsic alignment effect in weak lensing survey; in particular, we employed the linear alignment model by Hirata & Seljak (2004). Again, we were able to recover the right input values for what concerns neutrino mass and the A_{IA} parameter. The posterior PDFs and contours for the cases with and without intrinsic alignment are almost identical, while we find a degeneracy pattern in the $M_\nu - A_{IA}$ plane that is more pronounced when A_{IA} is negative. Also, such parameter seems not to suffer from any degeneracy with the other feedback parameters.

All in all, if the BCM is used as the baryon feedback fiducial model, measurements of M_ν from future surveys are likely not be affected by biases due to the degeneracy

between neutrino masses and the feedback parameters.

In Chapter 5 we extended previous works studying the clustering of relic neutrinos in the Milky Way, in view of future experiments aiming at the first direct detection of the cosmic neutrino background. We used the back-tracking technique to expand the original N -one-body method to a more realistic (cylindrical) description of the baryonic components of the Galaxy, as well as the contribution of nearby objects such as the Andromeda galaxy and the Virgo cluster. We found that the main contribution to the enhanced relic neutrino density comes from the DM halo of the Milky Way, especially for the largest considered neutrino masses. While the impact of Andromeda is found to be negligible, the contribution of Virgo cluster is relevant to obtain the correct number density for the smallest neutrino masses. The effect of the latter is not trivial, as its presence may actually divert some of the neutrinos that would otherwise cluster on the Milky Way if their mass (velocity) was large (small) enough. To quote some results, for $m_\nu = 10, 50, 100, 300$ meV, we obtain that the local number density of the relic neutrinos is respectively enhanced by 0.53%, 12%, 50% and 500% with respect to the cosmological average ($56 \text{ cm}^{-3} \text{ flavor}^{-1}$). Overall, we foresee a small enhancement of the detection rate in future experiments like PTOLEMY (which is of the order of $\sim 10 \text{ yr}^{-1}$), with a possible detection of a non-zero neutrino mass linearly depending on the energy resolution of the detector.

6.2 Future work

The main goal of this thesis was not to forecast the precision with which future experiments will be able to measure neutrino mass, but rather address, describe and characterize all the physical phenomena and systematics that may prevent or bias such measurement. Most of the works presented here are just first steps in tackling more complex problems that need much further investigation to be solved. All the physics and the cosmological observables introduced in this thesis can of course be used to probe and constrain also non-standard cosmologies and their parameters. Likewise, the analyses presented here can be easily generalized for such purposes. With this in mind, there are several directions that can be taken.

- With regard to the LP (Chapter 3), in that work we did not consider the impact of RSD on the LP position. Previous works have highlighted that the LP as measured from the monopole of the 2PCF is insensitive to RSD at the 0.5% level (Anselmi et al. (2016)) in the Λ CDM case; however, this has not been shown yet in the massive neutrino case. On a related note, while theoretical

arguments suggest that the LP is independent from the late-time acceleration of the Universe, no tests based on simulations have been carried out yet about the possibility that a redshift-dependent parameter of state for dark energy could spoil the standard ruler nature of the LP.

- About degeneracies between neutrino mass and baryon feedback, future developments concerning clustering need to include a bias model for galaxies as well as RSD. To further extend the work, it would be of great interest to explore the degeneracies of the feedback parameters with the cosmological ones both in clustering and shear. Finally, a possible improvement could in principle be brought to the constraints on these parameters by studying the cross-correlation between the two observables: to this end, a detailed study of the cross-covariance matrix is needed.
- As anticipated in Chapter 4, we are already extending the work presented there in the direction of non-standard DM models (Parimbelli et al. (in prep.)). While the goal remains the same, the plan is to run a set of simulations to predict the suppression/enhancement induced by the presence of warm DM, mixed DM (cold + warm) and isocurvature perturbations on the matter power spectrum. This suppression will then be fitted by extending the model by Viel et al. (2012) and translated to the shear one through eq. 1.60. We also plan to employ some realistic covariance matrices as computed from simulations (Schneider et al. (2020)), to assess the impact of the covariance between different multipoles induced by non-linearities (see eq. 1.63).
- The impressive amount of information contained in the Quijote simulation set can be exploited for multiple purposes. In particular, we plan to constrain cosmological parameters, taking particular care of the neutrino mass, employing three main “observables”: the total matter power spectrum, the halo mass function and the void size function. In doing so, we aim at using the full covariance matrix (including cross-covariances between different observables) computed from the 15,000 realizations of the fiducial model. Indeed, early results suggest that the use of different probes, even on a small survey volume, can drastically improve the constraints on neutrino mass and on cosmological parameter in general.

Another important feature of these simulations is the fact that they are enough to constitute a considerable training set for machine learning purposes. The goal

is to use machine learning to constrain the set of cosmological parameters θ in a likelihood-free way, given a generic observable f {PDF[$1 + \delta(\theta)$]}. This was already done as a test in Villaescusa-Navarro et al. (2019), where the random forest method was applied to the 1-D density field PDF smoothed on 5 Mpc/ h . With only 1600 simulations of training set, the algorithm was able to correctly predict σ_8 and Ω_m , while the failure to constrain Ω_b , h and n_s was expected using only the 1-D PDF with one smoothing scale.

Furthermore, Villaescusa-Navarro et al. (2019) also show that the Quijote simulations can use machine learning to predict the non-linear matter power spectrum of any cosmological parameter set within few % up to scales of $k \sim 1 h/\text{Mpc}$, with a significant reduction of computational cost.

- Related to the previous point, an interesting analysis with the Quijote could be done by using more realistic observables, such as the galaxy power spectrum in redshift-space. This work can be performed by populating DM halos with galaxies according to some (semi-)analytical model describing the number of galaxies per halo given the properties of the halos themselves. This procedure is known as Halo Occupation Distribution (HOD, first introduced in Zheng et al. (2005)). Usually these models predict that each halo has a certain probability of having a central galaxy (typically a step function centered on some threshold mass and with a given transition width) and a certain number of satellite galaxies (growing with the halo mass). To proceed in this direction, we would generate mock galaxy catalogues with this technique, also accounting for the dispersion velocities in DM halos. Then, we would measure the multipoles of the galaxy power spectrum in redshift-space for all the realization, also to obtain realistic covariance matrices for the subsequent MCMC fitting.

The measurement of neutrino masses will be one of the main goals of future surveys: its success (or failure) will in any case influence future research not only in cosmology, but also in particle physics. Therefore it is worth discussing about the possibility that future measurements will not go in the direction we expect.

We know that large-scale structure contains a lot of information about the underlying cosmology that still needs to be unveiled. Combining different probes, understanding their constraining power and assessing the systematics by which they are affected seems to be the key to disclose such information and open the path to new physics that could possibly resolve the yet unexplained features of our Universe. Some of these features include the nature of DM and also question the possibility that the

effect of DE could be indeed due to a modification of GR at large scales (modified gravity, MG). Knowing the exact value of the neutrino masses could open the way to test new physics not only in the Standard Model, but also at the cosmological level. Testing possible couplings between neutrinos and DM/DE to constrain fundamental interactions in the early Universe, constraining the growth of neutrino perturbations in the MG picture: these are just some of the possible ways that one could extend the standard cosmological model.

Another intriguing possibility is that particle physics experiment like PTOLEMY or KATRIN will measure a neutrino mass in significant tension with the complementary cosmological ones. This in principle does not mean that the whole cosmology needs to be refounded, as typical measures of M_ν from cosmological observables are model-dependent and refer to one-parameter extensions of the Λ CDM model obtained with Bayesian statistics (MCMC); however it does mean that the Λ CDM paradigm needs to be revised in order to reconcile this inconsistency. Possible solutions may involve modifications of gravity that may mimic the effect of neutrinos or again interactions between neutrinos and the dark sector. In conclusion, in view of upcoming surveys, we are on the edge of an exciting era for cosmology, both whether future results will confirm our predictions or they will be completely unexpected.

The work presented in this thesis addresses neutrinos in the extended frame of the Λ CDM paradigm. However, the approaches used here can be easily extended and generalized to probe any other additional effect to the Λ CDM paradigm: this is the main reason why this work can be considered as a first step in tackling any problem concerning the extension of the cosmological model.

Appendices



Non-linear power spectra: HALOFIT

A.1 A quick prediction for non-linearities

The prediction of the non-linear matter power spectrum up to very small scales ($k \sim 5 - 10 h/\text{Mpc}$) is a key ingredient for cosmic shear surveys and large-scale structure probes in general. Unfortunately, this is a prohibitive task for perturbation theory, since many of the assumptions made in the calculations break down at mildly non-linear scales. Therefore, one must rely on N -body simulations which on one hand solve the full non-linear system of equations but on the other hand are time consuming.

In the last two decades, alternative directions have been taken to overcome this issue when in need of a quick estimate of non-linear clustering. At the turn of the millennium the halo model was developed (see Cooray & Sheth (2002) for a review): this describes the full non-linear matter field as correlations between particles belonging to different dark matter halos. Despite its elegance, however, the halo model is way too simplistic to catch all the complicated aspects of matter (or galaxy) clustering and fails to reproduce the results from N -body simulations up to $\sim 20\%$ at the typical scale of halo sizes.

On the other hand, the increasing computing performances have allowed to run thousands of simulation, making it possible to find fitting formulae able to reproduce the non-linear clustering to a % level for a large number of cosmological models including non-standard ones. This procedure, commonly named HALOFIT, has been widely used in shear survey analyses (Abbott et al. (2018, 2019); Hildebrandt et al. (2017);

Köhlinger et al. (2017)). Contrarily to emulators (Heitmann et al. (2010, 2009); Lawrence et al. (2010b,a, 2017); DeRose et al. (2019); McClintock et al. (2019b); Zhai et al. (2019); McClintock et al. (2019a); Euclid Collaboration et al. (2019b); Angulo et al. (2020)), which return the non-linear correction to the linear power spectrum through interpolating techniques, HALOFIT consists of an actual fitting function, with a precision that nowadays reaches $\sim 5\%$ at $k \sim 10 h/\text{Mpc}$ for ΛCDM models.

In this Appendix we go quickly through the various and most famous HALOFIT versions used in literature, going in chronological order. For all of them, we use the following common notation:

- $P_{\text{lin}}(k)$ is the linear power spectrum.
- $\Delta_{\text{lin}}^2(k) = \frac{k^3 P_{\text{lin}}(k)}{2\pi^2}$ is the linear effective power per logarithmic interval of k .
- The same quantities with the subscript “nl” indicate that the non-linear power spectrum is involved.
- $\sigma^2(R) = \int_0^\infty d \ln k \Delta_{\text{lin}}^2(k) W^2(kR)$, is the root-mean square density fluctuation smoothed on a certain scale R , where the window function will be, where not otherwise specified, a Gaussian.
- k_σ is the non-linearity scale, for which $\sigma^2(1/k_\sigma, z) \equiv 1$.
- The effective index is $3 + n_{\text{eff}} = - \left. \frac{d \ln \sigma^2(R)}{d \ln R} \right|_{\sigma=1}$.
- The spectral curvature is $C = - \left. \frac{d^2 \ln \sigma^2(R)}{d \ln R^2} \right|_{\sigma=1}$.

A.2 The original HALOFIT

The first HALOFIT version (Smith et al. (2003)) was based on a set of DM only N -body simulations, featuring Einstein-de Sitter, open low-density and ΛCDM models. The description of the non-linear clustering happens through the summation of two terms, one labelled Q for “quasi-linear”, dominating at large scales, and one labelled H for “halo”, expressing correlations of particle pairs in the same DM halo.

$$\Delta_{\text{nl}}^2(k) = \Delta_Q^2(k) + \Delta_H^2(k). \quad (\text{A.1})$$

The single terms are given by

$$\Delta_Q^2(k) = \Delta_{\text{lin}}^2(k) \left\{ \frac{[1 + \Delta_{\text{lin}}^2(k)]^\beta}{1 + \alpha \Delta_{\text{lin}}^2(k)} \right\} \exp[-f(y)], \quad (\text{A.2})$$

where $y = k/k_\sigma$ and $f(y) = y/4 + y^2/8$, and

$$\Delta_H^2(k) = \frac{a y^{3f_1(\Omega_m)}}{1 + b y^{f_2(\Omega_m)} + [c f_3(\Omega_m) y]^{3-\gamma}} \frac{1}{1 + \mu y^{-1} + \nu y^{-2}}. \quad (\text{A.3})$$

The fitted parameters $(a, b, c, \alpha, \beta, \gamma, \mu, \nu)$ and the three $f_i(\Omega_m)$ functions are

- $\log a = 1.4861 + 1.8369 n_s + 1.6762 n_s^2 + 0.7940 n_s^3 + 0.1670 n_s^4 - 0.6206 C$
- $\log b = 0.9463 + 0.9466 n_s + 0.3084 n_s^2 - 0.9400 C$
- $\log c = -0.2807 + 0.6669 n_s + 0.3214 n_s^2 - 0.0793 C$
- $\alpha = 1.3884 + 0.3700 n_s - 0.1452 n_s^2$
- $\beta = 0.8291 + 0.9854 n_s + 0.3401 n_s^2$
- $\gamma = 0.8649 + 0.2989 n_s + 0.1631 C$
- $\log \mu = -3.5442 + 0.1908 n_s$
- $\log \nu = 0.9589 + 1.2857 n_s$
- $f_1(\Omega_m) = \Omega_m(z)^{-0.0307}$; $f_2(\Omega_m) = \Omega_m(z)^{-0.0585}$; $f_3(\Omega_m) = \Omega_m(z)^{0.0743}$.

A.3 Addition of massive neutrinos

The HALOFIT version by Bird et al. (2012) corrects the original version including the effect of massive neutrinos. By employing and fitting N -body simulations with two fluids (DM and neutrinos with masses up to 0.6 eV), the improved formulae are based on the same equations of Smith et al. (2003) but with slightly different coefficients and terms.

The halo term is modified to $\Delta_H^2(k) \rightarrow \Delta_H^2(k) (1 + Q_\nu)$, where f_ν is the neutrino fraction and

$$Q_\nu = \frac{f_\nu [2.080 - 12.4(\Omega_m - 0.3)]}{1 + 1.20 \times 10^{-3} y^3}. \quad (\text{A.4})$$

The quasi-linear term is modified as

$$\Delta_Q^2(k) = \Delta_{\text{lin}}^2(k) \left\{ \frac{[1 + \tilde{\Delta}_{\text{lin}}^2(k)]^{\tilde{\beta}}}{1 + \alpha \tilde{\Delta}_{\text{lin}}^2(k)} \right\} \exp[-f(y)], \quad (\text{A.5})$$

where

$$\tilde{\Delta}_{\text{lin}}^2(k) = \Delta_{\text{lin}}^2(k) \left(1 + \frac{26.3 f_\nu k}{1 + 1.5 k^2} \right) \quad (\text{A.6})$$

and

$$\tilde{\beta} = \beta + f_\nu (-6.49 + 1.44 n_s^2). \quad (\text{A.7})$$

Another slight change with respect to Smith et al. (2003) is $\gamma \rightarrow \gamma + 0.316 - 0.0765 n_s - 0.835 C$.

A.4 The Takahashi model

A revisiting and an improvement to the accuracy of the original HALOFIT was carried out by Takahashi et al. (2012). The new fitting formulae are calibrated on 16 cosmological models around the WMAP best-fit cosmological parameters (1, 3, 5, and 7 year results), including dark energy models with a constant equation of state. The actual formulae are the same of Smith et al. (2003) (eq. A.1), but with updated coefficients:

- $\log a = 1.5222 + 2.8553 n_{\text{eff}} + 2.3706 n_{\text{eff}}^2 + 0.9903 n_{\text{eff}}^3 + 0.2250 n_{\text{eff}}^4 - 0.6038 C + 0.1749 \Omega_\Lambda(z) (1 + w)$
- $\log b = -0.5642 + 0.5864 n_{\text{eff}} + 0.5716 n_{\text{eff}}^2 - 1.5474 C + 0.2279 \Omega_\Lambda(z) (1 + w)$
- $\log c = 0.3698 + 2.0404 n_{\text{eff}} + 0.8161 n_{\text{eff}}^2 + 0.5869 C$
- $\alpha = \left| 6.0835 + 1.3373 n_{\text{eff}} - 0.1959 n_{\text{eff}}^2 - 5.5274 C \right|$
- $\beta = 2.0379 - 0.7354 n_{\text{eff}} + 0.3157 n_{\text{eff}}^2 + 1.2490 n_{\text{eff}}^3 + 0.3980 n_{\text{eff}}^4 - 0.1682 C$
- $\gamma = 0.1971 - 0.0843 n_{\text{eff}} + 0.8460 C$
- $\mu = 0$
- $\log \nu = 5.2105 + 3.6902 n_{\text{eff}}$
- $f_1(\Omega_m) = \Omega_m(z)^{-0.0307}$
- $f_2(\Omega_m) = \Omega_m(z)^{-0.0585}$
- $f_3(\Omega_m) = \Omega_m(z)^{0.0743}$

With this new procedure, HALOFIT can achieve 5% precision for $k \leq 1 h/\text{Mpc}$ in the redshift range $0 \leq z \leq 10$ and 10% for $k \leq 10 h/\text{Mpc}$ in the range $0 \leq z \leq 3$.

A.5 HMcode: a halo model approach

HMcode is a modified version of the original halo model that adds some physically motivated degrees of freedom to halo profiles in order to relieve some discrepancies with the actual non-linear matter clustering, especially in the transition regime between the 1-halo and the 2-halo terms. It was released in two different versions. The former (Mead et al. (2015)) is based on the Overwhelmingly Large Simulations (Schaye et al. (2010); van Daalen et al. (2011)) and provides non-linear spectra accurate to 5% up to scales of $10 h/\text{Mpc}$ for ΛCDM models including baryon feedback. The latter (Mead et al. (2016)) besides updating some fitting coefficients, also includes the effect of massive neutrinos, dark energy models and screening mechanisms.

In the classical derivation of the halo model, the total matter power spectrum is given by the summation of two terms describing the correlation between particle pairs belonging to the same halo (1-halo term) and to different halos (2-halo term):

$$P_{\text{nl}}(k, z) = P_{1h}(k, z) + P_{2h}(k, z), \quad (\text{A.8})$$

where

$$P_{1h}(k, z) = \int_0^\infty dM \frac{M^2}{\bar{\rho}^2} \frac{dn}{dM}(z) u^2(k|M, z) \quad (\text{A.9})$$

$$P_{2h}(k, z) = P_{\text{lin}}(k) \left[\int dM \frac{M}{\bar{\rho}} \frac{dn}{dM}(z) b(M, z) u(k|M, z) \right]^2, \quad (\text{A.10})$$

while $u(k|M, z)$ is the Fourier transform of the NFW profile for a halo of mass M , $\frac{dn}{dM}$ is the halo mass function which we assume to be Sheth-Tormen (Sheth & Tormen (1999)) and $b(M)$ the corresponding halo bias. Halos are assumed to have a concentration that follows the Bullock distribution (Bullock et al. (2001)) with minimum concentration $A_{\text{bar}} = 4$.

The approach used by Mead et al. (2015, 2016) is to modify the fixed parameters of the halo model and tune them as functions of mass and redshift in order to resolve the intermediate scales problems.

The main quantities modified are the virialized halo overdensity Δ_v , the linear critical density for collapse δ_c and the minimum halo concentration A_{bar} . Depending on the physical processes and gravity models considered, the values of the new free parameters change. We only recap here the up-to-date ones, valid for DM only runs and flat ΛCDM cosmologies (see Table A.1).

- $\Delta_v = 200 \rightarrow 418 \Omega_m(z)^{-0.352}$

Parameter	Meaning	Original value	New halofit
$\Delta_v(z)$	Virialized halo overdensity	200	$418 \Omega_m(z)^{-0.352}$
$\delta_c(z)$	Critical density for collapse	1.686	$[1.59 + 0.0314 \ln \sigma_8(z)] \times [1 + 0.0123 \log \Omega_m(z)]$
$\eta(z)$	Halo bloating	0	$0.64 - 0.3 \sigma_8(z)$
$f_d(z)$	Linear damping factor	0	$0.0095 \sigma_{d,100}(z)^{1.37}$
$k_*(z)$	One-halo damping	0	$0.584 \sigma_{d,0}^{-1}(z)$
A_{bar}	Minimum halo concentration	4	3.43
$\alpha(z)$	Quasi-linear softening	1	$3.24 \times 1.85^{\alpha_{\text{eff}}}$

Table A.1: The Table shows the values of the parameters used by HMcode (Mead et al. (2015, 2016)) to fit the matter power spectrum from DM only simulations in Λ CDM cosmologies. In this work we typically use these parameters for the non-linear power spectrum.

- $\delta_c = 1.686 \rightarrow [1.59 + 0.0314 \ln \sigma_8(z)] \times [1 + 0.0123 \log \Omega_m(z)]$
- $A_{\text{bar}} = 4 \rightarrow 3.43$

The non-linear power spectrum gains a smoother transition from the 1-halo to the 2-halo terms through the introduction of a softening parameter

$$P_{\text{nl}}(k, z) = \{[P_{1h}(k, z)]^\alpha + [P_{2h}(k, z)]^\alpha\}^{1/\alpha} \quad (\text{A.11})$$

where

$$P_{1h}(k, z) = \left[\int_0^\infty dM \frac{M^2}{\bar{\rho}^2} \frac{dn}{dM} u^2(\nu^\eta k | M, z) \right] \left[1 - e^{-(k/k_*)^2} \right] \quad (\text{A.12})$$

$$P_{2h}(k, z) = P_{\text{lin}}(k, z) \left[1 - f_d \tanh^2(k \sigma_{d,0} / \sqrt{f_d}) \right]. \quad (\text{A.13})$$

The remaining free parameters are a halo bloating parameter η , a linear damping factor f_d and a 1-halo damping term k_* . All of them are redshift dependent quantities with values

$$\eta(z) = 0.64 - 0.3 \sigma_8(z) \quad (\text{A.14})$$

$$f_d(z) = 0.0095 \sigma_{d,100}(z)^{1.37} \quad (\text{A.15})$$

$$k_*(z) = 0.584 \sigma_{d,0}(z)^{-1} \quad (\text{A.16})$$

where

$$\sigma_{d,R}(z) = \frac{1}{3} \int_{-\infty}^{\infty} d \ln k \frac{\Delta_{\text{lin}}^2(k)}{k^2} W_{\text{TH}}^2(kR). \quad (\text{A.17})$$

Notice that in this case the window function is a top-hat in configuration space.

The quasi-linear softening is given by

$$\alpha(z) = 3.24 \times 1.85^{n_{\text{eff}}}, \quad (\text{A.18})$$

with a slightly different effective index with respect to the one defined above:

$$3 + n_{\text{eff}} = - \left. \frac{d \ln \sigma^2(R)}{d \ln R} \right|_{\sigma=\delta_c}. \quad (\text{A.19})$$

B

Solving the Poisson equation

B.1 A general solution

In this Appendix we explain how we solved the Poisson equation to finally compute the neutrino clustering at the Sun's position (see Chapter 5 for all the details).

The Poisson equation relates the density field to the gravitational potential in physical coordinates \mathbf{r} :

$$\nabla^2 \Phi(\mathbf{r}) = 4\pi G \rho(\mathbf{r}). \quad (\text{B.1})$$

The solution for this equation can be found in terms of Green's function. The Green's function for the Laplacian is $G_{\nabla^2}(\mathbf{r}) = -1/(4\pi|\mathbf{r}|)$, which yields the solution:

$$\Phi(\mathbf{r}) = -4\pi G \int d^3\mathbf{x} \frac{\rho(\mathbf{x})}{|\mathbf{r} - \mathbf{x}|}. \quad (\text{B.2})$$

In the case of spherical symmetry, this integral becomes:

$$\Phi(r) = -4\pi G \left[\frac{1}{r} \int_0^r dx x^2 \rho(x) + \int_r^\infty dx x \rho(x) \right]. \quad (\text{B.3})$$

Unfortunately, the previous treatment is of little use if no particular symmetry is involved in the problem. One typically expands the solution in spherical harmonics, but what we need is an exact solution. Taking the Fourier transform of both sides of eq. B.1 and using the fact that the equality obtained must be valid for any density distribution, we end up with:

$$\Phi_{\mathbf{k}} = -\frac{4\pi G \rho_{\mathbf{k}}}{k^2}. \quad (\text{B.4})$$

The solution to the Poisson equation is then found by Fourier transforming back the previous equation:

$$\Phi(\mathbf{r}) = -4\pi G \int \frac{d^3\mathbf{k}}{(2\pi)^3} \frac{\rho_{\mathbf{k}}}{k^2} e^{i\mathbf{k}\cdot\mathbf{r}} \quad (\text{B.5})$$

and the force per unit mass with respect to any Cartesian coordinate x_i is:

$$\frac{\partial\Phi}{\partial x_i}(\mathbf{r}) = -4\pi G \int \frac{d^3\mathbf{k}}{(2\pi)^3} \rho_{\mathbf{k}} \frac{ik_i}{k^2} e^{i\mathbf{k}\cdot\mathbf{r}}. \quad (\text{B.6})$$

B.2 Spherical symmetry

In this Section we provide solutions to the Poisson equation for the profiles we used in Chapter 5, namely the truncated NFW and the Einasto profiles.

B.2.1 Navarro-Frenk-White profile

The NFW profile is a fair approximation of the density profiles of DM halos. In principle, the only free parameters are a density normalization ρ_0 and a scale radius R_s . However, in this way the mass enclosed in a radius r would diverge at infinity, so there must be a point where the profile gets truncated. This so-called virial radius R_{vir} completes the truncated NFW profile:

$$\rho_{\text{t-NFW}}(r) = \frac{\rho_0}{\left(\frac{r}{R_s} + 1\right)^2} \Theta(r - R_{\text{vir}}), \quad (\text{B.7})$$

where $\Theta(x)$ is the Heaviside step-function. The total mass enclosed in the profile becomes finite in this way:

$$M_{\text{vir,t-NFW}} = 4\pi\rho_0 R_s^3 \left[\ln\left(1 + \frac{R_{\text{vir}}}{R_s}\right) - \frac{R_{\text{vir}}/R_s}{1 + \frac{R_{\text{vir}}}{R_s}} \right] \quad (\text{B.8})$$

To compute the potential we make use of eq. B.3 distinguishing between two cases. When $r > R_{\text{vir}}$ the second integral vanishes and the first returns the Keplerian potential $\Phi(r) = -\frac{GM_{\text{vir}}}{r}$. On the other hand, when $r < R_{\text{vir}}$,

$$\Phi(r) = -4\pi G \rho_0 R_s^2 \left[\frac{\ln\left(1 + \frac{r}{R_s}\right)}{r/R_s} - \frac{1}{1 + \frac{R_{\text{vir}}}{R_s}} \right]. \quad (\text{B.9})$$

All in all, we can compact the notation and write:

$$\Phi_{\text{t-NFW}}(r, \rho_0, R_s, R_{\text{vir}}) = -4\pi G \rho_0 R_s^2 \left[\frac{\ln\left(1 + \frac{m}{R_s}\right)}{r/R_s} - \frac{R_{\text{vir}}/M}{1 + \frac{R_{\text{vir}}}{R_s}} \right], \quad (\text{B.10})$$

where $m = \min(r, R_{\text{vir}})$ and $M = \max(r, R_{\text{vir}})$.

The derivatives can be easily computed through the chain rule:

$$\frac{\partial \Phi_{\text{t-NFW}}}{\partial x_i}(r) = 4\pi G \rho_0 R_s^2 \frac{x_i}{r^2} \left[\frac{\ln \left(1 + \frac{m}{R_s} \right)}{r/R_s} - \frac{R_{\text{vir}}/M}{1 + \frac{m}{R_s}} \right]. \quad (\text{B.11})$$

B.2.2 Einasto profile

The Einasto profile (Einasto (1965)) was the first proposed as a universal model for DM halos profiles and its shape can be rearranged as:

$$\rho_{\text{Ein}}(r) = \rho_0 e^{-(r/R_s)^\alpha} \quad (\text{B.12})$$

where ρ_0 is a normalization constant, R_s is a scale radius and α is the slope of the logarithm of the profile.

The mass enclosed in the profile is given by:

$$M_{\text{vir, Ein}} = \frac{4\pi \rho_0 R_s^3}{\alpha} \Gamma \left(\frac{3}{\alpha} \right). \quad (\text{B.13})$$

From Green's function analysis, we find that the potential generated by an Einasto halo is given by:

$$\Phi_{\text{Ein}}(r, \rho_0, R_s, \alpha) = -\frac{4\pi G \rho_0 R_s^2}{\alpha} \left[Y^{-1/\alpha} \Gamma \left(\frac{3}{\alpha}, 0, Y \right) + \Gamma \left(\frac{2}{\alpha}, Y, \infty \right) \right], \quad (\text{B.14})$$

where $Y = (r/R_s)^\alpha$ and we have defined the incomplete Γ function:

$$\Gamma(x, l, u) = \int_l^u dt t^{x-1} e^{-t}. \quad (\text{B.15})$$

The derivative is once again computed using the chain rule: $\frac{\partial \Phi_{\text{Ein}}}{\partial x_i} = \frac{d\Phi_{\text{Ein}}}{dY} \frac{dY}{dr} \frac{\partial r}{\partial x_i} = \frac{d\Phi_{\text{Ein}}}{dY} \frac{\alpha Y}{r} \frac{x_i}{r}$

$$\frac{\partial \Phi_{\text{Ein}}}{\partial x_i}(r) = \frac{4\pi G \rho_0 R_s^3}{\alpha r^2} \Gamma \left(\frac{3}{\alpha}, 0, Y \right) \frac{x_i}{r}. \quad (\text{B.16})$$

B.2.3 Milky Way bulge

The bulge of the Milky Way has an ellipsoidal form with a ratio of semi-axes of ~ 0.6 . However, the size of the bulge is much smaller than the distance of the Sun with respect to the galactic center (approximately 0.7 vs. 8 kpc), so for our purposes it can be approximated to a sphere of effective radius R_s .

From Misiriotis et al. (2006) we see that the bulge component of the Milky Way, once spherical symmetry is restored, follows a Sersic law with index $n = 4$ (i.e. a de Vaucouleurs profile):

$$\rho_b(r) = \rho_0 \exp \left[-A \left(\frac{r}{R_s} \right)^{1/4} \right] \left(\frac{r}{R_s} \right)^{-7/8}, \quad (\text{B.17})$$

with $A = 2n - \frac{1}{3} \approx 7.67$. Using this definition the bulge density at the Sun's position is approximately 0.02% of the one at R_s . This further *a posteriori* check reassures us about the spherical approximation.

The gravitational potential can be computed using equation B.3:

$$\Phi_b(r) = -\frac{G}{r} [M_{\text{in}}(r) + M_{\text{out}}(r)], \quad (\text{B.18})$$

where we defined $M_{\text{in}}(r) \equiv 4\pi \int_0^r dx x^2 \rho(x)$ and $M_{\text{out}}(r) \equiv 4\pi r \int_r^\infty dx x \rho(x)$. Applying this to equation B.17, we obtain:

$$\begin{aligned} M_{\text{in}}(r) = & \frac{\pi \rho_0 R_s^3}{16 A^{17/2}} \left\{ 2027025 \sqrt{\pi} \operatorname{erf}(X^{1/2}) - 2e^{-X} X^{1/2} \times \right. \\ & \times (128X^7 + 960X^6 + 6240X^5 + 34320X^4 + 154440X^3 + \\ & \left. + 540540X^2 + 1351350X + 2027025) \right\} \end{aligned} \quad (\text{B.19})$$

$$\begin{aligned} M_{\text{out}}(r) = & \frac{\pi \rho_0 R_s^3}{A^{17/2}} X^4 \left\{ 105 \sqrt{\pi} \operatorname{erfc}(X^{1/2}) + \right. \\ & \left. + 2e^{-X} X^{1/2} (8X^3 + 28X^2 + 70X + 105) \right\}, \end{aligned} \quad (\text{B.20})$$

where for sake of clarity we set $X = A \left(\frac{r}{R_s} \right)^{1/4}$.

The derivatives are computed according to the chain rule once again:

$$\frac{\partial \Phi_b}{\partial x_i}(r) = \frac{G x_i}{r^3} \left\{ [M_{\text{in}}(r) + M_{\text{out}}(r)] - \frac{X}{4r} \left[\frac{dM_{\text{in}}}{dX} + \frac{dM_{\text{out}}}{dX} \right] \right\}. \quad (\text{B.21})$$

B.3 Disks

All the relevant density profiles that are not spherically symmetric (hot gas, cold gas, stars in the disk) typically satisfy axial symmetry. Moreover the radial and the zenithal components are generally separable. In this Section we first provide a general solution to the Poisson equation in cylindrical coordinates and then the specific one for the exponential profile we used in Chapter 5.

B.3.1 General solution of Poisson equation in cylindrical coordinates

We will assume that the axially symmetric profiles have the following form:

$$\rho(R, z) = \rho_0 F(R) H(z). \quad (\text{B.22})$$

In such a case the Fourier transform of the density profile is given by:

$$\begin{aligned} \rho_{\mathbf{k}}(k, q) &= \int_0^\infty dR R \int_0^{2\pi} d\theta e^{-ikR \cos \theta} \int_{-\infty}^\infty dz e^{-iqz} \rho_0 F(R) H(z) = \\ &= 2\pi \rho_0 \int_0^\infty dR R F(R) J_0(kR) \int_{-\infty}^\infty dz e^{-iqz} H(z), \end{aligned} \quad (\text{B.23})$$

where $J_0(x)$ the 0-th order Bessel function of the first kind.

Consequently, the potential may be expressed in its most general form as:

$$\begin{aligned} \Phi(R, z) &= -2G\rho_0 \int_0^\infty dk k \left[\int_0^\infty ds s F(s) J_0(ks) \right] J_0(kR) \times \\ &\quad \times \int_{-\infty}^\infty dq e^{iqz} \frac{\left[\int_{-\infty}^\infty dt H(t) e^{-iqt} \right]}{k^2 + q^2}. \end{aligned} \quad (\text{B.24})$$

B.3.2 Exponential disks

In these cases the two zenithal and radial distributions are well approximated by exponential functions:

$$\rho_d(R, z) = \rho_0 e^{-R/R_s} e^{-|z|/z_s}, \quad (\text{B.25})$$

where now $R^2 = x^2 + y^2$ and R_s and z_s represent some scale radius and height, respectively.

In the case of exponential density profile, one gets, for the density Fourier transform:

$$\rho_{\mathbf{k}} = 4\pi\rho_0 \frac{z_s}{1 + (qz_s)^2} \frac{R_s^2}{[1 + (kR_s)^2]^{3/2}}, \quad (\text{B.26})$$

while the gravitational potential can be computed as:

$$\Phi_d(R, z) = -4\pi G\rho_0 z_s R_s^2 \int_0^\infty dk k \frac{\frac{1}{k} e^{-k|z|} - z_s e^{-|z|/z_s}}{[1 + (kR_s)^2]^{3/2} [1 - k^2 z_s^2]} J_0(kR). \quad (\text{B.27})$$

The derivative of this potential is different depending we are computing it with respect to the zenithal axis z or the galaxy plane (x, y) . For the former we can just

differentiate the integrand function; for the latter, we can use the relation between Bessel functions $\frac{\partial J_0(kR)}{\partial x_i} = \frac{\partial J_0(kR)}{\partial R} \frac{\partial R}{\partial x_i} = -k J_1(kR) \frac{x_i}{R}$:

$$\frac{\partial \Phi_d}{\partial \{x, y\}}(R, z) = 4\pi G \rho_0 z_s R_s^2 \frac{\{x, y\}}{R} \int_0^\infty dk k \frac{k \left(\frac{1}{k} e^{-k|z|} - z_s e^{-|z|/z_s} \right)}{[1 + (kR_s)^2]^{3/2} [1 - k^2 z_s^2]} J_1(kR), \quad (\text{B.28})$$

$$\frac{\partial \Phi_d}{\partial z}(R, z) = 4\pi G \rho_0 z_s R_s^2 \frac{z}{|z|} \int_0^\infty dk k \frac{e^{-k|z|} - e^{-|z|/z_s}}{[1 + (kR_s)^2]^{3/2} [1 - k^2 z_s^2]} J_0(kR). \quad (\text{B.29})$$

All these equations are Hankel transforms and can be easily computed with tools like FFTlog (Talman (1978); Hamilton (2000)).

Bibliography

- Abazajian, K. N. 2017, *Phys. Rep.*, 711, 1
- Abbott, T. M. C., Abdalla, F. B., Alarcon, A., et al. 2018, *Phys. Rev. D*, 98, 043526
- Abbott, T. M. C., Abdalla, F. B., Avila, S., et al. 2019, *Phys. Rev. D*, 99, 123505
- Aker, M., Altenmüller, K., Arenz, M., et al. 2019, *Phys. Rev. Lett.*, 123, 221802
- Alam, S., Ata, M., Bailey, S., et al. 2017, *MNRAS*, 470, 2617
- Alcock, C. & Paczynski, B. 1979, *Nature*, 281, 358
- Ali-Haïmoud, Y. & Bird, S. 2013, *MNRAS*, 428, 3375
- Alpher, R. A., Bethe, H., & Gamow, G. 1948, *Phys. Rev.*, 73, 803
- Altarelli, G. & Feruglio, F. 2004, *New Journal of Physics*, 6, 106
- Anderson, L., Aubourg, É., Bailey, S., et al. 2014, *Mon. Not. Roy. Astron. Soc.*, 441, 24
- Angulo, R. E., Zennaro, M., Contreras, S., et al. 2020, *arXiv e-prints*, arXiv:2004.06245
- Anselmi, S., Corasaniti, P.-S., Sanchez, A. G., et al. 2018a, *arXiv e-prints*, arXiv:1811.12312
- Anselmi, S., Corasaniti, P.-S., Starkman, G. D., Sheth, R. K., & Zehavi, I. 2018b, *Phys. Rev. D*, 98, 023527
- Anselmi, S., Starkman, G. D., Corasaniti, P.-S., Sheth, R. K., & Zehavi, I. 2018c, *Physical Review Letters*, 121, 021302
- Anselmi, S., Starkman, G. D., & Sheth, R. K. 2016, *Mon. Not. Roy. Astron. Soc.*, 455, 2474

- Archidiacono, M., Calabrese, E., & Melchiorri, A. r. 2011, Phys. Rev. D, 84, 123008
- Audren, B., Lesgourgues, J., Bird, S., Haehnelt, M. G., & Viel, M. 2013, J. Cosmology Astropart. Phys., 2013, 026
- Audren, B. et al. 2015, JCAP, 03, 036
- Baldauf, T. & Desjacques, V. 2017, Phys. Rev. D, 95, 043535
- Baldauf, T., Mirbabayi, M., Simonović, M., & Zaldarriaga, M. 2016, arXiv e-prints, arXiv:1602.00674
- Banerjee, A. & Dalal, N. 2016, J. Cosmology Astropart. Phys., 2016, 015
- Banerjee, A., Powell, D., Abel, T., & Villaescusa-Navarro, F. 2018, J. Cosmology Astropart. Phys., 2018, 028
- Baracchini, E., Betti, M. G., Biasotti, M., et al. 2018, arXiv e-prints, arXiv:1808.01892
- Bardeen, J. M., Bond, J. R., Kaiser, N., & Szalay, A. S. 1986, ApJ, 304, 15
- Bartelmann, M. & Schneider, P. 2001, Phys. Rep., 340, 291
- Battye, R. A., Davies, R. D., & Weller, J. 2004, MNRAS, 355, 1339
- Battye, R. A. & Moss, A. 2014, Phys. Rev. Lett., 112, 051303
- Baumann, D., Beutler, F., Flauger, R., et al. 2019, Nature Physics, 15, 465
- Baumann, D., Green, D., & Wallisch, B. 2018, JCAP, 2018, 029
- Beacom, J. F., Bell, N. F., & Dodelson, S. 2004, Phys. Rev. Lett., 93, 121302
- Bel, J., Pezzotta, A., Carbone, C., Sefusatti, E., & Guzzo, L. 2019, AAP, 622, A109
- Bennett, C. L., Larson, D., Weiland, J. L., et al. 2013, ApJS, 208, 20
- Bernal, J. L., Verde, L., & Riess, A. G. 2016, J. Cosmology Astropart. Phys., 2016, 019
- Bernardeau, F., Colombi, S., Gaztañaga, E., & Scoccimarro, R. 2002, Phys. Rep., 367, 1
- Betti, M. G. et al. 2019, JCAP, 07, 047

- Beutler, F., Saito, S., Brownstein, J. R., et al. 2014, MNRAS, 444, 3501
- Bharadwaj, S., Nath, B. B., & Sethi, S. K. 2001, Journal of Astrophysics and Astronomy, 22, 21
- Bharadwaj, S. & Sethi, S. K. 2001, Journal of Astrophysics and Astronomy, 22, 293
- Bird, S., Viel, M., & Haehnelt, M. G. 2012, MNRAS, 420, 2551
- Bland-Hawthorn, J. & Gerhard, O. 2016, Ann. Rev. Astron. Astrophys., 54, 529
- Blanes, S. & Moan, P. C. 2001, J. Comp. Phys., 170, 205
- Blas, D., Lesgourgues, J., & Tram, T. 2011, J. Cosmology Astropart. Phys., 2011, 034
- Bode, P., Ostriker, J. P., & Turok, N. 2001, ApJ, 556, 93
- Bond, J. R., Cole, S., Efstathiou, G., & Kaiser, N. 1991, ApJ, 379, 440
- Boylan-Kolchin, M., Bullock, J. S., & Kaplinghat, M. 2012, MNRAS, 422, 1203
- Brandbyge, J. & Hannestad, S. 2009, J. Cosmology Astropart. Phys., 2009, 002
- Brandbyge, J. & Hannestad, S. 2010, J. Cosmology Astropart. Phys., 2010, 021
- Brandbyge, J., Hannestad, S., Haugbølle, T., & Thomsen, B. 2008, J. Cosmology Astropart. Phys., 2008, 020
- Brandbyge, J., Hannestad, S., & Tram, T. 2019, J. Cosmology Astropart. Phys., 2019, 047
- Brown, A. G. A. et al. 2018, Astron. Astrophys., 616, A1
- Bryan, G. L. & Norman, M. L. 1998, Astrophys. J., 495, 80
- Bull, P., Ferreira, P. G., Patel, P., & Santos, M. G. 2015, ApJ, 803, 21
- Bullock, J. S., Kolatt, T. S., Sigad, Y., et al. 2001, MNRAS, 321, 559
- Capozzi, F., Di Valentino, E., Lisi, E., et al. 2017, Phys. Rev. D, 95, 096014
- Capozzi, F., Lisi, E., Marrone, A., & Palazzo, A. 2018, Prog. Part. Nucl. Phys., 102, 48

- Carbone, C., Petkova, M., & Dolag, K. 2016, *J. Cosmology Astropart. Phys.*, 2016, 034
- Castorina, E., Carbone, C., Bel, J., Sefusatti, E., & Dolag, K. 2015, *J. Cosmology Astropart. Phys.*, 2015, 043
- Castorina, E., Sefusatti, E., Sheth, R. K., Villaescusa-Navarro, F., & Viel, M. 2014, *J. Cosmology Astropart. Phys.*, 2, 049
- Chacko, Z., Dev, A., Du, P., Poulin, V., & Tsai, Y. 2020, *Journal of High Energy Physics*, 2020, 20
- Chang, T.-C., Pen, U.-L., Peterson, J. B., & McDonald, P. 2008, *Phys. Rev. Lett.*, 100, 091303
- Chiang, C.-T., Hu, W., Li, Y., & LoVerde, M. 2018, *Phys. Rev. D*, 97, 123526
- Chiang, C.-T., LoVerde, M., & Villaescusa-Navarro, F. 2019, *Phys. Rev. Lett.*, 122, 041302
- Chisari, N. E., Richardson, M. L. A., Devriendt, J., et al. 2018, *MNRAS*, 480, 3962
- Chudaykin, A. & Ivanov, M. M. 2019, *J. Cosmology Astropart. Phys.*, 2019, 034
- Clowe, D., Bradač, M., Gonzalez, A. H., et al. 2006, *ApJ*, 648, L109
- Cocco, A. G., Mangano, G., & Messina, M. 2007, *JCAP*, 06, 015
- Cole, S., Percival, W. J., Peacock, J. A., et al. 2005, *Mon. Not. Roy. Astron. Soc.*, 362, 505
- Coles, P. 1993, *MNRAS*, 262, 1065
- Cooke, R. J., Pettini, M., & Steidel, C. C. 2018, *ApJ*, 855, 102
- Cooray, A. & Sheth, R. 2002, *Phys. Rep.*, 372, 1
- Costanzi, M., Villaescusa-Navarro, F., Viel, M., et al. 2013, *J. Cosmology Astropart. Phys.*, 12, 012
- Crocce, M. & Scoccimarro, R. 2006, *Phys. Rev. D*, 73, 063519
- Croft, R. A. C. & Metzler, C. A. 2000, *ApJ*, 545, 561

- Dakin, J., Brandbyge, J., Hannestad, S., HaugbØlle, T., & Tram, T. 2019, *J. Cosmology Astropart. Phys.*, 2019, 052
- de Salas, P. F., Forero, D. V., Ternes, C. A., Tórtola, M., & Valle, J. W. F. 2018, *Phys. Lett. B*, 782, 633
- de Salas, P. F., Gariazzo, S., Lesgourgues, J., & Pastor, S. 2017, *JCAP*, 09, 034
- de Salas, P. F., Lattanzi, M., Mangano, G., et al. 2015, *Phys. Rev. D*, 92, 123534
- de Salas, P. F., Malhan, K., Freese, K., Hattori, K., & Valluri, M. 2019, *JCAP*, 10, 037
- de Salas, P. F. & Pastor, S. 2016, *JCAP*, 07, 051
- DeRose, J., Wechsler, R. H., Tinker, J. L., et al. 2019, *ApJ*, 875, 69
- Desjacques, V., Crocce, M., Scoccimarro, R., & Sheth, R. K. 2010, *Phys. Rev. D*, 82, 103529
- Desjacques, V., Gong, J.-O., & Riotto, A. 2013, *J. Cosmology Astropart. Phys.*, 2013, 006
- Desjacques, V., Jeong, D., & Schmidt, F. 2018, *Phys. Rep.*, 733, 1
- Desmond, H., Jain, B., & Sakstein, J. 2019, *Phys. Rev. D*, 100, 043537
- Di Valentino, E., Melchiorri, A., Linder, E. V., & Silk, J. 2017, *Phys. Rev. D*, 96, 023523
- Dolag, K., Borgani, S., Murante, G., & Springel, V. 2009, *Mon. Not. Roy. Astron. Soc.*, 399, 497
- Donato, F., Gentile, G., Salucci, P., et al. 2009, *Monthly Notices of the Royal Astronomical Society*, 397, 1169
- Dutton, A. A. & Macciò, A. V. 2014, *Mon. Not. Roy. Astron. Soc.*, 441, 3359
- Eckert, D., Ettori, S., Coupon, J., et al. 2016, *A&A*, 592, A12
- Efstathiou, G. & Lemos, P. 2018, *MNRAS*, 476, 151
- Eilers, A.-C., Hogg, D. W., Rix, H.-W., & Ness, M. 2019, *Astrophys. J.*, 871, 120

- Einasto, J. 1965, Trudy Astrofizicheskogo Instituta Alma-Ata, 5, 87
- Eisenstein, D. J. & Hu, W. 1998, The Astrophysical Journal, 496, 605, n/a
- Eisenstein, D. J., Seo, H.-J., Sirko, E., & Spergel, D. N. 2007, ApJ, 664, 675
- Eisenstein, D. J., Zehavi, I., Hogg, D. W., et al. 2005, ApJ, 633, 560
- Escudero, M. & Fairbairn, M. 2019, Phys. Rev. D, 100, 103531
- Esteban, I., Gonzalez-Garcia, M. C., Hernandez-Cabezudo, A., Maltoni, M., & Schwetz, T. 2019, JHEP, 01, 106
- Euclid Collaboration, Blanchard, A., Camera, S., et al. 2019a, arXiv e-prints, arXiv:1910.09273
- Euclid Collaboration, Knabenhans, M., Stadel, J., et al. 2019b, MNRAS, 484, 5509
- Fouque, P., Solanes, J. M., Sanchis, T., & Balkowski, C. 2001, Astron. Astrophys., 375, 770
- Gariazzo, S., de Salas, P. F., & Pastor, S. 2019, JCAP, 1907, 014
- Gerbino, M., Lattanzi, M., Mena, O., & Freese, K. 2017, Physics Letters B, 775, 239
- Giusarma, E., Gerbino, M., Mena, O., et al. 2016, Phys. Rev. D, 94, 083522
- Goldstein, H., Poole, C., & Safko, J. 2002, Classical mechanics (Addison Wesley)
- Gonzalez-Garcia, M. C. & Nir, Y. 2003, Reviews of Modern Physics, 75, 345
- Grieb, J. N., Sánchez, A. G., Salazar-Albornoz, S., & Dalla Vecchia, C. 2016, Mon. Not. Roy. Astron. Soc., 457, 1577
- Guo, R.-Y., Zhang, J.-F., & Zhang, X. 2019, J. Cosmology Astropart. Phys., 2019, 054
- Guth, A. H. 1981, Phys. Rev. D, 23, 347
- Hamilton, A. J. S. 2000, Mon. Not. Roy. Astron. Soc., 312, 257
- Hamilton, A. J. S., Rimes, C. D., & Scoccimarro, R. 2006, MNRAS, 371, 1188
- Hannestad, S. & Schwetz, T. 2016, J. Cosmology Astropart. Phys., 2016, 035

- Hannestad, S., Upadhye, A., & Wong, Y. Y. Y. 2020, arXiv e-prints, arXiv:2006.04995
- Harnois-Déraps, J., van Waerbeke, L., Viola, M., & Heymans, C. 2015, MNRAS, 450, 1212
- Harrison, E. R. 1970, Phys. Rev. D, 1, 2726
- Heavens, A., Refregier, A., & Heymans, C. 2000, Mon. Not. Roy. Astron. Soc., 319, 649
- Heitmann, K., Higdon, D., White, M., et al. 2009, ApJ, 705, 156
- Heitmann, K., White, M., Wagner, C., Habib, S., & Higdon, D. 2010, ApJ, 715, 104
- Henden, N. A., Puchwein, E., Shen, S., & Sijacki, D. 2018, MNRAS, 479, 5385
- Hildebrandt, H., Köhlinger, F., van den Busch, J. L., et al. 2020, A&A, 633, A69
- Hildebrandt, H., Viola, M., Heymans, C., et al. 2017, MNRAS, 465, 1454
- Hinshaw, G., Larson, D., Komatsu, E., et al. 2013, ApJS, 208, 19
- Hirata, C. M. & Seljak, U. 2004, Phys. Rev. D, 70, 063526
- Hirsch, M. & Valle, J. W. F. 2004, New Journal of Physics, 6, 76
- Hoekstra, H. & Jain, B. 2008, Annual Review of Nuclear and Particle Science, 58, 99
- Hubble, E. 1929, Proceedings of the National Academy of Sciences, 15, 168
- Hui, L. & Parfrey, K. P. 2008, Phys. Rev. D, 77, 043527
- Ichiki, K. & Takada, M. 2012, Phys. Rev. D, 85, 063521
- Iršič, V., Viel, M., Berg, T. A. M., et al. 2016, Monthly Notices of the Royal Astronomical Society, 466, 4332
- Ivanov, M. M., Simonović, M., & Zaldarriaga, M. 2019, arXiv e-prints, arXiv:1912.08208
- Jenkins, A., Frenk, C. S., White, S. D. M., et al. 2001, MNRAS, 321, 372
- Jing, Y. P., Zhang, P., Lin, W. P., Gao, L., & Springel, V. 2006, ApJ, 640, L119
- Joachimi, B. et al. 2015, Space Sci. Rev., 193, 1

- Joudaki, S., Hildebrandt, H., Traykova, D., et al. 2020, *A&A*, 638, L1
- Kafle, P. R., Sharma, S., Lewis, G. F., Robotham, A. S. G., & Driver, S. P. 2018, *Mon. Not. Roy. Astron. Soc.*, 475, 4043
- Kaiser, N. 1984, *ApJ*, 284, L9
- Kaiser, N. 1987, *MNRAS*, 227, 1
- Kalberla, P. M. W., Burton, W. B., Hartmann, D., et al. 2005, *Astron. Astrophys.*, 440, 775
- Kenney, J. F. & Keeping, E. 1951, *Mathematics of statistics. Part 2* (Princeton, N.J)
- Kilbinger, M., Heymans, C., Asgari, M., et al. 2017, *MNRAS*, 472, 2126
- Klypin, A., Holtzman, J., Primack, J., & Regos, E. 1993, *ApJ*, 416, 1
- Klypin, A., Kravtsov, A. V., Valenzuela, O., & Prada, F. 1999, *ApJ*, 522, 82
- Knox, L. & Millea, M. 2020, *Phys. Rev. D*, 101, 043533
- Köhlinger, F., Viola, M., Joachimi, B., et al. 2017, *MNRAS*, 471, 4412
- Kreisch, C. D., Pisani, A., Carbone, C., et al. 2019, *MNRAS*, 488, 4413
- Lawrence, E., Heitmann, K., Kwan, J., et al. 2017, *ApJ*, 847, 50
- Lawrence, E., Heitmann, K., White, M., et al. 2010a, *CosmicEmu: Cosmic Emulator for the Dark Matter Power Spectrum*
- Lawrence, E., Heitmann, K., White, M., et al. 2010b, *ApJ*, 713, 1322
- Leauthaud, A., Saito, S., Hilbert, S., et al. 2017, *MNRAS*, 467, 3024
- Lesgourgues, J. 2011, *arXiv e-prints*, arXiv:1104.2932
- Lesgourgues, J. & Pastor, S. 2006, *Phys. Rep.*, 429, 307
- Lesgourgues, J. & Tram, T. 2011, *JCAP*, 2011, 032
- Lewis, A., Challinor, A., & Lasenby, A. 2000, *ApJ*, 538, 473
- Limber, D. N. 1953, *ApJ*, 117, 134
- Lippich, M., Sánchez, A. G., Colavincenzo, M., et al. 2019, *MNRAS*, 482, 1786

- Loeb, A. & Wyithe, J. S. B. 2008, *Phys. Rev. Lett.*, 100, 161301
- LoVerde, M. 2014a, *Phys. Rev. D*, 90, 083530
- LoVerde, M. 2014b, *Phys. Rev. D*, 90, 083518
- Lovisari, L., Reiprich, T. H., & Schellenberger, G. 2015, *A&A*, 573, A118
- Mangano, G., Miele, G., Pastor, S., et al. 2005, *Nuclear Physics B*, 729, 221
- Mann, R. G., Peacock, J. A., & Heavens, A. F. 1998, *MNRAS*, 293, 209
- Marinacci, F., Pakmor, R., & Springel, V. 2014, *Mon. Not. Roy. Astron. Soc.*, 437, 1750
- Massara, E., Villaescusa-Navarro, F., & Viel, M. 2014, *J. Cosmology Astropart. Phys.*, 2014, 053
- McCarthy, I. G., Bird, S., Schaye, J., et al. 2018, *MNRAS*, 476, 2999
- McCarthy, I. G., Schaye, J., Bird, S., & Le Brun, A. M. C. 2017, *MNRAS*, 465, 2936
- McClintock, T., Rozo, E., Banerjee, A., et al. 2019a, arXiv e-prints, arXiv:1907.13167
- McClintock, T., Rozo, E., Becker, M. R., et al. 2019b, *ApJ*, 872, 53
- McLachlan, R. I. 1995, *SIAM J. Sci. Comput.*, 16, 151
- McMillan, P. J. 2017, *Mon. Not. Roy. Astron. Soc.*, 465, 76
- McQuinn, M., Zahn, O., Zaldarriaga, M., Hernquist, L., & Furlanetto, S. R. 2006, *ApJ*, 653, 815
- Mead, A. J., Heymans, C., Lombriser, L., et al. 2016, *MNRAS*, 459, 1468
- Mead, A. J., Peacock, J. A., Heymans, C., Joudaki, S., & Heavens, A. F. 2015, *MNRAS*, 454, 1958
- Merritt, D. & Tremblay, B. 1994, *Astrophys. J.*, 108, 514
- Mertsch, P. 2019, arXiv e-prints, arXiv:1910.01172
- Mertsch, P., Parimbelli, G., de Salas, P. F., et al. 2020, *JCAP*, 2020, 015
- Meszaros, P. 1974, *A&A*, 37, 225

- Misiriotis, A., Xilouris, E. M., Papamastorakis, J., Boumis, P., & Goudis, C. D. 2006, *Astron. Astrophys.*, 459, 113
- Mo, H., van den Bosch, F. C., & White, S. 2010, *Galaxy Formation and Evolution* (Cambridge)
- Mohapatra, R. N. & Smirnov, A. Y. 2006, *Annual Review of Nuclear and Particle Science*, 56, 569
- Moore, B., Ghigna, S., Governato, F., et al. 1999, *The Astrophysical Journal*, 524, L19
- Mummery, B. O., McCarthy, I. G., Bird, S., & Schaye, J. 2017, *MNRAS*, 471, 227
- Murgia, R., Iršič, V., & Viel, M. 2018, *Phys. Rev. D*, 98, 083540
- Navarro, J. F., Frenk, C. S., & White, S. D. M. 1996, *Astrophys. J.*, 462, 563
- Navarro, J. F., Frenk, C. S., & White, S. D. M. 1997, *ApJ*, 490, 493
- Noda, E., Peloso, M., & Pietroni, M. 2017, *jcap*, 2017, 007
- Noh, Y., White, M., & Padmanabhan, N. 2009, *Phys. Rev. D*, 80, 123501
- O'Dwyer, M., Anselmi, S., Starkman, G. D., et al. 2020, *Phys. Rev. D*, 101, 083517
- Oman, K. A., Navarro, J. F., Fattahi, A., et al. 2015, *MNRAS*, 452, 3650
- Padmanabhan, N., White, M., & Cohn, J. D. 2009, *Phys. Rev. D*, 79, 063523
- Padmanabhan, N., Xu, X., Eisenstein, D. J., et al. 2012, *Mon. Not. Roy. Astron. Soc.*, 427, 2132
- Palanque-Delabrouille, N., Yèche, C., Baur, J., et al. 2015a, *J. Cosmology Astropart. Phys.*, 2015, 011
- Palanque-Delabrouille, N., Yèche, C., Lesgourgues, J., et al. 2015b, *J. Cosmology Astropart. Phys.*, 2015, 045
- Parfrey, K., Hui, L., & Sheth, R. K. 2011, *Phys. Rev. D*, 83, 063511
- Parimbelli, G., Anselmi, S., Viel, M., et al. 2020, *arXiv e-prints*, arXiv:2007.10345
- Parimbelli, G., Scelfo, G., & Viel, M. in prep., (in prep.)

- Parimbelli, G., Viel, M., & Sefusatti, E. 2019, JCAP, 2019, 010
- Pato, M. & Iocco, F. 2015, *Astrophys. J.*, 803, L3
- Peebles, P. J. E. 1973, *ApJ*, 185, 413
- Peloso, M., Pietroni, M., Viel, M., & Villaescusa-Navarro, F. 2015, JCAP, 7, 001
- Penzias, A. A. & Wilson, R. W. 1965, *ApJ*, 142, 419
- Perlmutter, S., Aldering, G., Goldhaber, G., et al. 1999, *ApJ*, 517, 565
- Perotto, L., Lesgourgues, J., Hannestad, S., Tu, H., & Y Y Wong, Y. 2006, *J. Cosmology Astropart. Phys.*, 10, 013
- Philcox, O. H. E., Ivanov, M. M., Simonović, M., & Zaldarriaga, M. 2020, arXiv e-prints, arXiv:2002.04035
- Planck Collaboration. 2018, arXiv e-prints, arXiv:1807.06205
- Planck Collaboration, Ade, P. A. R., Aghanim, N., et al. 2016, *A&A*, 594, A13
- Planck Collaboration, Aghanim, N., Akrami, Y., et al. 2018, arXiv e-prints, arXiv:1807.06209
- Portail, M., Wegg, C., Gerhard, O., & Martinez-Valpuesta, I. 2015, *Mon. Not. Roy. Astron. Soc.*, 448, 713
- Press, W. H. & Schechter, P. 1974, *ApJ*, 187, 425
- Primack, J. R., Holtzman, J., Klypin, A., & Caldwell, D. O. 1995, *Phys. Rev. Lett.*, 74, 2160
- Pritchard, J. R. & Pierpaoli, E. 2008, *Phys. Rev. D*, 78, 065009
- Reed, D., Gardner, J., Quinn, T., et al. 2003, *MNRAS*, 346, 565
- Riess, A. G., Casertano, S., Yuan, W., Macri, L. M., & Scolnic, D. 2019, *ApJ*, 876, 85
- Riess, A. G., Filippenko, A. V., Challis, P., et al. 1998, *AJ*, 116, 1009
- Ringwald, A. & Wong, Y. Y. Y. 2004, JCAP, 12, 005
- Ross, A. J., Beutler, F., Chuang, C.-H., et al. 2017, *MNRAS*, 464, 1168

- Ruggeri, R., Castorina, E., Carbone, C., & Sefusatti, E. 2018, *J. Cosmology Astropart. Phys.*, 3, 003
- Sánchez, A. G., Baugh, C. M., & Angulo, R. E. 2008, *Mon. Not. Roy. Astron. Soc.*, 390, 1470
- Sánchez, A. G., Crocce, M., Cabré, A., Baugh, C. M., & Gaztañaga, E. 2009, *MNRAS*, 400, 1643
- Sánchez, A. G., Kazin, E. A., Beutler, F., et al. 2013, *Mon. Not. Roy. Astron. Soc.*, 433, 1202
- Sánchez, A. G., Scoccimarro, R., Crocce, M., et al. 2017, *MNRAS*, 464, 1640
- Sánchez, A. G., Scóccola, C. G., Ross, A. J., et al. 2012, *MNRAS*, 425, 415
- Santos, M., Bull, P., Alonso, D., et al. 2015, in *Advancing Astrophysics with the Square Kilometre Array (AASKA14)*, 19
- Schäling, B. 2014, *The Boost C++ Libraries* (XML Press)
- Schaye, J., Dalla Vecchia, C., Booth, C. M., et al. 2010, *MNRAS*, 402, 1536
- Schneider, A., Stoira, N., Refregier, A., et al. 2020, *J. Cosmology Astropart. Phys.*, 2020, 019
- Schneider, A. & Teyssier, R. 2015, *J. Cosmology Astropart. Phys.*, 12, 049
- Schneider, A., Teyssier, R., Potter, D., et al. 2016, *J. Cosmology Astropart. Phys.*, 2016, 047
- Schneider, A., Teyssier, R., Stadel, J., et al. 2019, *J. Cosmology Astropart. Phys.*, 2019, 020
- Schuster, N., Hamaus, N., Pisani, A., et al. 2019, *JCAP*, 2019, 055
- Scoccimarro, R. 2004, *Phys. Rev. D*, 70, 083007
- Scoccimarro, R., Zaldarriaga, M., & Hui, L. 1999, *ApJ*, 527, 1
- Sefusatti, E., Crocce, M., Pueblas, S., & Scoccimarro, R. 2006, *Phys. Rev. D*, 74, 023522

- Semboloni, E., Hoekstra, H., Schaye, J., van Daalen, M. P., & McCarthy, I. G. 2011, MNRAS, 417, 2020
- Seo, H.-J., Eckel, J., Eisenstein, D. J., et al. 2010, The Astrophysical Journal, 720, 1650
- Seo, H.-J., Siegel, E. R., Eisenstein, D. J., & White, M. 2008, Astrophys. J., 686, 13
- Sgier, R. J., Réfrégier, A., Amara, A., & Nicola, A. 2019, J. Cosmology Astropart. Phys., 2019, 044
- Sheth, R. K. & Tormen, G. 1999, MNRAS, 308, 119
- Silk, J. 1968, ApJ, 151, 459
- Singh, S. & Ma, C.-P. 2003, Phys. Rev. D, 67, 023506
- Smith, R. E. 2009, MNRAS, 400, 851
- Smith, R. E. & Angulo, R. E. 2019, MNRAS, 486, 1448
- Smith, R. E., Peacock, J. A., Jenkins, A., et al. 2003, MNRAS, 341, 1311
- Smith, R. E., Scoccimarro, R., & Sheth, R. K. 2008, Phys. Rev. D, 77, 043525
- Smoot, G. F., Bennett, C. L., Kogut, A., et al. 1992, ApJ, 396, L1
- Sprenger, T., Archidiacono, M., Brinckmann, T., Clesse, S., & Lesgourgues, J. 2019, J. Cosmology Astropart. Phys., 2019, 047
- Springel, V. 2005, MNRAS, 364, 1105
- Springel, V., Yoshida, N., & White, S. D. M. 2001, New Astronomy, 6, 79
- Stadel, J. G. 2001, PhD thesis, UNIVERSITY OF WASHINGTON
- Sun, M., Voit, G. M., Donahue, M., et al. 2009, ApJ, 693, 1142
- Takada, M. & Hu, W. 2013, Phys. Rev. D, 87, 123504
- Takada, M. & Jain, B. 2004, MNRAS, 348, 897
- Takahashi, R., Sato, M., Nishimichi, T., Taruya, A., & Oguri, M. 2012, ApJ, 761, 152

- Talman, J. D. 1978, *J. Comput. Phys.*, 29, 35
- Tanabashi, M., Hagiwara, K., Hikasa, K., et al. 2018, *Phys. Rev. D*, 98, 030001
- Taruya, A., Nishimichi, T., Saito, S., & Hiramatsu, T. 2009, *Phys. Rev. D*, 80, 123503
- Tegmark, M., Eisenstein, D. J., Strauss, M. A., et al. 2006, *Phys. Rev. D*, 74, 123507
- Teyssier, R. 2002, *A&A*, 385, 337
- Trotta, R. & Melchiorri, A. 2005, *Phys. Rev. Lett.*, 95, 011305
- Troxel, M. A. & Ishak, M. 2015, *Phys. Rep.*, 558, 1
- Troxel, M. A., MacCrann, N., Zuntz, J., et al. 2018, *Phys. Rev. D*, 98, 043528
- Tulin, S. & Yu, H.-B. 2018, *Phys. Rep.*, 730, 1
- Vagnozzi, S., Brinckmann, T., Archidiacono, M., et al. 2018, *JCAP*, 2018, 001
- Vagnozzi, S., Giusarma, E., Mena, O., et al. 2017, *Phys. Rev. D*, 96, 123503
- van Daalen, M. P., Schaye, J., Booth, C. M., & Dalla Vecchia, C. 2011, *MNRAS*, 415, 3649
- Veropalumbo, A., Marulli, F., Moscardini, L., Moresco, M., & Cimatti, A. 2016, *Mon. Not. Roy. Astron. Soc.*, 458, 1909
- Verza, G., Pisani, A., Carbone, C., Hamaus, N., & Guzzo, L. 2019, *JCAP*, 2019, 040
- Viel, M., Becker, G. D., Bolton, J. S., & Haehnelt, M. G. 2013, *Phys. Rev. D*, 88, 043502
- Viel, M., Haehnelt, M. G., & Springel, V. 2010, *J. Cosmology Astropart. Phys.*, 2010, 015
- Viel, M., Lesgourgues, J., Haehnelt, M. G., Matarrese, S., & Riotto, A. 2005, *Phys. Rev. D*, 71, 063534
- Viel, M., Markovič, K., Baldi, M., & Weller, J. 2012, *MNRAS*, 421, 50
- Villaescusa-Navarro, F., Alonso, D., & Viel, M. 2017, *MNRAS*, 466, 2736
- Villaescusa-Navarro, F., Banerjee, A., Dalal, N., et al. 2018a, *ApJ*, 861, 53

- Villaescusa-Navarro, F., Bird, S., Peña-Garay, C., & Viel, M. 2013, *J. Cosmology Astropart. Phys.*, 2013, 019
- Villaescusa-Navarro, F., Bull, P., & Viel, M. 2015, *ApJ*, 814, 146
- Villaescusa-Navarro, F., Genel, S., Castorina, E., et al. 2018b, *Astrophys. J.*, 866, 135
- Villaescusa-Navarro, F., Hahn, C., Massara, E., et al. 2019, arXiv e-prints, arXiv:1909.05273
- Villaescusa-Navarro, F., Marulli, F., Viel, M., et al. 2014, *J. Cosmology Astropart. Phys.*, 3, 011
- Villaescusa-Navarro, F., Miralda-Escudé, J., Peña-Garay, C., & Quilis, V. 2011, *JCAP*, 2011, 027
- Vlah, Z., White, M., & Aviles, A. 2015, *JCAP*, 2015, 014
- Wagner, C., Schmidt, F., Chiang, C. T., & Komatsu, E. 2015, *MNRAS*, 448, L11
- Watkins, L. L., Evans, N. W., & An, J. H. 2010, *Mon. Not. Roy. Astron. Soc.*, 406, 264
- Weinberg, S. 1962, *Phys. Rev.*, 128, 1457
- Weinberg, S. 1972, *Gravitation and Cosmology: Principles and Applications of the General Theory of Relativity* (New York: John Wiley and Sons)
- White, M. 2014, *MNRAS*, 439, 3630
- Xu, X., Padmanabhan, N., Eisenstein, D. J., Mehta, K. T., & Cuesta, A. J. 2012, *Mon. Not. Roy. Astron. Soc.*, 427, 2146
- Yohana, E., Li, Y.-C., & Ma, Y.-Z. 2019, *Research in Astronomy and Astrophysics*, 19, 186
- Zeldovich, Y. B. 1972, *Monthly Notices of the Royal Astronomical Society*, 160, 1P
- Zennaro, M., Bel, J., Villaescusa-Navarro, F., et al. 2017, *MNRAS*, 466, 3244
- Zhai, Z., Tinker, J. L., Becker, M. R., et al. 2019, *ApJ*, 874, 95
- Zhan, H. & Tyson, J. A. 2018, *Reports on Progress in Physics*, 81, 066901
- Zhang, J. & Zhang, X. 2018, *Nature Commun.*, 9, 1833
- Zheng, Z., Berlind, A. A., Weinberg, D. H., et al. 2005, *ApJ*, 633, 791